NBS TECHNICAL NOTE 1099

NBS
PUBLICATIONS

U.S. DEPARTMENT OF COMMERCE / National Bureau of Standards

Electromagnetic Compatibility and Interference Metrology

M.T. Ma
M. Kanda

The National Bureau of Standards[1] was established by an act of Congress on March 3, 1901. The Bureau's overall goal is to strengthen and advance the nation's science and technology and facilitate their effective application for public benefit. To this end, the Bureau conducts research and provides: (1) a basis for the nation's physical measurement system, (2) scientific and technological services for industry and government, (3) a technical basis for equity in trade, and (4) technical services to promote public safety. The Bureau's technical work is performed by the National Measurement Laboratory, the National Engineering Laboratory, the Institute for Computer Sciences and Technology, and the Institute for Materials Science and Engineering.

The National Measurement Laboratory

Provides the national system of physical and chemical measurement; coordinates the system with measurement systems of other nations and furnishes essential services leading to accurate and uniform physical and chemical measurement throughout the Nation's scientific community, industry, and commerce; provides advisory and research services to other Government agencies; conducts physical and chemical research; develops, produces, and distributes Standard Reference Materials; and provides calibration services. The Laboratory consists of the following centers:

- Basic Standards[2]
- Radiation Research
- Chemical Physics
- Analytical Chemistry

The National Engineering Laboratory

Provides technology and technical services to the public and private sectors to address national needs and to solve national problems; conducts research in engineering and applied science in support of these efforts; builds and maintains competence in the necessary disciplines required to carry out this research and technical service; develops engineering data and measurement capabilities; provides engineering measurement traceability services; develops test methods and proposes engineering standards and code changes; develops and proposes new engineering practices; and develops and improves mechanisms to transfer results of its research to the ultimate user. The Laboratory consists of the following centers:

- Applied Mathematics
- Electronics and Electrical Engineering[2]
- Manufacturing Engineering
- Building Technology
- Fire Research
- Chemical Engineering[2]

The Institute for Computer Sciences and Technology

Conducts research and provides scientific and technical services to aid Federal agencies in the selection, acquisition, application, and use of computer technology to improve effectiveness and economy in Government operations in accordance with Public Law 89-306 (40 U.S.C. 759), relevant Executive Orders, and other directives; carries out this mission by managing the Federal Information Processing Standards Program, developing Federal ADP standards guidelines, and managing Federal participation in ADP voluntary standardization activities; provides scientific and technological advisory services and assistance to Federal agencies; and provides the technical foundation for computer-related policies of the Federal Government. The Institute consists of the following centers:

- Programming Science and Technology
- Computer Systems Engineering

The Institute for Materials Science and Engineering

Conducts research and provides measurements, data, standards, reference materials, quantitative understanding and other technical information fundamental to the processing, structure, properties and performance of materials; addresses the scientific basis for new advanced materials technologies; plans research around cross-country scientific themes such as nondestructive evaluation and phase diagram development; oversees Bureau-wide technical programs in nuclear reactor radiation research and nondestructive evaluation; and broadly disseminates generic technical information resulting from its programs. The Institute consists of the following Divisions:

- Ceramics
- Fracture and Deformation[3]
- Polymers
- Metallurgy
- Reactor Radiation

[1] Headquarters and Laboratories at Gaithersburg, MD, unless otherwise noted; mailing address Gaithersburg, MD 20899.
[2] Some divisions within the center are located at Boulder, CO 80303.
[3] Located at Boulder, CO, with some elements at Gaithersburg, MD.

Electromagnetic Compatibility and Interference Metrology

M.T. Ma
M. Kanda

Electromagnetic Fields Division
Center for Electronics and Electrical Engineering
National Engineering Laboratory
National Bureau of Standards
Boulder, Colorado 80303

U.S. DEPARTMENT OF COMMERCE, Malcolm Baldrige, Secretary

NATIONAL BUREAU OF STANDARDS, Ernest Ambler, Director

Issued July 1986

National Bureau of Standards Technical Note 1099
Natl. Bur. Stand. (U.S.), Tech Note 1099, 178 pages (July 1986)
CODEN:NBTNAE

U.S. GOVERNMENT PRINTING OFFICE
WASHINGTON: 1986

For sale by the Superintendent of Documents, U.S. Government Printing Office, Washington, DC 20402

CONTENTS

ELECTROMAGNETIC COMPATIBILITY AND INTERFERENCE METROLOGY

edited by
M. T. Ma and M. Kanda

Electromagnetic Fields Division
National Bureau of Standards
Boulder, CO 80303

The material included in this report is intended for a short course on electromagnetic compatibility/interference (EMC/EMI) metrology to be offered jointly by the staff of the Fields Characterization Group (723.03) and the Interference Characterization Group (723.04) of the Electromagnetic Fields Division (723). The purpose of this short course is to present a review of some of the radiated EMC/EMI measurement methods, to which the National Bureau of Standards (NBS) at Boulder, Colorado, has made significant contributions during the past two decades. The technical foundation for these methods, and interpretations of the measured results are emphasized, as well as strengths and limitations.

The entire course is presented in nine chapters with the introductory part given as Chapter 1. The particular measurement topics to be covered are: i) open sites (Chapters 2 and 6), ii) transverse electromagnetic cells (Chapter 3), iii) techniques for measuring the electromagnetic shielding of materials (Chapter 4), iv) anechoic chambers (Chapter 5), and v) reverberating chambers (Chapter 8). In addition, since small probe antennas play an important role in some of the EMC/EMI measurements covered herein, a separate chapter on various probe systems developed at NBS is given in Chapter 7. Selected contemporary EMI topics such as the characterization and measurement of a complex EM environment, interferences in the form of out-of-band receptions to an antenna, and some conducted EMI problems are also briefly discussed (Chapter 9).

Key words: anechoic chamber; complex electromagnetic environment; conducted electromagnetic interference (CEMI); electromagnetic compatibility (EMC); measurement methodology; open sites; out-of-band responses; probes; radiated electromagnetic interference (EMI); reverberating chamber; shielding of materials; transverse electromagnetic (TEM) cell.

Chapter 1. INTRODUCTION

Electromagnetic compatibility/interference (EMC/EMI) may not be household words yet, but their effects are widely apparent because of the prolific use of electronics and digital circuits in a variety of products (television sets, personal computers, microwave ovens, automobiles, etc.). Over the years, the undesirable effects of the electromagnetic environment have been described by several terms such as radio frequency interference (RFI), radio noise, electromagnetic pollution, EMC and EMI. The IEEE Dictionary defines EMC and EMI as follows [1]:

EMC: The capability of electronic equipment or systems to be operated in the intended operational electromagnetic environment at designed levels of efficiency.

EMI: Impairment of a wanted electromagnetic signal by an electromagnetic disturbance.

One of the first recorded cases of EMI was documented in 1927 by the Federal Aviation Agency [2]. They observed that an aircraft altimeter was giving faulty readings and the problem was caused by interference generated by the ignition system of the aircraft. The first EMC military standard was published in 1945, entitled "Interference Measurements, Radio, Methods of 150 kc to 20 Mc (for components and complete assemblies)" [3].

Some electronic equipment such as transmitters are designed to supply radio-frequency (RF) power at selected frequencies to antennas, from which the signal is radiated intentionally. Signals which are radiated at other than the intended frequencies are undesirable and called spurious emissions, a form of EMI. Other electronic equipment such as computers are designed to function as nonradiators. Ideally, a computer performs its tasks and all signals generated within the system are contained and not radiated. However, in practice, some of these internal signals may be radiated as EMI.

The process of establishing the electromagnetic compatibility of electronic equipment usually requires two steps. First, measurements are made to determine if any undesired signals being radiated from the equipment (radiated EMI) and/or appearing on the power lines, control lines, or data lines of the equipment (conducted EMI) exceed limits set forth by the using agency. This kind of measurement is commonly referred to as emission testing. The second step is to expose the electronic equipment to selected levels of electromagnetic (EM) fields at various frequencies to determine if the equipment can perform satisfactorily in its intended operational environment. This process is referred to as susceptibility or immunity testing.

The limits or requirements set forth for EMC testing are usually established by regulatory agencies such as:

1) Federal Communications Commission (FCC), USA,
2) Department of Defense (DoD), EMC Military Standards,
3) Interdepartmental Special Committee on Radio Interference (IRAC), USA,
4) National Center for Devices and Radiological Health (NCDRH), USA,
5) Verboard Deutscher Elektrotechniker (VDE), West Germany,
6) Other foreign agencies.

In addition to the specifications by these regulatory agencies, there are a number of voluntary EMI standards available for use. These standards are usually published by professional organizations that utilize the expertise of many who donate their time and effort in the preparation of documents. A few examples of these organizations are:

1) American National Standards (ANS) Committee C63 on Radio-Electrical Coordination, and Committee C95 on RF Radiation Levels for Personal Safety,
2) Institute of Electrical and Electronics Engineers, Inc. (IEEE), EMC Society Standards Committee,
3) Society of Automotive Engineers (SAE),
4) Electronic Industries Association (EIA) G46 Committee on EMC,
5) Radio Technical Commission for Aeronautics (RCTA),
6) International Special Committee on Radio Interference (CISPR), and
7) International Standards Organization (ISO).

There are numerous measurement methods available for making radiated EMC/EMI tests depending on the following considerations:

1) size of the test equipment,
2) frequency range,
3) test limits,
4) types of fields to be measured (electric or magnetic),
5) polarization of the field, and
6) electrical characteristics of the test signal (frequency or time domain).

Because each method has limitations of one kind or another, no one method is ideal for all tests. Certain regulatory standards such as MIL-STD 462 [4] or FCC part 15 [5] do specify a particular method.

The purpose of this short course is to review some of the radiated EMC/EMI measurement methods, in which the National Bureau of Standards (NBS) at Boulder, Colorado has been involved in the past two decades [6]. The technical foundation for these methods, and the interpretation of measured results are emphasized, as well as strengths and limitations. The entire course is presented in nine chapters with the introductory part as Chapter 1. The specific measurement methods to be covered are:

1) open sites (Chapters 2 and 6),
2) transverse electromagnetic (TEM) cells (Chapter 3),
3) techniques for measuring electromagnetic shielding of materials (Chapter 4),
4) anechoic chambers (Chapter 5), and
5) reverberating chambers (Chapter 8).

In addition, since small probe antennas play an important role in some of the EMC/EMI measurement methods covered in this short course, a separate chapter on various probe systems developed at NBS is included (Chapter 7). Furthermore, selected contemporary topics such as the characterization and measurement of a complex EM environment, interferences in the form of out-of-band receptions by an antenna in modern communication systems, and some of the conducted EMI problems are also briefly discussed (Chapter 9). Necessary laboratory demonstrations at the NBS site (if the course is conducted in Boulder) showing how to make the required measurements are also considered an integral part of the course.

Chapter 2, covers open site facilities. An open site consists of a large ground plane which provides a well-defined EM environment for making measurements. Such measurement facilities have been in use for a long time, and are still required for complying with testing regulations set by many agencies and committees. They can be employed to perform both radiated emission and susceptibility tests. The fundamentals such as the effects due to mutual impedances between the transmitting and receiving antennas involved in the measurement, the degree of impedance mismatches between the antenna terminal and a receiver, insertion loss, various definitions for site attenuation, some practical measurement procedures, and comparisons between actual measurement results and theoretical predictions will be discussed. This chapter was contributed by R. G. FitzGerrell (723.04) and M. Kanda (723.03).

A related chapter on use of an open site for performing standard calibration services and other measurements from 10 kHz to 10 GHz is given in Chapter 6. Both the electric-field and magnetic-field standards, the definition of antenna factor, a simple model for theoretical computation of the field strength produced by those commonly used antennas, and measurement arrangements will be given. This chapter was prepared by E. B. Larsen and M. Kanda of 723.03.

Chapter 3 contains a discussion of transverse electromagnetic (TEM) cells. A TEM cell is an expanded section of transmission line used to create an isolated testing environment for low-frequency applications. The cell's characteristic impedance, cut-off frequencies, higher-order modes, detailed field distribution inside the cell when it is used for susceptibility testing, resonant frequencies, measurement considerations for both emission and susceptibility, and interpretations of measurement results will be covered. This chapter was prepared by M. T. Ma, M. L. Crawford, and P. F. Wilson, all of 723.04.

The topics of measuring the electromagnetic shielding effectiveness of materials, comparisons of measurement results by various techniques, and interpretation of results based on theoretical models will be discussed in Chapter 4. This chapter was contributed by P. F. Wilson, J. W. Adams and M. T. Ma, all of 723.04.

Chapter 5 deals with anechoic chamber measurements. The prime objective of using an anechoic chamber is to simulate a free-space condition over a finite test volume inside the chamber for testing and calibration purposes. Methods of determining net power supplied to a source antenna and necessary near-field corrections in transmitting antenna gains will be presented. This chapter was contributed by M. Kanda, R. D. Orr, and W. J. Anson of 723.03.

A summary of the development of various probe antennas at NBS for accurate measurements of EM fields is given in Chapter 7. Earlier and recent models, their special features, considerations for future models, a suggested mathematical modeling for diodes included in the measurement system, and application of electro-optic techniques will be discussed in this chapter. This chapter was contributed by M. Kanda and K. D. Masterson of 723.03.

Chapter 8 presents a relatively new measurement tool, namely, the reverberating chamber. The main purpose is to generate a statistically average field throughout a test zone inside the chamber for various high-frequency applications. The field strength level so generated is usually very high. The basic principle involved in this facility, theoretical considerations for designing a reverberating chamber, measurement specifics, the chamber quality factor, characterization of the field environment created inside the chamber, and interpretations of measurement results will be covered. The chapter was contributed by M. L. Crawford and M. T. Ma of 723.04.

Chapter 9 summarizes three selected contemporary EMI topics: the characterization and measurement of a complex electromagnetic environment contributed by J. P. Randa and M. Kanda of 723.03; out-of-band EMI problems contributed by D. A. Hill of 723.04; and some conducted EMI problems contributed by B. A. Bell of the Electronic Instrumentation and Metrology Group (722.02) of the Electrosystems Division (722) in Gaithersburg, MD.

REFERENCES

[1] Jay, F. ed. IEEE Standard Dictionary of Electrical and Electronics Terms, ANS/IEEE Std 100-1977, 2nd ed., New York, NY: Wiley and Sons; 1977.

[2] Donaldson, E. E.; Free, W. R.; Robertson, D. W.; Woody, J. A. Field measurements made in an enclosure. Proc. IEEE, Vol. 66(4): 464-472; 1978 April.

[3] Jan-I-225, Joint Army-Navy Specification. Interference measurements, radio methods of, 150 kilocycles to 20 Megacycles (for components and complete assemblies). 1945 June 14.

[4] MIL-STD-462. Electromagnetic interference characteristics, measurement of. 1967 July 31.

[5] FCC methods of measurement of radio emission from computing devices FCC Rules, pt. 15, Subpt. J, Appendix A (July 1981) and FCC 83-352 order on general docket 80-284, Appendix B. 1983 July.

[6] Ma, M. T; Kanda, M; Crawford, M. L; Larsen, E. B. A review of electromagnetic compatibility/interference measurement methodologies. Proc. IEEE, Vol. 73(3): 388-411; 1985 March.

Traditionally, open-site measurements provide a straightforward approach to evaluating the EMI characteristics of the electronic equipment under test. An ideal site consists of obstruction-free plane ground and the hemisphere above it, both infinite in extent. The quality of measurements made using natural earth as the site depends on the ground constants. To obtain more reliable measurement results, a metal ground plane or screen of a reasonable size is normally recommended. The size used at NBS is a 30m x 60m wire mesh ground with an approximate lower frequency limit in the neighborhood of 20 MHz. One important factor to be determined in application of this facility is the site attenuation or insertion loss between a source and a receiver. The site attenuation is herein defined as the ratio of the input power to the transmitting antenna (or the voltage at the source signal generator) to the power at the load impedance connected to the receiving antenna (or the voltage appearing across the load). Thus, this definition includes mismatch losses but not balun or cable losses. As will be seen later, once the site attenuation is determined accurately, the characteristics of an unknown emission source can then be evaluated by the measurement results from a standard receiving antenna. The information so obtained is, of course, important for assessing the electromagnetic environment created by this unknown emitter.

To facilitate the evaluation of this factor, two polarization-matched antennas (one for transmitting and one for receiving) are set up above a ground plane as shown in Fig. 2.1. The following parameters must also be specified: horizontal separation distance between the two antennas; antenna type and polarization; and impedances of the transmitting and receiving systems connected to the antenna terminals. Sometimes, the relative insertion loss defined as the power indicated by the receiver at an initial receiving antenna height compared with that at different heights, is evaluated instead. Under this situation, site attenuation is then defined as the minimum relative insertion loss measured between the terminals of two polarization-matched antennas located on the test site when the receiving antenna is moved vertically over a specified height range while the transmitting antenna height remains unchanged [1]. Site attenuation is then determined as a function of frequency and horizontal separation distance between the antennas for a given transmitting antenna height above the ground. In this chapter, all the measurements are made from the NBS wire mesh ground screen and results are presented in accordance with this latter definition.

Site attenuation measurement data obtained from a given site can be used to compare with those from a standard or reference site to assess the site quality. Deviation between the measured site attenuation and the theoretical result based on an ideal site then serves as an indication of site imperfection.

2.1 Site Attenuation Calculations

Considering an antenna system shown in Fig. 2.1 from the circuit viewpoint and assuming that the reciprocity principle applies, we have

$$\begin{aligned} V_1 &= I_1 Z_{11} + \alpha I_1 Z_{11'} + I_2 Z_{12} + \alpha I_2 Z_{12'} \quad , \\ -I_2 Z_r &= I_1 Z_{12} + \alpha I_1 Z_{1'2} + I_2 Z_{22} + \alpha I_2 Z_{22'} \quad , \end{aligned} \tag{2.1}$$

where

Z_{rs} = mutual impedance between #r and #s antennas (r' and s' indicate images of #r and #s antennas),

V_1 = input voltage for #1 (transmitting) antenna,

I_1 = input current for #1 antenna,

I_2 = output current for #2 (receiving) antenna,

Z_r = impedance of the receiver attached to the feedpoint of antenna #2,

and

α = ground reflection coefficient.

Application of the relation $Z_{1'2} = Z_{2'1}$ to (2.1) yields

Z_{i1} = input impedance of #1 antenna = V_1/I_1

$$= Z_{11} + \alpha Z_{11'} - (Z_{12} + \alpha Z_{1'2})^2/(Z_{22} + \alpha Z_{22'} + Z_r) , \tag{2.2}$$

and

$$Z_{i2} = \text{input impedance of \#2 antenna}$$
$$= Z_{22} + \alpha Z_{22'} - (Z_{12} + \alpha Z_{1'2})^2/(Z_{11} + \alpha Z_{11'} + Z_s) , \tag{2.3}$$

where

Z_s = impedance of the signal generator, connected to the feedpoint of antenna #1.

The power supplied to the transmitting antenna (#1) is then given by

$$P_t = \frac{1}{2} |I_1|^2 \, \mathrm{Re}(Z_{i1}) \quad , \tag{2.4}$$

the voltage induced at the output terminal of the receiving antenna (#2) by

$$V_2 = I_1(Z_{12} + \alpha Z_{1'2}) + \alpha I_2 Z_{22'} = I_1 Z_m \quad , \tag{2.5}$$

where

$$Z_m = Z_{12} + \alpha Z_{1'2} + \alpha (I_2/I_1) Z_{22'} \quad . \tag{2.6}$$

The maximum possible power accepted by a matched receiver is

$$P_r = \frac{1}{8} \frac{|V_2|^2}{\mathrm{Re}(Z_{i2})} \quad . \tag{2.7}$$

In accordance with the site attenuation measurement method described in the I.E.C. document [2], we have

$$S^2_{IEC} = \text{I.E.C. (power) site attenuation} = P_t/P_r$$
$$= 4 \, \mathrm{Re}(Z_{i1}) \, \mathrm{Re}(Z_{i2}) \, |I_1|^2/|V_2|^2 \quad . \tag{2.8}$$

Note that the above relation is true only under the ideal (conjugate match) condition. In practice, this condition is certainly not realistic, because the input impedances, Z_{i1} and Z_{i2}, are varying as a function of horizontal separation distance and antenna heights while the receiver load may be a constant.

From the definition of the site attenuation measurement method described in the FCC document [3], the site attenuation (voltage) is given by

$$S_{FCC} = \frac{1}{2} \frac{|Z_S + Z_{i1}| \cdot |Z_R + Z_{i2}| \cdot |I_1|}{Z_R \cdot |V_2|} \quad , \tag{2.9}$$

where Z_S is the characteristic impedance of a coaxial cable connected to the transmitting antenna, Z_R is that connected to the receiving antenna, and V_2 is given in (2.5).

If the impedances of the transmitting and receiving antennas are matched at both terminals of the coaxial cables, and both antennas are identical and have the same height above the ground plane, $Z_S = Z_{i1} = Z_{i2} = Z_R$ = real (resistive only), the (power) site attenuation defined by I.E.C. becomes equal to the square of the (voltage) site attenuation of F.C.C., i.e.,

$$S^2_{IEC} = S^2_{FCC} \quad . \tag{2.10}$$

In practice, the coaxial cable and antenna terminal are, most likely, not matched. Then mismatch loss has to be incorporated into the calculation. Because of possible mismatch, the net power out of the transmitting antenna, P'_t , is given by

$$P'_t = P_{inc} \left[1 - \frac{Z_{i1} - Z_S}{Z_{i1} + Z_S}\right] \quad , \tag{2.11}$$

where P_{inc} represents the power supplied to the transmitting antenna.

The actual input current, I'_1 , then becomes

$$I'_1 = [P'_t \;/\; \mathrm{Re}(Z_{i1})]^{1/2} \quad , \tag{2.12}$$

and the open-circuit voltage induced at the feedpoint of the receiving antenna is

$$V'_2 = |I'_1 \; Z_m| \quad , \tag{2.13}$$

where Z_m is given in (2.6)

The actual power received by the receiver is

$$P'_r = \mathrm{Re}(Z_R) \; [V'_2 \;/ |Z_R + Z_{i2}|]^2 \quad . \tag{2.14}$$

Since Z_{i2} is a function of antenna height, frequency, and ground constants, its value changes accordingly. For a fixed Z_R, frequency, and ground, we record the maximum value of P'_r when the receiving antenna height is changed. The site attenuation (based on power consideration) is then defined as

$$S^2_{NBS} = 10 \log \left[P_{inc}/(P'_r)_{max}\right] \quad \mathrm{dB} \quad . \tag{2.15}$$

2.2 Mutual Impedance Calculations

Since the site attenuations defined in either (2.8), (2.9) or (2.15) involve the mutual impedance, we now show how to calculate the mutual impedance between dipole antennas. For the two monopoles above a perfectly conducting plane shown in Fig. 2.2, which may be considered to represent two dipole antennas in free space, the mutual impedance between antenna #1 and antenna #2 is defined as

$$Z_{21} = - V_{21}/I_1(0) \quad , \tag{2.16}$$

where $I_1(0)$ is the base current in antenna #1, and the open-circuit voltage V_{21} produced at antenna #2 by $I_1(0)$ is given by

$$V_{21} = \frac{1}{I_2(0)} \int_0^{h_2} E_{z21} \; I_2(z) \; dz \quad , \tag{2.17}$$

with $I_2(z)$ as the current distribution along antenna #2, E_{z21} as the parallel component of the incident field along antenna #2, and h_2 as the length of antenna #2.

The current distribution on antenna #2 is assumed to be sinusoidal in this chapter for simplicity reason,

$$I_2(z) = I_{2m} \sin k(h_2 - z) \tag{2.18}$$

with $k = 2\pi/\lambda$ (λ = wavelength), and the parallel field component E_{z21} due to an assumed sinusoidal current distribution, $I_{1m} \sin k(h_1 - z)$, on antenna #1 is given by

$$E_{z21} = -j\, 30\, I_{1m} \left(\frac{\exp(-jk\, r_1)}{r_1} + \frac{\exp(-jk\, r_2)}{r_2} - 2 \cos kh_1 \frac{\exp(-jk\, r_0)}{r_0} \right) , \tag{2.19}$$

where h_1 is the length of antenna #1, d is the horizontal separation distance between antennas,

$$r_o = [d^2 + z^2]^{1/2} ,$$

$$r_1 = [d^2 + (h_1 - z)^2]^{1/2} ,$$

and

$$r_2 = [d^2 + (h_1 + z)^2]^{1/2} .$$

Inserting (2.17) and (2.19) into (2.16), we obtain an expression for the mutual impedance. For the case of half-wave dipole antennas (quarter-wave monopoles), $h_1 = h_2 = \lambda/4$, a much simplified expression results [4]:

$$Z_{21} = R_{21} + j\, X_{21} , \tag{2.20}$$

where

$$R_{21} = 15\{2Ci(kd) - Ci[(k^2d^2 + \pi^2)^{1/2} - \pi] - Ci[(k^2d^2 + \pi^2)^{1/2} + \pi]\} ,$$

and

$$X_{21} = 15\{Si[(k^2d^2 + \pi^2)^{1/2} - \pi] + Si[(k^2d^2 + \pi^2)^{1/2} + \pi] -2Si(kd)\} .$$

Similar expressions may be derived for other antenna lengths [4]. The above sine integral Si(x) and cosine integral Ci(x) are defined respectively as

$$Si(x) = \int_0^x \frac{\sin \nu}{\nu} d\nu , \tag{2.21}$$

and

$$Ci(x) = - \int_x^\infty \frac{\cos \nu}{\nu} d\nu . \tag{2.22}$$

The cosine integral Ci(x) may also be rewritten as:

$$Ci(x) = \ln x + C - S_1(x) , \tag{2.23}$$

where C = 0.577 is known as the Euler's constant, and

$$S_1(x) = \int_0^x \frac{1 - \cos \nu}{\nu} d\nu$$

$$= \frac{x^2}{2 \cdot 2!} - \frac{x^4}{4 \cdot 4!} + \frac{x^6}{6 \cdot 6!} - \cdots \qquad (2.24)$$

Figure 2.3 shows the amplitude and phase of the mutual impedance between equal-length dipole antennas as a function of antenna separation distance. More general cases of the mutual impedance calculations for collinear or echelon arrangements with arbitrary antenna lengths can be found in [5].

2.3 Measurement Technique and Results

The test range geometry and mutual-impedance relations have been shown in Fig. 2.1 for horizontal polarization. The value of the base current, $I_1(0)$, is calculated by assuming that one watt of power is delivered to the transmitting dipole (#1 antenna, P_{inc} = 1 W) which has an input impedance given in (2.2). In our calculation of Z_{i1}, we have simplified the procedure by neglecting Z_{12} and $Z_{1'2}$, thus assuming that the input impedance of the transmitting dipole is unaffected by the current induced in the receiving dipole's finite load impedance. For calculating Z_m in (2.6), we have neglected $Z_{22'}$. The value of Z_{11} is calculated using equations given by Schelkunoff [6]. The input impedance of the receiving dipole, Z_{i2}, is calculated in the same manner, and is then used to calculate the received power according to (2.14). The site attenuation is then calculated using (2.15) with $Z_S = Z_R$ = 100 Ω. We also have assumed that the site has a perfectly conducting ground (α = −1 for horizontal polarization, and +1 for vertical polarization).

Since the relative insertion loss represents the ratio of the power delivered to the transmitting dipole terminals to the power received at the receiving dipole terminals, it is a positive quantity. Site attenuation is the minimum insertion loss occurring when the receiving dipole is scanned in height. The height-scan patterns presented in Fig. 2.4 show calculated insertion loss for horizontally polarized (HP) and vertically polarized (VP) dipoles with a 3 m separation distance. The transmitting dipole is 2 m above perfectly conducting ground. Site attenuation is the single minimum value of each pattern. Figure 2.5 shows site attenuation versus frequency for separation distance (d) of 3 m, 10 m, and 30 m. Heights scanned are 1 m to 4 m at the 3 m and 10 m separation distances, and 2 m to 6 m at the 30 m separation distance except for vertical polarization when the half-length of the receiving dipole would touch the ground [1]. The lower tip of the vertically polarized dipole is always positioned 5 cm or more above the ground. Calculated site attenuation provides an ideal reference. Deviations of measured data from the reference indicate site imperfection.

Figure 2.6 shows the measurement procedure used for determining site attenuation. The reference relative insertion loss obtained from Fig. 2.6(a) is a received signal level expressed in dBm, dependent upon the output level of the signal generator and balun, cable, and attenuator losses. The output level remains fixed during the measurement procedure and is somewhat arbitrary. It is less than the maximum level acceptable by the receiver but great enough so that the signal level in Fig. 2.6(b) is well above the ambient noise level.

The dipole antennas used to measure site attenuation at NBS have hybrid junctions for antenna baluns. Equal length coaxial cables from the dipole terminals to the hybrid junction form a 100-Ω, balanced shielded transmission line. As a result, the receiving and transmitting system impedances are 100 Ω. This value is used to calculate the reference site attenuation data shown in Fig. 2.5, as the solid lines for very thin dipoles and (++) points for dipoles with dimensions of those actually used for the measurements. To insure that this impedance is approximately 100 Ω, miniature 3 dB attenuators are permanently installed in the four separate cables at the point of attachment to the dipole terminals.

The receiving dipole is moved up and down over the specified height range by a person below the ground screen who observes the receiver display. The maximum received signal level is recorded by a peak sample-and-hold circuit in the receiver. The magnitude of the difference between the reference insertion loss value and this maximum measured value gives site attenuation directly. No additional measurements or corrections are required. The measured data are shown as the circles in Fig. 2.5.

2.4 Error Estimate

Test range antenna heights and separation distance are set within ± 1 cm assuming the ground screen surface is perfectly flat. Dipole height is measured at the dipole feedpoint. The extensible dipoles droop about 16 cm at the tips at 30 MHz. No effort is made to keep these dipoles straight. Calculated errors in site attenuation are at most ±0.09 dB as a result of possible positioning errors (neglecting dipole droop).

The stability of the receiver, signal generator, hybrid junctions, and cables combination is determined by the repeatability of the reference insertion loss measurements, Fig. 2.6(a), performed before and after each subset of measurements. (The three subsets of measurement frequencies are determined by the frequency ranges of the three sets of hybrid junctions.) Over these typically two-hour time periods, the difference between the initial and final reference insertion loss data is at most ±0.11 dB. This variability appears to be predominantly caused by cable handling, connector mating, and moving the signal generator. Since this is a relative insertion loss measurement, not an absolute one, the primary uncertainty is the manufacturer's specified "cumulative fidelity" for the receiver (spectrum analyzer) of "≦ ±1.0 dB over 0 to 80 dB display, 20-30°C". Therefore, a simple worst-case error estimate is (±0.09 ±0.11 ±1.0) ≦ ±1.2 dB.

The statistics of the measured data imply that the uncertainty may be less than half of this worst-case estimate if it is assumed that the calculated data are correct. The average difference between the measured and calculated [calculated - measured, dB] data for horizontal polarization is -0.2 dB with a standard deviation of 0.4 dB calculated using the dB values.

The data for the single measurement set upon which this chapter is based are shown in Table 1. This was the first set of data measured after the preliminary set used to determine the suitability of the various test components. Failure of the air supported fabric cover over the NBS ground screen facility has temporarily halted further measurements. The greatest difference between measured and calculated site attenuation is 1.02 dB for horizontal polarization, where the effect of feed cable reflections is negligible, and 1.94 dB for vertical polarization.

REFERENCES

[1] FitzGerrell, R. G. Site attenuation. Symposium record of the 1985 IEEE Int. Symp. on EMC; 1985 August; Wakefield, MA. 612-617. Also, IEEE Trans. on EMC; EMC-28(1): 1986 February.

[2] I.E.C. 12A (Secretariate) W, 1978 April.

[3] FCC Bulletin, OCE 44 (Docket No. 21371, Appendix B). Calibration of a radiation measurement site: site attenuation. U.S. Government Printing Office, Washington, D. C.; 1977 September.

[4] Jordan, E. C. Electromagnetic Waves and Radiating Systems. Englewood Cliffs, N. J.: Prentice-Hall; 1950.

[5] King, H. E. Mutual impedance of unequal length antennas in echelon. IEEE Trans. Antennas Propag., Vol. AP-5(3): 306-313; 1957 July.

[6] Schelkunoff, S. A.; Friis, H. T. Antennas, Theory and Practice. New York, N. Y.: Wiley and Sons; 1957.

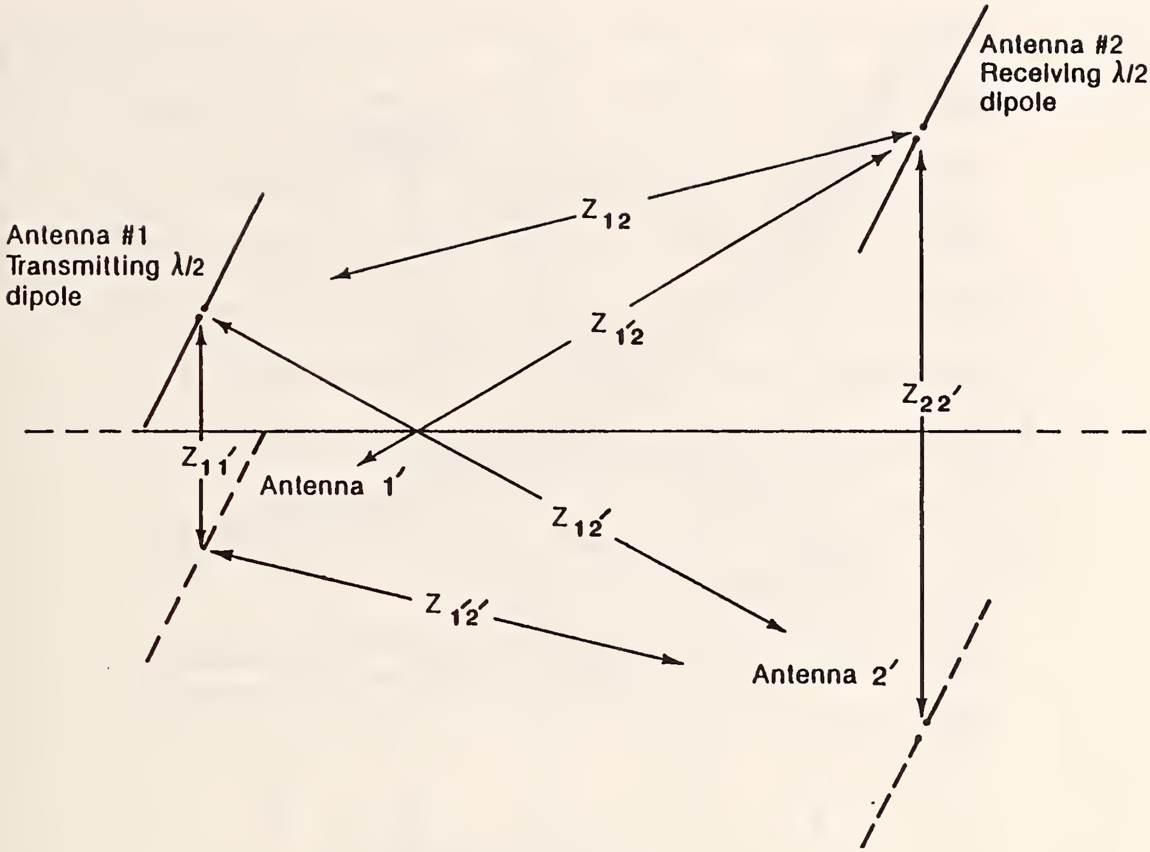

Figure 2.1. Two half-wave dipoles above a ground plane.

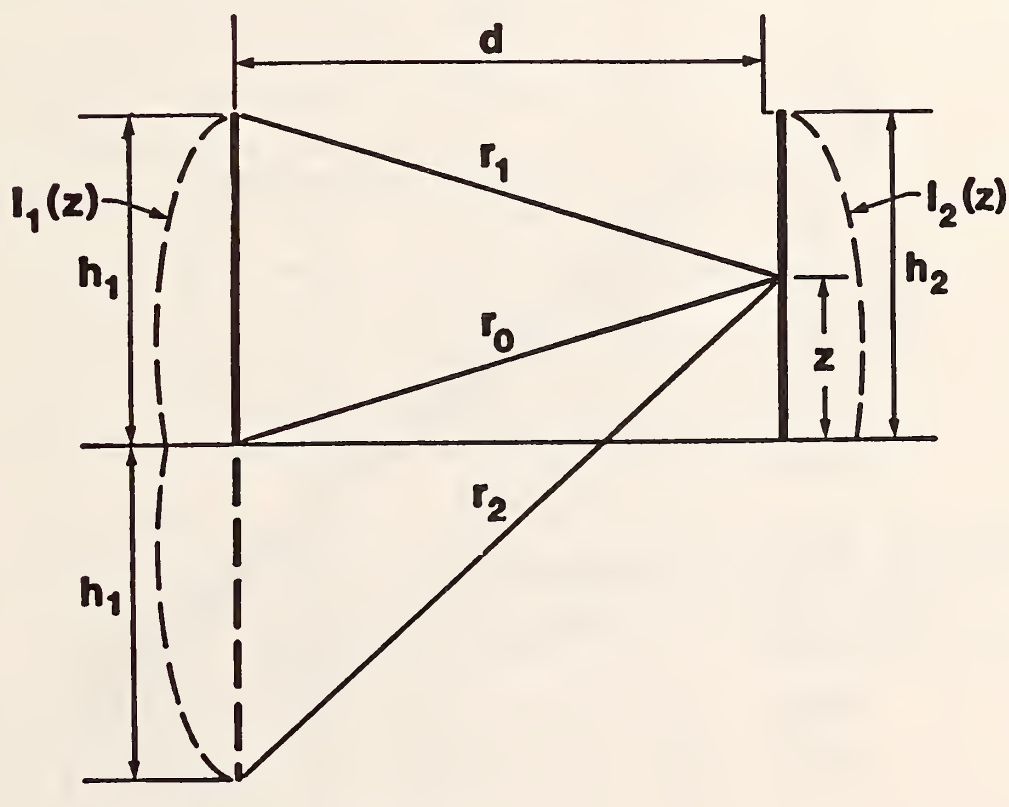

Figure 2.2. Computation of mutual impedance.

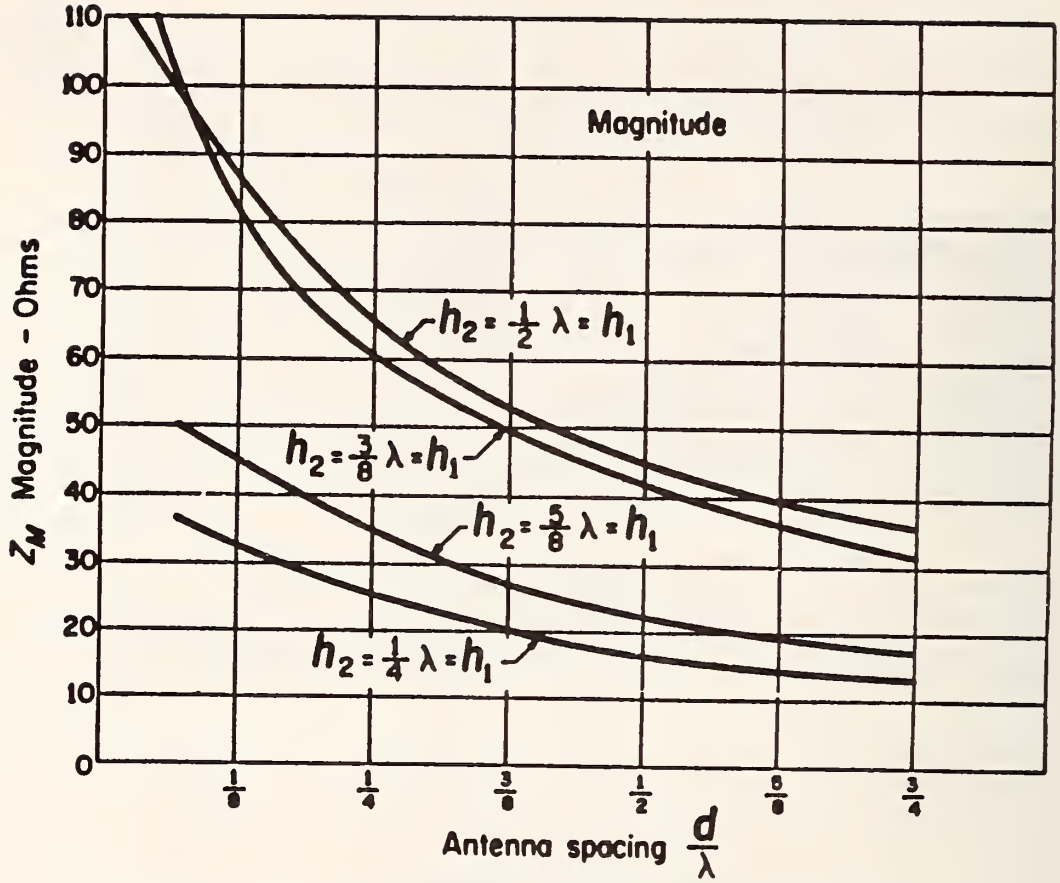

Figure 2.3.(a). Magnitude of the mutual impedance between two equal-length dipole antennas.

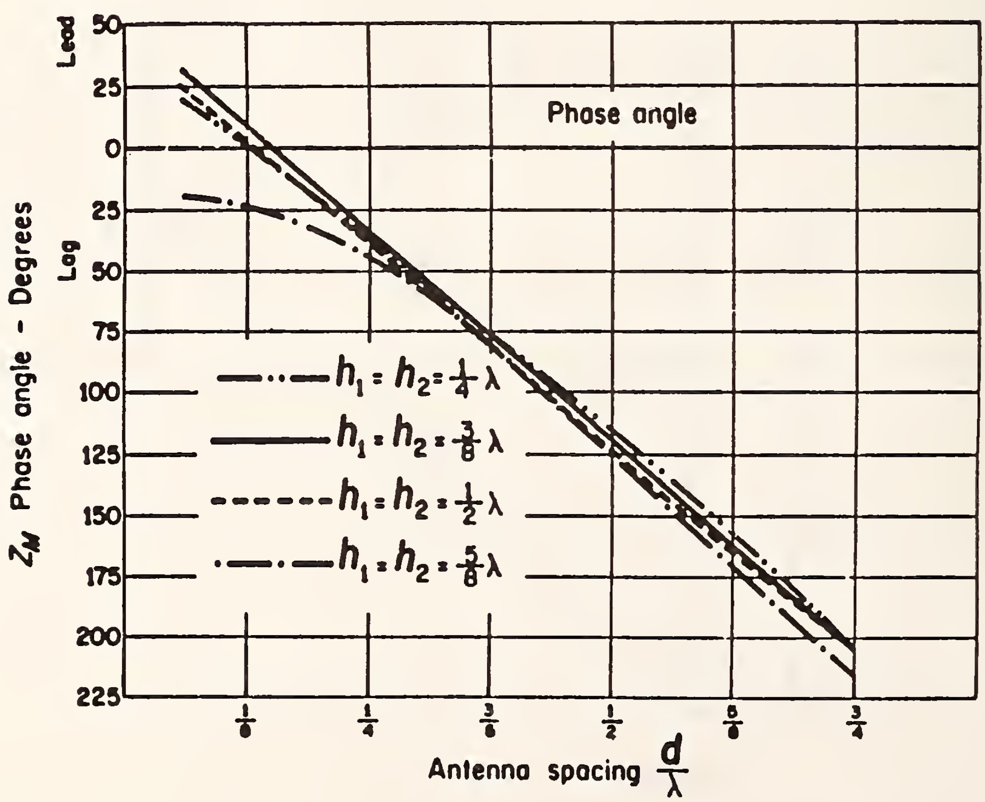

Figure 2.3(b). Argument of the mutual impedance between two equal-length dipole antennas.

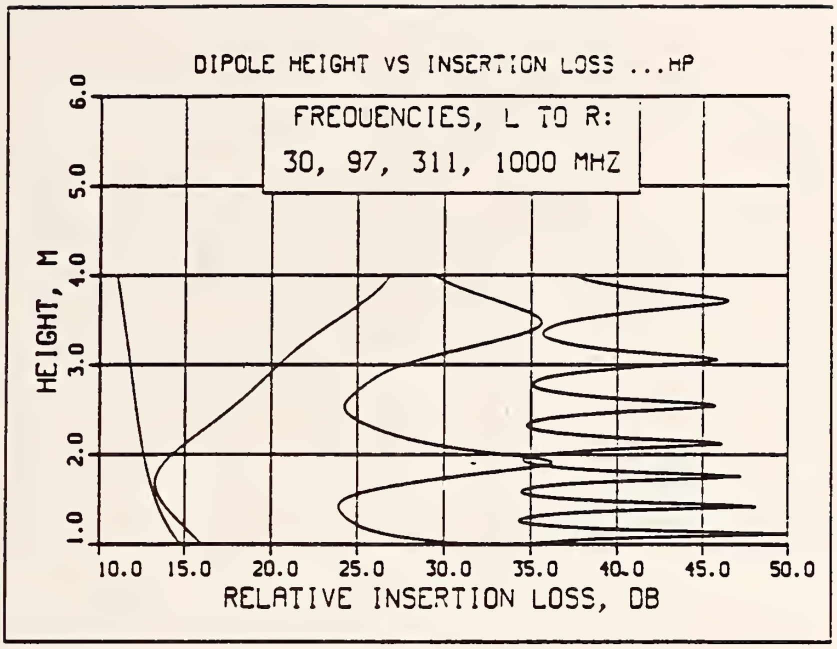

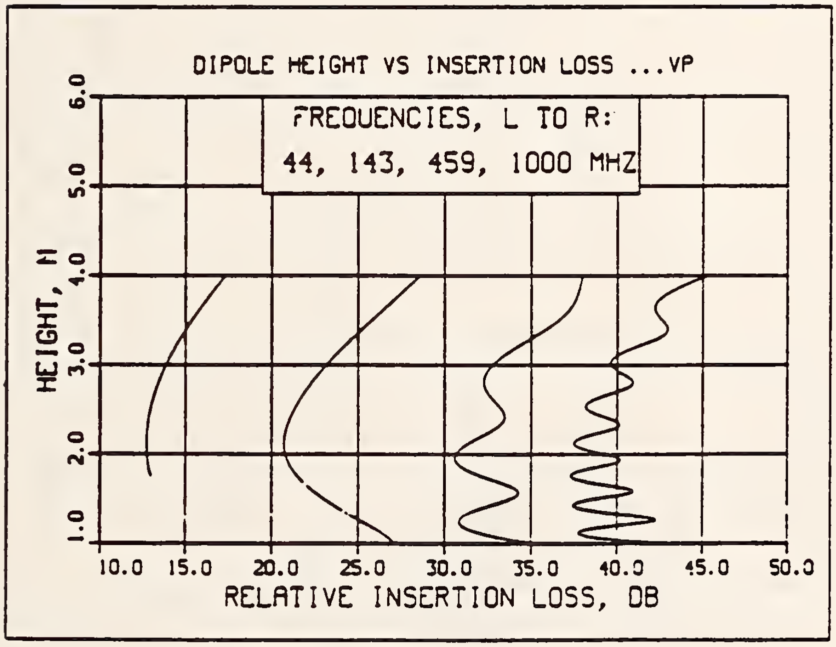

Figure 2.4. Selected relative insertion loss data calculated for horizontally polarized (HP) and vertically polarized (VP) dipoles over perfect ground. Separation distance is 3 m; transmitting dipole height is 2 m.

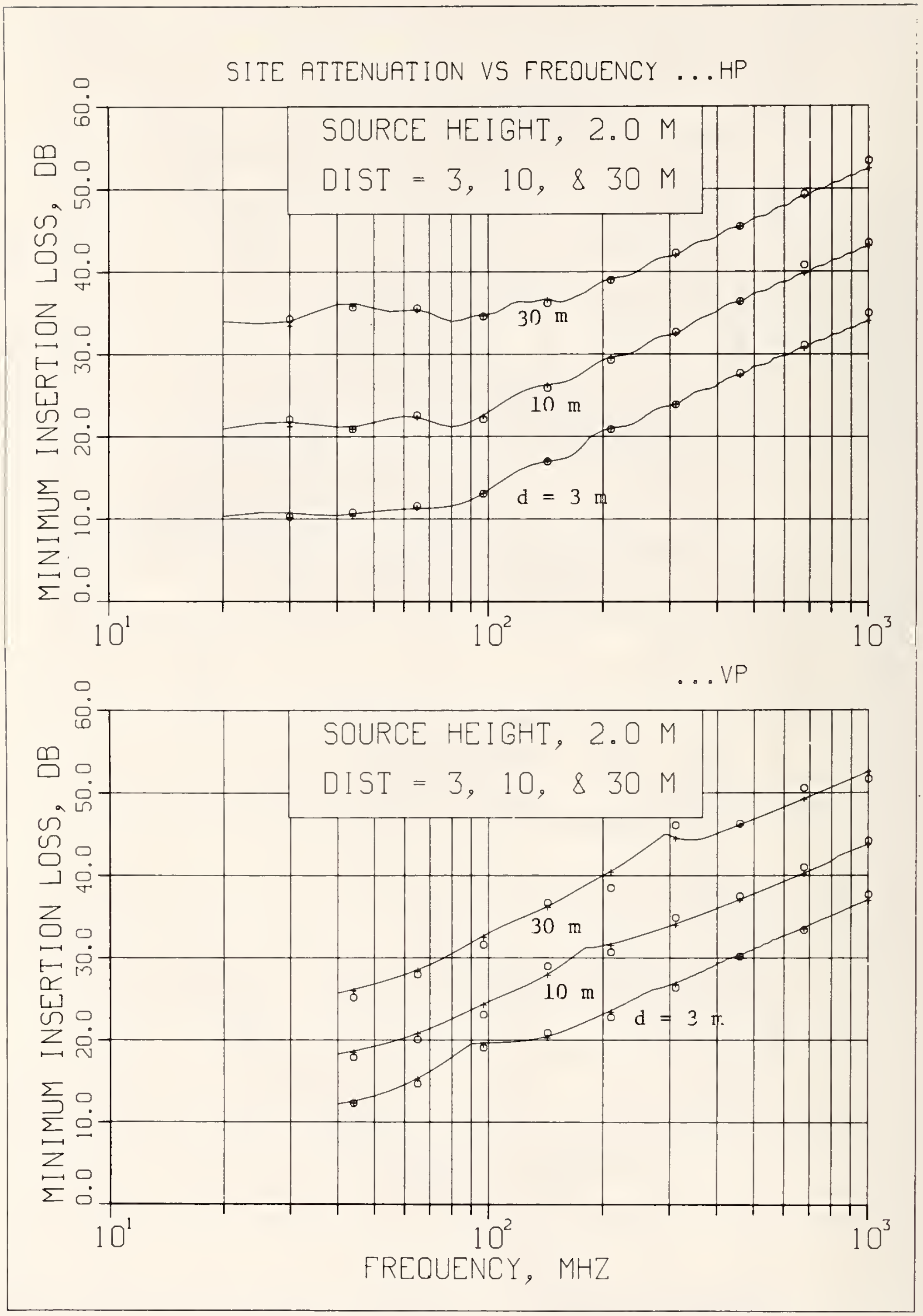

Figure 2.5. Site attenuation for horizontally polarized (HP) and vertically polarized (VP) dipoles over perfect ground. Solid curves are calculated for half-wave dipoles with radius of 1.E-30 m; + + points are calculated for dimensions of actual dipoles. Measured data are shown as o o.

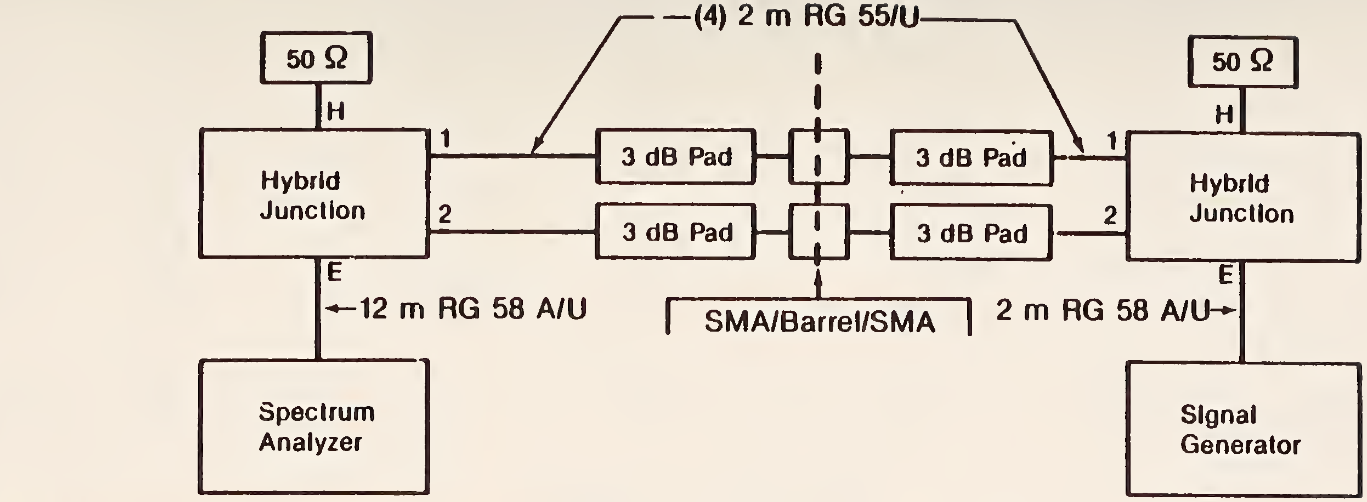

(a) Measure reference insertion loss

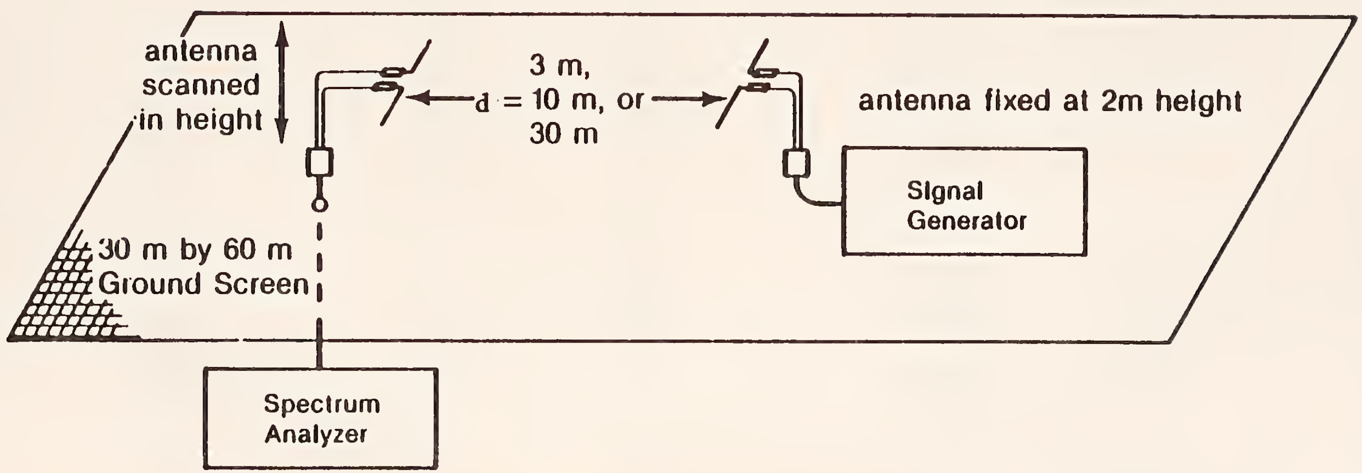

(b) Measure reference insertion loss plus site attenuation

Figure 2.6. Schematic diagram of measurement procedure for determining site attenuation.

Table 1. Measured and Calculated Site Attenuation Data, dB

Horizontal Polarization

Frequency, MHz	3 m Distance		10 m Distance		30 m Distance	
	meas.	calc.	meas.	calc.	meas.	calc.
30.0	10.3	10.182	22.1	21.238	34.3	33.461
44.0	10.8	10.357	20.9	20.912	35.7	35.850
65.0	11.6	11.389	22.6	22.332	35.6	35.350
97.0	13.1	13.124	22.1	22.446	34.6	34.689
143.0	17.0	17.142	25.9	26.261	36.2	36.630
210.0	20.9	20.954	29.3	29.527	39.0	39.057
311.0	23.9	23.903	32.7	32.455	42.3	41.977
459.0	27.7	27.401	36.4	36.370	45.5	45.435
677.0	31.1	30.720	40.8	39.777	49.4	49.078
1000.0	35.0	34.045	43.5	43.112	53.4	52.439

Vertical Polarization

Frequency, MHz	3 m Distance		10 m Distance		30 m Distance	
	meas.	calc.	meas.	calc.	meas.	calc.
44.0	12.3	12.312	17.9	18.507	25.2	26.014
65.0	14.7	15.286	20.1	20.782	28.0	28.508
97.0	19.1	19.438	23.1	24.295	31.6	32.530
143.0	20.9	20.268	29.0	27.909	36.7	36.152
210.0	22.8	23.412	30.7	31.529	38.5	40.437
311.0	26.4	26.798	34.9	33.998	46.1	44.459
459.0	30.2	30.212	37.5	36.998	46.3	46.068
677.0	33.4	33.531	41.0	40.202	50.6	49.230
1000.0	37.7	36.961	44.2	43.779	51.7	52.576

Chapter 3. TRANSVERSE ELECTROMAGNETIC (TEM) CELLS

One of the main limitations inherent in most EMC/EMI susceptibility tests is the requirement of an antenna to radiate electromagnetic waves. Typical antennas are bandwidth limited, and do not have linear phase response versus frequency. Hence, they are useful primarily for frequency-domain measurements, and their applications to transient, impulsive EMI testing and evaluation are very limited. In addition, for accurate measurements, the separation distance between the source antenna and equipment under test (EUT) should be sufficiently large to ensure far-field conditions. This is not always possible, especially in confined chambers or enclosures. Quite often, the requirements of sensitivity and a high-level testing field dictate the need for near-field measurements, which introduce other problems related to field uniformity over the test volume occupied by the EUT and interaction effects. Some of these difficulties may be eliminated or minimized by using TEM cells, because they themselves serve as the transducer and thus eliminate the use of antennas.

The TEM cell was designed based on the concept of an expanded transmission line operated in a TEM mode. As shown in Fig. 3.1, it consists of a section of rectangular coaxial transmission line (RCTL) with tapered sections at both ends. The taper is used as a transition to match the RCTL to standard 50-Ω coaxial cable connectors at the two ports of the cell. The taper sections should be gradual and long enough to minimize perturbation of the TEM wave as it passes from one section to the other. It is generally recommended that this length be at least one half of the cell's width. One of the two ports is usually terminated with a 50-Ω load, while the other port is connected to either a source or a receiver, depending on whether the cell is used for radiated susceptibility or emission testing. The TEM cell provides a shielded environment without introducing the multiple reflections experienced with a conventional shielded enclosure [1]. Hence, external EM signals will not affect the measurement of low-level radiated emission from the EUT. Alternately, a high-level test field generated inside a cell for performing radiated susceptibility tests will not interfere with external electronic systems.

To support a TEM mode, the cell is necessarily a two-conductor system with the region between the inner and outer conductors (either upper or lower chamber) used as the test zone. The cross section of a TEM cell is depicted in Fig. 3.2. Although the center septum (inner conductor) is normally designed to be midway between the top and bottom outer conductors, its position can be modified to have a vertical offset to allow a larger test zone provided by one of the chambers [2],[3]. We limit our discussions in this chapter only to cells with symmetrically located inner conductors, however.

TEM cells offer several advantages in performing EMC/EMI measurements of electrically small equipment and devices. They are portable, simple to build [4], useful for broadband swept-frequency measurements, and capable of providing test field strengths from a few microvolts per meter to a few hundred volts per meter. The cost to build a TEM cell is much lower than those facilities such as anechoic chambers and shielded enclosures. The TEM field generated between the inner and outer conductors simulates very closely a planar far field in free space, and has constant amplitude and linear phase characteristics [5].

The application of TEM cells has limitations. The usable frequency range is from dc to an upper limit determined by the appearance of high-order modes [2],[6],[7]. The volume available for testing purposes is inversely proportional to the upper frequency limit. In addition, since the EUT is placed at the center of the test zone, its size should be small relative to the test volume in order that the field structure associated with the ideal TEM mode existing in an empty cell will not be significantly perturbed.

The most important aspect for a TEM cell user to recognize is that the results obtained from measurements made inside a cell have to be interpreted correctly. The characteristics of an EUT inside a TEM cell are different from those in other environments such as free space [8]. Thus interpretation is crucial, especially if a meaningful comparison with other measurement methods is attempted.

Before presenting the details of using a TEM cell to make radiated susceptibility and emission tests, we will first summarize some basic TEM cell properties.

3.1 Impedance

The characteristic impedance, Z_o, of an RCTL may be expressed in terms of the distributed capacitance per unit length of the transmission line, C_o, by [2],[8]:

$$Z_o = \eta_o \varepsilon_o / C_o \tag{3.1}$$

where $\eta_o = 120\pi$ is the free-space intrinsic impedance in ohms, and $\varepsilon_o = (10)^{-9}/36\pi$ is the air permittivity in farads per meter.

Determination of C_o may be achieved by the method of conformal transformation whereby the geometry of Fig. 3.2 is transformed into a simpler configuration whose capacitance is already known. Because of symmetry, the total capacitance per unit length is just twice that due to either the upper or lower chamber. It can be expressed exactly in terms of the Jacobian elliptical function, which has to be computed numerically [8]. If, however, the aspect ratio satisfies the condition $b/a \leqq 1$, an approximate but simpler expression may be obtained [8]:

$$C_o/\varepsilon_o = 4(w/b) + \frac{8}{\pi} \ln\left(1 + \coth \frac{\pi g}{2b}\right) - \Delta C/\varepsilon_o \quad , \tag{3.2}$$

where the cell parameters a, b, g, and w, all in meters, are indicated in Fig. 3.2. In this form, it is easy to identify the first term, $4w/b$, as the plate capacitance between the center septum and the horizontal walls (top and bottom outer conductors), the second term involving the gap parameter g as the fringing capacitance between the edge of the septum and the vertical sidewalls, and the third term $\Delta C/\varepsilon_o$ as a correction needed to account for the interaction between the two edges. Under the practical condition, $w/b \geqq 1/2$, ΔC is negligible. A graphical presentation for C_o/ε_o is given in Fig. 3.3.

If a characteristic impedance value of, say, 50Ω is desired, we require $C_o/\varepsilon_o = 7.54$. A number of possible TEM cells may be designed, based on (3.2) or Fig. 3.3, to meet this requirement.

3.2. Higher-Order Modes

As mentioned before, the upper frequency limit for a TEM cell is determined by the appearance of higher-order modes which perturb the desired TEM-mode field distribution [2],[6],[7],[9]-[13]. For an infinitely long central RCTL section, the cutoff wavelengths for the first few higher-order modes may be determined numerically [10]. Figure 3.4 presents results for various cell configurations. Alternately, if the gap is small such that terms of the order $(\pi g/2a)^2$ and $(k_c g)^2$ can be neglected when compared to unity, the modal equations listed in Table 3.1 may be used to find the cutoff wavenumbers k_c and frequencies f_c of the first few higher-order modes [13].

In reality, the cell is finite in length and the tapers cause it to act as a cavity. The resonant frequencies f_{res} associated with a particular mode of cutoff frequency f_c are given by

$$f_{res} = \left[f_c^2 + (pc/2d)^2 \right]^{1/2} \quad , \tag{3.3}$$

where p is an integer, $c = 3(10)^8$ m/s is the speed of light, and d (in meters) is the resonance length. Because of the tapered sections, d is not well defined. An average "overall cell length" is usually taken as a first approximation [6]. However, for best results the resonant length needs to be determined mode by mode and cannot be specified theoretically. Some empirical data do exist [12], [13].

It is important to note that a) the influence of the first few higher-order TE modes does not become significant until approaching a resonant frequency, and b) if the septum of the cell is centered symmetrically, the odd-order TE modes are not excited in the empty cell (these modes may exist when an EUT is placed in the cell). Thus the upper useful frequency can exceed the multimode cutoff frequency of the first higher-order mode, but should be less than this mode's associated resonant frequency. For example, the cutoff and resonance frequencies for a cell with a = b = 1 m, w/a = 0.8 (or g/a = 0.2), and d = 4 m are approximately 43 MHz and 66 MHz. Such a cell should be useful at frequencies up to approximately 60 MHz. However, because the TEM cell is a high-Q cavity, the resonances appear at sharply defined frequencies. Thus, there may well exist windows between resonances where TEM cell usage is still quite valid. This very much depends on the particular cell application [12].

Efforts have been made to extend the use of TEM cells to frequencies above cutoff by installing RF absorbers inside the cell [11]. While this effort helps to lower the Q factor of the cell and suppress the multimoding effects, it also has some effect on the fundamental TEM mode. Thus care must be exercised when considering the placement of absorbing materials inside a TEM cell.

3.3 Field Distribution

An analytical expression for the electric field inside an empty TEM cell over the cross section shown in Fig. 3.2, when operated in a TEM mode, is also available in terms of Jacobian elliptical functions [2],[8]. Numerical results for the electric field in a typical symmetric cell are presented in Fig. 3.5. The results have been normalized with respect to V/b, which represents the electric field at the center of the test zone (x = 0, y = b/2) where

$$V = (P_n Z_o)^{1/2} \tag{3.4}$$

is the voltage in volts between the inner and outer conductors, P_n the net power in watts flowing through the cell, and Z_o the characteristic impedance in ohms given in (3.1). Normalized results in the form of x and y components are given in Tables 3.2 and 3.3. Field distribution for certain higher-order modes, while not the major concern of TEM cell users, may be found elsewhere [2],[12],[13].

3.4 Performing Radiated Susceptibility Tests

The main purpose of radiated susceptibility testing is to determine if and how EM energy is coupled into the EUT so as to cause degradation to the equipment's performance. Thus, a criterion for what constitutes degradation of the EUT and how this is translated into measurable parameters is normally established by the user. This criterion may be in the form of video or audio indicators, or by other means when the EMI coupling exceeds a predetermined threshold.

The following steps are suggested as a systematic approach for making the radiated susceptibility evaluation [14].

Step 1. Place the EUT inside the TEM cell: The first step is to place the EUT in a TEM cell, centered in the lower half space below the septum. The first position (position A) as shown in Fig. 3.6a is near the floor but insulated from the floor with approximately 2 cm of foam dielectric. Plastic foams with dielectric constants of 1.04 and 1.08 are readily available, are almost invisible electrically, and make good supporting material. If grounding of the equipment case is desired, the EUT would then be placed on the floor. This position (position A) is used to minimize exposure of the input/output leads associated with an EUT to the test field (to be explained in step 2). Another common EUT position (position B) for testing, as shown in Fig. 3.6b, is midway between the septum and the floor. Again, the EUT is supported on a foam material of low dielectric constant. This position (position B) increases the exposure of leads to the test field. A comparison of the test results to be taken later for both positions A and B should give some indication of how energy is coupled into the EUT. After placing the EUT in positions A and B, the EUT may be reoriented as desired, relative to the field polarization. Typically, the first orientation is with the EUT lying flat as in normal use. Care must be taken to record the placement location and how this is done so that it can be repeated if necessary. It may be helpful to mark the bottom of the cell with a uniform array of scribe marks to assist in determining placement locations precisely.

Step 2. Access the EUT as required for operation and performance monitoring: The EUT input/output and ac power cables should approximate those anticipated for use. Cables should be the same length if possible, be terminated into their equivalent operational impedances so as to simulate the EUT in its operational configuration, and be carefully routed inside the cell to minimize field perturbation. Dielectric guides or holders may be installed in the cell to assure repeatability of the placement location of the cables. These may be placed on the floor to allow the cables to be covered with conductive tape (minimum exposure) and/or on dielectric standoffs to provide coupling of the test field to the leads. If required, any excess portion of the EUT's leads (wiring harness) may be carefully coiled and covered with conductive tape on the floor of the cell. When the leads are bundled together, it may be helpful to twist the input/output monitor leads as separate conductor pairs or use shielded cables to minimize cross coupling between them. It may also be necessary to space the windings in the coil to avoid introducing resonances associated with the coil inductance and distributed capacitance. If braided RF shielding is used, it should be placed in electrical contact with the cell floor, and not in contact with the case of the EUT unless a common ground between the EUT and cell is required. Grounding the two together will influence the results of the susceptibility measurements. The input and output leads, after being connected to the appropriate feedthroughs for accessing and operating the EUT, should also be filtered to prevent RF leakage from the cell, otherwise the shielding integrity of the measurement system will suffer. Care must be exercised in selecting these filters so they do not significantly affect the measured results. The monitor leads used for sensing and telemetering the performance of the EUT may require special high-resistance lines made of carbon-impregnated plastic or fiber optic lines to prevent perturbation of, or interaction with, the test environment. DC signals or signals with frequency components below 1 kHz may be monitored via the high-resistance lines. Radio frequency signals should be monitored via fiber optic lines.

If the monitor signal is at a frequency or frequencies sufficiently different from the susceptibility test frequency or frequencies, metallic leads may be used with appropriate filtering (high-pass, low-pass, band-pass, etc.) at the bulkhead. Such leads, however, will cause some perturbation of the test field; thus, their placement location must be carefully defined for future reference. Note that a separate, shielded filter compartment should be provided on the outside of the cell for housing the filters, as shown in Figs. 3.6a and b.

Step 3. Connect the measurement system as shown in Figures 3.7 and 3.8: Figures 3.7 and 3.8 show the block diagrams of systems using the TEM cell for susceptibility measurements. These figures are used for frequencies from approximately 10 MHz to the recommended upper frequency for the particular cell used. At frequencies below 10 MHz, the dual directional coupler and power meters are replaced by a voltage monitor tee and RF voltmeters. Figure 3.7 is a diagram of essentially a discrete (manually operated) system or can be used for swept frequency testing. Figure 3.8 is a diagram of a system for automated testing under computer control, which allows the test field level in the cell to be carefully controlled and progressively increased over selected frequency ranges and intervals while monitoring the EUT performance. If degradation occurs as determined from a pre-established threshold limit and as evidenced by the EUT monitors, the computer can respond interactively with the EUT, thus limiting the test field level and preventing damage to the EUT. The computer can also be used to store the raw data, process the data incorporating correction factors as needed and output the results to printers or plotters according to the software instructions and format.

Step 4. Initialize the measurement system: This includes zeroing the appropriate instrumentation and measuring the residual offset values of the EUT monitors with the RF source turned off and the EUT turned on in the desired operation mode. These values are then recorded for future reference.

Step 5. Establish the test field and determine the EUT response: After initialization of the measurement system, the RF source is then turned on at the desired test frequency, modulation rate, test wave form, etc., and its output level is increased gradually until the maximum required test level is reached or the EUT response monitors indicate vulnerability. Care must be exercised to ensure that sufficient time is spent at each frequency and field level to allow the EUT to respond. The EUT susceptibility profile is then determined for each position (A or B as shown in Figs. 3.6a and b) and orientation. It may be necessary to test all three orthogonal orientations of the EUT inside the cell. This is required if all surfaces of the EUT to be tested are to be polarization matched to the TEM field of the cell.

If the test frequency is below 10 MHz, the electric field level in V/m generated inside the cell is determined by the RF voltmeter reading, V_{rf} in volts, in accordance with V_{rf}/b, where b is the separation in meters between the septum and the floor. When the test frequency is 10 MHz or above, where the electric length of the cell is significant, the electric field level is determined by V/b, where V is given in (3.4) and the net power, in watts, may be determined by

$$P_n = C_f P_i - C_r P_r \tag{3.5}$$

with C_f and C_r as the respective forward and reverse coupling ratios of a calibrated bi-directional coupler, and P_i and P_r as the indicated incident and reflected coupler sidearm power readings in watts. Note that the absolute level of the test electric field inside the cell is a function of the location of the EUT in the test zone. An appropriate correction can be made based upon the particular cell's cross section. Note also that the size of the EUT relative to the test volume can influence the determination of the amplitude of the test field [see Sect. 3.5].

If the objective of the measurement program is simply to reduce the vulnerability of the EUT to EMI without the additional requirement of determining worst-case susceptibility as a function of absolute exposure field level, one EUT orientation with input/output lead configuration may be tested in one particular operational mode under a pre-selected susceptibility test-field waveform and level. Similar tests may then be duplicated at the same test position with the same lead configuration and test-field waveform and level, after the corrective measures such as providing additional shielding, etc. are made to the EUT. These testing results are then compared to determine the degree of improvement.

Sometimes, it is desirable to monitor the field distribution inside the cell using small calibrated electric and/or magnetic probes, while an EUT is in position. If this is the case, one must be careful in interpreting these monitored results, because the results are a combination of the incident TEM field launched inside the cell and the scattered fields from the EUT and its leads in the near-field. The field so monitored can be quite different from the unperturbed test field, leading to potentially erroneous conclusions. Whenever possible, it is preferable to mount the field-monitoring probes in the other half space of the cell in the mirror image location of the EUT in order to avoid the interaction between the probe and EUT.

3.5 EUT Scattering in a TEM Cell

As indicated earlier, a test object will scatter the incident TEM mode. If the EUT is kept small compared to the chamber height and the operating wavelength, it is reasonable to assume that the cell environment will not be significantly perturbed from its empty state. Small obstacle theory, the dual of small aperture theory, may be used to investigate this problem in a more formal manner [15]. When only the TEM mode is considered, the cell may be viewed as a simple transmission line circuit. The EUT introduces a load which may be represented and analyzed by an equivalent T-network. This allows us to investigate the effects of the load perturbation on the overall TEM cell transmission line characteristics, such as the input impedance. The excitation of the initial higher-order modes may also be studied. This enables one to theoretically assess the expected field perturbation due to EUT scattering. These two topics are discussed briefly below. A more detailed discussion may be found in [15].

The T-network representing the EUT loading may be included in the TEM cell transmission line circuit as shown in Fig. 3.9. The EUT is assumed to be centered in the central test section of length $2L_{RCTL}$. Ideally, the tapered sections of length L_{TAPER} will have the same characteristic impedance (50 Ω) as the test zone, i.e. $Z_{RCTL} = Z_{TAPER} = Z_0$. In practice there is some deviation, thus the taper sections are shown explicitly in the circuit model. Let a_0 and b_0 represent the forward and backward scattering coefficients for the TEM mode. Explicit expressions depending on the polarizabilities of the EUT may be found in [15]. Small obstacle theory predicts that the load impedances Z_a and Z_b (see fig. 3.9) will be given by

$$Z_a = -Z_0 \left\{ \frac{a_0 - b_0}{2 + a_0 - b_0} \right\} \tag{3.6}$$

$$Z_b = -Z_0\{\frac{1}{a_0 + b_0} + \frac{1}{2}\} - \frac{1}{2} Z_a .$$

If the TEM mode is weakly scattered (a_0 and b_0 small), then Z_a and Z_b are approximately given by

$$Z_a = -Z_0\{\frac{a_0 - b_0}{2}\}$$
$$Z_b = -Z_0\{\frac{1}{a_0 + b_0}\} . \quad (3.7)$$

As the EUT size vanishes, both a_0 and b_0 tend toward zero. Therefore $Z_a \to 0$ (short circuit) and $Z_b \to \infty$ (open circuit) as expected.

Tests were performed in a typical NBS cell to assess the validity of the above circuit representation. The cell has dimensions a = 15 cm, b/a = 1, and g/a = .17, yielding a theoretical characteristic impedance Z_0 of 51.6 Ω. Cell impedances were also measured with a time-domain reflectometer. This technique yielded $Z_{TAPER} \approx 51$ Ω and $Z_{RCTL} \approx 49.5$ Ω. Agreement between the theoretical impedance computation, actual measured impedances, and the desired 50-Ω value is usually considered acceptable if they are within 2 Ω. In the figures that follow, the measured impedance values are used in the circuit model. The central section is 30 cm long (L_{RCTL}) while each of the tapers is 25 cm (L_{TAPER}) in length. Figure 3.10 shows the measured and computed (based on fig. 3.9) input impedances (magnitude) for the empty cell terminated with a 50-Ω load. At low frequencies (< 100 MHz), the well-defined 50-Ω load impedance dominates. As frequency is increased, the taper and RCTL impedances become important and the mismatches begin to cause standing-wave variations from the load value. Theory agrees well with the measured data below 400 MHz.

Figure 3.11 shows input impedance data for the same TEM cell loaded with a conducting sphere. The sphere diameter is 43% of the test chamber height. The theoretical curve is little perturbed from the measured data even though this test object occupies a significant portion of the chamber. In fact, both of these curves are similar to the empty-cell data. This type of data suggests that the impedance characteristics of the cell are not highly sensitive to the presence of an EUT.

The scattering coefficients for higher-order modes in a TEM cell may be worked out in a manner similar to those for the TEM mode (a_0,b_0). This enables us to study the field perturbation due to the EUT presence. Rather than consider any specific position in the cell we will look at the primary TEM mode field components (E_y,H_x) at the test chamber center (x=0,y=b/2) as a function of z, the longitudinal distance from the EUT. Figure 3.12 shows data for the same cell and sphere as tested in the previous figures. The frequency was chosen such that $k_0a = 1.4$ which is very near the cutoff frequency of the first higher-order mode. The scattered TE_{10} and TE_{11} modes are included in addition to the scattered TEM mode. The TE_{01} mode does not significantly contribute for a centrally located EUT. As may be seen, there is greater perturbation in the backward direction (z < 0) versus the forward (z > 0). This results from: 1) $|b_0| > |a_0|$, and 2) the phase beating between the reflected and incident TEM mode. If the contributions from the individual modes are considered separately, it turns out that the scattered TEM mode accounts for almost all the perturbation. In the backward direction the electric field is reduced while the magnetic field is increased resulting in a decrease in the wave impedance in the cell. One implication of this data is that if a field probe is used to estimate the strength of the incident TEM mode, it should be located forward of the EUT for best results. This figure represents somewhat of an extreme case since the EUT is large and the operating frequency is near the upper limit of the cell. Even so, the deviation in the primary field components is less than 10%.

These examples indicate that the TEM cell environment is not greatly affected by reasonably sized test objects. Smaller spheres would have yielded correspondingly smaller variations. For EUTs of different shapes scattering could possibly be accentuated somewhat due to corners, points, etc., but the same conclusions should hold true. Experience and theory suggest that limiting major EUT dimensions to less than one third the test chamber height should avoid significant perturbations.

3.6 Performing Radiated Emission Tests

Electronic or electromechanical equipment may emit energy which interferes or interacts with the normal operation of either the system and/or other receptors. To ensure the EMC of such systems, it is important to determine quantitatively their radiation characteristics. Since a TEM cell is a reciprocal device, it can be used to detect the emission too.

Equipment not designed as a radiator represents unintentional leakage sources which may be considered electrically small. As such, the leakage currents on the exterior surfaces of the equipment, treated here as an EUT, can be modeled as equivalent electric and magnetic short dipole sources [16]-[18]. These dipole sources may then be combined vectorially to form a composite equivalent source consisting of three orthogonal electric and three orthogonal magnetic dipole moments as represented in Fig. 3.13, each having an amplitude and a phase.

When an unknown source object (EUT) is placed at the center of a TEM cell, its emission couples into the fundamental TEM mode and propagates toward the two ports of the cell. With a hybrid junction inserted into a loop connecting the cell outputs as shown in Fig. 3.14, we are able to measure the sum and difference powers and the relative phase between the sum and difference outputs. This way of measuring the relative phase is very advantageous because it avoids the complication of having to establish an absolute phase reference physically connected to the EUT. Systematic measurements of the powers and relative phases at six different EUT orientations are sufficient to determine the amplitudes and phases of the unknown equivalent component dipole moments as depicted in Fig. 3.13, from which the corresponding detailed radiation pattern and total power radiated by the unknown source in free space can then be computed [16].

For the purpose of describing the source (EUT) position and related experimental procedures, it is necessary to establish a coordinate system (x,y,z) for the TEM cell with the origin at the geometric center of the inner conductor. The unknown source EUT may be placed at $(0, y_o, 0)$. We assign another coordinate system (x', y', z') with respect to the center of the EUT, as shown in Fig. 3.15.

Initially, we align x-x', y-y', and z-z' as shown in Fig. 3.15a. The first measurement orientation is obtained by rotating the EUT counterclockwise by an angle of $\pi/4$ about the z'-axis so that its position relative to the TEM cell is shown in Fig. 3.15b. We measure the sum and difference powers in watts and the relative phase in degrees between the sum and difference outputs, and designate them respectively as P_{s1}, P_{d1}, and ϕ_1. We then rotate the EUT by an additional $\pi/2$, also counterclockwise about the z'-axis as displayed in Fig. 3.15c to the second measurement orientation. We measure the sum power, difference power, and the relative phase between them as P_{s2}, P_{d2}, and ϕ_2.

We next align the coordinate frames such that $x = y'$, $y = z'$, and $z = x'$, as shown in figure 3.16. Then we rotate the EUT counterclockwise by an angle of $\pi/4$ about the x'-axis serving as the third measurement orientation, take the sum power P_{s3}, difference power P_{d3}, and the relative phase between the sum and difference outputs ϕ_3. Rotating the EUT counterclockwise by another $\pi/2$ about the x'-axis and taking the same sequence of measurements yield P_{s4}, P_{d4}, and ϕ_4.

Finally, we align the coordinate frames in accordance with $x = z'$, $y = x'$, and $z = y'$, as shown in figure 3.17, rotate the EUT in a similar manner about the y'-axis, and measure P_{s5}, P_{d5}, ϕ_5; P_{s6}, P_{d6}, and ϕ_6.

After collecting the measured sum and difference powers and applying the Lorentz reciprocity theorem, we obtain the following [18]:

$$m_{ex}^2 = (P_{s1} + P_{s2} - P_{s3} - P_{s4} + P_{s5} + P_{s6})/(2q^2) \quad (3.8)$$

$$m_{ey}^2 = (P_{s1} + P_{s2} + P_{s3} + P_{s4} - P_{s5} - P_{s6})/(2q^2) \quad (3.9)$$

$$m_{ez}^2 = (-P_{s1} - P_{s2} + P_{s3} + P_{s4} + P_{s5} + P_{s6})/(2q^2) \quad (3.10)$$

$$m_{mx}^2 = (P_{d1} + P_{d2} - P_{d3} - P_{d4} + P_{d5} + P_{d6})/(2k^2q^2) \quad (3.11)$$

$$m_{my}^2 = (P_{d1} + P_{d2} + P_{d3} + P_{d4} - P_{d5} - P_{d6})/(2k^2q^2) \quad (3.12)$$

$$m_{mz}^2 = (-P_{d1} - P_{d2} + P_{d3} + P_{d4} + P_{d5} + P_{d6})/(2k^2q^2) \quad ; \quad (3.13)$$

$$m_{ex}m_{ey} \cos\Theta_{e1} = (P_{s1} - P_{s2})/(2q^2) \quad (3.14)$$

$$m_{ey}m_{ez} \cos\Theta_{e2} = (P_{s3} - P_{s4})/(2q^2) \quad (3.15)$$

$$m_{ez}m_{ex} \cos\Theta_{e3} = (P_{s5} - P_{s6})/(2q^2) \quad (3.16)$$

$$m_{mx}m_{my} \cos\Theta_{m1} = (P_{d2} - P_{d1})/(2k^2q^2) \quad (3.17)$$

$$m_{my}m_{mz} \cos\Theta_{m2} = (P_{d4} - P_{d3})/(2k^2q^2) \quad (3.18)$$

$$m_{mz}m_{mx} \cos\Theta_{m3} = (P_{d6} - P_{d5})/(2k^2q^2) \quad ; \quad (3.19)$$

where

$$\Theta_{e1} = \psi_{ex} - \psi_{ey}, \quad \Theta_{e2} = \psi_{ey} - \psi_{ez}, \quad \Theta_{e3} = \psi_{ez} - \psi_{ex}, \quad (3.20)$$

$$\Theta_{m1} = \psi_{mx} - \psi_{my}, \quad \Theta_{m2} = \psi_{my} - \psi_{mz}, \quad \Theta_{m3} = \psi_{mz} - \psi_{mx}; \quad (3.21)$$

and q is the normalized amplitude of the vertical electric field which would exist at the center of an empty TEM cell when it is operated in a receiving mode and is excited by an input power of 1 W at one end and terminated at the other end with a matched load. Thus, $q = (50)^{1/2}/b$ in $\Omega^{1/2}/m$, which is determined by the height of the cell.

In obtaining (3.8) through (3.19), we have assumed that the frequency of the unknown interference source (EUT) to be detected by the spectrum analyzer included in the measurement instrumentation as shown in Fig. 3.14 is such that it allows only propagation of the dominant mode inside the cell. The size of the interference source to be tested must be small relative to the test volume of the cell. This is required to minimize the potential perturbation to the field distribution inside the cell, as was cautioned before. Under the above assumptions, we see from (3.8)-(3.10) that the amplitudes, m_{ei}, i = x, y, z, of the unknown component electric dipole moments in ampere-meters are obtainable by the sum powers only, and from (3.11)-(3.13) that the amplitudes, m_{mi}, of the unknown component magnetic dipole moments in ampere-square meters are obtainable by the difference powers only.

Once m_{ei} and m_{mi} are determined , they can be used to compute the total power, in watts, radiated in free space by the same source as

$$P_T = \frac{40\pi^2}{\lambda^2}[m_{ex}^2 + m_{ey}^2 + m_{ez}^2 + k^2(m_{mx}^2 + m_{my}^2 + m_{mz}^2)] \quad (3.22)$$

Note that if one is interested only in determining the total power radiated by the source, which may be the case in practice, all we need to extract are m_{ei}^2 and m_{mi}^2 based on the measured powers.

The corresponding far-field radiation pattern in free space depends, however, also on the relative phases among the component dipole moments of the same and mixed kinds. The former (same kind) can be extracted by (3.14)-(3.19) with the constraining conditions that $\Sigma\Theta_{ei} = 0$ and $\Sigma\Theta_{mi} = 0$, while the latter (mixed kind), $\psi_{ei} - \psi_{mj}$, i,j = x,y,z but $i \neq j$, is much more complicated, involving the component dipole moments determined in (3.8)-(3.13) and the measured relative phases, ϕ_i, i = 1, 2, ..., 6, between the sum and difference outputs. This is the reason why these relative phases are also measured and recorded. Detailed procedures of extracting $\psi_{ei} - \psi_{mj}$ may be found elsewhere [18].

Note, however, that if one suspects beforehand that the unknown interference source may be characterized by one kind of dipole moment only (either electric or magnetic), the relative phase measurement will not be required [18]. In addition, if the source is believed to be made of electric dipole moments only, then the sum power measurements will suffice to determine the radiation characteristics of the source. Similarly, the difference power measurements will be the dominant ones if the source is essentially magnetic dipoles.

Once the total power radiated in free space by the unknown source is determined as in (3.22), the equivalent electric field strength, in V/m, due to the same source in free space at a distance d will then be:

$$E = 5.477(P_T)^{1/2}/d \quad (3.23)$$

Naturally, when the measured powers and phases are not contaminated by background noise or other inaccuracies, the source parameters so extracted and the radiation characteristics so computed are accurate and proven to be unique [18]. In the practical world, however, the experimental data are always degraded somewhat by background noise, equipment limitations, and the reading accuracy. These measurement imperfections will cause uncertainties in the deduced results. A report giving necessary mathematical derivations for, and performing the analysis of, these uncertainties is available [19].

The method outlined above has been successfully tested by a simulated example and two practical examples, one with a known small spherical dipole representing the electric type [16],[18], and the other with a known small loop antenna representing the magnetic type [20]. The deduced radiation characteristics such as the strength of dipole moment and the total power radiated by the spherical dipole in free space agree very well with the measured results obtained by other means [21].

Quite often, the equipment performance degradation or failure is also dependent upon the interfering signal waveform. For this case, time-domain analysis may be required. TEM cells can be used to satisfy this need too. For example, the block diagram shown in Fig. 3.18 may be applied with the oscilloscope either connected directly to the cell measurement port, or with the oscilloscope connected to the predetection or postdetection outputs of the receiving instrument. The latter arrangement using a receiver with the oscilloscope provides greater measurement sensitivity. In either arrangement, the oscilloscope must be synchronized with either the periodic detected signal from the cell or with an EUT-monitored periodic signal represented by the dashed line from the EUT. The measurement results can then be recorded by photographing the oscilloscope display. If the emission is random in nature, the oscilloscope cannot be synchronized properly and the detected signal must be either recorded with a video disk or tape recorder to be played back frame by frame for analysis, or analyzed statistically using amplitude probability distribution analyzers, etc.

3.7 Examples of Some TEM Cell Applications

TEM cells have been used for a number of applications. Initial work involved the development of a cell to establish high-level fields for biological effects research [22].

During the early development, it was realized that its broadband frequency response made it a prime candidate for use in TEMPEST testing of EUT [23] and as an EM pulse simulator [24]. The largest known TEM cell in existence (8m x 20m x 24m) is located at Sandia Laboratories, in Albuquerque, New Mexico, and it is used as a dual purpose facility for both EM pulse testing and CW susceptibility testing of whole weapon systems. NBS recognized the cell's potential for use as a calibration tool for establishing standard TEM fields. Considerable development and theoretical work were done at NBS to carefully evaluate various TEM cells for this purpose [6],[25]. TEM cells have also been used extensively for radiated susceptibility testing of components by the automotive industry, as evidenced by the formal adoption of TEM cell testing methods by the Society of Automotive Engineers (SAE) in the frequency range of 14 kHz to 200 MHz [26]. One motor vehicle manufacturer has constructed a very large cell with a test volume of 2m x 5m x 7m for whole-vehicle testing [27]. Another large cell, 2.8m x 2.8m x 5.6m, is in use at AT&T Information Systems for measuring both susceptibility and emissions of communication equipment [28],[29]. More recently, 2m x 2m x 4m TEM cells have been evaluated and proposed for use by the Electronics Industries Association (EIA) to measure TV/VCR immunity to EMI [30],[31]. Finally, a recent application is the use of a pair of TEM cells, called the dual TEM cell (one cell on top of the other), with a common aperture created between them to evaluate the shielding effectiveness of materials [32],[33].

REFERENCES

[1] Free, W. R. Radiated EMI measurements in shielded enclosures. Proc. IEEE Int. Symp. on EMC; 1967 July; Washington, D. C. 43-53.

[2] Tippet, J. C. Modal characteristics of rectangular coaxial transmission line. PhD dissertation, Dept. of Electrical Engineering, Univ. of Colorado, Boulder, CO. 1978.

[3] Crawford, M. L.; Workman, J. L. Asymmetric versus symmetric TEM cell for EMC measurements. Proc. IEEE Symp. on EMC; 1978 June; Atlanta, GA. 204-208.

[4] Decker, W. F.; Wilson, W. A.; Crawford, M. L. Construction of a large transverse electromagnetic cell. Nat. Bur. Stand. (U.S.) Tech. Note 1011; 1979 February.

[5] Crawford, M. L. Generation of standard EM fields using TEM transmission cells. IEEE Trans. on Electromag. Compat., EMC-16(no.4): 189-195; 1974 November.

[6] Tippet, J. C.; Chang, D. C.; Crawford, M. L. An analytical and experimental determination of the cutoff frequencies of higher-order TE modes in a TEM cell. Nat. Bur. Stand. (U.S.) Int. Rep. 76-841; 1976 June.

[7] Tippet, J. C.; Chang, D. C. Higher order modes in rectangular coaxial line with infinitely thin inner conductor. Nat. Bur. Stand. (U.S.) Int. Rep. 78-873; 1978 March.

[8] Tippet, J. C.; Chang, D. C. Radiation characteristics of dipole sources located inside a rectangular, coaxial transmission line. Nat. Bur. Stand. (U.S.) Int. Rep. 75-829; 1976 January.

[9] Mittra, R.; Itoh, T. A new technique for the analysis of the dispersion characteristics of microstrip lines. IEEE Trans. on Microwave Theory & Tech., MTT-19(1): 47-56; 1971 January.

[10] Gruner, L. High order modes in rectangular coaxial waveguides. IEEE Trans on Microwave Theory & Tech., MTT-15(8): 483-485; August 1967.

[11] Crawford, M. L.; Workman, J. L.; Thomas, C. L. Expanding the bandwidth of TEM cells for EMC measurements. IEEE Trans. on Electromag. Compat., EMC-20(3): 368-375; 1978 August.

[12] Hill, D. A. Bandwidth limitations of TEM cells due to resonances. J. Microwave Power, 18(2): 181-195; 1983.

[13] Wilson, P. F.; Ma, M. T. Simple, approximate expressions for higher-order modes and resonances in TEM cells. IEEE Trans. on Electromag. Compat., EMC-28(3): xxx; 1986 August.

[14] Crawford, M. L. Improving the repeatability of EM susceptibility measurements of electronic equipment when using TEM cells. SAE Technical Paper Series 830607, SAE Int. Congress and Exp.; Detroit, MI. 1983 Feb. 28 - Mar. 4.

[15] Wilson, P. F.; Ma, M. T. Small aperture analysis of the dual TEM cell and an investigation of test object scattering in a single TEM cell. Nat. Bur. Stand. (U. S.) Tech. Note 1076; 1984 October.

[16] Sreenivasiah, I.; Chang, D. C.; Ma, M. T. Characterization of electrically small radiating sources by tests inside a transmission line cell. Nat. Bur. Stand. (U.S.) Tech. Note 1017; 1980 February.

[17] Sreenivasiah, I.; Chang, D. C.; Ma, M. T. Emission characteristics of electrically small radiating sources from tests inside a TEM cell. IEEE Trans. on Electromag. Compat., EMC-23(3): 113-121; 1981 August.

[18] Ma, M. T.; Koepke, G. H. A method to quantify the radiation characteristics of an unknown interference source. Nat. Bur. Stand. (U.S.) Tech. Note 1059; 1982 October.

[19] Ma, M. T.; Koepke, G. H. Uncertainties in extracting radiation parameters for an unknown interefence source based on power and phase measurements. Nat. Bur. Stand. (U.S.) Tech. Note 1064; 1983 June.

[20] Koepke, G. H.; Ma, M. T. A new method for determining the emission characteristics of an unknown interference source. Proc. 5th Symp. Tech. Exhibition on EMC; 1983 March; Zurich, Switzerland.

[21] Crawford, M. L.; Workman, J. L. Predicting free-space radiated emissions from electronic equipment using TEM cell and open-field site measurements. Proc. IEEE Int. Symp. on EMC; 1980 October; Baltimore, MD. 80-85.

[22] Skaggs, G. A. High frequency exposure chamber for radiobiological research. NLR Memo, Rep. 2218; 1971 February.

[23] Crawford, M. L. Measurement of electromagnetic radiation from electronic equipment using TEM transmission cells. Nat. Bur. Stand. (U.S.) Int. Rep. 73-306; 1973 February.

[24] Pollard, N. A broadband electromagnetic environments simlulator (EMES). IEEE Int. Symp. on EMC; 1977 August; Seattle, WA.

[25] Crawford, M. L. Generation of standard EM fields for calibration of power density meters, 20 kHz to 1000 MHz. Nat. Bur. Stand. (U.S.) Int. Rep. 75-804; 1975 January.

[26] Society of Automotive Engineers (SAE) Recommended Practice. Electromagnetic susceptibility procedures for vehicle components (except aircraft) - SAE J1113; 1984 June.

[27] Vrooman, G. F. E. An indoor 60 Hz to 40 GHz facility for total vehicle EMC testing. SAE technical paper series 831001, SAE passenger car meeting, Dearborn, MI; 1983 June 6-9.

[28] Heirman, D. N. Automated immunity measurements. Proc. 6th Symp.Tech. Exhibition on EMC; 1985 March; Zurich, Switzerland.

[29] Crawford, M. L. Comparison of open-field, anechoic chamber and TEM cell facilities/techniques for performing electromagnetic radiated emission measurements. IEEE Int. Symp. on EMC; 1983 August; Arlington, VA. 13-418.

[30] Hermeling, G. C. Method for immunity measurements on home entertainment products using the 2 meter TEM cell. IEEE Int. Symp. on EMC; 1983 August; Arlington, VA. 574-580.

[31] EIA Interim Standard No. 32 (proposed). Immunity of television receivers and video cassette recorders (VCRs) to direct radiation from radio transmissions, 0.5 to 30 MHz.; revised Sept. 6, 1984.

[32] Faught, A. N., Jr.; Dowell, J. T.; Scheps, R. D. Shielding material insertion loss measurements using a dual TEM cell systems. IEEE Int. Symp. on EMC; 1983 August; Arlington, VA. 286-290.

[33] Wilson, P. F.; Ma, M. T. Shielding effectiveness measurements with a dual TEM cell. IEEE Trans. on Electromag. Compat., EMC-27(3): 137-142; 1985 August.

[34] Wilson, P. F.; Chang, D. C.; Ma, M. T. Excitation of a TEM cell by a vertical electric hertzian dipole. Nat. Bur. Stand. (U.S.) Tech. Note 1073; 1981 March.

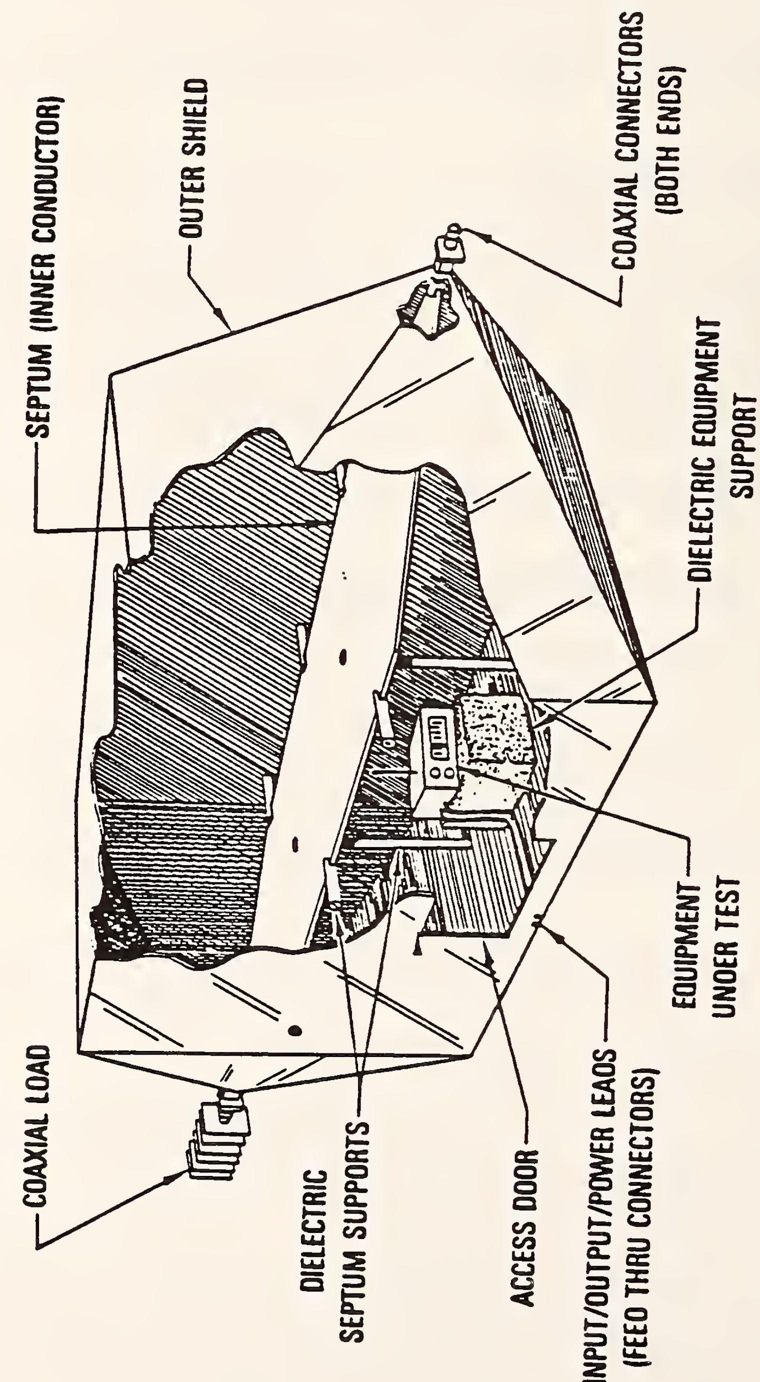

Figure 3.1 An NBS TEM cell.

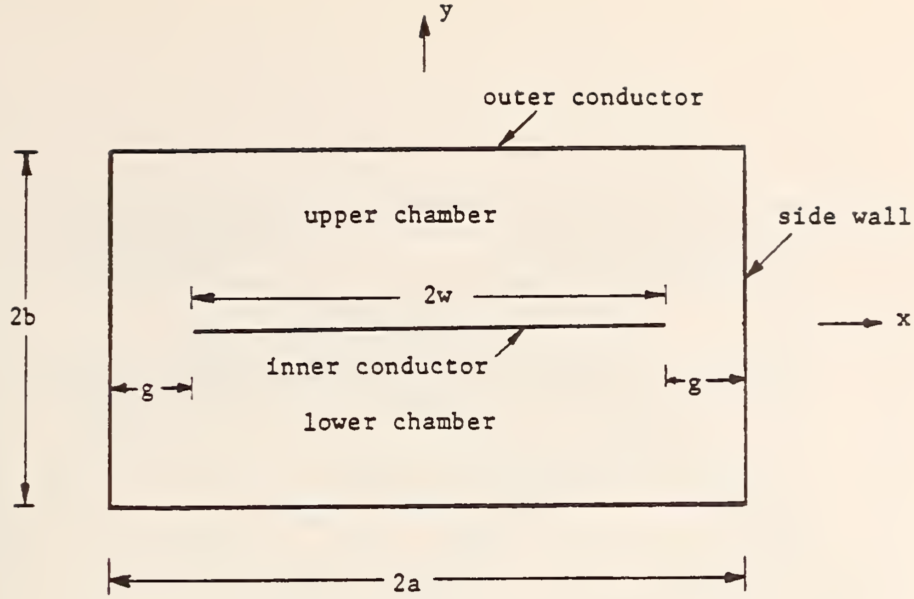

Figure 3.2 Cross section of a TEM cell.

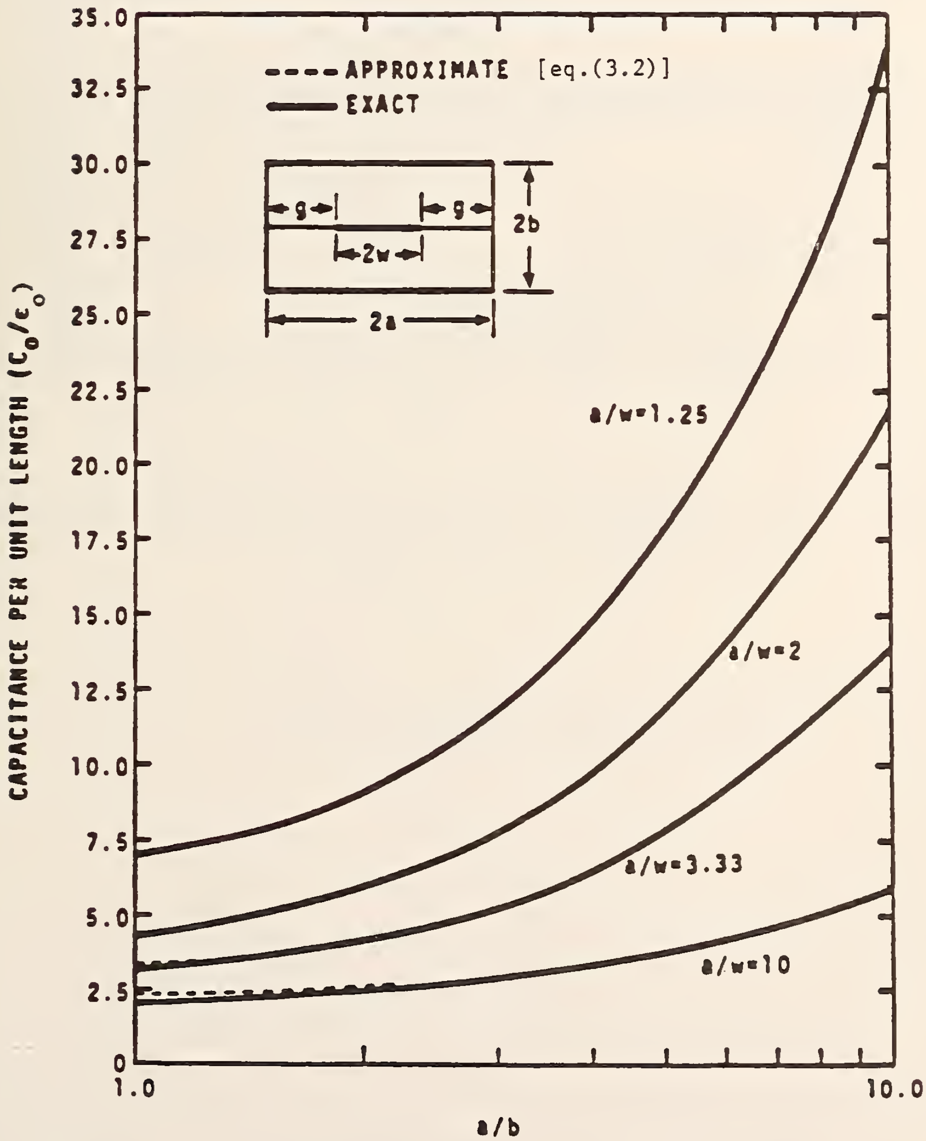

Figure 3.3 Capacitance characteristics of a TEM cell.

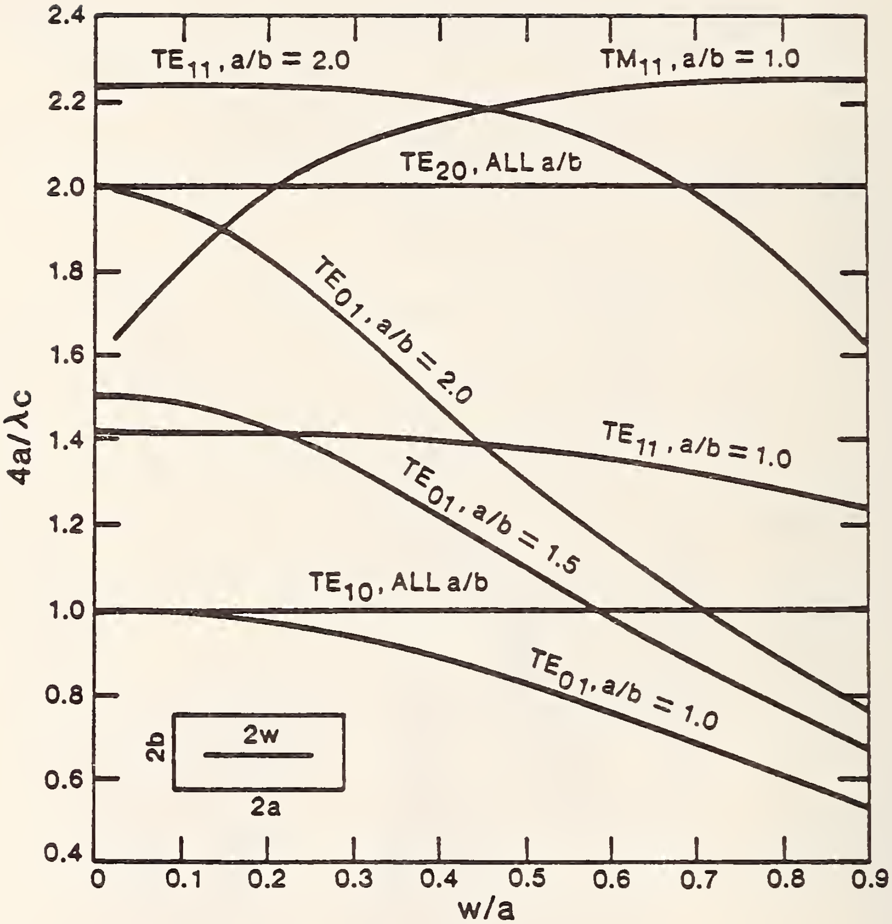

Figure 3.4 Cutoff wavelengths of the first few higher order gap-perturbed modes in a TEM cell.

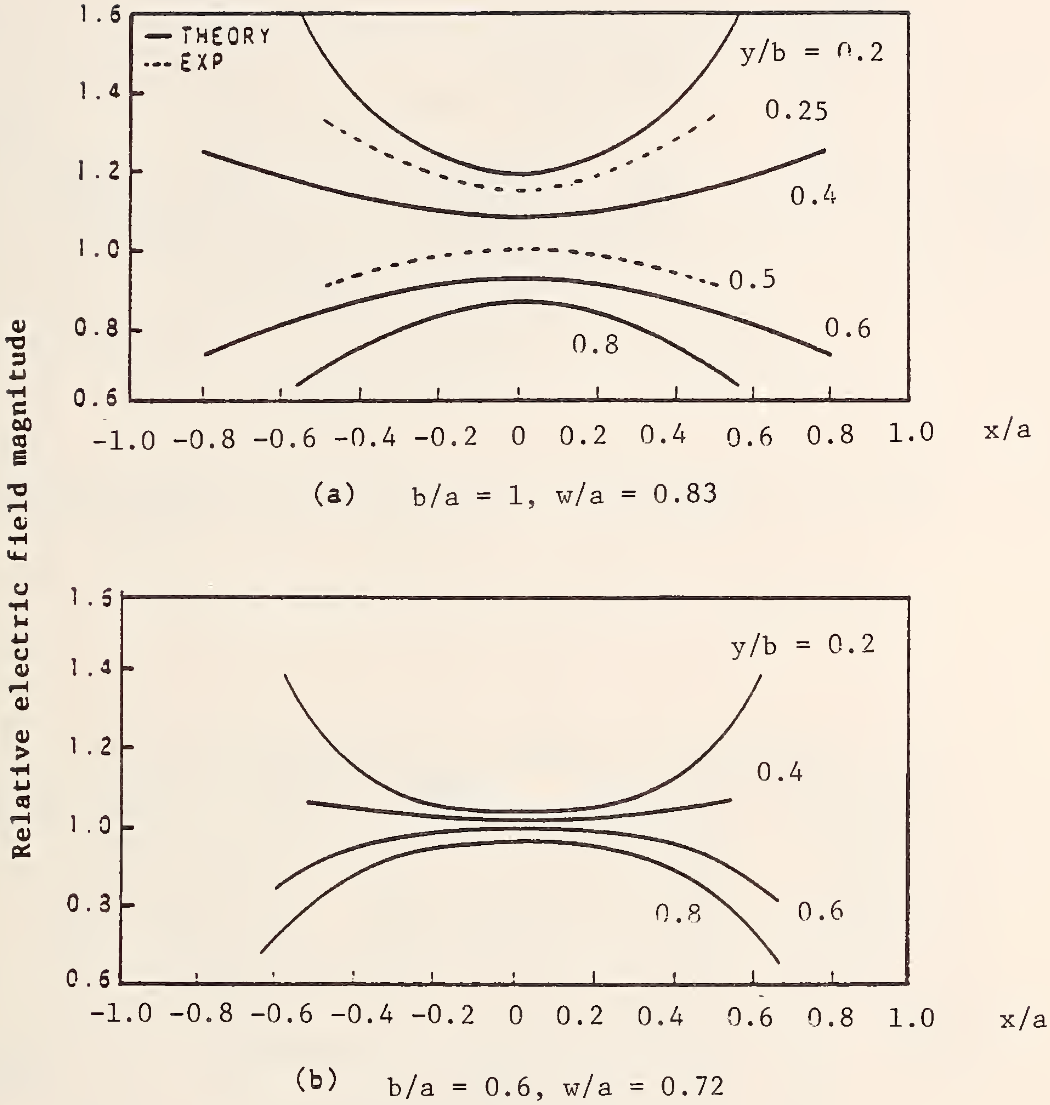

Figure 3.5 Normalized magnitude of the electric field of the TEM mode inside an RCTL.

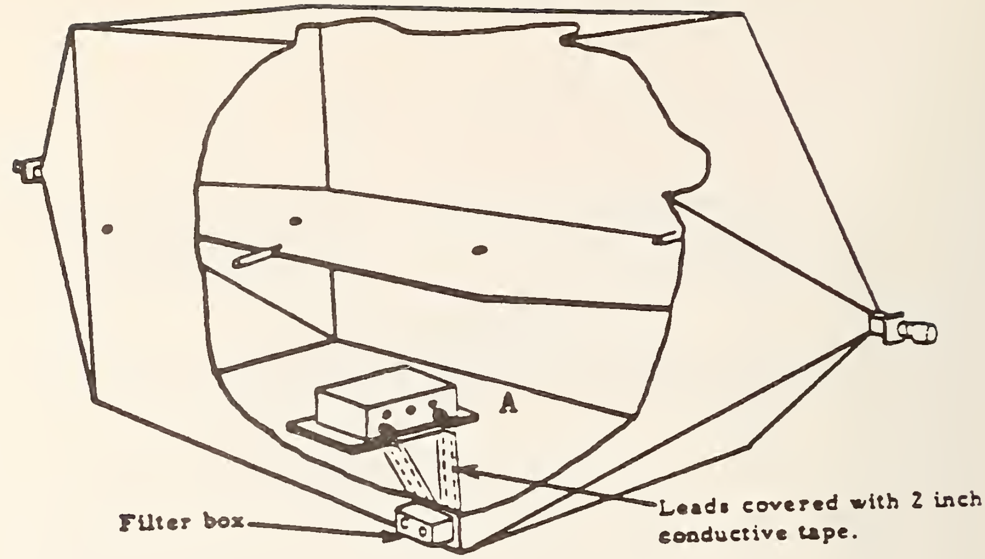

Figure 3.6a EUT near floor of TEM cell for minimum exposure of leads to test field.

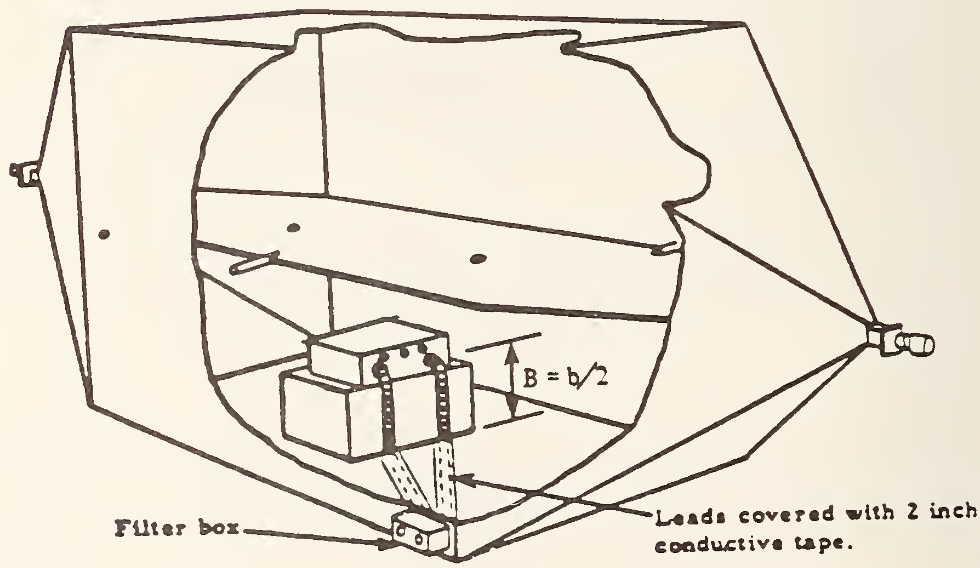

Figure 3.6b. EUT centered in test zone midway between septum and floor.

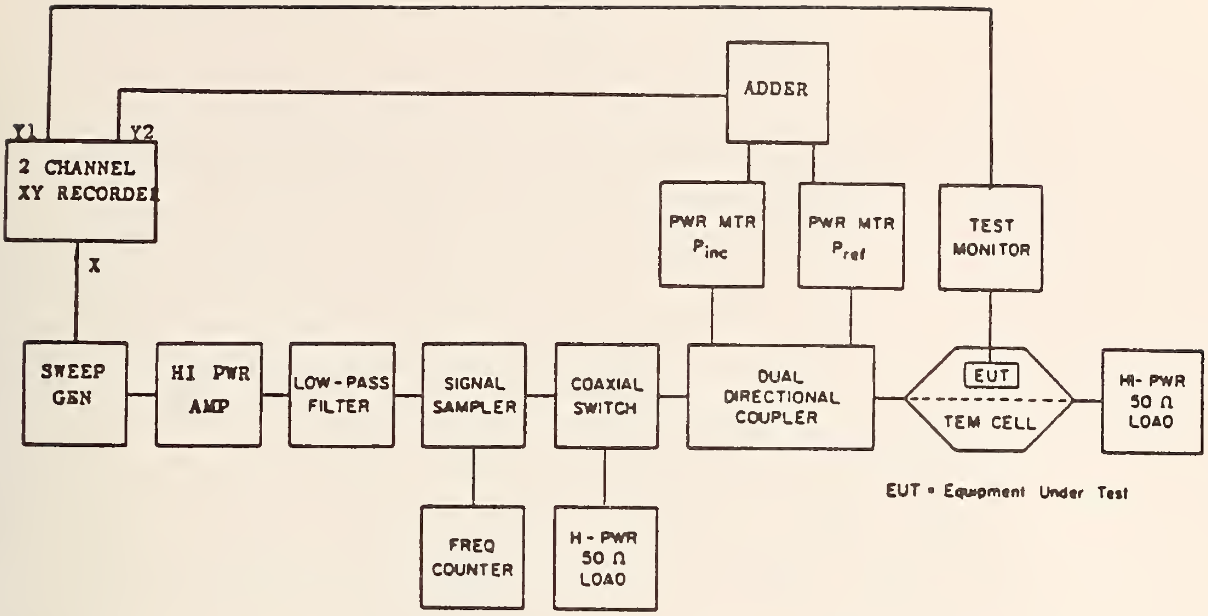

Figure 3.7 Block diagram of system for susceptibility testing of equipment at frequencies ≥10 MHz.

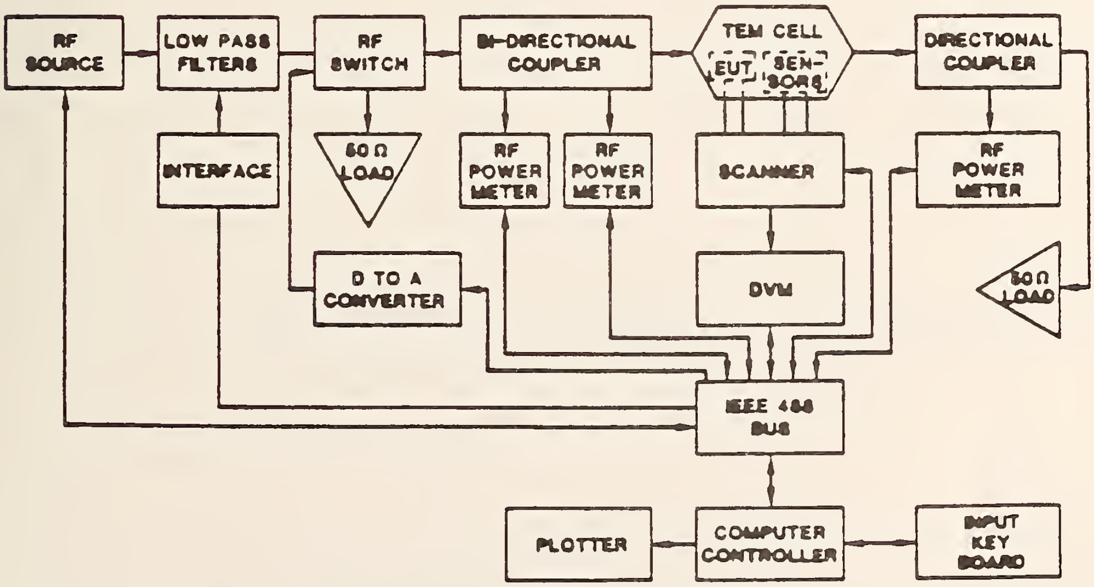

Figure 3.8 Block diagram of automated TEM cell susceptibility measurement system.

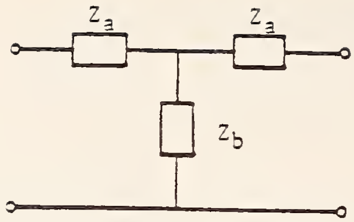

(a)

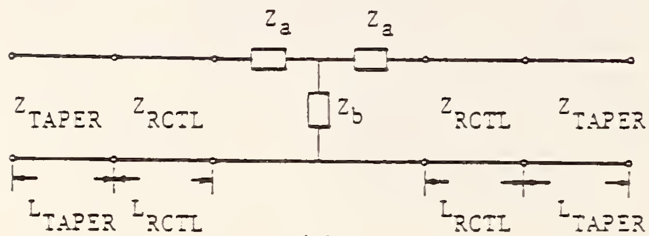

(b)

Figure 3.9 (a) The equivalent T-network circuit for a small scattering obstacle; and

(b) The TEM cell transmission-line circuit, including the small obstacle loading.

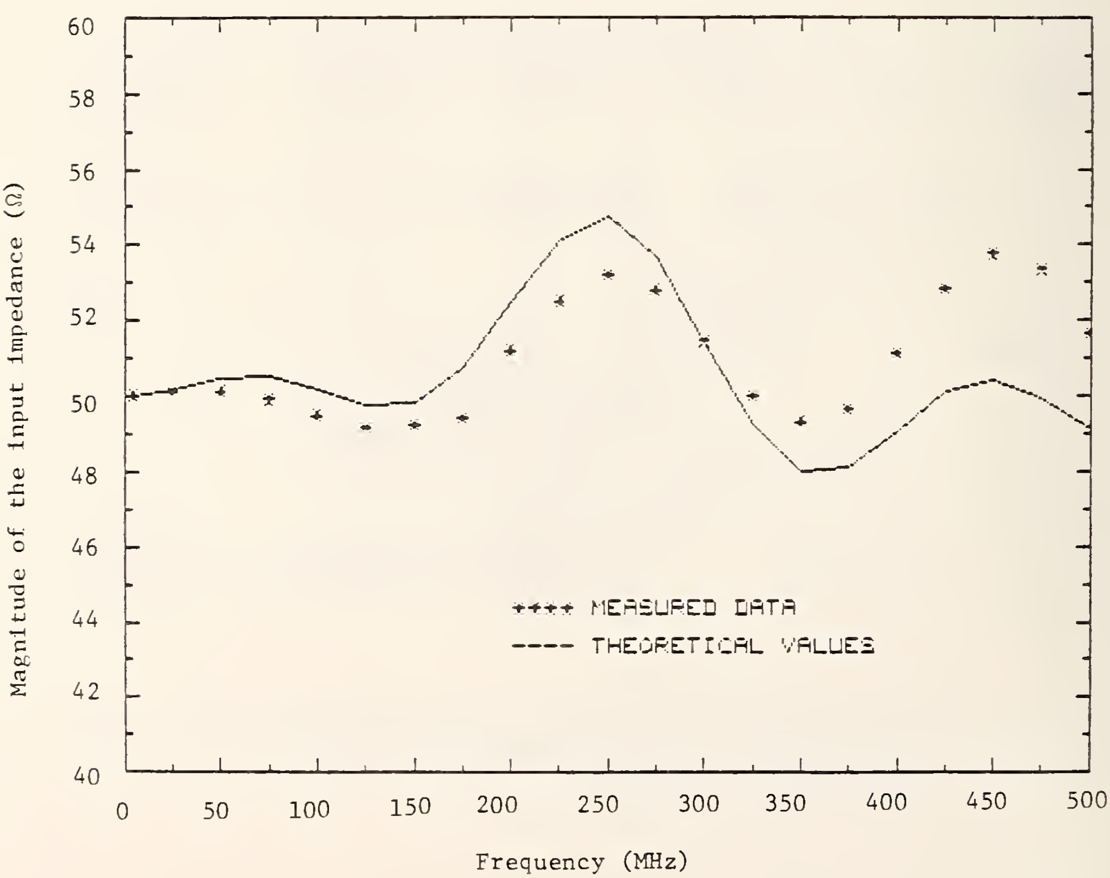

Figure 3.10 Magnitude of the input impedance for an empty TEM cell terminated with a 50-ohm load.

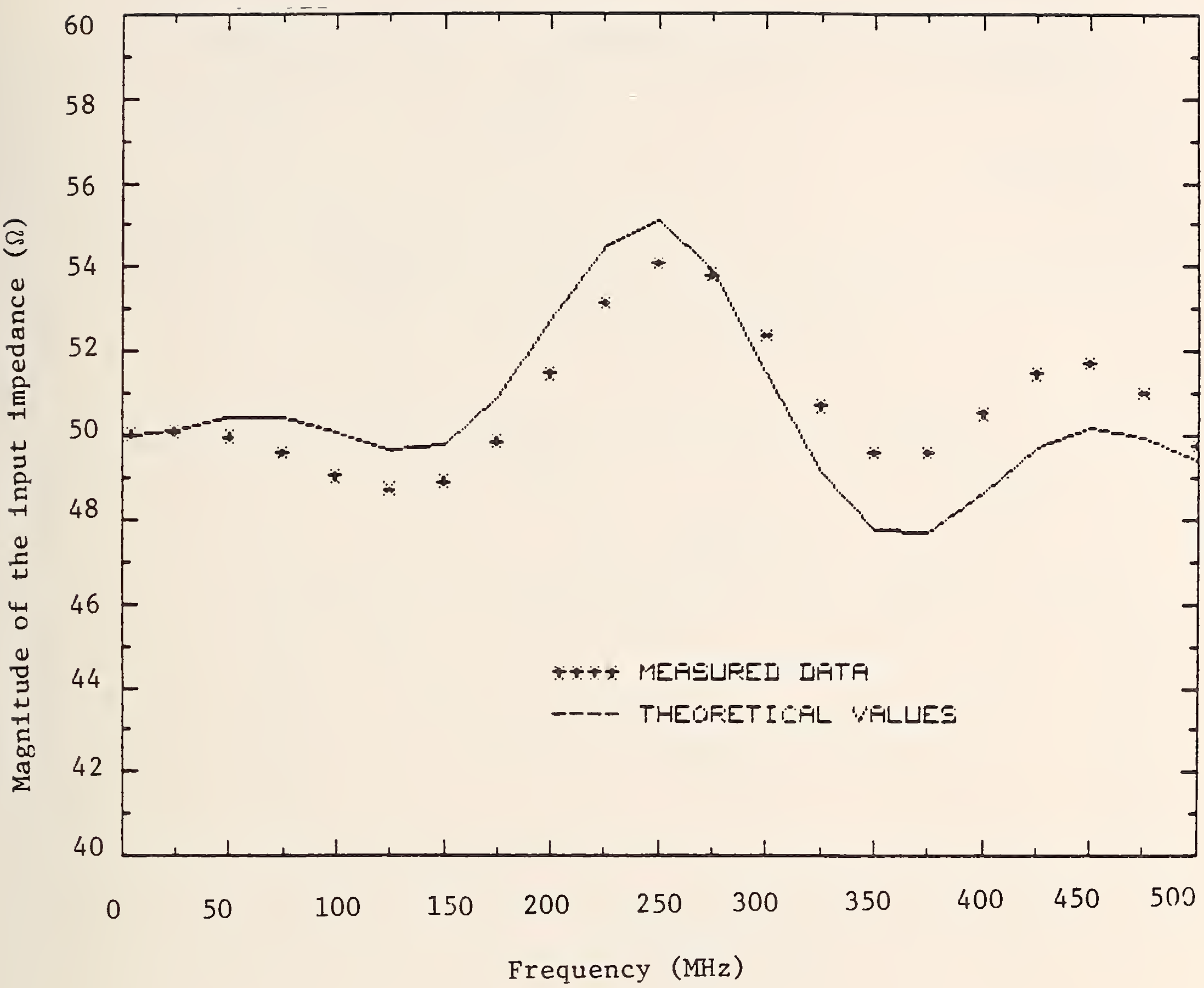

Figure 3.11 Magnitude of the input impedance for the same TEM cell (as in fig. 3.10) loaded with a conducting sphere of 5.5 cm in diameter.

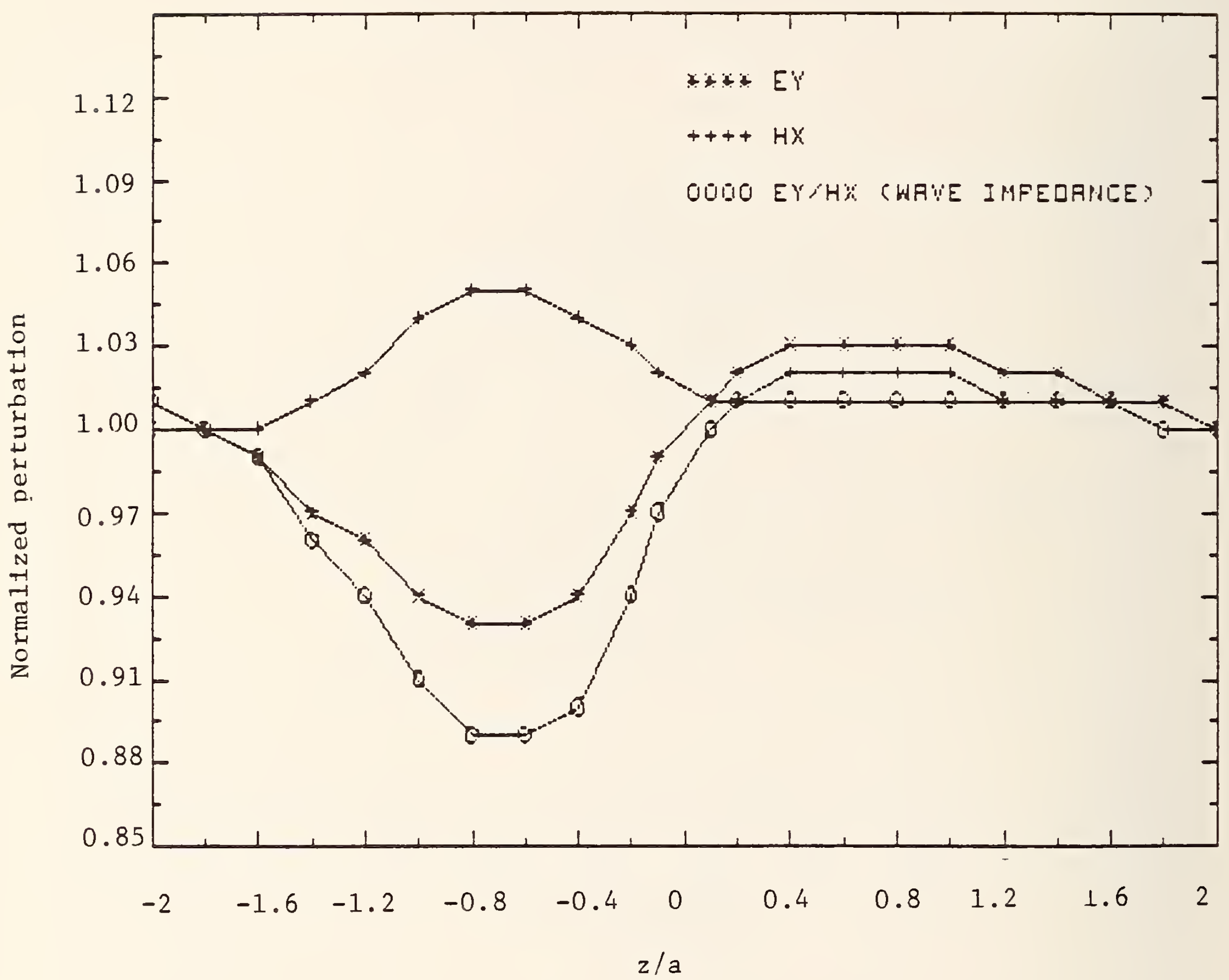

Figure 3.12 Field perturbation in the same TEM cell (as in fig. 3.10) by a conducting sphere of 5.5 cm in diameter at a frequency such that ka = 1.4 .

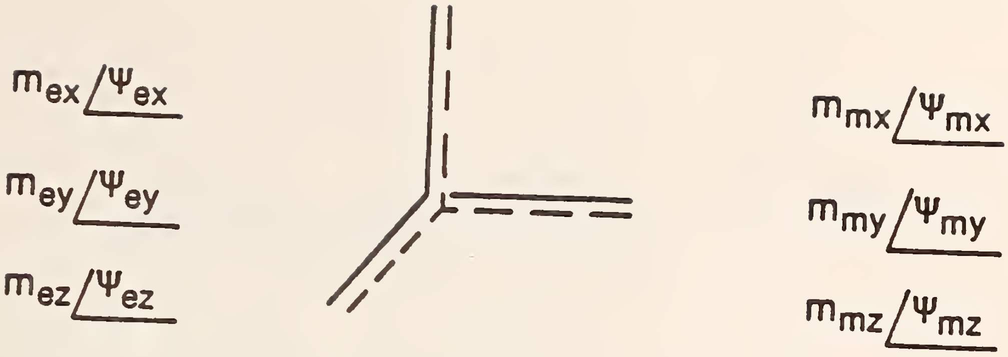

Figure 3.13 An unknown electrically small source is considered to be made of equivalent three orthogonal electric and three orthogonal magnetic dipoles.

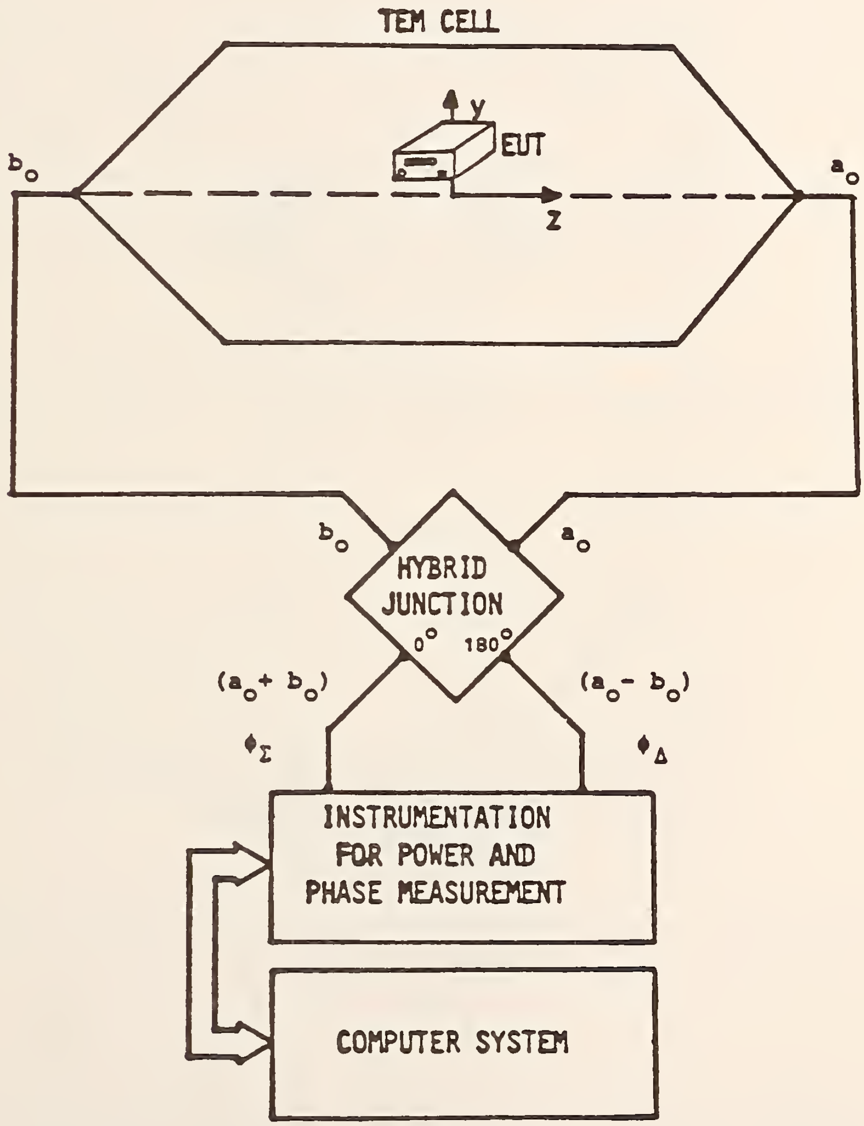

Figure 3.14 Emissions testing measurement system.

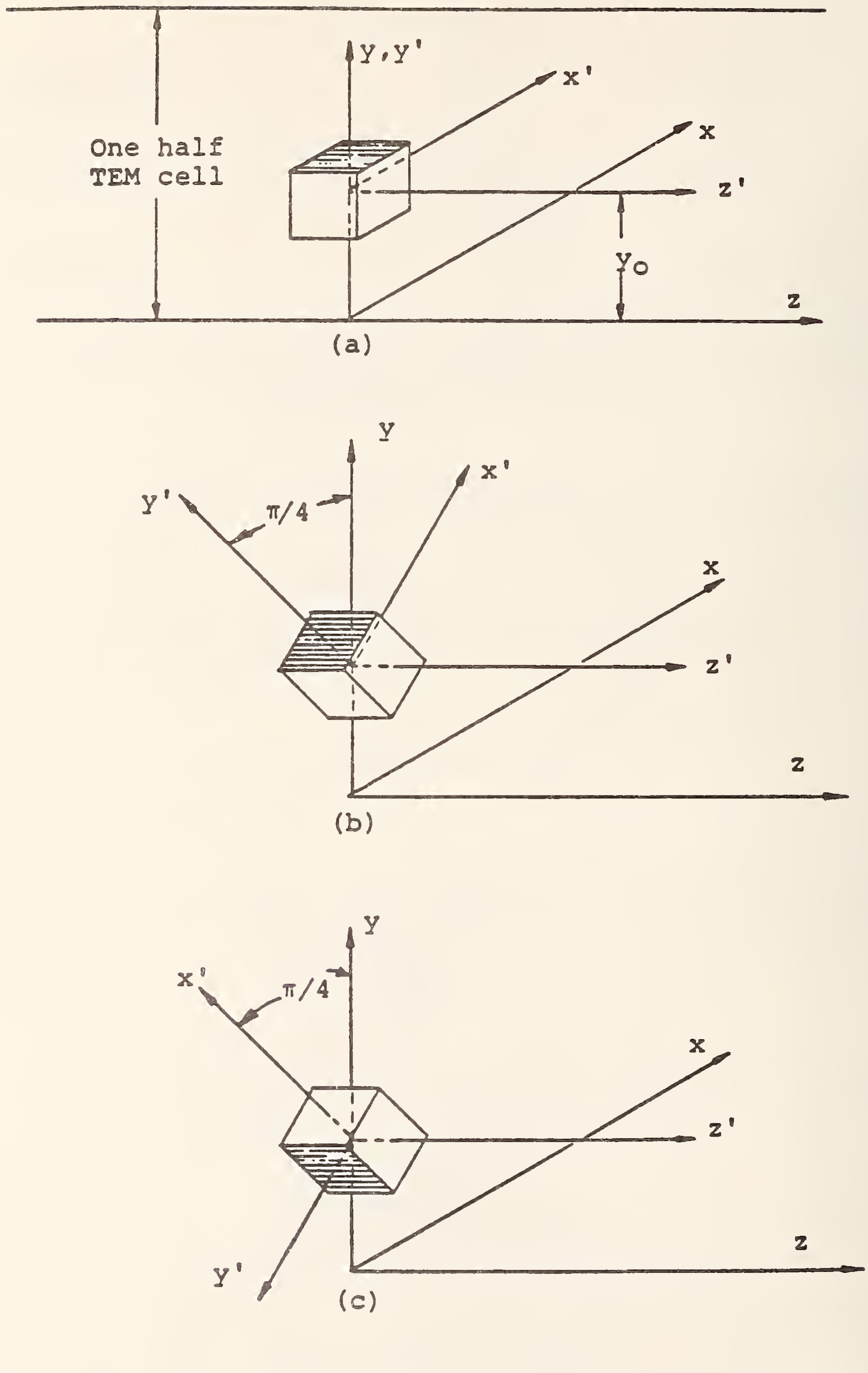

Figure 3.15 Two EUT orientations in the TEM cell.

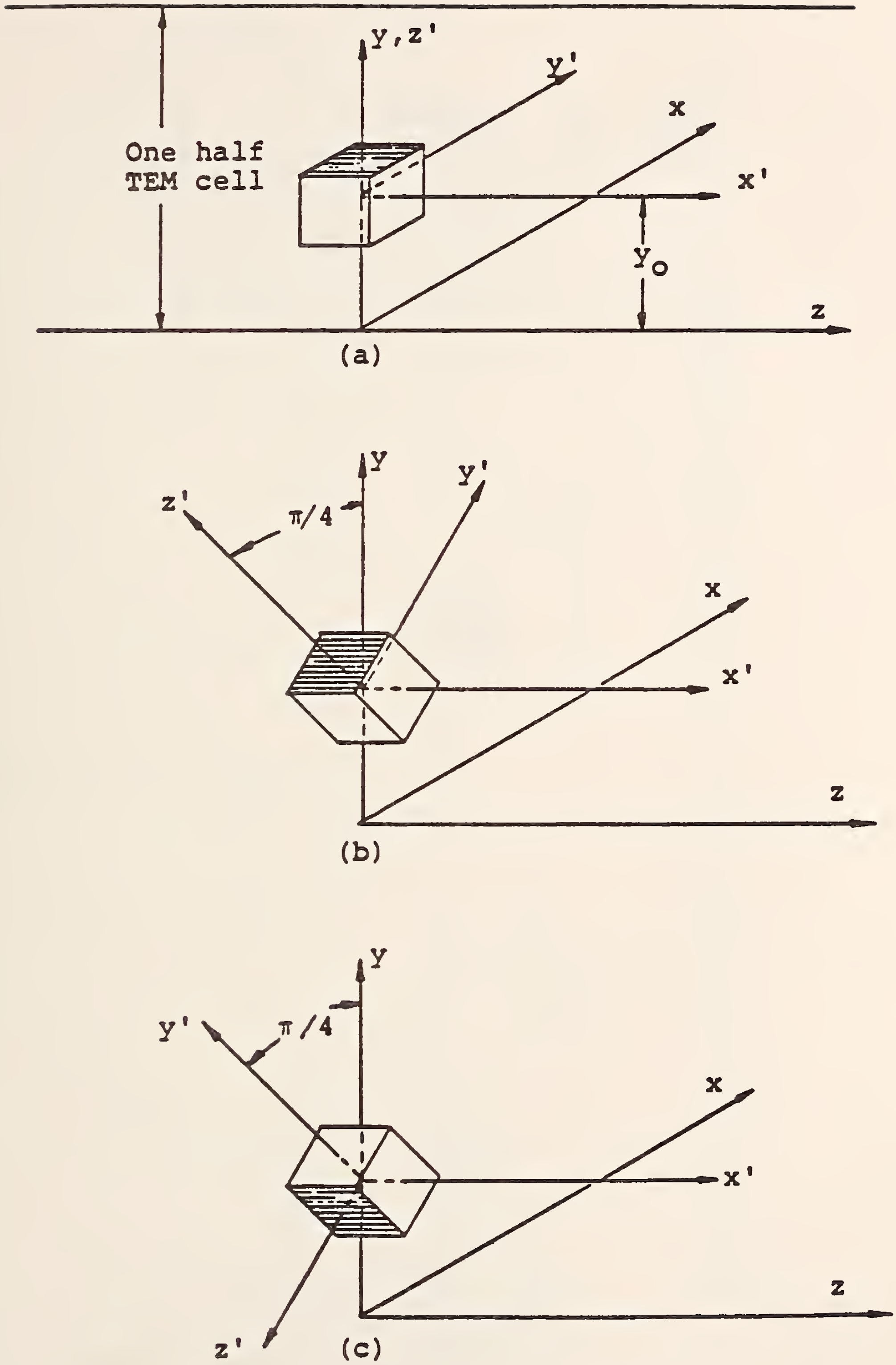

Figure 3.16 Another two EUT orientations in the TEM cell.

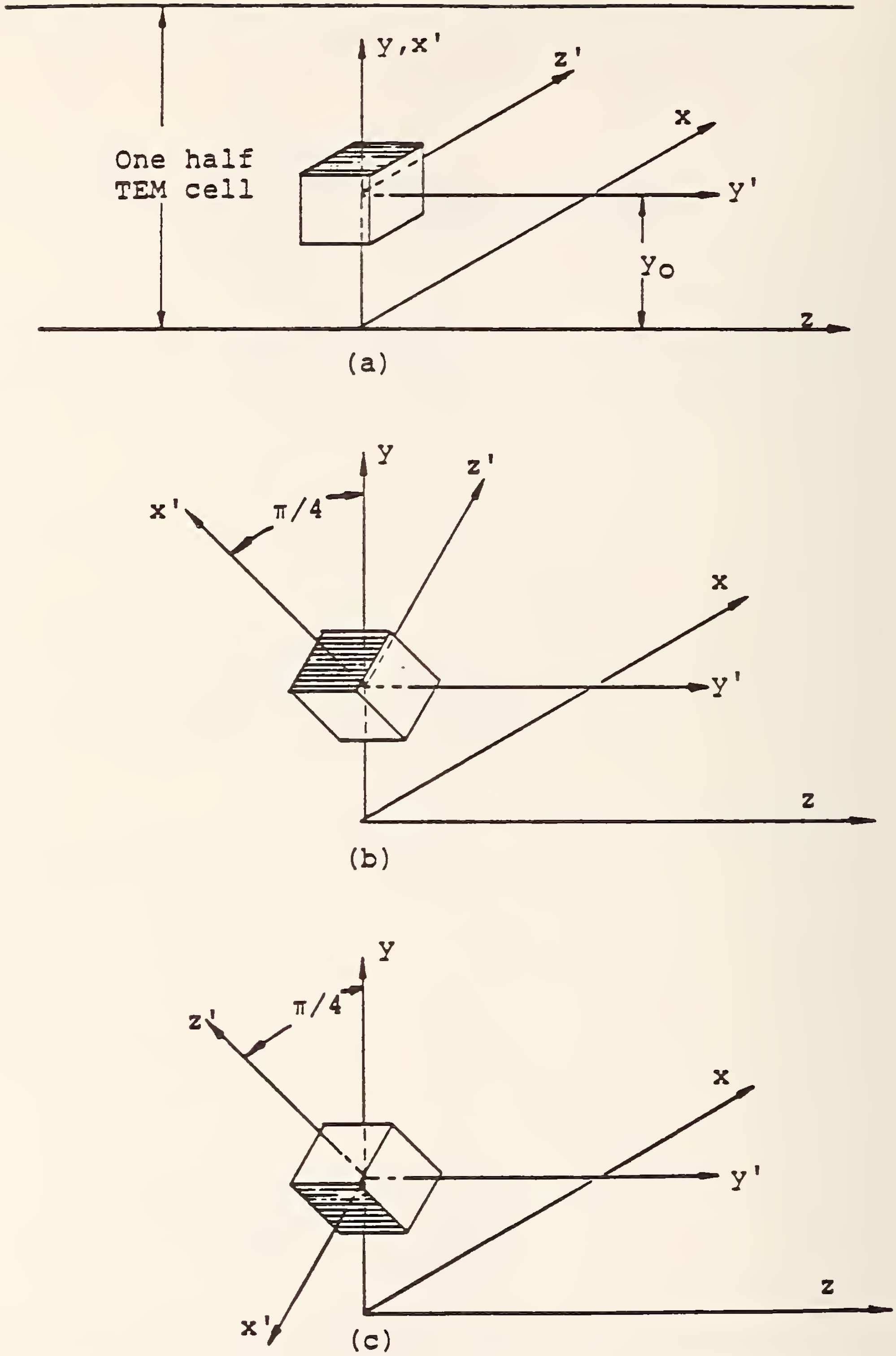

Figure 3.17 Final two EUT orientations in the TEM cell.

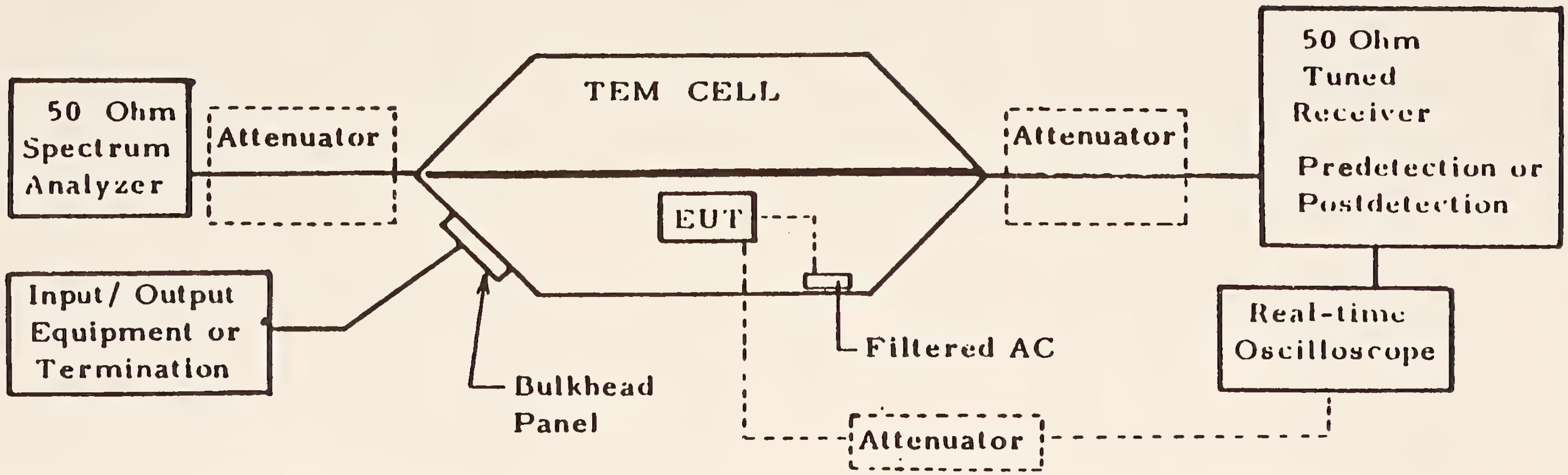

Figure 3.18 Block diagram of measurement system for time domain analysis of radiated emissions from EUT using a TEM cell. (Attenuator required for hard line sync of some EUT.)

Table 3.1 Small-gap modal equations applicable to symmetric TEM cells.

Mode [ref]	Modal Equation $(f_c = \frac{150}{\pi}\,\frac{x}{b}$ (MHz))
TE_{01} [13]	$x \tan x = \frac{\pi}{2}(\frac{b}{a})\,[\ln(\frac{2a}{\pi g}) + R_{TE_{01}}]^{-1}$ $R_{TE_{01}} = \sum_{p=1}^{\infty} \frac{1}{p}\,(\coth\frac{p\pi b}{a} - 1)\cos^2(\frac{p\pi g}{a})$
TE_{10}	$x = \frac{\pi}{2}(\frac{b}{a})$
TE_{11} [13]	$x = [y^2 + (\frac{\pi b}{2a})^2]^{1/2}$ $y \tan y = \frac{\pi}{\cos^2(\frac{\pi g}{2a})}\,(\frac{b}{a})\,[\ln(\frac{8a}{\pi g}) - 2\cos^2(\frac{\pi g}{2a}) + R_{TE_{11}}]^{-1}$ $R_{TE_{11}} = 2\sum_{p=1}^{\infty} \frac{1}{2p+1}\,(\coth\frac{(2p+1)\pi b}{2a} - 1)\cos^2(\frac{2p+1}{2a})\,\pi g$
TE_{02}	$x = \pi$
TE_{12}, TM_{12}	$x = \pi\,[1 + (\frac{b}{2a})^2]^{1/2}$
TE_{20}	$x = \pi\,\frac{b}{a}$
TE_{21} [13]	$\frac{\cot x}{x} + \frac{2\cos^2(\frac{\pi g}{a})\cot y}{y} = \frac{2}{\pi}(\frac{a}{b})\,[\ln(\frac{2a}{\pi g}) - \cos^2(\frac{\pi g}{a}) + R_{TE_{21}}]$ $y = [x^2 - (\pi\,\frac{b}{a})^2]^{1/2}$ $R_{TE_{21}} = \sum_{p=2}^{\infty} \frac{1}{p}\,(\coth\frac{p\pi b}{a} - 1)\cos^2(\frac{p\pi g}{a})$
TM_{11} [13]	$x = [y^2 + (\frac{\pi b}{2a})^2]^{1/2}$; $\frac{\tan y}{y} = \frac{2}{\pi}(\frac{a}{b})\,[(\frac{2a}{\pi g})^2 + 1 - R_{TM_{11}}]^{-1}$ $R_{TM_{11}} = \frac{4a}{\pi g}\sum_{p=1}^{\infty}[\coth\frac{(2p+1)\pi b}{2a} - 1]\,J_1[\frac{(2p+1)\pi g}{2a}]$

Table 3.2 Normalized field distribution in a TEM cell with a = 25 cm, b = 25 cm, w = 20.64 cm; (a) x component and (b) y component.

y = b	25	0.000	0.000	0.000	0.000	0.000	0.000
	20	0.000	0.060	0.129	0.208	0.278	0.307
	15	0.000	0.108	0.245	0.422	0.600	0.680
	10	0.000	0.127	0.311	0.620	1.029	1.237
	5	0.000	0.090	0.248	0.647	1.684	2.285
	0	0.000	0.000	0.000	0.000	0.000	3.603
		0	5	10	15	20	25 x

(a)

y = b	25	0.824	0.793	0.698	0.530	0.289	0.000
	20	0.853	0.825	0.736	0.568	0.315	0.000
	15	0.935	0.917	0.852	0.699	0.410	0.000
	10	1.049	1.025	1.051	0.977	0.652	0.000
	5	1.153	1.186	1.298	1.499	1.343	0.000
	0	1.196	1.245	1.431	1.986	6.640	0.000
		0	5	10	15	20	25 x

(b)

Table 3.3 Normalized field distribution in a TEM cell with a = 25 cm, b = 15 cm, w = 18.025 cm; (a) x component and (b) y component.

y = b	15	0.000	0.000	0.000	0.000	0.000	0.000
	12	0.000	0.024	0.067	0.143	0.220	0.249
	9	0.000	0.040	0.121	0.284	0.462	0.517
	6	0.000	0.043	0.141	0.410	0.763	0.871
	3	0.000	0.028	0.101	0.440	1.247	1.112
	0	0.000	0.000	0.000	0.000	1.969	1.254
		0	5	10	15	20	25 x

(a)

y = b	15	0.966	0.946	0.872	0.698	0.394	0.000
	12	0.972	0.956	0.890	0.724	0.411	0.000
	9	0.989	0.981	0.944	0.807	0.464	0.000
	6	1.010	1.015	1.028	0.979	0.557	0.000
	3	1.028	1.046	1.120	1.311	0.645	0.000
	0	1.035	1.058	1.164	1.664	0.000	0.000
		0	5	10	15	20	25 x

(b)

How best to achieve adequate shielding is a concern of both the users and manufacturers of electronic equipment. Shielding here refers to the practice of protecting some region from electromagnetic (EM) radiation due to outside sources (susceptibility) or to the avoidance of leaking unwanted radiation (emission). Shielding performance depends on both the electrical properties of the materials used and on the construction of the shield (joints, seams, apertures, geometry, etc.). This chapter is concerned with the basic problem of determining material shielding properties. Traditionally, shielding depended on the use of metals whose EM properties are well understood. Increasingly though, complex materials are replacing metals and the intrinsic shielding effectiveness (SE) of these new materials may be difficult to predict. As a result, there is significant interest in developing measurement techniques which yield meaningful SE data. Two examples serve as illustrations.

Molded plastics have largely replaced metal boxes as housings for electronic equipment in commercial applications. Plastic is basically transparent to EM radiation; therefore, some metal-like property must be added to insure proper shielding. Existing approaches include conductive sprays, metal fibers injected during the molding process, foil inserts, metallization, electro-plating, and others [1]. Shielding-associated costs may well exceed 10% of the production cost [2]. Thus, it is important to make the most cost-effective choice among shielding methods, particularly when large production runs are involved. Recent FCC regulations applicable to commercial electronics combined with the adverse consequence of failing to pass FCC testing make the need for accurate SE data at the design stage all the more acute.

Avionics is another area where measured SE data are needed. Metal aircraft frames are being replaced partially or wholly with light-weight, high-strength composites and laminates. These materials may or may not adequately shield the sensitive electronic equipment housed inside an aircraft. As in commercial electronics, circuits continue to be miniaturized, operating at ever lower power levels. As a result, the amount of spurious radiation necessary to disrupt normal operation is also decreasing. Again, the need for reliable SE data at the design stage can be critical.

Most SE test procedures essentially follow the arrangement depicted in Fig. 4.1. Power from a transmitting antenna (P_t) is coupled to a receiving antenna with no test material present (P_r) and then with the test material introduced (P_r'), as shown in Figs. 4.1a and b respectively. The ratio of the received powers gives the resulting insertion loss (IL),

$$IL = 10 \log(P_r/P_r') \qquad \text{dB} \tag{4.1}$$

Insertion loss represents a quantitative measure of SE provided by the test material. Thus, the basic problem is quite simply stated. The difficulty is to separate the actual material properties tested from external factors such as antenna types used, orientations, antenna separation distance, field distribution, transient effects, etc. [3]. Is one truly measuring shielding when the material is inserted, or perhaps some other EM characteristics such as a change in an antenna input impedance? The present discussion will investigate these considerations based on a fairly general theoretical model. The emphasis will be on the importance of recognizing and understanding the effects of these factors when interpreting SE data.

4.1 Theory -- Small-Aperture Coupling

The simplest model of an EM shield is an infinite plane sheet separating a source from a receiver. This case is fundamental to understanding shielding theory. Much work has been done on this problem including Schelkunoff's basic transmission line description [4]-[8] applicable to planar-sheet, cylindrical, and spherical shielding, as well as the important case of low-impedance (magnetic-field) shielding [9]-[12]. An analysis of the plane-shield case reveals the basic mechanisms by which a material provides shielding: reflection, absorption, and internal re-reflection [9]. Realistically, however, infinitely large test samples are not available nor practical. A number of test procedures involve covering an aperture with a piece of shield material. Therefore, it is instructive to consider the problem of coupling through a small aperture. Our intention is to use this model as a means of illustrating some of the variables affecting SE measurements.

Consider the geometry shown in Fig. 4.2a. A set of fields, $\bar{E}_i$, $\bar{H}_i$, is incident on an empty aperture in a perfectly conducting screen. A cylindrical coordinate system (ρ, ϕ, z) will be located at the aperture center, with the z axis directed normally to the aperture surface as shown. If the aperture is electrically small, that is of dimension much less than a wavelength, then the fields penetrating the aperture to the other side of the screen (z > 0) will be similar to those produced by a set of equivalent dipole moments. The formal derivation of small-aperture coupling is well detailed elsewhere [13]. The present discussion requires only that we quote one basic result; namely, the fields produced by the equivalent dipole moments are given by [14]:

$$\bar{E}(R,\omega) = \frac{e^{-jk_0R}}{4\pi\varepsilon_0} \{ (\frac{1}{R^3} + j \frac{k_0}{R^2}) [3\hat{R} (\hat{R} \cdot \bar{P}_0) - \bar{P}_0] - \frac{k_0^2}{R} [\hat{R} \times (\hat{R} \times \bar{P}_0)] + \frac{1}{c} (j \frac{k_0}{R^2} - \frac{k_0^2}{R}) (\hat{R} \times \bar{M}_0)\} \tag{4.2}$$

$$\bar{H}(R,\omega) = \frac{-jk_0R}{4\pi} \{ (\frac{1}{R^3} + j \frac{k_0}{R^2})[3\hat{R} (\hat{R} \cdot \bar{M}_0) - \bar{M}_0] - \frac{k_0^2}{R} [\hat{R} \times (\hat{R} \times \bar{M}_0)] - c(j \frac{k_0}{R^2} - \frac{k_0^2}{R})(\hat{R} \times \bar{P}_0)\}$$

where a time convention of exp($j\omega t$) has been assumed, $k_0 = \omega/c$, c is the speed of light, $R = (\rho^2 + z^2)^{1/2}$ is the distance from the aperture center to the observation point, ε_0 is the free-space permittivity, $\hat{R}$ is the normalized position vector, [$\hat{R} = (\hat{\rho}\rho + \hat{z}z)/R$], $\bar{P}_0$ is the equivalent electric dipole moment due to the aperture fields, and $\bar{M}_o$ is the equivalent magnetic dipole moment.

The dipole moments depend on 1) the incident fields exciting the aperture and 2) the geometry of the aperture. This situation leads to the following standard decomposition:

$$\bar{P}_0 = \bar{\bar{\alpha}}_e \cdot \varepsilon_0 \bar{E}(\bar{0}) = \hat{z}\, \varepsilon_0\, \alpha_e\, E_z(\bar{0}) \tag{4.3}$$

$$\bar{M}_0 = \bar{\bar{\alpha}}_m \cdot \bar{H}(\bar{0}) = \hat{\rho}\, \alpha_m\, H_\rho(\bar{0})$$

where $\bar{\bar{\alpha}}_e$ and $\bar{\bar{\alpha}}_m$ are the electric and magnetic aperture polarizabilities dyadics (the geometry term), and $\bar{E}(\bar{0})$ and $\bar{H}(\bar{0})$ are the incident fields at the aperture center $\bar{0}$. The electric dipole moment is normal to the aperture ($\bar{\bar{\alpha}}_e = \hat{z}\, \alpha_e\, \hat{z}$) while the magnetic dipole moment is tangential ($\bar{\bar{\alpha}}_m = \hat{\rho}\, \alpha_m\, \hat{\rho}$) where, as implied by (4.3), we have oriented the ρ axis to coincide with the tangential component of the incident magnetic field.

Equations (4.2) and (4.3) together yield expressions for the penetrating fields. For the near-field ($k_0R << 1$) and far-field ($k_0R >> 1$) special cases, we find respectively that:

$$\bar{E}(R,\omega) = \frac{\alpha_e\, E_z(\bar{0})}{4\pi} \frac{e^{-jk_0R}}{R^3} [\hat{\rho} \frac{3\rho z}{R^2} + \hat{z} (\frac{3z^2}{R^2} - 1)]$$

(near-field)

$$\bar{H}(R,\omega) = \frac{\alpha_m H_\rho(\bar{0})}{4\pi} \frac{e^{-jk_0R}}{R^3} [\hat{\rho}(\frac{3\rho^2}{R^2} - 1) + \hat{z} \frac{3\rho z}{R^2}] \quad ; \tag{4.4}$$

and

$$\bar{E}(R,\omega) = - \frac{k_0^2}{4\pi} \frac{e^{-jk_0R}}{R} [\frac{\rho}{R} (\hat{\rho} \frac{z}{R} - \hat{z} \frac{\rho}{R}) \alpha_e E_z(\bar{0})$$

$$+ \hat{\phi} \eta_0 \frac{z}{R} \alpha_m H_\rho(\bar{0})]$$

(far-field)

$$\bar{H}(R,\omega) = - \frac{k_0^2}{4\pi} \frac{e^{-jk_0R}}{R} [- \frac{z}{R} (\hat{\rho} \frac{z}{R} - \hat{z} \frac{\rho}{R}) \alpha_m H_\rho(\bar{0})$$

$$+ \hat{\phi} \frac{1}{\eta_0} \frac{\rho}{R} \alpha_e E_z(\bar{0})] \quad ;$$

where $\eta_0 = 120\pi$ is the free-space impedance, and $\hat{\phi}$ is the unit vector.

A typical receiving antenna will respond primarily to either the electric or magnetic field with the received power proportional to the square of the appropriate component in the far-field case. Thus, each of the far-field components in (4.4) leads to a type of insertion loss measurement via (4.1). Idealizing the problem, we let $\bar{A}$ represent the receiving antenna's response to any of the field components, denoted by $\bar{F}(R,\omega)$. The far-field insertion loss should then behave like

$$IL = 20 \log \left| \frac{\bar{F}(R, \omega) \cdot \bar{A}}{\bar{F}'(R,\omega) \cdot \bar{A}} \right| \quad , \tag{4.5}$$

where the prime denotes the loaded aperture case, as depicted in Fig. 4.2b. Although (4.5) is strictly true only in the far-field case, we shall also apply it to near-field expressions in order to demonstrate the types of variations possible.

Equation (4.5), with one of the field components in (4.4) inserted, may now be used to examine some of the factors influencing insertion loss measurements. It should again be emphasized that (4.5) does not represent any specific measurement procedure per se; rather, it serves to illustrate some basic properties likely to be encountered in shielding studies featuring coupling through an aperture. We will consider the following variables: receiving antenna orientation, incident field distribution, and shielding material parameters.

4.2 Effects of the Receiving Antenna Orientation

Consider Fig. 4.2a. Intuitively one would probably locate the receiving antenna along the z axis, or boresight. In this case, $\rho = 0$, $z \neq 0$, and (4.5) yields

$$IL = 20 \log \left| \frac{\alpha_e E_z(\bar{0})}{\alpha_e' E_z'(\bar{0})} \right| = IL_E$$

$(\hat{z} \cdot \bar{A} \neq 0$, $\bar{E}$-measured, near field),

$$IL = 20 \log \left| \frac{\alpha_m H_\rho(\bar{0})}{\alpha_m' H_\rho'(\bar{0})} \right| = IL_H \tag{4.6}$$

$(\hat{\rho} \cdot \bar{A} \neq 0$, $\bar{H}$-measured, near field)

$$IL = IL_H \quad \left\{ \begin{array}{l} \hat{\phi} \cdot \bar{A} \neq 0, \ \bar{E}\text{-measured, far field} \\ \hat{\rho} \cdot \bar{A} \neq 0, \ \bar{H}\text{-measured, far field} \end{array} \right\}$$

where, as before, a prime denotes a loaded aperture quantity. In the near-field case, insertion loss depends on either electric-field coupling (IL_E) or magnetic-field coupling (IL_H) through the material. If, however, the receiving antenna is located in the far field, (4.6) reveals that we are considering IL_H regardless of the type of antenna used. For a typical conductive shield material, the difference between IL_E and IL_H can be dramatic. Thus, an insertion loss measurement can change significantly as we move from the near field to far field, as would be expected.

Another consideration is the effect of loading the aperture on the incident waveform. Ideally, the incident fields would be unchanged, that is $E_z(\bar{0}) = E'_z(\bar{0})$ and $H_\rho(\bar{0}) = H'_\rho(\bar{0})$. If this is indeed the case, then

$$\begin{aligned} IL_E &\to 20 \log |\alpha_e/\alpha'_e| \\ IL_H &\to 20 \log |\alpha_m/\alpha'_m| \quad , \end{aligned} \tag{4.7}$$

a desirable result, since we are primarily interested in measuring the material shielding properties which are contained in α'_e and α'_m. In general, the loading of the aperture could affect the transmitting antenna's characteristics, especially if the aperture is loaded in the near field of the transmitter. In fact, if the aperture is viewed as an impedance, loading the aperture might actually provide a better impedance match leading to greater field penetration with the shield material in place. This type of "gain" behavior has been observed in practice.

Suppose we now shift the receiving antenna from a boresight location to a grazing orientation ($z = 0$, $\rho \neq 0$). Insertion loss should then behave as follows:

$$\begin{aligned} &IL_E \quad (\hat{z} \cdot \bar{A} \neq 0, \ \bar{E}\text{-measured, near or far field}), \\ &IL_H \quad (\hat{\rho} \cdot \bar{A} \neq 0, \ \bar{H}\text{-measured, near field}) \\ &IL_E \quad (\hat{\phi} \cdot \bar{A} \neq 0, \ \bar{H}\text{-measured, far field}) \quad . \end{aligned} \tag{4.8}$$

We now find a different set of field coupling dependencies.

For receiving antenna orientations between these two extremes, both electric- and magnetic-field couplings will contribute. The implication of the above discussion is apparent; the choice of receiving antenna location can significantly affect an insertion-loss measurement, independent of the particular shield material being tested. One needs to recognize what type of coupling is being measured if results are to be given a proper interpretation.

4.3 Effects of Incident Field Distribution

Three types of incident field are usually associated with shielding measurements: plane wave, high impedance, and low impedance. The choice of incident-field type can certainly affect an insertion-loss measurement, as can be demonstrated via (4.5).

For a plane wave with an assumed normal incidence, both the electric and magnetic fields will be tangential to the aperture. Thus, $E_z(\bar{0}) = 0$, and in all cases (4.5) reduces to

$$IL \to IL_H \qquad \text{(normal plane wave)} \tag{4.9}$$

For a plane wave incident from a grazing angle, two polarizations are possible: $\bar{E}$ in or perpendicular to the plane of incidence. In the latter case, both $E_z(\bar{0})$ and $H_\rho(\bar{0})$ are zero and negligible fields will be coupled through the aperture. For $\bar{E}$ parallel to the plane of incidence, both $E_z(\bar{0})$ and $H_\rho(\bar{0})$ are present with $E_z(\bar{0}) = \eta_0 H_\rho(\bar{0})$. If the receiving antenna is also in the far field, we find that,

$$IL = 20 \log \left| \frac{E_z(\bar{0}) \{\frac{\rho}{R} [\hat{\rho} \frac{z}{R} - \hat{z} \frac{\rho}{R}] \alpha_e + \hat{\phi} \frac{z}{R} \alpha_m\} \cdot \bar{A}}{E'_z(\bar{0}) \{\frac{\rho}{R} [\hat{\rho} \frac{z}{R} - \hat{z} \frac{\rho}{R}] \alpha'_e + \hat{\phi} \frac{z}{R} \alpha'_m\} \cdot \bar{A}} \right|$$

($\bar{E}$-measured, far field, grazing plane wave)

(4.10)

$$IL = 20 \log \left| \frac{E_z(\bar{0}) \{\frac{z}{R} [\hat{\rho} \frac{z}{R} - \hat{z} \frac{\rho}{R}] \alpha_m + \hat{\phi} \frac{\rho}{R} \alpha_e\} \cdot \bar{A}}{E'_z(\bar{0}) \{\frac{z}{R} [\hat{\rho} \frac{z}{R} - \hat{z} \frac{\rho}{R}] \alpha'_m + \hat{\phi} \frac{\rho}{R} \alpha'_e\} \cdot \bar{A}} \right|$$

($\bar{H}$-measured, far field, grazing plane wave).

If the receiving antenna is located in the near field, then $IL \to IL_E$ if $\bar{E}$ is measured, while $IL \to IL_H$ if $\bar{H}$ is measured. Equation (4.10) indicates that both the material electric and magnetic shielding properties are important for the grazing plane-wave case, whereas a normal plane wave (4.9) largely tests the material magnetic shielding properties only. As discussed in the previous section, the effects of α_e and α_m in (4.10) may be decoupled individually by reorienting the receiving antenna.

If a high-impedance incident field is applied, as produced by an electric dipole near the aperture for example, then $H_\rho(\bar{0}) << E_z(\bar{0})$ and

$$IL \to IL_E \text{ (high-impedance field)} \tag{4.11}$$

independent of the receiving antenna type. Analogously, a low-impedance field implies that $H_\rho(\bar{0}) >> E_z(\bar{0})$, thus

$$IL \to IL_H \text{ (low-impedance field)} \tag{4.12}$$

in all cases. Comparing (4.12) and (4.9), we see that insertion-loss measurements using coaxial magnetic loops should yield results similar to those based on a normally incident plane wave if aperture coupling is used. If we were coupling fields through a plane sheet of material, this conclusion would not hold since in one case the wave impedance is low and in the other (plane wave) the wave impedance is η_0. Again, it should be emphasized that the range of values defined by IL_E and IL_H can be large; thus the choice of incident field significantly affects the resulting insertion-loss measurements. This point can be explained by considering some realistic material parameters.

4.4 Material Factors

The loaded aperture polarizabilities are difficult to specify in general, as is the effect of loading on the incident field. If, however, we limit our attention to a circular aperture of radius r and retain only the first-order terms in $k_0 r$, then approximate loaded aperture polarizabilities are available for the thin conductive sheet model depicted in Fig. 4.2b, based on a formulation by Casey [15]. We find that

$$\frac{\alpha_m}{\alpha_m'} = 1 + \frac{j\ 160\ k_0 r\ \sigma h}{1 + 2\pi\ \sigma h R_c} + O(k_0^2 r^2) \tag{4.13}$$

and

$$\frac{\alpha_e}{\alpha_e'} \to \infty \quad ,$$

where σ and h are the material conductivity and thickness, and R_c is a possible contact resistance between the material and the aperture plane conductor. As indicated, to this order of approximation, α_e' is negligible. Note that the above magnetic polarizability ratio depends on material properties (σ and h) as desired, but also on the aperture size ($k_0 r$) and the contact resistance R_c which have no intrinsic relationship to the material EM shielding properties. Given any SE measurement procedure, it is important to recognize these extrinsic factors even if they cannot be isolated out.

Equation (4.13) may be inserted into (4.6) to generate some representative values for IL_H. We see that $IL_E \to \infty$ for this approximation. Clearly, this will not be the case in practice, but it is well known that any reasonable conductor will provide high levels of shielding against electric fields. Magnetic-field shielding, as measured by IL_H, tends to be more of a problem. For example, suppose an aluminum sheet [$\sigma = 3.72(10)^7$ S/m] of thickness h $= 1.27\ (10)^{-4}$ m [5 mils] is deposited on a plastic substrate. This might model a conductive spray applied to the plastic housing of some piece of electronic equipment. Assuming that $H_\rho(\bar{0}) \approx H_\rho'(\bar{0})$, and choosing $k_0 r = 0.2$ as a typical value, we obtain

$$IL_H = 10 \log \left| 1 + \left[\frac{1.51(10)^5}{1 + 2.96(10)^4\ R_c}\right]^2 \right| \quad \text{dB.} \tag{4.14}$$

If the contact resistance is zero, a value IL_H = 103.6 dB results. This would indicate quite good magnetic-field shielding. However, suppose some contact resistance exists, say R_c = 0.01 Ω. Then IL_H reduces to 54.1 dB. If R_c rises to 1 Ω, IL_H = 14.3 dB. Thus, a 1-Ω resistance reduces IL_H by 89.3 dB, a rather significant change which has nothing to do with the material itself. In fact, variations in R_c could mask actual shielding properties. Contact resistance could be a problem where conductivity-filled plastics are used, since surface resins could cause R_c to be relatively high. The above example also indicates that the range of IL_E to IL_H could be large. As discussed, changing the antenna orientation or incident field can shift IL between these values. One is tempted to speculate that given any test material, changing these various factors could yield any level of insertion loss desired.

Insertion-loss measurements are a valuable tool to the EMC engineer; however, this tool must be used carefully. The basic point is that insertion-loss data may well depend more on the measurement procedure than on the material tested. Thus, when one attempts to evaluate the shielding capability of various materials, it is very important to understand how shielding data are obtained.

4.5 Measurement Techniques

We have seen that the key to understanding SE data is to evaluate the measurement procedure itself. We now turn our attention to the practical task of obtaining shielding data, reviewing specific methods which have been tested at NBS.

The particular methods of measurement studied at NBS are: a variation of MIL-STD 285 [16], a pair of circular coaxial transmission-line holders, a time-domain system in free space and through an aperture in a shielded room [17], a dual TEM cell [18],[19], and an apertured TEM cell in a reverberating chamber [20]. As expected from the above discussions, there can be substantial disagreement among the measured values of SE for the same material when these different methods are used.

A longstanding SE test procedure is the use of a shielded room approach based on a modification of MIL-STD 285 [16]. A source is placed inside a shielded room, a receiver outside, and coupling is via an aperture in one of the walls. This method is simple, and shielded rooms are widely available. However, repositioning the source antenna can vary results up to ±40 dB because of room resonances [21]. In view of this wide variation of results, only by taking a tremendous number of measurements and "averaging" can any meaningful data be obtained. This is prohibitively time consuming and costly. Reproducing results using different shielded rooms is extremely difficult. The data shown in Fig. 4.3 are for a piece of plastic-aluminum-plastic, layered, fabric-like material obtained in a shielded room of dimensions 2.34m X 2.10m X 3.0m and with a 46 cm^2 aperture. Tuned dipole, biconical, or TEM horn antennas were used at two different distances and two sets of data were taken with and without material over the aperture. Data were taken at close frequency intervals in order to see effects of mode resonances. Due to the large number of modes that can exist within the shielded room, the orientation and impedance of the fields exciting the aperture is largely unknown. Therefore, it is difficult to specify whether shielded-room measurements simulate near-field or far-field shielding conditions.

True far-field testing using an infinite sheet of the material under test (MUT) is impractical. A realistic alternative is to use a waveguide to excite and receive the fields resulting in a simple, well isolated system. If the waveguide is to simulate a free-space plane wave, then a two-conductor transmission line supporting a transverse electromagnetic (TEM) wave is the logical choice. Two such coaxial holders will be considered. The most commonly used holder at present is that proposed by the American Society for Tests and Materials (ASTM) Committee D09.12.14 (for EMI shielding) as one of the emergency standards (ES 7-83). The holder is essentially an expanded section of 50-Ω circular coaxial line which may be disassembled to allow the insertion of an annular (washer shaped) test sample [22], as shown in Fig. 4.4. This fixture features continuous inner and outer conductors of dimensions 4.35 cm and 9.90 cm respectively.

A coaxial line such as the ASTM holder may be analyzed as a transmission line with the MUT represented as a loaded section [20]. However, if we recognize that the coaxial holder is primarily a low-frequency device, it should be adequate to model it as a simple circuit as shown in Fig. 4.5, where Z_0 is the characteristic impedance of the transmission line (50 Ω), and Z_L represents the impedance of the MUT. Based on this model IL should behave like

$$IL = 20 \left| 1 + \frac{Z_0}{2Z_L} \right| \quad . \tag{4.15}$$

The primary difficulty is that contact impedance Z_C between the MUT and the conductors can degrade results. Because the conductors are continuous, the contact impedance will appear in series with the MUT [23]. Thus, in (4.15) we would replace Z_L by $Z_L + Z_C$, or

$$IL = 20 \log \left| 1 + \frac{Z_0}{2(Z_L + Z_C)} \right| \; . \tag{4.16}$$

This expression indicates that contact impedance tends to degrade the measured insertion loss since the effective load impedance (denominator) is increased.

A second type of circular coaxial holder is a flanged version developed at NBS [24], as depicted in Fig. 4.6. It is similar to the ASTM design, except that two large flanges are used to hold a round disk of the MUT in place and capacitive loading couples the TEM mode through the MUT. It has an inner conductor diameter of 3.2 cm and an outer conductor diameter of 7.6 cm. The flange has an outer diameter of 13.3 cm. The "unloaded" reference measurement involves two pieces of the MUT which match the dimensions of the flanges while leaving the space between the inner and outer conductors empty. This tends to overcome the contact impedance problem except at frequencies too low to generate sufficient displacement currents in the MUT. A circuit model for the flanged holder is more complicated due to the capacitive effects [20]. However, if the capacitive coupling is strong, then analysis predicts that IL behavior will be similar to that of the idealized circuit shown in Fig. 4.5. In fact, we need good conductivity on only one side of the MUT to reduce the flanged holder IL expression to that of equation (4.15).

Figure 4.7 shows measured IL data up to 1 GHz from both holders for an aluminum-Mylar layered material. At these frequencies the aluminum-Mylar sample is electrically thin, thus we should have [20]

$$Z_0/Z_L \approx \eta_0 \sigma d \ , \tag{4.17}$$

where η_0 is the free-space wave impedance (377 Ω), σ is the conductivity of the MUT, and d is its thickness. Inserting this into (4.15) we see that an electrically thin MUT in a coaxial holder should ideally yield

$$IL = 20 \log \left| 1 + \frac{1}{2} \eta_0 \sigma d \right| \ . \tag{4.18}$$

This expression is independent of frequency and represents reflection alone. The flanged holder yields a flat IL curve of approximately 24 decibels. The ASTM holder yields a significantly lower IL level even when the material is silver painted to lower the contact impedance. If σd is known for a particular thin material, then (4.18) should allow one to predict the expected IL level. Conversely, measured results (when flat) yield an effective σd value; in this case IL = 24 decibels implies that σd = .079 for the aluminum-Mylar material. This value will be used later in discussing the near-field techniques.

Figure 4.8 shows data for the plastic-aluminum-plastic material. Because the surface of this material is insulating, we expect that contact impedance could be a problem. Again the flanged holder yields a flat IL of approximately 28 decibels, while the continuous conductor configuration data are more variable, even when the MUT is silver painted.

The upper frequency limit for usage of these coaxial holders is approximately 1 GHz while the lower limit (here 1 MHz) is determined largely by equipment. The dynamic range for these holders is 90-100 decibels and 15-30 minutes are required to generate a typical IL curve.

The coaxial holders are limited in frequency due to the appearance of higher-order modes which perturb the desired TEM mode field distribution. In order to gain plane-wave SE data at higher frequencies a time-domain signal approach is being investigated. The MUT is either a large sheet, as shown in Fig. 4.9, or a small sample mounted over an aperture in a large conducting screen (or shielded room). A short pulse is used as the source signal. Unwanted signal paths to the receiving antenna can be time windowed and only the direct path signal retained. This makes the large sheet, or the conducting screen, appear to be infinite in extent for some short interval. Time-domain data may be transformed to the frequency domain using Fourier transform techniques. If the source antenna is $\lambda/2\pi$ removed from the MUT, the arriving fields should be approximately plane wave. Coupling may be modeled in the frequency domain as a sequence of transmission functions representing propagation to the MUT from the source antenna (P_1), transmission through the MUT (T), aperture transmission (A) if applicable, and propagation to the receiving antenna (P_2) [20],[25]. For an insertion-loss measurement the propagation functions divide out and we are left with

$$IL = 20 \log |1/T| \ . \tag{4.19}$$

For a highly conductive screen excited by a normal plane wave we find [25]

$$T \approx \frac{2\eta}{\eta_0 \sinh \gamma d} \ , \tag{4.20}$$

where $\eta = (j\omega\mu/\sigma)^{1/2}$ is the material intrinsic impedance, and $\gamma = (j\omega\mu\sigma)^{1/2}$ is the propagation constant in the material. If $|\gamma d|$ is small which is the case for an electrically thin MUT, then (4.20) reduces to

$$T \approx 2/\eta_0 \sigma d \ . \tag{4.21}$$

If this expression is inserted into (4.19), we see that IL is approximately given by

$$IL \approx 20 \log\left|\frac{1}{2}\,\eta_0 \sigma d\right| . \tag{4.22}$$

This agrees with the coaxial holder expression (4.18) if $\eta_0 \sigma d >> 1$.

Figure 4.10 shows IL data for the same layered aluminum-Mylar material, obtained with the time-domain technique. Both a large sheet and an apertured screen are used. In the latter case the MUT may be mounted either on the source or receiver side. The IL data due to large sheet free-space simulation tend to be around 28-30 decibels which is somewhat higher than found in the coaxial holders. For the MUT mounted on the source side over a screen aperture we see basic agreement to the large sheet data above 1 GHz. The aperture significantly reduces coupling below 1 GHz thus the dynamic range there is poor. If the MUT is mounted on the receiving antenna side of the screen, results are further affected. The fields exciting the MUT are no longer plane wave, rather they are the aperture fields. Thus we now see resonance behavior. The implication is that if small samples are to be used over apertures, they should be mounted on the source antenna side if far-field simulation data are desired. Figure 4.11 shows data for the plastic-aluminum-plastic sample. Again the large-sheet IL data are somewhat higher than in the flanged coaxial holder (30-34 dB vs. 28 dB), but overall agreement is quite reasonable. The source-side data agree well with the large-sheet results except below 1 GHz, where as noted above, dynamic range begins to fall.

The frequency range for this method is from 200 MHz to 3.5 GHz. Shorter pulses would allow the upper frequency limit to be extended even further. Measurement time is fast (5-10 minutes) and repeatability is good. The present dynamic range is 50-60 decibels if a large sheet of MUT is used, and is lower for an aperture measurement particularly below 1 GHz.

In addition to far-field shielding data, it is also important to test the material near-field shielding performance. One such near-field method is the dual TEM cell (DTC). A single TEM cell is a section of expanded rectangular coaxial transmission line, as discussed in Chapter 3. The dual TEM cell fixture, Fig. 4.12, uses one cell to drive another via an aperture in a common wall. Coupling can be well modeled using small aperture theory. The sensing cell has two output ports. By summing (Σ) and differencing (Δ) these two output signals, the coupling of the normal electric-field (high-impedance) and tangential magnetic-field (low-impedance) components through the MUT may be monitored separately and simultaneously. One may show that [20]

$$IL(\Sigma) = 20 \log|\alpha_e/\alpha_e'|$$

and (4.23)

$$IL(\Delta) = 20 \log|\alpha_m/\alpha_m'|,$$

where α_e is the electric polarizability in the direction normal to the aperture, α_m is the magnetic polarizability tangential to the aperture and normal to the direction of propagation in the TEM cells, and the prime denotes the presence of the MUT as before. Thus $IL(\Sigma)$ gives a measure of the electric-field penetration through the MUT while $IL(\Delta)$ measures the magnetic-field penetration. It should be noted that the aperture itself also influences these quantities.

Sample results for the aluminum-Mylar material are given in Fig. 4.13. As expected of a good conductor, IL is greater for the electric-field component (sum power curve) than for the magnetic (difference power curve). A theoretical curve for magnetic-field IL is also given based on loaded aperture polarizabilities derived from Casey [15],[20] and the coaxial holder σd value discussed earlier. Agreement is quite good. Resonances associated with higher-order modes in the TEM cells begin to appear around 770 MHz; thus practical use of the present fixture is limited to frequencies below 1 GHz. These data may be compared to the 24-30 decibels IL characteristic of the two far-field simulation techniques. The magnetic-field IL curve is expected to be less than the plane-wave level, approaches zero along with the frequency, and is tending toward the free-space simulation level with increased frequency. However, the electric-field curve does not always exceed the free-space level as expected. Figure 4.14 shows sum and difference IL curves for the plastic-aluminum-plastic MUT. Again electric-field shielding exceeds magnetic, a distinct resonance appears around 770 MHz, and the theoretical difference-power curve is in good agreement.

The dynamic range of this system is 50-60 decibels, repeatability is good, and approximately 30 minutes are required to generate a single curve.

An alternative to the DTC is to use a reverberation chamber to excite an apertured TEM cell. A reverberating chamber is a modified shielded room which allows us to generate a high-frequency, statistically known field. (Details on reverberating chambers are referred to Chapter 8.) The analysis is similar to that for the DTC [20]. Figure 4.15 shows IL data for the aluminum-Mylar sample. Results are very similar to those obtained in the DTC except that the electric-field shielding (sum power) tends to be somewhat lower and more variable. Half of the DTC was used for this study; thus the upper frequency limit is the same (less than 1 GHz). The use of smaller cells will enable us to extend coverage to higher frequencies. Figure 4.16 shows data for the plastic-aluminum-plastic material. Proper use of the reverberating chamber requires that it be highly multi-moded. The dimensions of the NBS chamber are such that below 200 MHz the number of modes is insufficient; thus in both curves we see poor results below this frequency. The dynamic range of this system is 90-100 decibels, and repeatability is good. However, the time required to produce a single curve is long, in the order of 3 to 4 hours.

Some other measurement methods have also been tried by the EMC community. For example, near-field testing using a dual box has been suggested by ASTM as another emergency standard [26]. This technique is essentially a scaled version of a shielded room and therefore suffers the same reproducibility problem. Conductivity measurements via the transfer-impedance method [27] can be used to predict plane-wave shielding. Additional variations of the coaxial line and dual box methods have also been reported [28].

REFERENCES

[1] Miller, M. B. Materials and techniques used in EMI/RFI shielding of plastic chassis for electronic systems. EMI/RFI Shielding Plastics Symposium Record (Society of Plastics Engineering); 1984 June; Chicago, IL. 139-150;

[2] Armstrong, H. W. The long term environmental effects upon conductive coatings for plastic enclosures. MIDCON/82 Conference Record, 28/2/1-5; 1982 November; Dallas, TX.

[3] Franceschetti, G.; Papas, C. H. Steady state and transient electromagnetic coupling through slabs. IEEE Trans. Antennas and Propag. AP-27(5): 590-596; 1970 September.

[4] Schelkunoff, S. A. Electromagnetic Waves. New York, NY: Van Nostrand; 1943. 303-315.

[5] Cowdell, R. B. New dimensions in shielding. IEEE Trans. Electromag. Compat. EMC-10(1): 158-167; 1968 March.

[6] Stirrat, W. A. USAECOM contributions to shielding theory. IEEE Trans. Electromag. Compat. EMC-10(1): 63-66; 1968 March.

[7] Schulz, R. B.; Plantz, V. C.; Brush, D. R. Low-frequency shielding resonance. IEEE Trans. Electromag. Compat. EMC-10(1): 7-15; 1968 March.

[8] Babcock, L. F. Computer determination of electromagnetic wave shielding effectiveness. IEEE Trans. Electromag. Compat.EMC-10(1): 331-334; 1968 March.

[9] Levy, S. Electromagnetic shielding effect of an infinite plane conducting sheet placed between circular coaxial coils. Proc. IRE, vol. 24(6): 923-941; 1936 June.

[10] Moser, J. R. Low-frequency shielding of a circular loop electromagnetic field source. IEEE Trans. Electromag. Compat. EMC-9(1): 6-18; 1967 March.

[11] Bannister, P. R. New theoretical expressions for predicting shielding effectiveness for the plane shield case. IEEE Trans. Electromag. Compat. EMC-10(1): 2-7; 1968 March.

[12] Bannister, P. R. Further notes for predicting shielding effectiveness for the plane shield case. IEEE Trans. Electromag. Compat. EMC-11(2): 50-53; 1969 May.

[13] Collin, R. E. Field Theory of Guided Waves, New York, NY: McGraw-Hill; 1960; 288-298.

[14] Taylor, C. D. Electromagnetic pulse penetration through small apertures. IEEE Trans. Electromag. Compat. EMC-15(1): 17-26; 1973 February.

[15] Casey, K. F. Low-frequency electromagnetic penetration of loaded apertures. IEEE Trans. Electromag. Compat. EMC-23(4): 367-377; 1981 November.

[16] MIL-STD 285 Attenuation measurements for enclosures, electromagnetic shielding, for electronic test purposes, method of. DoD; 1956 June.

[17] Ondrejka, A. R.; Adams, J. W. Shielding effectiveness measurement techniques. IEEE Natl. Symp. on EMC; April 1984; San Antonio, TX.

[18] Wilson, P. F.; Ma, M. T. Shielding effectiveness measurements with a dual TEM cell. IEEE Trans. Electromagn. Compat. EMC-27(3): 137-142; 1985 August.

[19] Faught, A. N. Jr.; Dowell, J. T.; Scheps, R. D. Shielding material insertion loss measurement using a dual TEM cell system. IEEE Int. Symp. on EMC; 1983 August; Arlington, VA. .

[20] Wilson, P. F.; Ma, M. T. A study of techniques for measuring the electromagnetic shielding effectiveness of materials. Nat. Bur. Stand. (U.S.) Tech. Note 1095; 1986 May.

[21] Free, W. R. Radiated EMI shielded enclosures. IEEE Int. Symp. on EMC; 1967 July; Washington, D. C. 43-53.

[22] Simon, R. M.; Stutz, D. Test methods for shielding materials. EMC Tech., vol. 2; 39-48; 1983.

[23] Weck, R. A. Thin-film shielding for microcircuit applications and a useful laboratory tool for plane-wave shielding evaluations. IEEE Trans. Electromagn. Compat. EMC-10(2): 105-112; 1968 March.

[24] Adams, J. W.; Vanzura, E. J. Shielding effectiveness measurements of plastics. Nat. Bur. Stand. (U.S.) Int. Rept. 85-3035; 1986 January.

[25] Ari, N.; Hansen, D.; Schar, H. Electromagnetic pulse (EMP) penetration through circular apertures in the frequency domain. Proc. IEEE, vol. 73(2): 368-369; 1985 February.

[26] Oberholtzer, L. C.; Mauriello, A. J.; Stutz, D. E. A treatise of the new ASTM EMI shielding standard. ITEM 1984; 174-178.

[27] Dike, G; Wallenburg, R.; Birkin, J. Electromagnetic relationships between shielding effectiveness and transfer impedance. IEEE Int. Symp. on EMC; 1979 October; San Diego, CA. 133-138.

[28] Hariya, E.; Masahiro, U. Instruments for measuring the electromagnetic shielding effectiveness. IEEE Int. Symp. on EMC; October 1984; Tokyo, Japan. 800-805.

(a) Unloaded coupling.

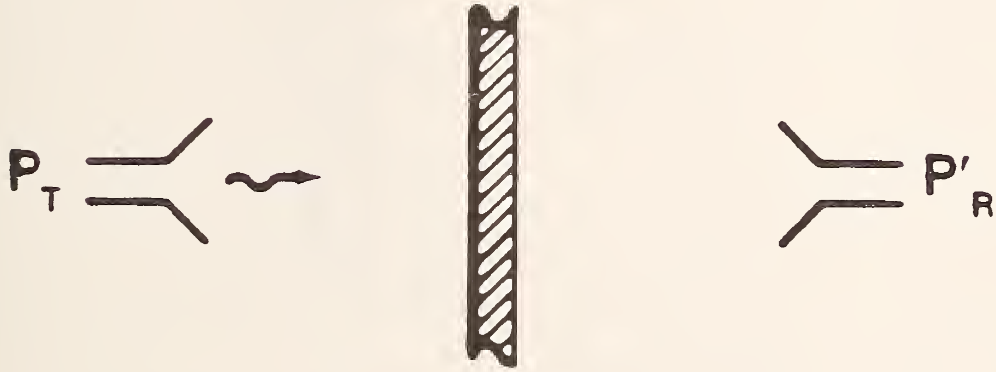

(b) Loaded coupling.

$$IL = 10 \log \left| \frac{P_R}{P'_R} \right| dB$$

Figure 4.1 A typical arrangement for measuring shielding effectiveness of materials.

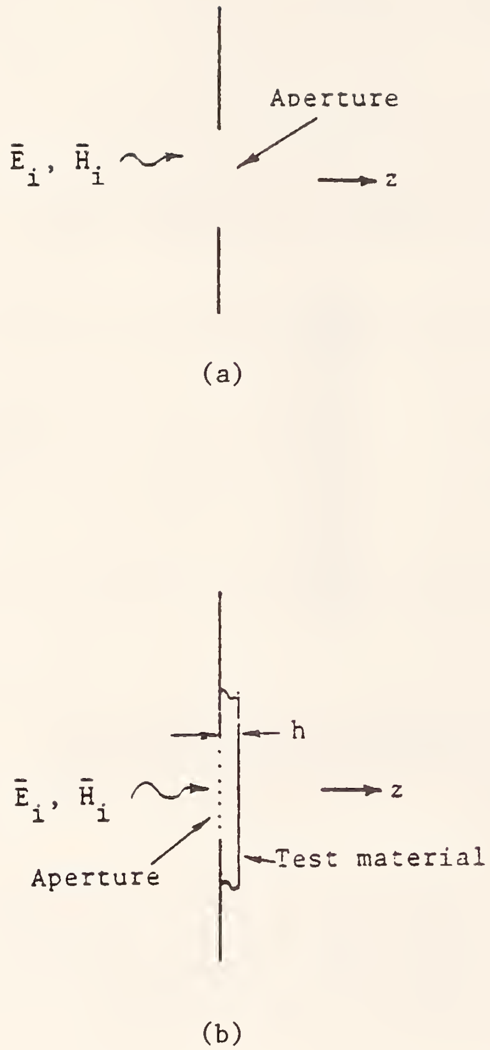

Figure 4.2 An arrangement for aperture SE measurement:
(a) Fields incident on an empty aperture,
(b) Fields incident on a loaded aperture.

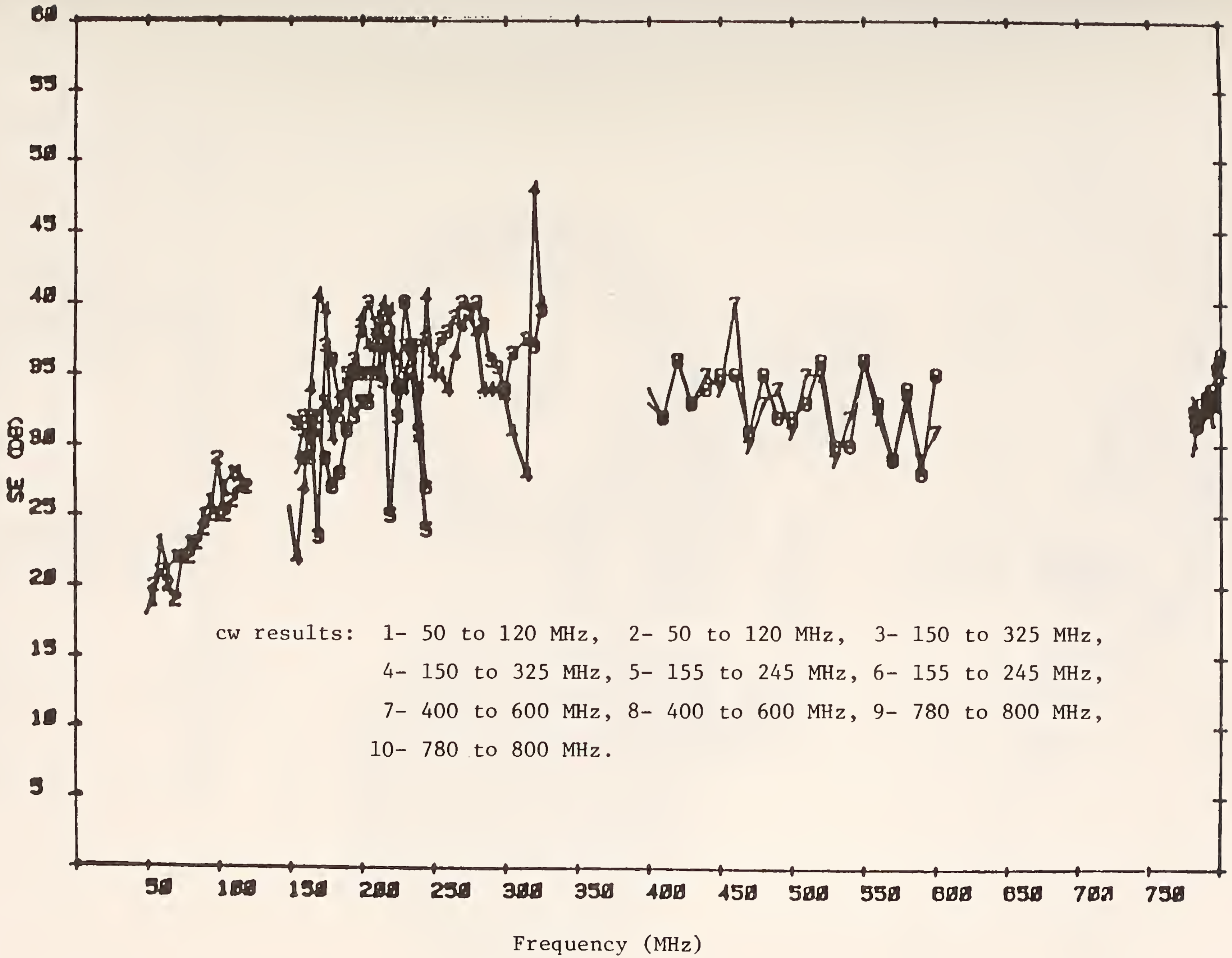

Figure 4.3 Insertion loss data for a plastic-aluminum-plastic sample measured in a shielded room using multiple antennas and locations.

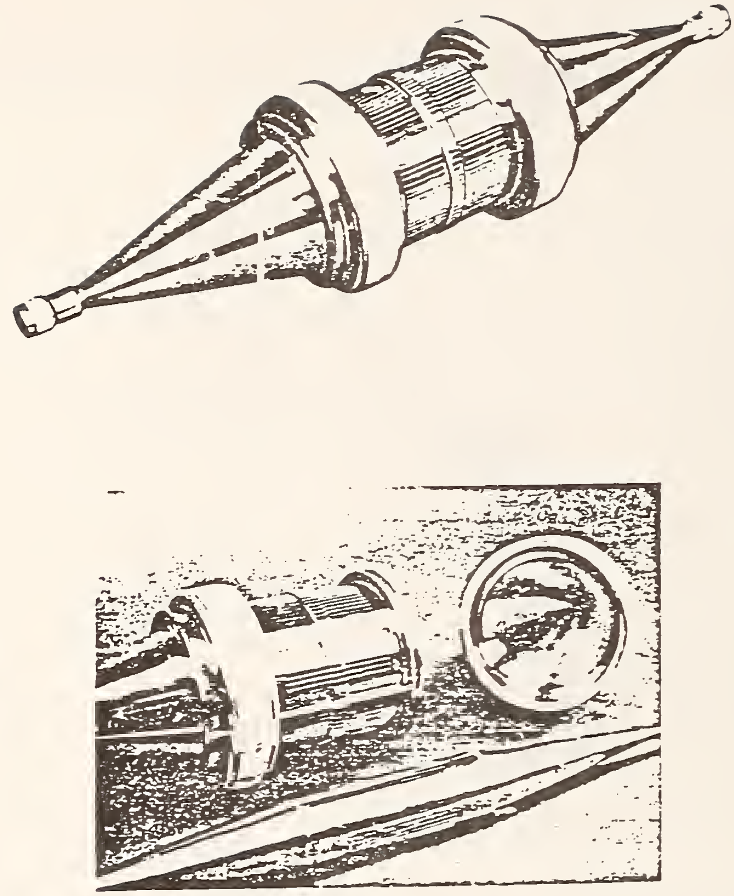

Figure 4.4 ASTM model of circular coaxial transmission-line holder.

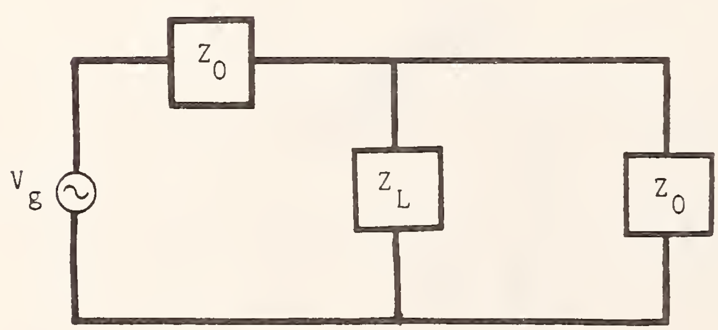

Figure 4.5 Idealized coaxial holder circuit model.

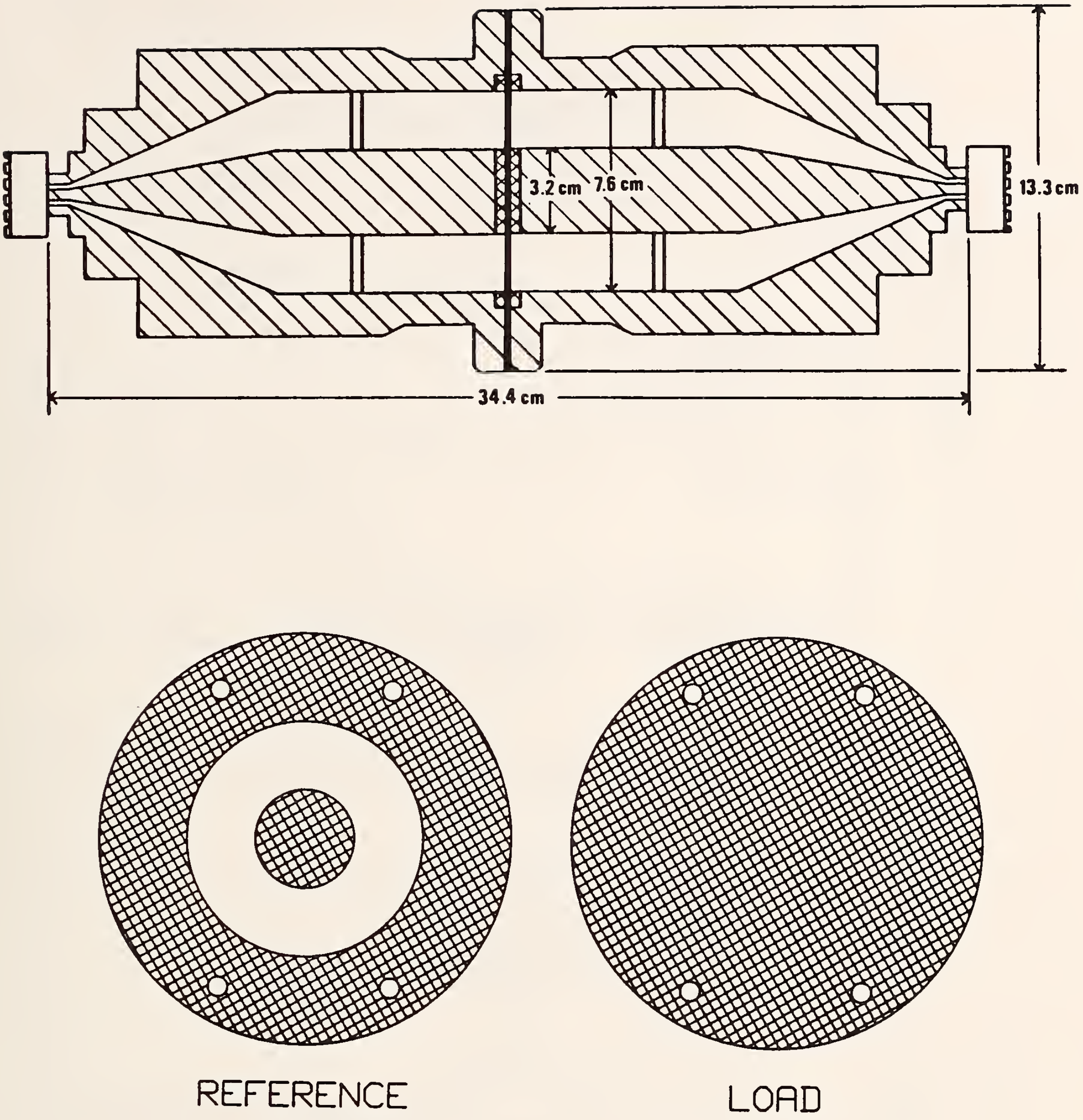

Figure 4.6 The NBS flanged coaxial transmission-line holder.

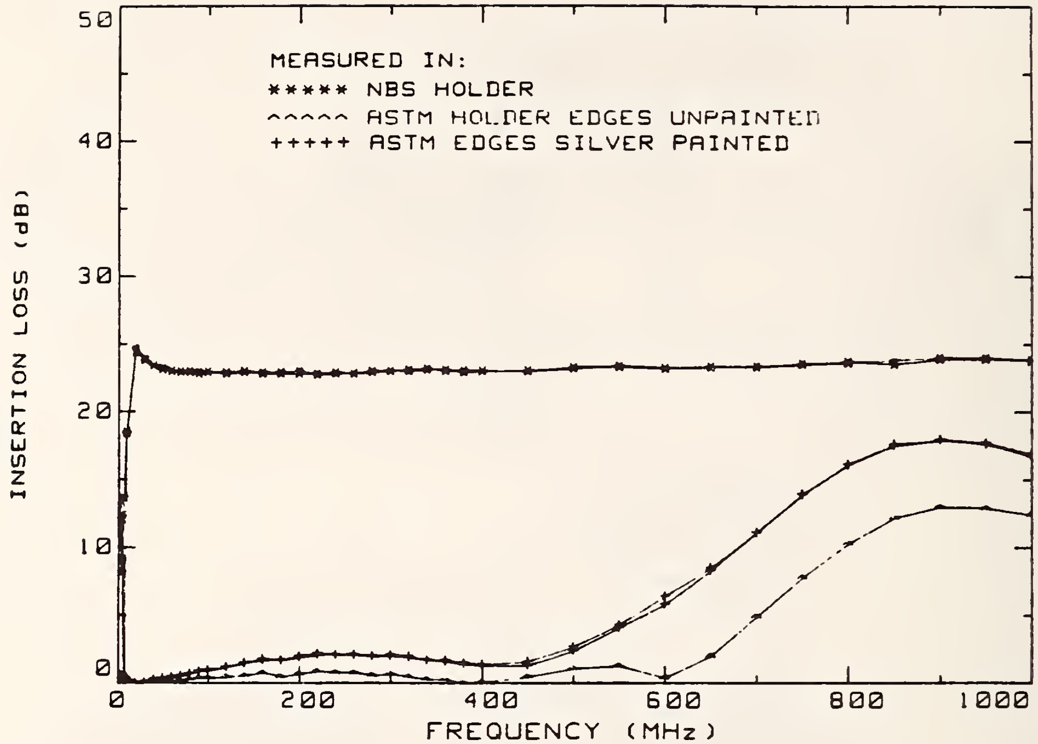

Figure 4.7 Insertion losses for an aluminum-Mylar sample measured in the ASTM and flanged circular coaxial holders.

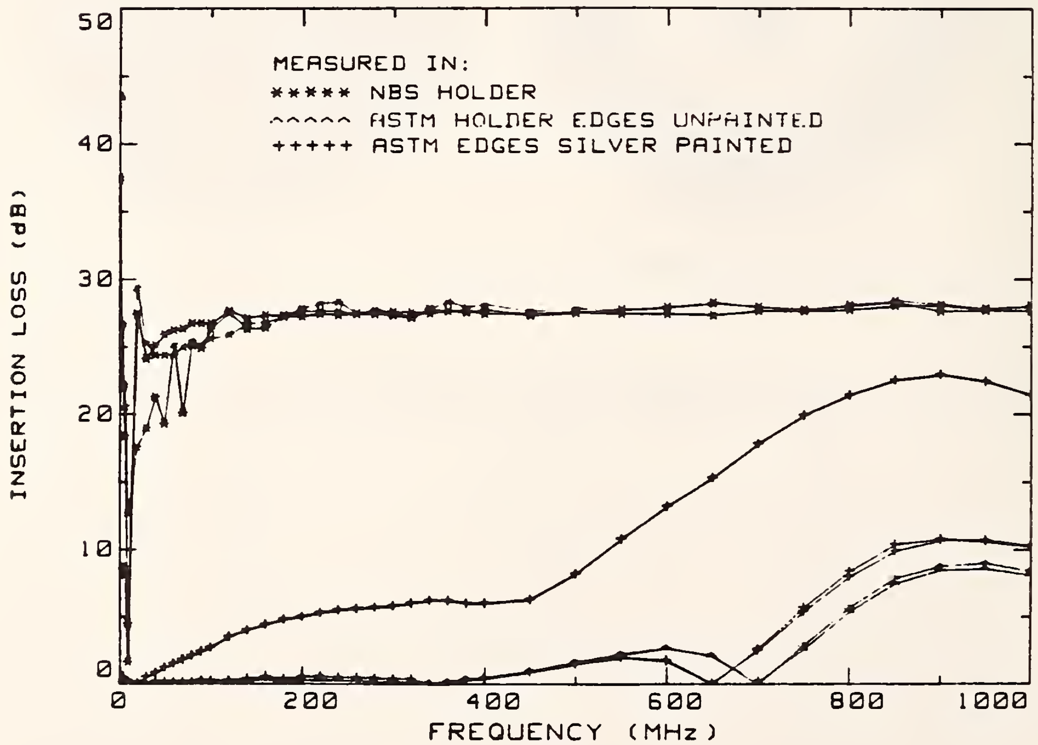

Figure 4.8 Insertion losses for a plastic-aluminum-plastic sample measured in the ASTM and flanged circular coaxial holders.

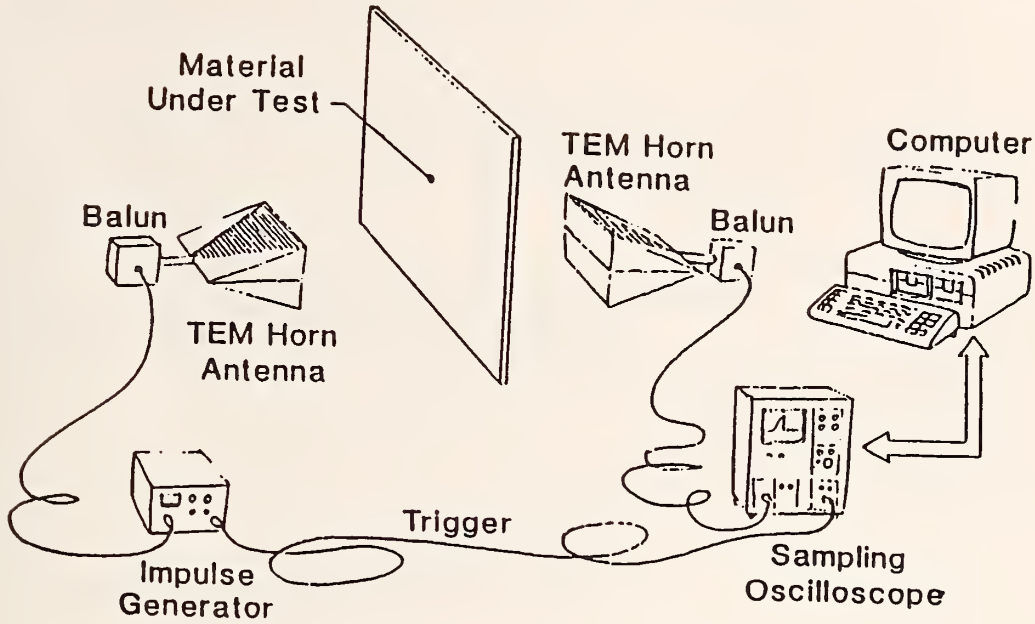

Figure 4.9 The time-domain measurement system.

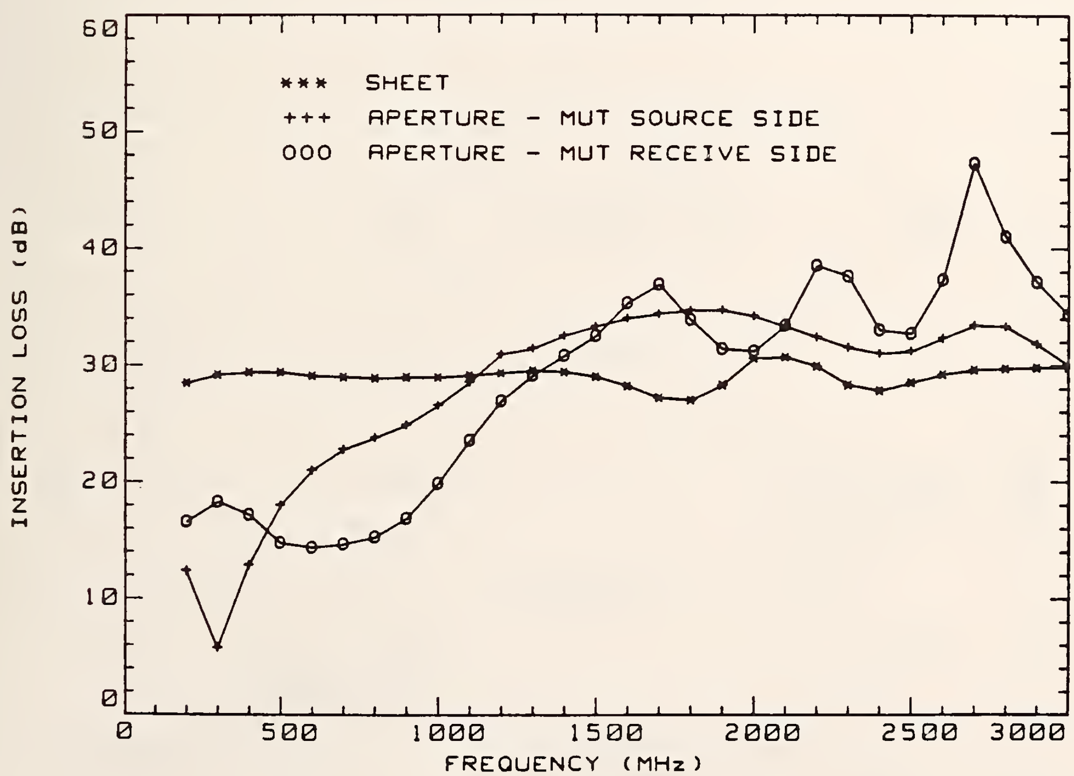

Figure 4.10 Insertion losses for an aluminum-Mylar sample measured with a time-domain signal.

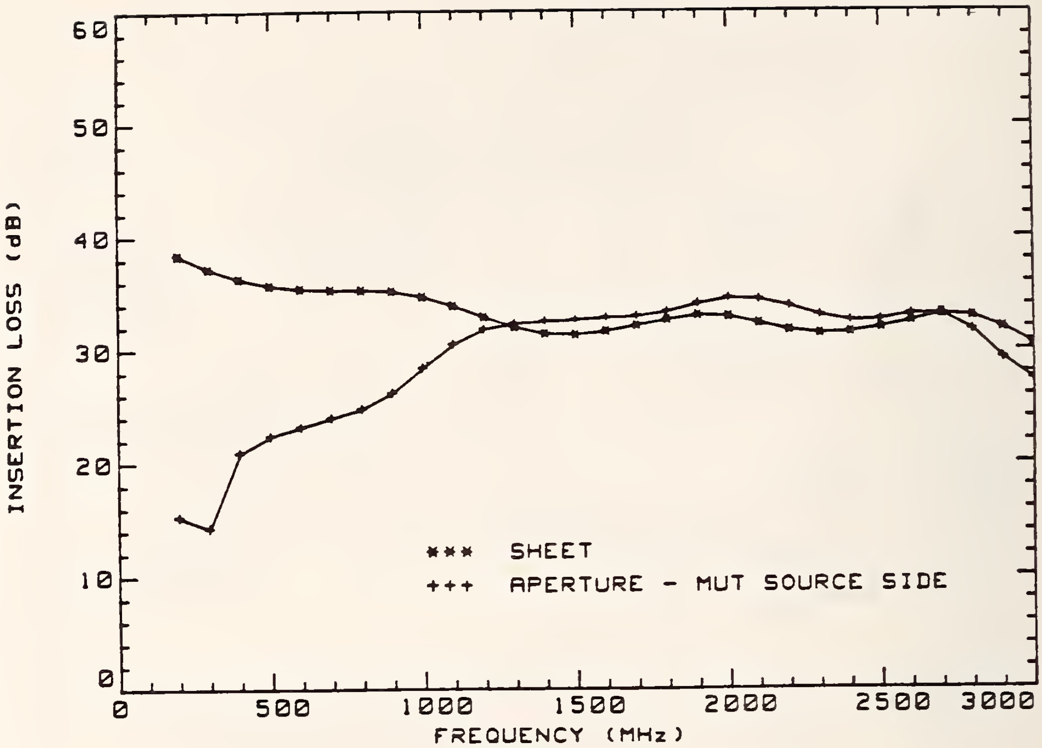

Figure 4.11 Insertion losses for a plastic-aluminum-plastic sample measured with a time-domain signal.

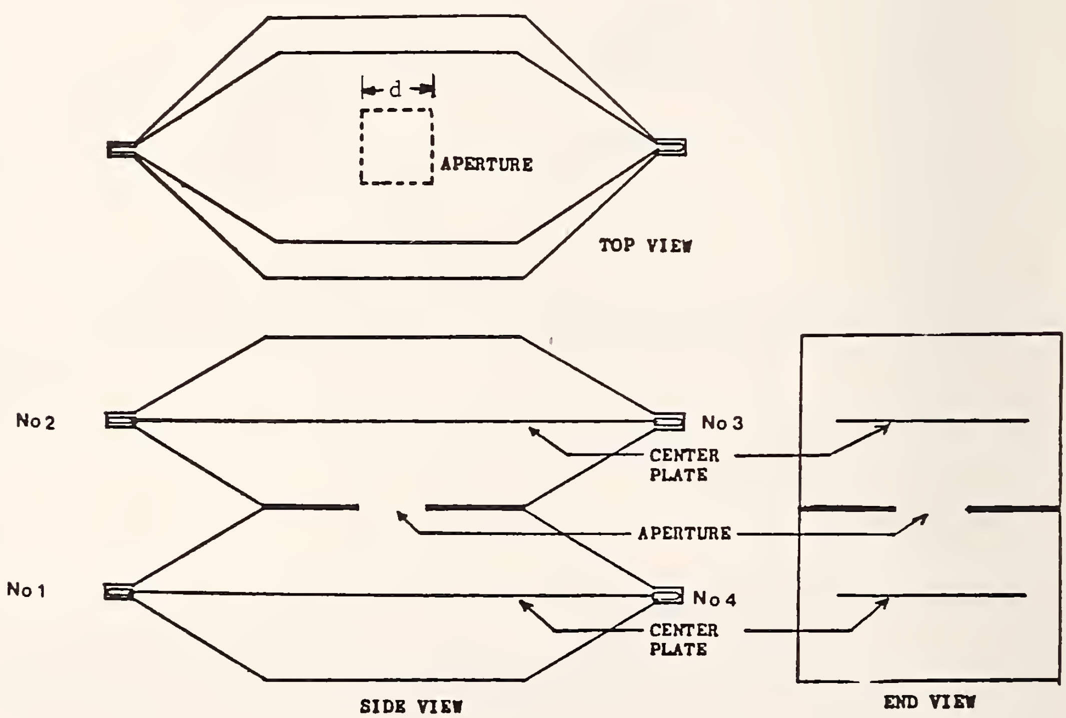

Figure 4.12 A dual TEM cell. The particular model used at NBS has the following dimensions: a = 9 cm, b = 6 cm, g = 2.2 cm, and d = 5.08 cm, where d is the aperture side length, and a, b, and g have the same meanings as those in Chapter 3 for a single TEM cell.

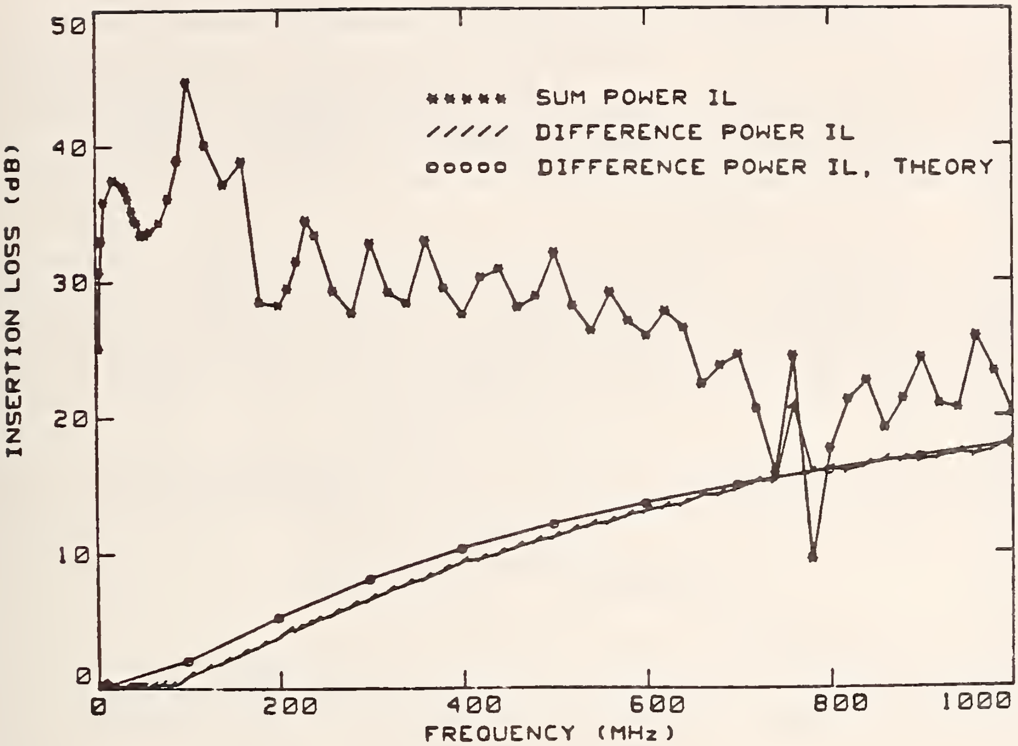

Figure 4.13 Insertion losses for an aluminum-Mylar sample measured in the dual TEM cell shown in Figure 4.12.

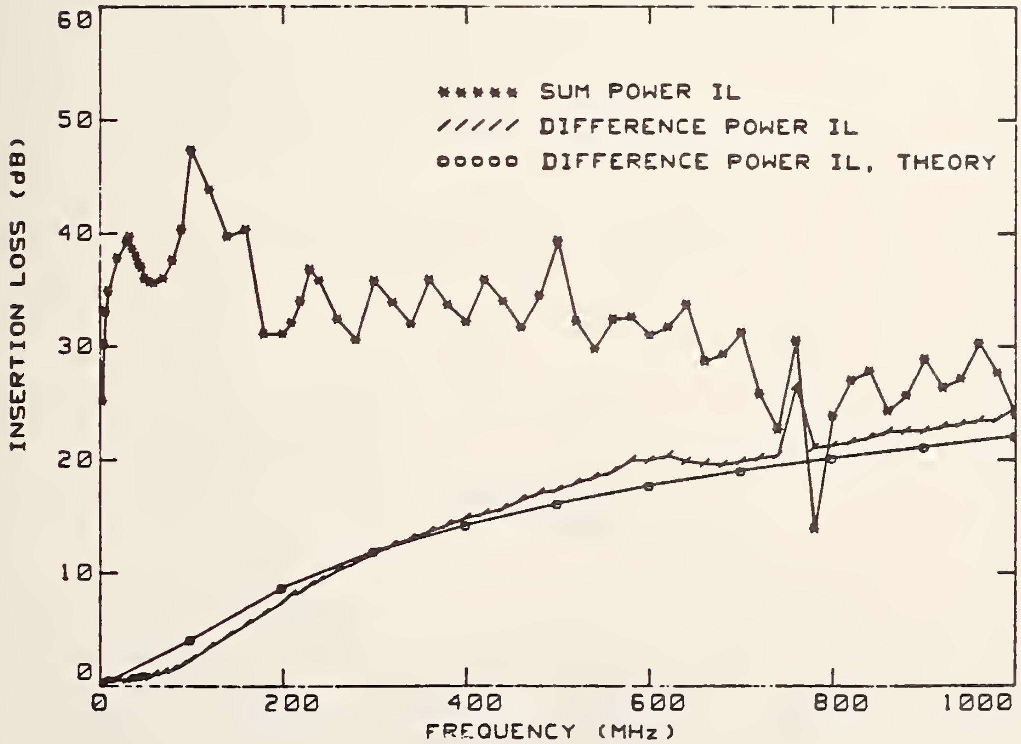

Figure 4.14 Insertion losses for a plastic-aluminum-plastic sample measured in the dual TEM cell shown in Figure 4.12.

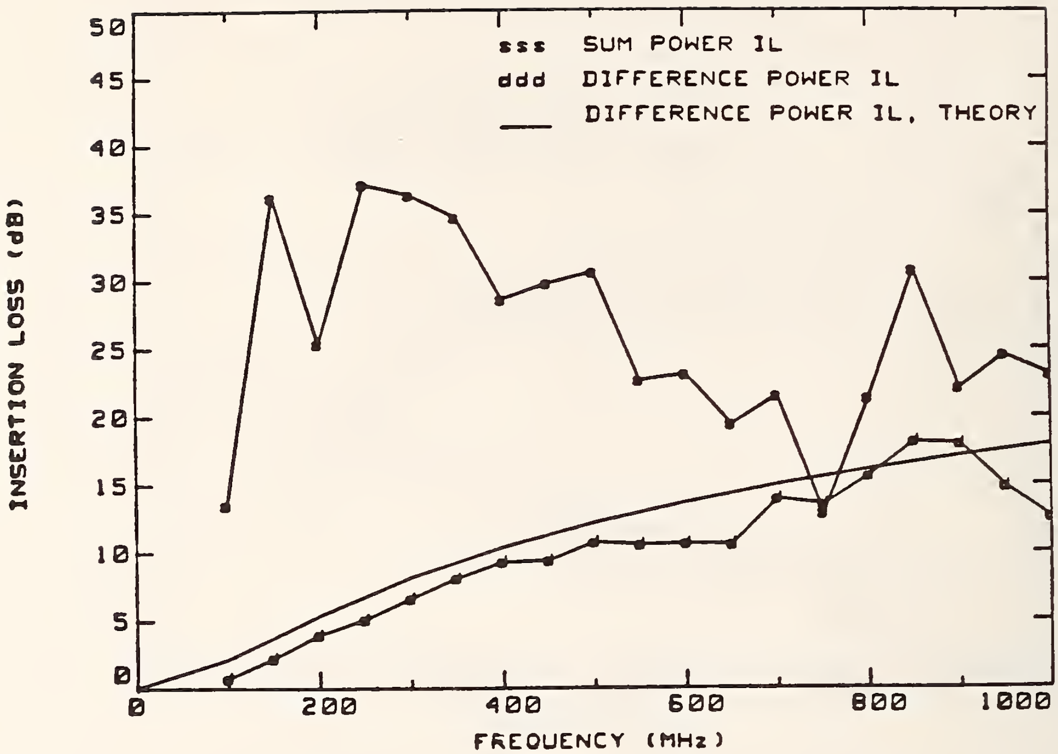

Figure 4.15 Insertion losses for an aluminum-Mylar sample measured with an apertured TEM cell in a reverberating chamber.

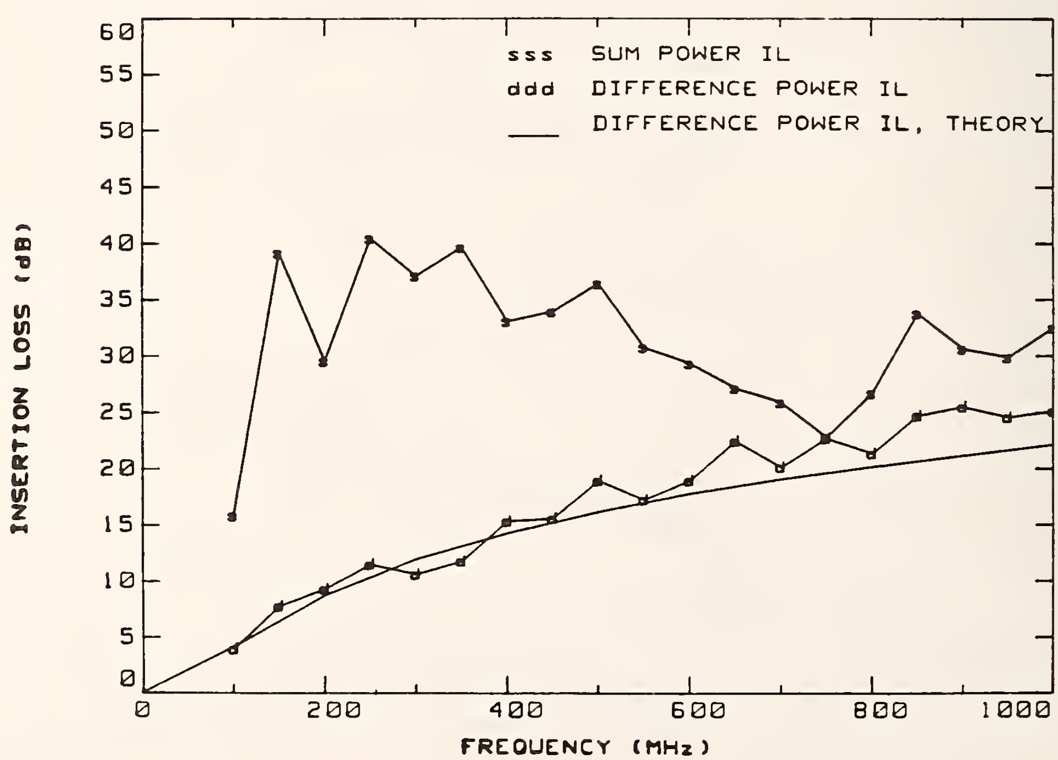

Figure 4.16 Insertion losses for a plastic-aluminum-plastic sample measured with an apertured TEM cell in a reverberating chamber.

Microwave anechoic chambers are currently in use for a variety of indoor antenna and EMI/EMC measurements. The prime requirement is that an appropriate transmitting antenna at one location within the chamber generates a plane-wave field throughout another volume of the chamber of dimensions sufficient to perform tests. This volume is frequently referred to as a quiet zone and its "quietness", or reflectivity level, will determine the performance of an anechoic chamber.

The anechoic chamber at NBS is shown in a side view in Fig. 5.1. Pyramidal horns or open-ended waveguide (OEG) antennas are used as sources of chamber illumination at a position in the access doorway with their apertures inside the plane of the absorber points on the chamber wall. A cart on precision tracks located under the measurement axis can be moved horizontally through a distance of 5 m by a stepping-motor drive system. There are gaps in the absorber on the floor to accommodate each rail.

The purpose of this chapter is to discuss how to establish a standard EM field, and the methodology for evaluating the corresponding errors associated with antenna and EMI/EMC measurements in an anechoic chamber.

5.1 Measurement of the Net Power to Source Antennas

One potential error in the standard EM field to be established by the source antenna arises from the uncertainty in the net power delivered to it. In turn, this uncertainty reflects our lack of knowledge of the amplitudes and phases of the various reflection and transmission coefficients in the power delivery system, as well as the uncertainty in measurements of the power incident upon, and reflected from, the source antenna. Thus, we wish to compute more accurately the net power delivered to a standard transmitting antenna from measurements of incident and reflected powers obtained with a dual directional coupler. Our power delivery and measurement system can be represented by a four-port black box as shown in Fig. 5.2. The port terminations and numbering are:

(1) power meter to monitor the forward (throughput) power,

(2) power meter to monitor the power reflected from the standard transmitting antenna,

(3) source of the CW RF power,

(4) transmitting antenna.

The net power delivered to the transmitting antenna representing the difference between incident and reflected powers is given by [1]:

$$P_{net} = P_{inc} - P_{ref}$$

$$= \frac{P_1}{(1 - |\Gamma_1|^2)} \left|\frac{S_{34}}{S_{13}}\right|^2 |g(S, \Gamma)|^2$$

$$- \frac{P_2}{(1 - |\Gamma_2|^2)} \frac{1}{|S_{24}|^2} |h(S, \Gamma)|^2 \quad . \tag{5.1}$$

The symbols P_1 and P_2 are, respectively, power meter readings at ports 1 and 2, Γ_1 and Γ_2 represent the corresponding reflection coefficients observed looking into power meters 1 and 2, S_{ij} is the scattering parameter defined as the ratio of the complex wave amplitude emerging from port i to that incident upon port j, $g(S,\Gamma)$ and $h(S,\Gamma)$ are functions of the system S-parameters and the reflection coefficients of ports 1, 2 and 4 [1]. In an ideal coupler, i.e, zero reflection coefficient for all coupler input ports and infinite directivity ($S_{11} = S_{22} = S_{33} = S_{44} = S_{14} = S_{41} = S_{23} = S_{32} = 0$), and for a matched power meter at port 1 ($\Gamma_1 = 0$), it can be shown [1] that $g(S,\Gamma) = h(S,\Gamma) = 1$. Unless the magnitudes and phases of the system S-parameters and the reflection coefficients are well determined, $g(S,\Gamma)$ and $h(S,\Gamma)$ are not calculable. The extent of deviation from unity is, therefore, taken to be an error contribution to the determination of the net power delivered to the standard antenna. Although the degree of deviation from unity is a function of the system S and Γ parameters, it is found to be, in general, less than 1%. [1].

To compute the net power given in (5.1), the terms S_{34}/S_{13} and $1/S_{24}$ need to be determined. Although the magnitudes of S_{13}, S_{24}, and S_{34} could be measured with a network analyzer, the system implemented at NBS for establishing standard EM fields is a self-calibrating system which utilizes a standard flat-plate short and a matched termination. When a short ($\Gamma_4 = 1$) is placed at port 4, the ratio of power measurements P_2 and P_1 gives

$$\frac{P_2}{P_1} = \left|\frac{S_{24}\,S_{34}}{S_{13}}\right|^2 \frac{1-|\Gamma_2|^2}{1-|\Gamma_1|^2}\,(1+|\Delta_1|^2) \quad , \tag{5.2}$$

where $\Delta_1(S,\Gamma)$ is a complex quantity much less than unity [1]. The second step in evaluating the net power delivered to a transmitting antenna is to replace the short at port 4 with a well-matched power meter. The ratio of the two power measurements P_1 and P_4 is

$$\frac{P_1}{P_4} = \left|\frac{S_{13}}{S_{34}}\right|^2 \frac{1-|\Gamma_1|^2}{1-|\Gamma_4|^2}\,(1+|\Delta_2|^2) \quad , \tag{5.3}$$

where Δ_2 is another complex quantity much less than unity [1]. From (5.2) and (5.3), a value for $|1/S_{24}|^2$ is obtained. In summary, we perform two power-ratio measurements with a standard short and a matched termination in order to determine $|S_{34}/S_{13}|^2$ and $|S_{24}|^2$. The terms, Δ_1 and Δ_2, involve the products of the system S parameters and reflection coefficients Γ. Since the magnitudes and phases of Δ_1 and Δ_2 cannot be easily determined, the extent of deviation from zero is, therefore, taken to be another error contribution. Moreover, the uncertainty in the power-ratio measurements, P_2/P_1 and P_1/P_4, and the uncertainty in the reflection measurements Γ_1, Γ_2, and Γ_4 also contribute an error in the determination of $|S_{34}/S_{13}|$ and $|S_{24}|$. The detailed discussion on this topic may be found elsewhere [1]. Thus, the net power supplied to a transmitting antenna is determined from the absolute power measurements, P_1, P_2, and P_4.

5.2 Near-Zone Gain of Open-Ended Rectangular Waveguide

The EM field measurements in an anechoic chamber are usually performed in the near-field region of the transmitting standard antenna, and the approach used to establish the standard field strength is to calculate the radiated field strength in the near-field region of the transmitting antenna. The antenna considered for this purpose consists of a series of open-ended waveguides below 500 MHz and a series of rectangular pyramidal horns above 500 MHz.

The near-zone gain of an open-ended, unflanged rectangular waveguide is calculated from a forward near-field power pattern, which is determined from the conventional far-field power pattern by use of the plane-wave scattering theorem [2].

The geometry of the open-ended rectangular waveguide is shown in Fig. 5.3. The E-plane pattern, $E_E(\theta)$, is predicted quite accurately by inserting the electric and magnetic fields of the propagating TE_{10} mode into the Stratton-Chu formula and integrating over the aperture of the waveguide [3]. Thus, we have

$$E_E(\theta) = A_E \frac{\{1 + (\beta/k)\cos\theta + \Gamma[1 - (\beta/k)\cos\theta]\}}{[1 + \beta/k + \Gamma(1 - \beta/k)]} \cdot \frac{\sin(kb\sin\theta/2)}{kb\sin\theta/2} \quad (5.4)$$

where the normalized propagating constant β/k for the TE_{10} mode equals $[1 - (\pi/ka)^2]^{1/2}$, with k being the free-space wave number, and Γ is the reflection coefficient of the TE_{10} mode from the end of the waveguide. The constant A_E, which is related to the amplitude of the incident TE_{10} mode, will be defined later.

In the case of the H-plane fields, the aperture integration of the Stratton-Chu formulas with the electric and magnetic fields of the TE_{10} mode neglects the fringe currents and, therefore, produces much too broad an H-plane pattern. Using an accurate estimate of the fringe currents on the $x = \pm a/2$ sides of the rectangular waveguide from a numerical solution to the electric-field integral equation applied to the open-ended rectangular waveguide [4], we obtain for the H-plane pattern

$$E_H(\theta) = A_H\left[\frac{(\cos\theta + \beta/k) + \Gamma(\cos\theta - \beta/k)}{(\pi/2)^2 - (ka\sin\theta/2)^2} + C_o\right]\cos(ka\sin\theta/2) \quad (5.5)$$

The constant A_H is related to A_E in (5.4) by

$$A_E = A_H\{(2/\pi)^2[1 + \beta/k + \Gamma(1 - \beta/k)] + C_o\} \quad (5.6)$$

The constant C_o is calculated by equating the radiated power determined from the far-field to the total input power determined from the TE_{10} mode field.

Once the far-field power pattern of an open-ended rectangular waveguide is determined, the plane-wave scattering theorem enables us to predict its near-field power pattern [5]. The near-zone gain of this antenna is then determined by integrals of its near-field power pattern. The evaluation of the uncertainty of the near-zone gain will be performed by comparing it with the experimental results [6].

5.3 Near-Zone Gain Calculations of Rectangular Pyramidal Horns

The approach used at NBS to establish a standard field at frequencies above 500 MHz involves the use of a series of rectangular pyramidal horns. In deriving the near-zone gain of a pyramidal horn by the Kirchhoff method, Schelkunoff accounted for the effect of the horn flare by introducing a quadratic phase error in the dominant mode field along the aperture coordinates [7]. Geometrical optics and single diffraction by the aperture edges yields essentially the Kirchhoff results. The proximity effect in the Fresnel zone can also be approximated by a quadratic phase error in the aperture field.

To improve Schelkunoff's equation by taking into account the reflection of the diffracted fields from the horn interior and double diffraction at the aperture, the concepts of the geometrical theory of diffraction are used to determine the on-axis near-zone gain of an E-plane pyramidal horn. Taking into account the preceding considerations, we obtain the improved near-zone gain of a pyramidal horn [8]:

$$G = \frac{32\,ab}{\pi\lambda^2} R_E R_H \quad (5.7)$$

where R_E and R_H are the gain reduction factors due to E-plane and H-plane flares, respectively. The pertinent horn dimensions used in (5.7) are shown in Fig. 5.4. The factor $32\,ab/(\pi\lambda^2)$ is the gain of an in-phase field distribution uniform across one dimension of a rectangular aperture and cosinusoidal across the other.

The H-plane flare of the horn is given by [8]:

$$R_H = \frac{\pi^2\{[C(u) - C(v)]^2 + [S(u) - S(v)]^2\}}{4(u - v)^2}, \tag{5.8}$$

where C and S are the Fresnel integrals defined as

$$C(w) - jS(w) = \int_0^w \exp(-j\pi t^2/2)\, dt \quad , \tag{5.9}$$

and their arguments u and v are defined as

$$u = A + B, \quad v = -A + B ,$$

with

$$A = \frac{a}{(2\lambda \ell_H')^{1/2}} \quad , \quad B = \frac{1}{a} (\lambda \ell_H' /2)^{1/2},$$

$$\ell_H' = r\ell_H/(r + \ell_H) \tag{5.10}$$

and r being the distance between the center of the horn aperture to the field point.

The E-plane factor R_E is given by [8]:

$$R_E = \frac{1 + \cos\phi_o}{4w^2} \left|\exp(-jk\ell_E \cos\phi_o) + 2v(\ell_E', \pi - \phi_o) + \frac{\pi a'}{a} S_2\right|^2 , \tag{5.11}$$

where

$$w = \frac{b}{(2\lambda\ \ell_E')^{1/2}\cos(\phi_o/2)} \quad , \text{ and } \quad \ell_E' = r\ell_E/(r + \ell_E) \quad .$$

The factor $v(\ell, \alpha)$ is given by:

$$v(\ell, \alpha) = - \frac{\exp(k\ell \cos\alpha)}{2} [1 - (1 - j) D] \quad , \tag{5.12}$$

with

$$D = C[(4k\ell/\pi)^{1/2} \cos(\alpha/2)] - j\ S[(4k\ell/\pi)^{1/2} \cos(\alpha/2)] \quad .$$

The factor S_2 is defined as

$$S_2 = \sum_{i=1}^{m} v(\ell_E, \frac{\pi}{2} - i\phi_o)\ f(d_i, \pi - \phi_o, \frac{\pi}{2} - i\phi_o) \quad , \tag{5.13}$$

where

$$f(d, \theta, \theta_o) = v(d, \theta - \theta_o) + v(d, \theta + \theta_o) \quad , \tag{5.14}$$

$d_i = 2\ell \sin(i\phi_o)$ is the ray-path length between single and double diffractions, and m is the largest integer less than $\pi/2\phi_o$.

The near-zone gain, (5.7), of a pyramidal horn is then used to calculate the radiated field strength in the near zone of the antenna. The typical gain reduction factors R_E and R_H expressed in decibels are shown in Fig. 5.5. The evaluation of the uncertainty of the gain reduction factors will be performed by comparing the theoretical values with the experimental results [6].

5.4 Reflections from Anechoic Chamber Walls

The failure of the chamber to provide a true, free-space test environment affects the measurement accuracies. The performance of a rectangular RF anechoic chamber can be checked by measuring the relative insertion loss versus separation distance between a source antenna and a receiving antenna [9].

Relative insertion loss is the ratio of power received by a receiving antenna or probe for the initial test position to that received for different test positions. It is assumed that the input impedances of the source antenna and probe and the power transmitted by the source antenna all remain unchanged. If the anechoic chamber were a perfect free-space simulator, the relative insertion loss would vary with distance according to the free-space transmission loss formula given by [7]

$$P_r/P_t = g_s g_p(\lambda/4\pi d)^2 \tag{5.15}$$

where P_t is the net power transmitted by the source antenna, P_r the power received by the probe, g_s the near-zone gain of the source antenna, g_p the near-zone gain of the receiving probe, d the antenna separation distance in meters, and λ the wavelength in meters.

Measured data are compared to the free-space transmission loss calculated using the appropriate near-zone antenna gains. Disagreement between the measured insertion loss and calculated transmission loss is a measure of reflections from chamber surfaces, assuming the near-zone gain calculations are exact for the separation distance considered. The measured relative insertion loss versus antenna separation distance provides voltage-standing-wave-ratio (VSWR) data by means of a longitudinal probe scan. Rear-wall reflections and source-to-probe interactions are often resolvable at all frequencies, but reflections from the ceiling, side walls and floor are difficult to identify at frequencies below 500 MHz because the VSWR period is too long. Figure 5.6 shows an example of measured relative insertion loss with calculated free-space transmission loss along the axis of the horn antenna.

REFERENCES

[1] Kanda, M.; Orr, R. D. A radio-frequency power delivery system: procedures for error analysis and self-calibration. Nat. Bur. Stand. (U.S.) Tech. Note 1083; 1985 August.

[2] Kerns, D. M. Plane-Wave Scattering-Matrix Theory of Antennas and Antenna-Antenna Interactions, NBS Monograph 162; 1981 June.

[3] Stratton, J. A. Electromagnetic Theory. New York, NY: McGraw-Hill; 1941.

[4] Yaghjian, A. D. Approximate formulas for the far fields and gain of open-ended rectangular waveguide. Nat. Bur. Stand. (U.S.) Int. Rept. 83-1689; 1983 May.

[5] Yaghjian, A. D. Efficient computation of antenna coupling and fields within the near-field region. IEEE Trans. Antennas and Propag. AP-30(1): 133-138; 1982 January.

[6] Kanda, M; Orr, R. D. Near-field gain of a horn and an open-ended waveguide: comparison between theory and experiment. Fifth International Conference on Electromagnetic Compatibility, Institution of Electronic and Radio Engineers; September 29 to October 2, 1986; University of York, England.

[7] Schelkunoff, S. A. Electromagnetic Waves. New York, NY: Nostrand Reinhold; 1943.

[8] Jull, E. V. Errors in the predicted gain of pyramidal horns. IEEE Trans. Antennas and Propag. AP-21(1): 25-31; 1973 January.

[9] FitzGerrell, R. G. Using free-space transmission loss for evaluating anechoic chamber performance. IEEE Trans. Electromag. Compat. EMC-24(3): 356-358; 1982 August.

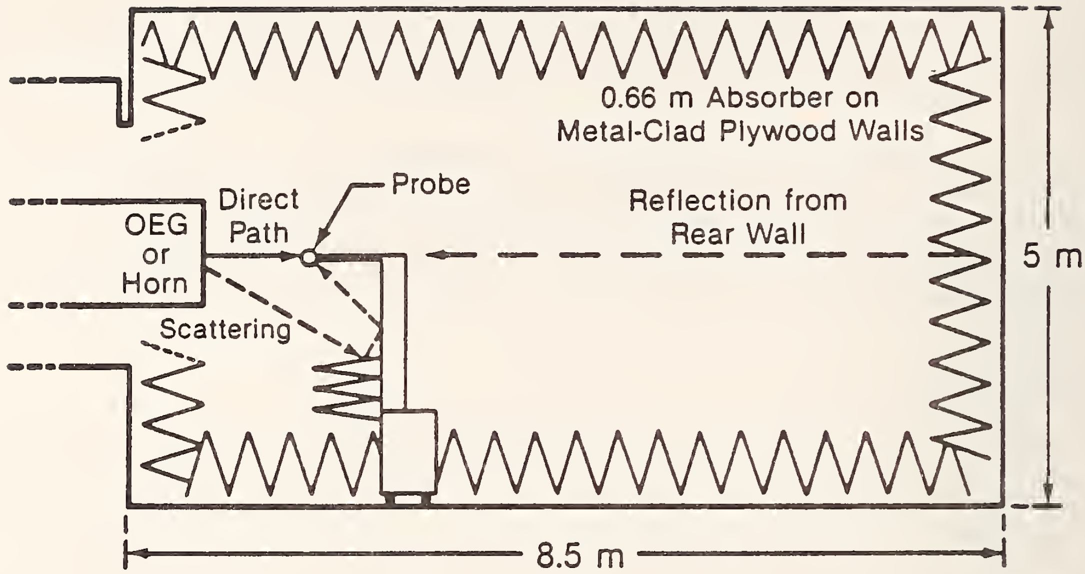

Figure 5.1 Side view of the NBS anechoic chamber.

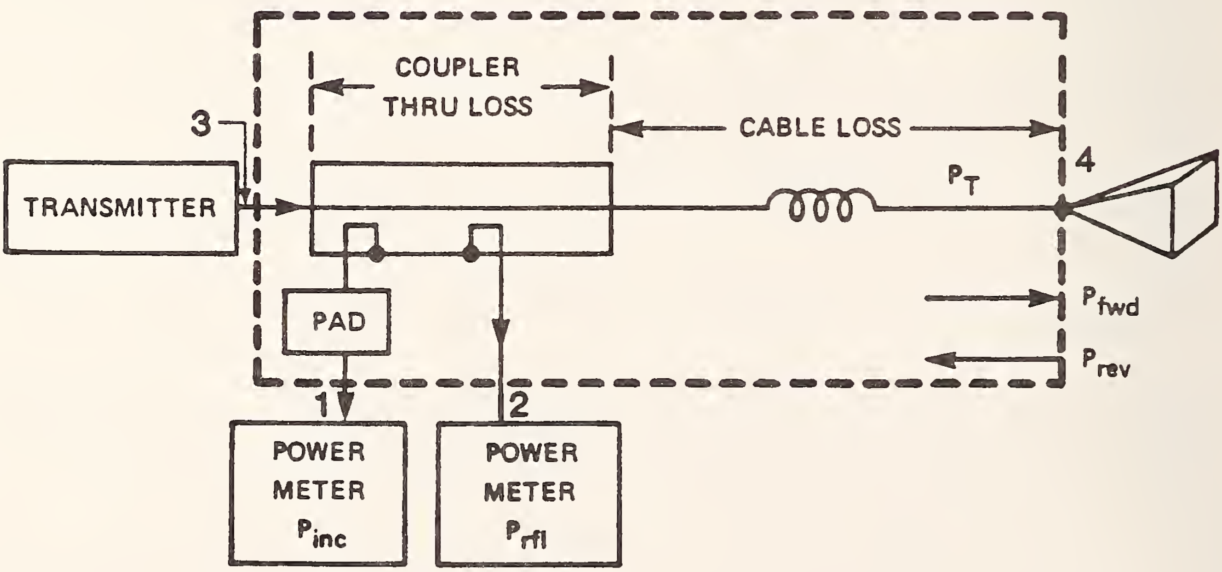

Figure 5.2 Measuring the net power to a standard antenna.

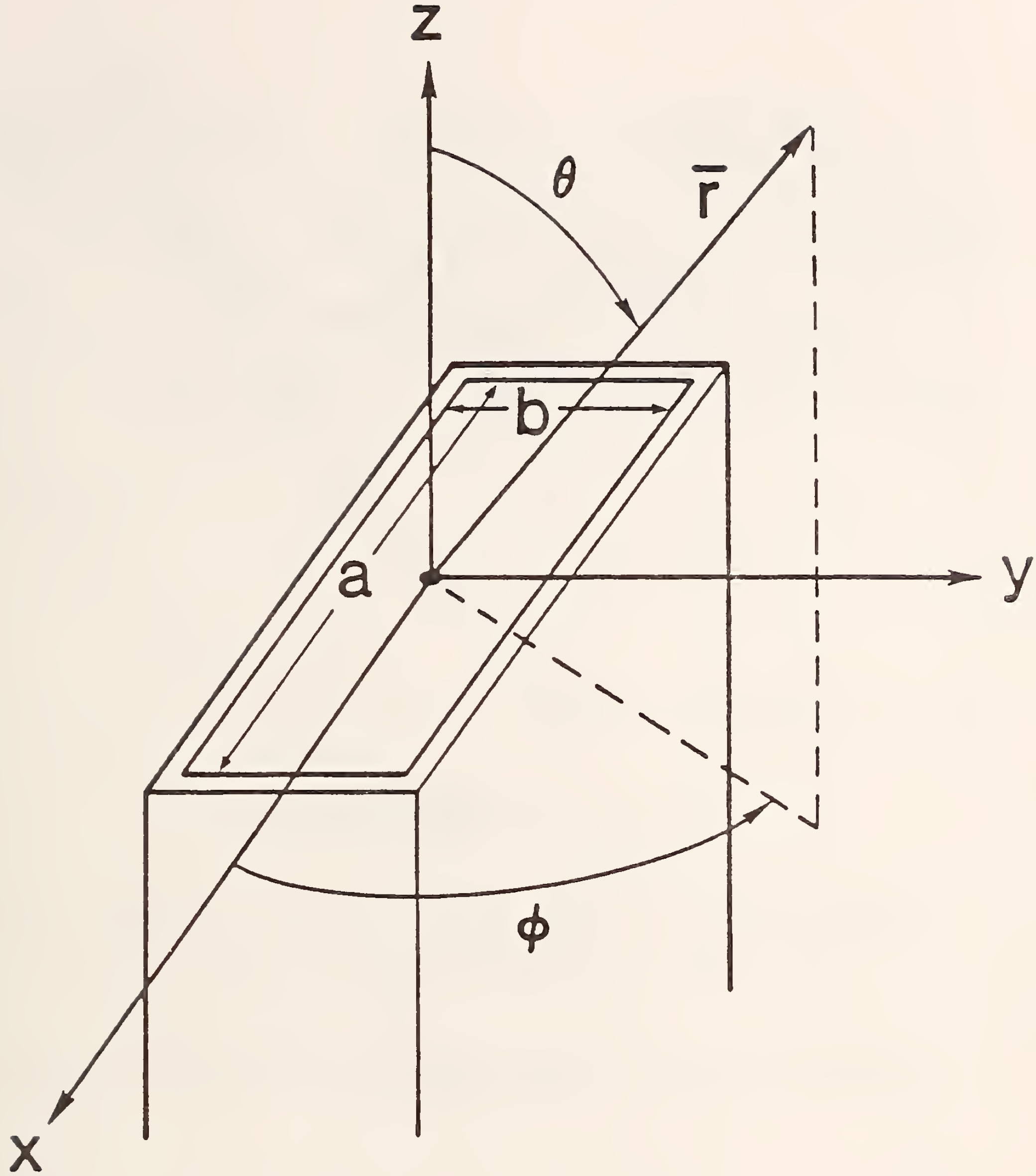

Figure 5.3 Geometry of open-ended rectangular waveguide.

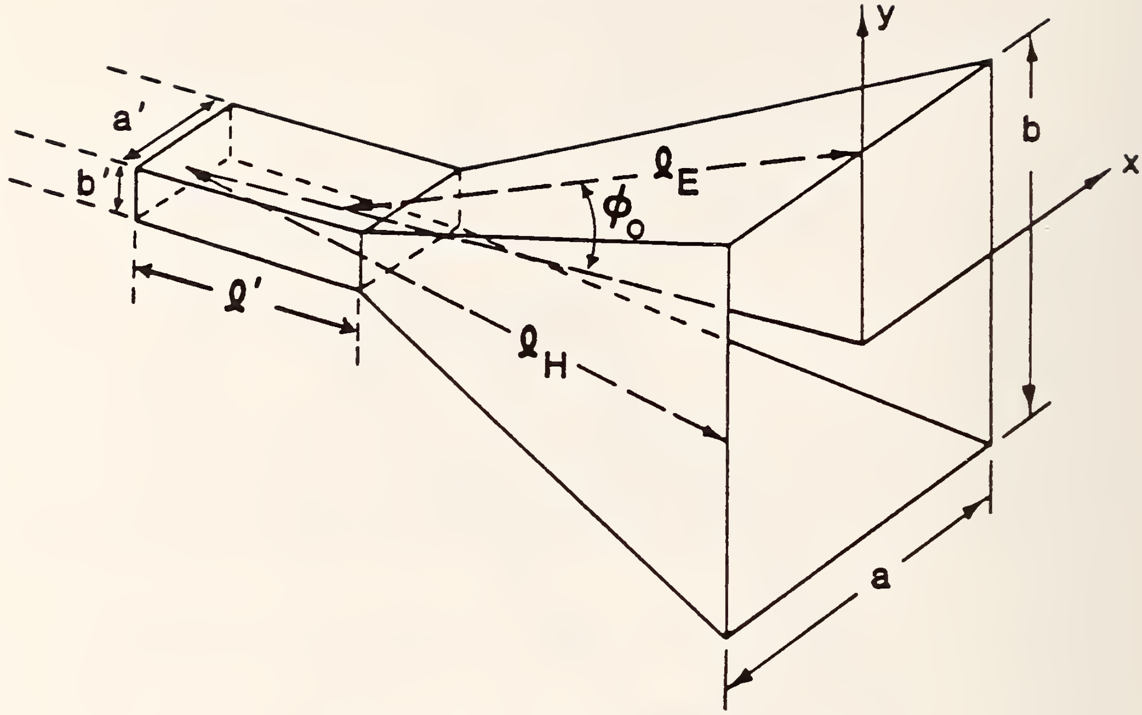

Figure 5.4 Pyramidal horn dimensions.

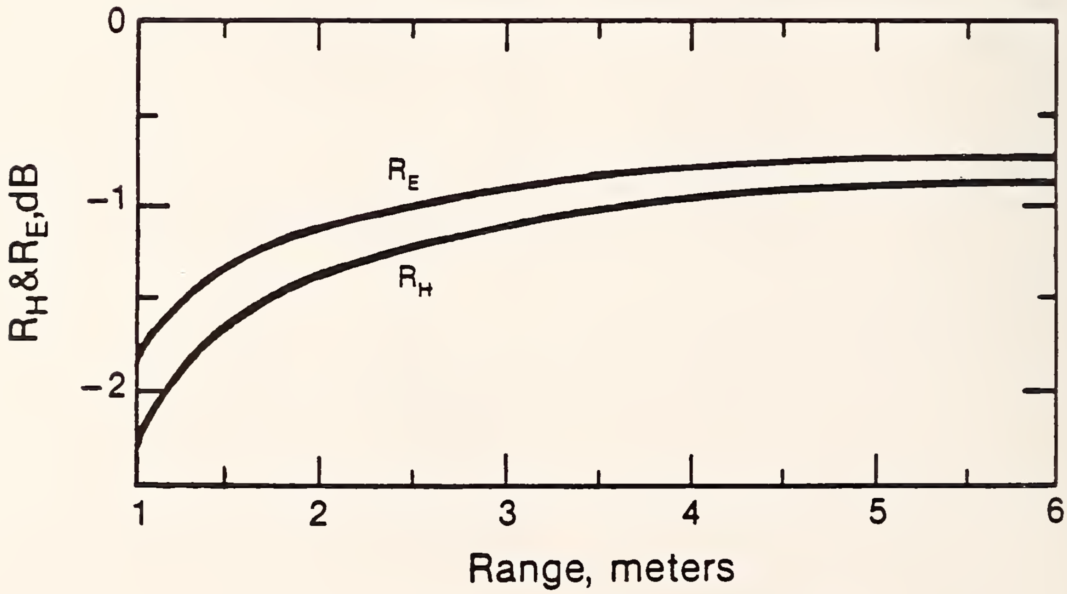

Figure 5.5 Near-zone gain reduction factors, R_H and R_E, of a typical pyramidal horn at 1,000 MHz.

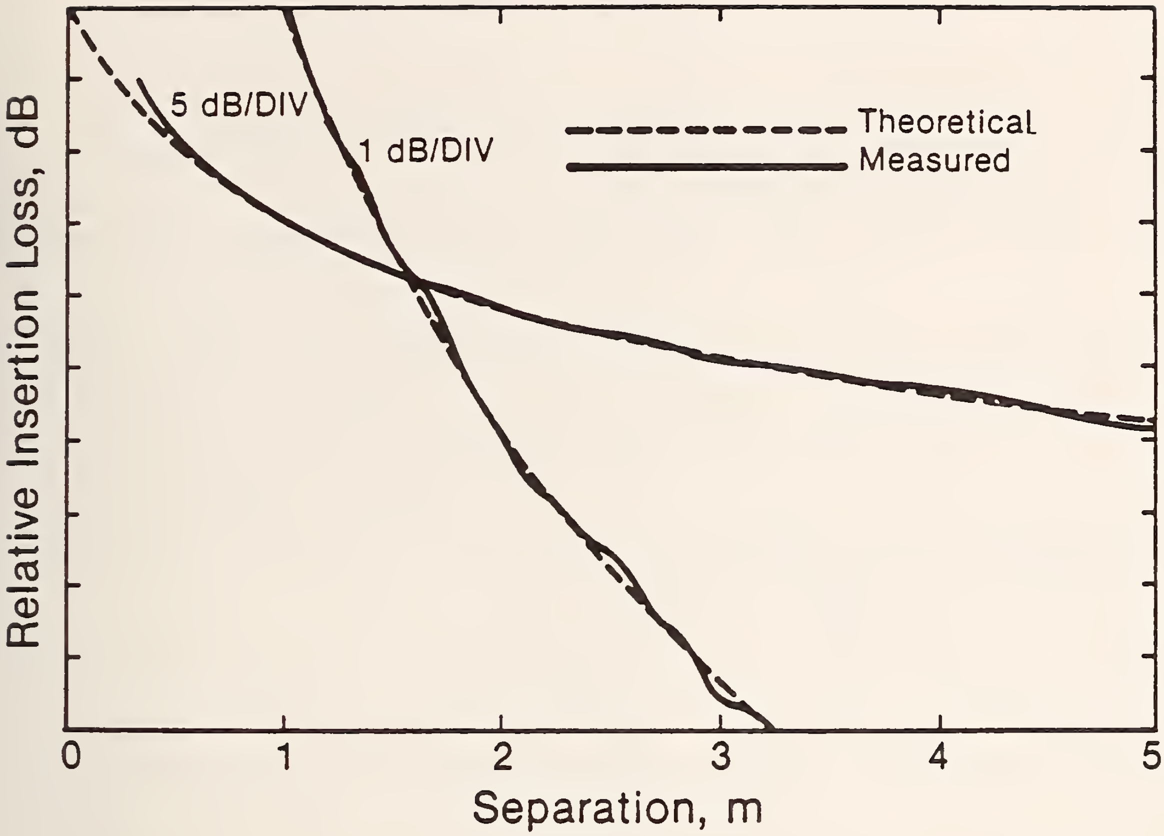

Figure 5.6 Relative insertion loss between a horn antenna (main beam) and a probe, with the free-space transmission loss curve fitted at a separation distance of 1 m. Frequency = 500 MHz.

The National Bureau of Standards offers a calibration service for field strength meters and EMI antennas in the frequency range of 10 kHz to 1,000 MHz [1]-[3]. The main part of a calibration consists of determining the "antenna factor" (K) which permits a receiver (RF voltmeter) to be used with the calibrated antenna to make measurements of field strength. The factor (K) can be used to convert the receiver dial indication in μV or dBμV to field strength in μV/m or dBμV/m. The types of antennas involved are basically loops for measuring the magnetic field from 10 kHz to 50 MHz, dipoles for measuring the electric field from 25 to 1,000 MHz, and monopoles for vertically polarized electric fields from 30 kHz to 300 MHz.

There are two independent techniques by which field strength can be evaluated. These are called the "standard field" method and the "standard antenna" method. The former consists of generating a calculable standard field component which is determined in terms of the type and dimensions of a transmitting antenna, its current distribution or net delivered power, the distance from the transmitting antenna to the field point, and the effect of ground reflections (if present). The latter method consists of generating an unknown field, but measuring it with a calculable receiving antenna. The voltage or current induced in a standard antenna by the component of field being evaluated is measured. The field-strength value is then calculated in terms of this induced voltage, the dimensions and form of the receiving antenna, and its orientation with respect to the field vector.

At frequencies below about 50 MHz for loop antennas, a quasi-static near-zone magnetic field is produced by a balanced single-turn transmitting loop of 10-cm radius. Above 25 MHz for dipole-type antennas, a radiated far-zone electric field is produced and evaluated in terms of the open-circuit voltage induced in a self-resonant receiving dipole. Between 30 kHz and 300 MHz for vertical monopoles and small probes, an elliptically polarized electromagnetic field is produced by a transmitting monopole above a 30 m x 60 m conducting ground screen. The instrumentation used by NBS and the uncertainties for these calibrations are discussed in this chapter. All the techniques described here for field-strength standards are applicable only for steady-state RF fields with sinusoidal time variation. They are not intended for use with pulsed fields or other broadband applications.

6.1 Standards for Field Strength Meters, 10 kHz to 10 GHz

For most field strength meters, the first part of a calibration is checking the receiver as a tunable RF voltmeter [4],[5]. This generally includes measurement of linearity (dial indication vs. input level) and checking the internal step attenuators at several frequencies [3]. A summary of these tests is given as follows:

Type of NBS Measurement	Frequency range	Amplitude range	Calibration uncertainty
1. Receiver indication as a function of signal frequency, at a few voltage levels.	10 kHz-400 MHz 400 MHz-1,000 MHz 1 GHz-10 GHz	1 μV-10 mV 10 μV-10 mV 100 μV-100 mV	± 1/2 dB ± 3/4 dB ± 1 dB
2. Attenuation of the step attenuators at a few frequencies.	10 kHz-1 GHz 1 GHz-10 GHz	(0 - 80 dB) (0 - 80 dB)	± 1/4 dB ± 1/2 dB
3. Receiver linearity, which is independent of frequency.	10 kHz-1 GHz 1 GHz-10 GHz	10 μV-100 mV 10 μV-100 mV	± 1/4 dB ± 1/2 dB

6.2 Magnetic Field Strength Standards for Loops, 10 kHz to 50 MHz

The standard field method is used here. The response of an electrically small receiving loop antenna is proportional to the average normal component of magnetic field strength incident on the antenna. At NBS, a calculable quasi-static magnetic field is produced for calibrating these antennas, using a circular single-turn balanced transmitting loop. The current in this loop of 10-cm radius is approximately constant in amplitude and phase around the loop.

The receiving loop antenna being calibrated is positioned on the same axis as the transmitting loop at a distance of 1.5 to 3 m. Figure 6.1 shows the NBS calibration setup.

The normal component of the magnetic field, averaged over the area of the receiving loop, is given by [6]:

$$H \approx \frac{I r_1^2}{2R_0^3} \left[1 + \frac{15}{8} \left(\frac{r_1 r_2}{R_0^2} \right)^2\right] (1 + k^2 R_0^2)^{1/2} \quad (6.1)$$

where H = RMS value of the magnetic field, A/m,
I = RMS current in the transmitting loop, A,
r_1 = radius of the transmitting loop, m,
r_2 = radius of the receiving loop, m,
$R_0 = (d^2 + r_1^2 + r_2^2)^{1/2}$,
d = axial distance between the two loops, m,
$k = 2\pi/\lambda$, and
λ = free-space wavelength, m.

The current in the transmitting loop is measured with a vacuum thermocouple calibrated with direct current. It is at the top of the loop winding, as shown in Fig. 6.1, and its dc output is measured with a millivoltmeter. The RF/dc substitution error of the thermocouple is < 1% at frequencies up to 50 MHz. Equation (6.1) is accurate within ± 0.2% if $kR_0 \leqq 1$ and $r_1 r_2/R_0^2 \leqq 1/16$. At higher frequencies, the correction term $(1 + k^2 R_0^2)^{1/2}$ becomes appreciable for the usual spacing of 1.5 to 3 m used at NBS. The uncertainty of calibrating loop antenna factors at NBS is ± 1/4 dB for frequencies up to 5 MHz, ± 1/2 dB between 5 and 30 MHz, and ± 1 dB between 30 and 50 MHz.

While coaxial loops are normally used for calibrating purposes, the two loops can also be positioned in the same plane. Co-planar loops are advantageous under certain conditions, e.g., with some ferrite core antennas in which the core length is large. In this case, the calibrating value of the magnetic field is half of that given by (6.1).

The calibration and subsequent measurement of magnetic field (H) are often expressed in terms of the electric field (E) that would exist if the measurement were made in free space, in which case $E/H = 120\pi\ \Omega$. When such a field-strength meter is used to make measurements near the ground, the indicated value of the electric field is not necessarily valid. The same is true for measurements made in the near zone of a transmitting antenna. However, the value of the magnetic component (H) can still be measured correctly.

For calibrating loops or H-field probes at a higher field level, it is possible to use the calculable magnetic field generated in a TEM cell (see chapter 3), or at the center of a flat multi-turn coil, or at the midpoint of a Helmholtz coil pair.

6.3 Electric Field Strength Standards for Dipoles, 25 to 1,000 MHz [1],[7]

The standard antenna method is used for this purpose. The magnitude of the electric field component at a given point in a locally generated field is determined at NBS from the open-circuit voltage (V_{oc}) induced in a standard half-wave receiving dipole. The field-site instrumentation is shown in Fig. 6.2. The induced voltage is measured across the center gap of the dipole, which is oriented horizontally and parallel to the electric-field vector of the incident field. In using the standard antenna method, a plane-wave field is generated by a suitable transmitting antenna such as a log-periodic or half-wave dipole. The magnitude of this incident field is measured with the standard dipole by the relation

$$E_{inc} = V_{oc}/L_{eff} \quad , \quad (6.2)$$

where

E_{inc} = strength of the locally generated field, V/m,
V_{oc} = open-circuit voltage induced in the standard dipole, V, and
L_{eff} = effective length of the standard dipole, m .

The RF voltage picked up by the half-wave standard dipole is measured in terms of the rectified dc voltage, as detected by a high-impedance Schottky diode connected in shunt across the center gap of the antenna. The diode output is filtered by a balanced RC network, and this dc voltage is measured with a high-impedance dc voltmeter. As shown in Fig. 6.3, the RF/dc substitution of the detector network in the standard dipole is determined by applying a known RF voltage at 50 MHz across the standard dipole gap. The antenna rods making up the dipole are removed for this measurement.

The high impedance of the diode "voltmeter" eliminates the necessity for a separate measurement of the dipole impedance, since the source impedance of a resonant dipole is low compared with that of the voltmeter. Another advantage of this approach is that the measurement of E_{inc} is not affected appreciably by the presence of ground or other perturbing objects. However, a subsequent measurement of field strength by the calibrated customer dipole will be affected by ground due to impedance change of the customer's dipole, which is loaded with a 50-Ω receiver. Also, the standard dipole used to measure E_{inc} lacks frequency selectivity, so it is not possible to perform the NBS calibration in the presence of strong interfering signals.

The range of filtered dc output voltage used at NBS is normally 0.5 to 1.5 volts, which is generally sufficient to avoid calibration uncertainty caused by ambient fields and temperature changes of the diode detector. The response of the diode voltmeter is independent of frequency up to about 500 MHz, with slightly increased response above this frequency due to the approaching series-resonant frequency of the diode mount.

Effective length of a receiving dipole is a measure of the E-field intercept length, analogous to the effective area of an aperture antenna. The effective length is derived in terms of the current distribution on a transmitting dipole. The reciprocity theorem is invoked in order to use the same value of L_{eff} for a receiving dipole. It should be noted that L_{eff} cannot be defined in terms of the current distribution on a receiving dipole. By definition, the effective length of a transmitting dipole is

$$L_{eff} = \frac{\text{Moment of dipole current distribution}}{\text{Input current at the feed point (center) of the dipole}} .$$

Assuming a cosinusoidal current distribution on an infinitesimally thin dipole, the effective length of a half-wave dipole in free space is

$$L_{eff} = \lambda/\pi \qquad (6.3)$$

However, the current distribution on a real dipole is not exactly cosinusoidal. An approximate solution for the current distribution on a cylindrical transmitting dipole was derived by Schelkunoff [8],[9] and this solution is used for calculating L_{eff} of the NBS standard dipole. Also, in order to achieve self resonance of the dipole (zero reactance), it is necessary to make its length slightly shorter than $\lambda/2$. The required length for resonance as derived by Schelkunoff depends on the dipole length-to-diameter ratio, and is

$$\text{Required length } L = (\lambda/2)\left[1 - \frac{0.2257}{\ln(\lambda/D) - 1}\right] , \qquad (6.4)$$

where D is the diameter of the standard dipole in meters.

The effective length of a thin dipole near resonance is given by

$$L_{eff} = \frac{\lambda}{\pi} \tan(\pi L/2\lambda) \qquad (6.5)$$

If a half-wave dipole is shortened slightly to obtain zero reactance, the theoretical resistance (R_{in}) depends on the length-to-diameter radio (L/D) as follows:

L/D ratio	L/λ at resonance	Dipole R_{in}
50	0.47	61 Ω
500	0.48	66 Ω
50,000	0.49	70 Ω

The standard dipole sets used for field strength calibration at NBS are made of cylindrical metal tubes which are 3 to 5 percent shorter than the free-space $\lambda/2$. To the first approximation, equation (6.3) can be used to calculate L_{eff} for these dipoles.

As indicated in Fig. 6.2, the antenna factor (K) of a customer's antenna or other antenna under test (AUT) is determined by placing the antenna in the same field environment at the same position as the standard dipole, and using the following relation:

$$K = E_{inc}/V_{50\Omega}$$

or (6.6)

$$K_{dB} = 20 \log E_{inc} - 20 \log V_{50\Omega} \quad ,$$

where $V_{50\Omega}$ is the voltage produced by the AUT across a 50Ω load in volts, and E_{inc} is obtained from the standard dipole measurement by means of (6.2).

Note that the possible impedance mismatch between the antenna and its load (50Ω receiver) is included in the value of K. Figure 6.4 is a graph of the theoretically expected antenna factor for a thin $\lambda/2$ dipole. Most often, the antenna factor may be expressed in decibels as follows:

$$K_{dB} = E_{inc_{dB/\mu V/m}} - V_{50\Omega_{dB\mu V}} \quad . \tag{6.7}$$

In this form, K is a dimensionless ratio given in terms of the incident E-field with respect to 1 μV/m, and the antenna response across the load with respect to 1 μV.

With the K factor so determined, an unknown E-field can be obtained with the calibrated antenna in terms of the measured pickup voltage at the 50-Ω receiver by

$$E = K\, V_{50\Omega} \quad , \tag{6.8}$$

or

$$E_{dB\mu V/m} = V_{50\Omega_{dB\mu V}} + K_{dB} \quad . \tag{6.9}$$

It could be noted that the customer's receiver, with attached antenna, can also be calibrated as a system to measure the field strength directly.

A field-strength measurement made with the calibrated AUT may be in error if it is made at a lower antenna height than that used during the calibration (about 3 m), or if the electrical ground constants at the measuring site are appreciably different from those at the calibrating site [1]. This results from a change in input impedance of the customer's antenna due to the proximity of the ground. A change of impedance does not affect the measurement of V_{oc} by the open-circuit standard dipole, but changes the mismatch between the customer's antenna and a 50Ω receiver. However, if the customer's antenna is calibrated at a height greater than 2λ, the calibration results in essentially a free-space value. The error is generally less than 10% for heights greater than 0.5λ. The error would also decrease if the antenna load impedance (receiver input impedance) were high, and would approach zero as the load impedance approaches ∞. Also, if the receiver had a sufficiently large value of input impedance, the calibration would be independent of the antenna polarization and of the ground properties. Figure 6.5 is a graph of the impedance of a typical dipole, and Fig. 6.6 is a graph of the impedance of a typical loop for comparison.

The National Bureau of Standards usually determines antenna factor at an outdoor site (a 30-m x 60-m ground screen) which is provided with an air-inflated all-weather cover. The calibration uncertainty at the present time is about ± 1 dB.

6.4 Electric Field Strength Standards for Vertical Monopoles, 30 kHz to 300 MHz (Also Standard-Field Method)

After considering several approaches for generating a standard (calculable) field to calibrate vertically polarized antennas, the system chosen at NBS consists of a thin cylindrical transmitting monopole over a 30-m x 60-m metallic ground plane. The field strength is calculated in terms of the magnitude and distribution of the monopole current and other factors, such as monopole height, horizontal distance from the transmitting monopole to the field point, vertical height of this field point above the ground plane, and conductivity of the ground system.

The basic arrangement of the NBS standard-field system is shown in Fig. 6.7. The height of the transmitting monopole is adjustable, with a maximum height of about 3 m. The electrical height of this antenna is $\lambda/4$ at 25 MHz, but only 0.0003λ at 30 kHz. At frequencies above 25 MHz, the antenna height is reduced to a $\lambda/4$ value. The base diameter of the monopole used is about 1 cm. The monopole is excited through a coaxial cable from the transmitting room located beneath the concrete ground slab.

The magnitudes of the three field components E_z, E_ρ, and H_ϕ of a transmitting $\lambda/4$ monopole above a perfect ground plane of infinite extent are given as follows, with the geometry for these field shown in Fig. 6.8.

$$E_z = 30\ I_0 \left(\frac{\exp(-jkr_1)}{r_1} + \frac{\exp(-jkr_2)}{r_2}\right), \tag{6.10}$$

$$E_\rho = \frac{30\ I_0}{\rho}\left[\left(z - \frac{\lambda}{4}\right)\left(\frac{\exp(-jkr_1)}{r_1}\right) + \left(z + \frac{\lambda}{4}\right)\left(\frac{\exp(-jkr_2)}{r_2}\right)\right], \tag{6.11}$$

$$H_\phi = \frac{I_0}{4\pi\rho}\left(\exp(-jkr_1) + \exp(-jkr_2)\right), \tag{6.12}$$

where

E_z = vertical E component, V/m.

E_ρ = horizontal E component, V/m,

H_ϕ = magnetic (H) field encircling the monopole, A/m,

I_0 = RMS base current of the monopole, A,

k = $2\pi/\lambda$, and

z, ρ, r_1, and r_2 = distances to the field point, m.

For frequencies near self resonance, the monopole base current is measured with an RF ammeter consisting of a thermoconverter, which has been calibrated with known values of dc current. At lower frequencies where the monopole input impedance is a high capacitive reactance, the base current is calculated from Ohm's law in terms of the base voltage measured with a vacuum-tube voltmeter and the theoretical input impedance. At very low frequencies, the input impedance $Z_{in} = 1/(j\omega C_a)$, where the antenna capacitance may be calculated from Schelkunoff's equation [9]:

$$C_a = \frac{55.63\ h}{\ln(h/a) - 1}, \qquad \text{pF} \tag{6.13}$$

where h is the monopole height and a is the monopole radius, both in meters. For a 3-m monopole 1 cm in diameter, C_a = 30.9 pF.

For a finite ground plane, the current on a vertical monopole will depart from the ideal sinusoidal distribution of a filamentary monopole. This does not seem to affect seriously the calculated values of far-zone field components. But the low-frequency, near-zone, quasi-static, electrical-field components so calculated will have greater uncertainty.

Examples of calculated standard-field data are shown in Fig. 6.9 for a 3-m monopole operating at 25 MHz, for which the electrical length is $\lambda/4$. The base current used in this case is 1 A. Vertical and horizontal components of the electric field are plotted versus horizontal distance from the antenna, for a height 1.22 m (4 ft.) above the ground plane. Similar curves are shown in Fig. 6.10 for the same antenna at a frequency of 200 kHz, which corresponds to the near-zone case.

If a transmitting monopole is electrically short, the current distribution may be considered triangular approximately. The field equations under this condition are more complicated than those given in (6.10)-(6.12), but can be programmed [10]. It should be noted that the EM field values in the half space above ground are the same as those in each half volume of a center-fed $\lambda/2$ dipole in free space. The input impedance of a monopole above perfect ground is half that of a dipole in free space. The power required to generate a given field strength is half that required for a dipole, but the radiated power goes into half the volume, so the field is the same. Measurements of Z_{in} at the NBS ground-screen facility with a commercial impedance meter were performed to check the theoretical values from 0.5 to 50 MHz. Measurements of the monopole capacitance were made at lower frequencies with a commercial Q meter. Also, checks have been made of the calculated electric field versus measurements with a small active calibrated field-strength probe. The agreement found between the various techniques was within 1 dB at all frequencies checked.

A metal ground plane having a thickness of several skin depths, so that the ground currents will not penetrate through, exhibits essentially infinite conductivity for the frequency range covered here. The dimensions of the NBS ground screen (30 m x 60 m) are several times the height of the monopole used (up to 3 m) in order to minimize the effect of wave reflections from the edges of the plane. At low frequencies where the ground screen is electrically small, it is difficult to achieve capacitive coupling to the reinforced concrete slab or to the surrounding earth, even though the underground transmitting room has a large ground rod. Therefore, further experimental testing is required of field uniformity versus azimuth angle, and field-strength reduction versus distance from the transmitting antenna.

For the purpose of calibration, the antenna factor (K) of the AUT is determined by immersing it in a calculated vertically polarized field (E_z) about 20 m from the NBS transmitting monopole. A coax cable is usually attached to, and considered part of, the antenna when calibrating K. The equation used is the same as that for calibrating dipoles, namely (6.6) or (6.7). The theoretically expected antenna factor of an electrically-short monopole above a perfect ground is given by

$$K = (1/h_{eff})\left|\left(1 + \frac{Z_a}{50}\right)\right| , \tag{6.14}$$

where h_{eff} is the effective height of the receiving monopole in meters, and Z_a is the monopole input impedance in ohms.

For example, for a 1-m whip of 0.5-cm diameter at frequencies below 10 MHz, $h_{eff} = 0.5$ m and $C_a = 11$ pF. In this case $Z_a \approx -j\ 14470/f$,MHz and $K \approx 579/f$,MHz, where f,MHz is the operating frequency in MHz.

It can be seen that the antenna factor of a short monopole (or dipole) is inversely proportional to frequency, while the antenna factor of a resonant monopole (or dipole) is directly proportional to frequency.

An unknown electric field strength (E) can be determined with a calibrated monopole by measuring its output voltage with a 50-Ω receiver or spectrum analyzer, and using (6.9).

The calibration of monopole antenna factors at NBS is performed at the outdoor ground-screen site for frequencies from 30 kHz to 300 MHz with an uncertainty of ± 1 dB. For frequencies up to 10 MHz and for monopoles or probes having a height less than 0.5 m, these calibrations can also be performed in a large TEM cell with the same uncertainty.

REFERENCES

[1] Greene, F. M. NBS field-strength standards and measurements (30 Hz to 1000 MHz). Proc. IEEE, vol. 55(6): 970-981; 1967 June.

[2] Taggart, H. E. Field strength and RFI standards at the National Bureau of Standards. IEEE Int. Symp. on EMC. 1968 July; Seattle, WA.

[3] Taggart, H. E.; Workman, J. L. Calibration principles and procedures for field strength meters (30 Hz to 1 GHz). Nat. Bur. Stand. (U.S.) Tech. Note 370; 1969 March.

[4] The radio frequency interference meter. NAVSHIPS 98180, U. S. Navy; 1962 July.

[5] Clark, D. R. An investigation into existing calibration methods of field intensity meters. RADC-TR-64-527; 1965 January.

[6] Greene, F. M. The near-zone magnetic field of a small circular-loop antenna. J. Res. Nat. Bur. Stand. (U.S.). 71C(4): 1967 October-December.

[7] IEEE Standard, Methods for measuring electromagnetic field strength for frequencies below 1000 MHz in radio wave propagation. IEEE Std. 302; 1969 August.

[8] Greene, F. M.; Solow, M. Development of very-high-frequency field intensity standards. J. Res. Nat. Bur. Stand. (U.S.). 44: 527-547; 1950 May.

[9] Schelkunoff, S. A.; Friis, H. T. Antennas, Theory and Practice. New York, NY: John Wiley and Sons; 1952.

[10] Jordan, E. C. Electromagnetic Waves and Radiating Systems. Englewood Cliffs, NJ: Prentice-Hall; 1950.

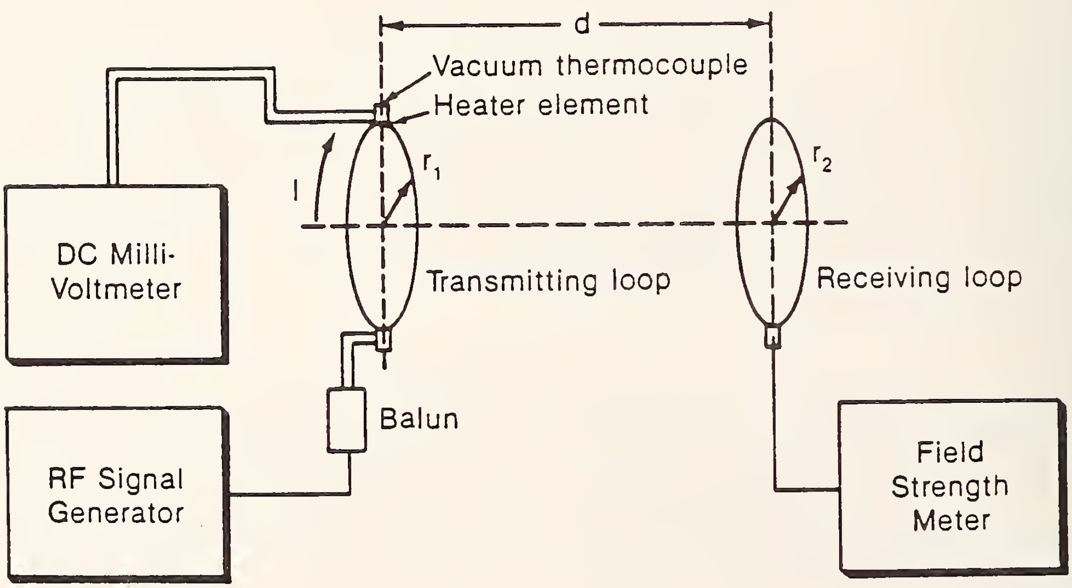

Figure 6.1. Diagram of the NBS measurement system for calibrating loop antennas.

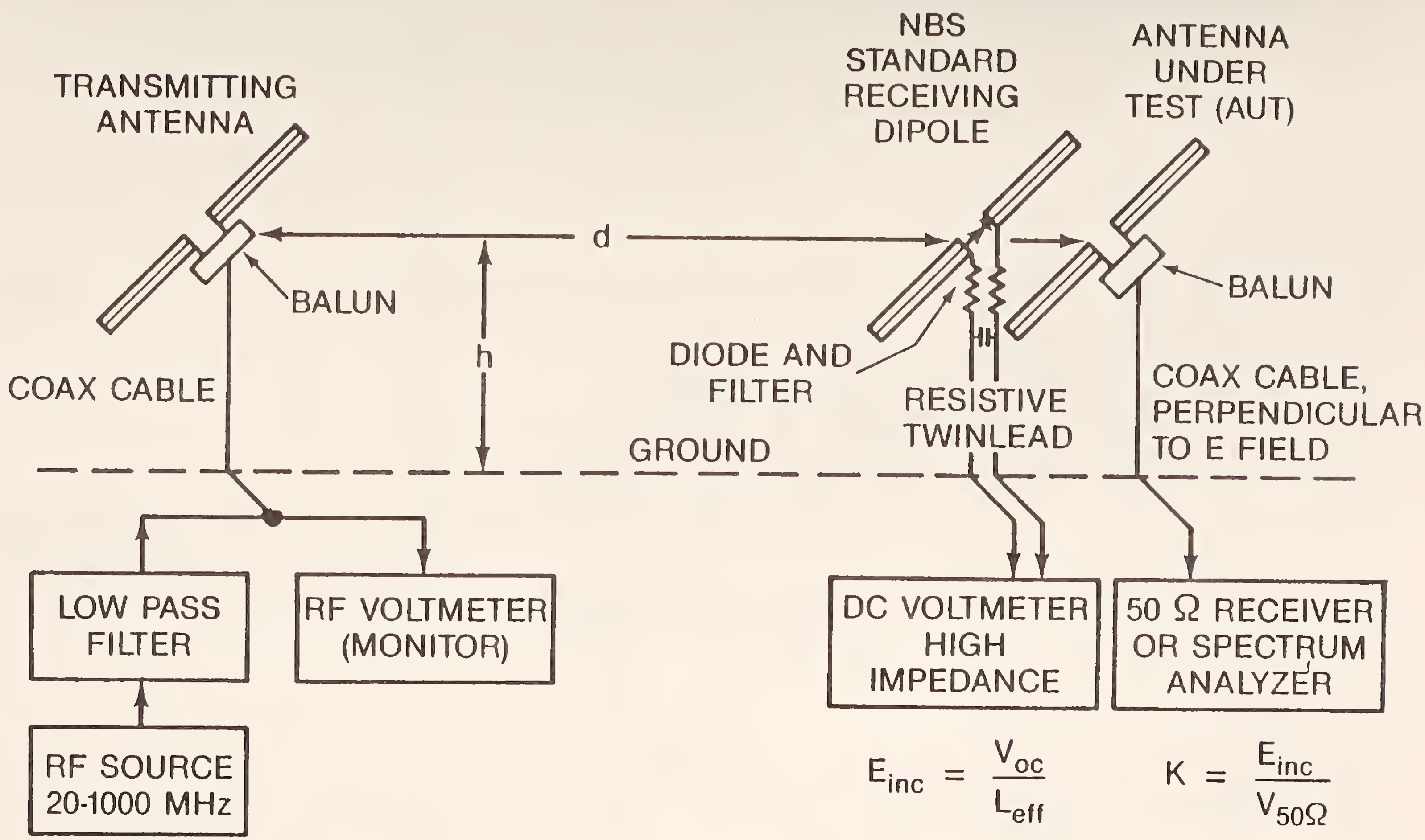

Figure 6.2. Field site instrumentation for calibrating horizontal dipoles, 25 to 1000 MHz.

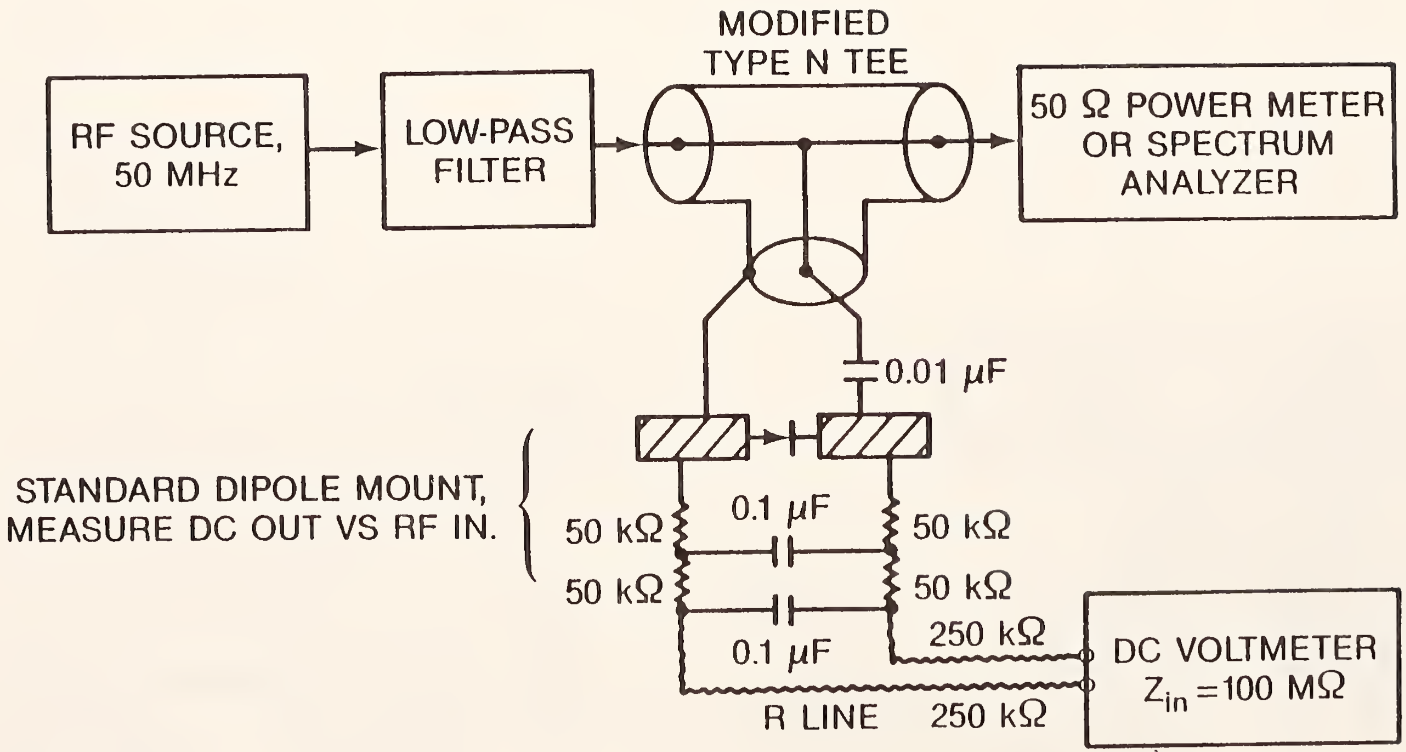

Figure 6.3. Instrumentation for measuring V_{oc} versus V_{dc} of the NBS standard dipole.

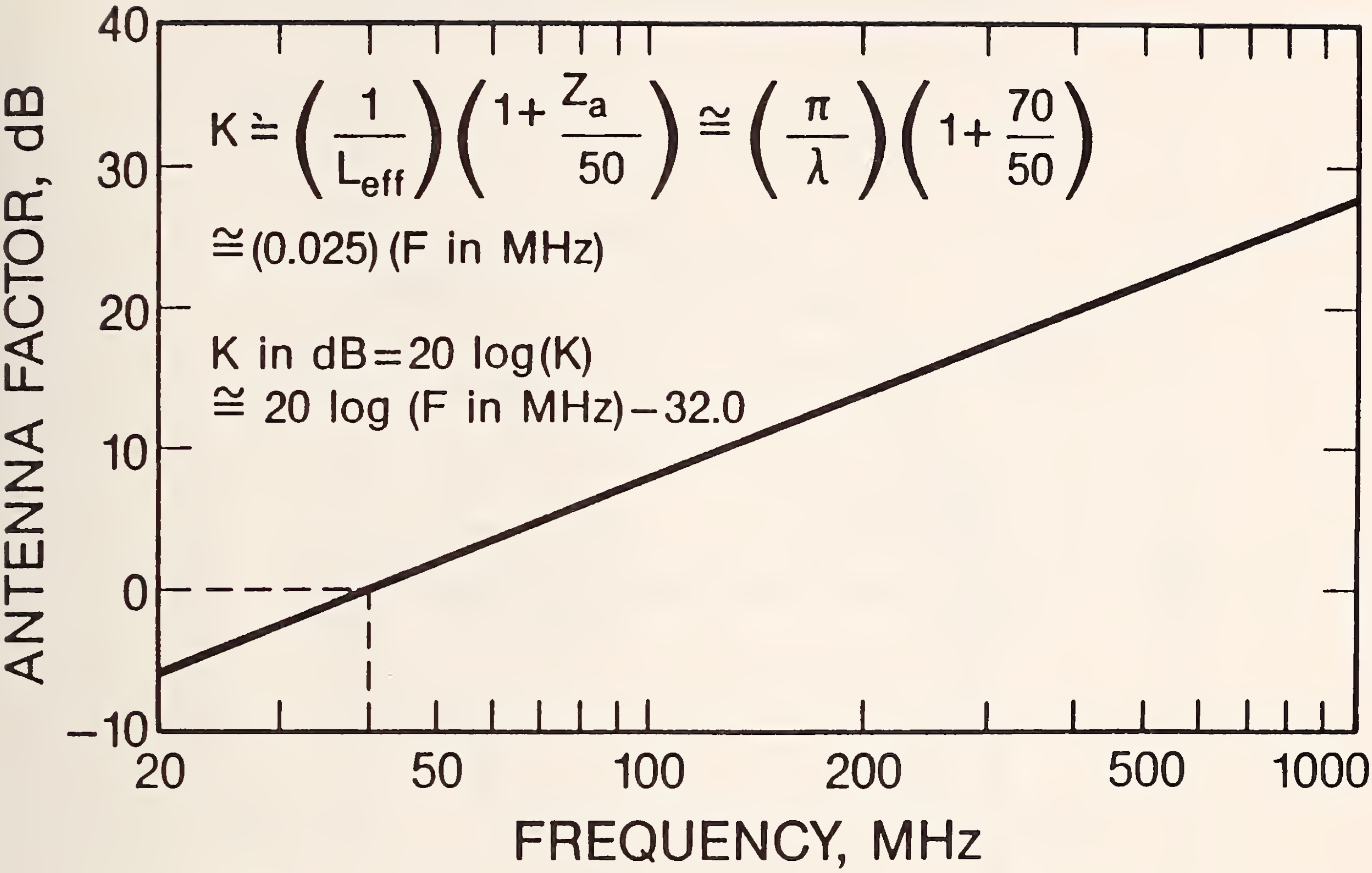

Figure 6.4. Theoretically expected antenna factor of a thin λ/2 dipole and 50 Ω receiver, excluding cable loss and balun loss.

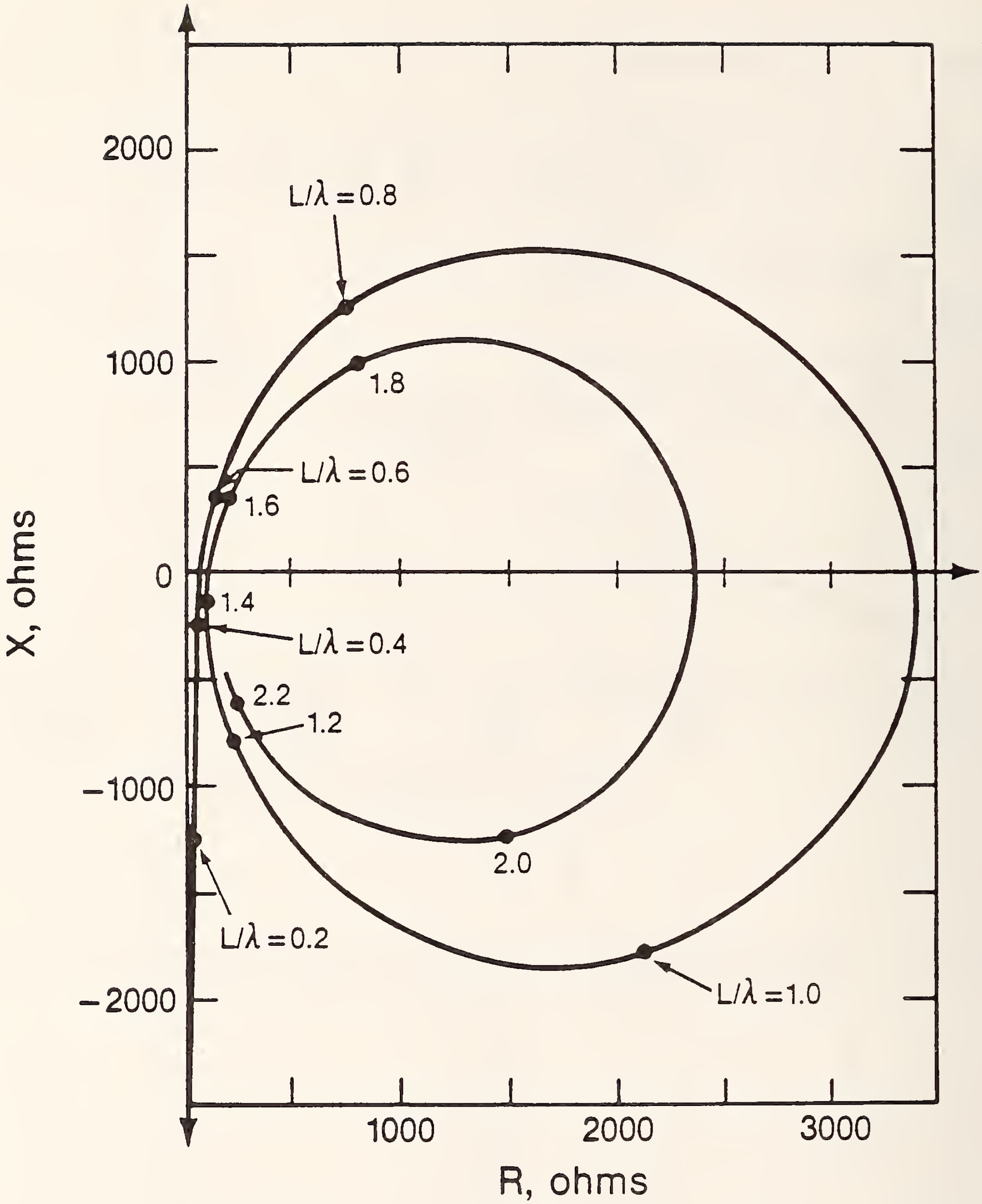

Figure 6.5. Free space impedance of a dipole antenna, length/diameter ratio = 2000.

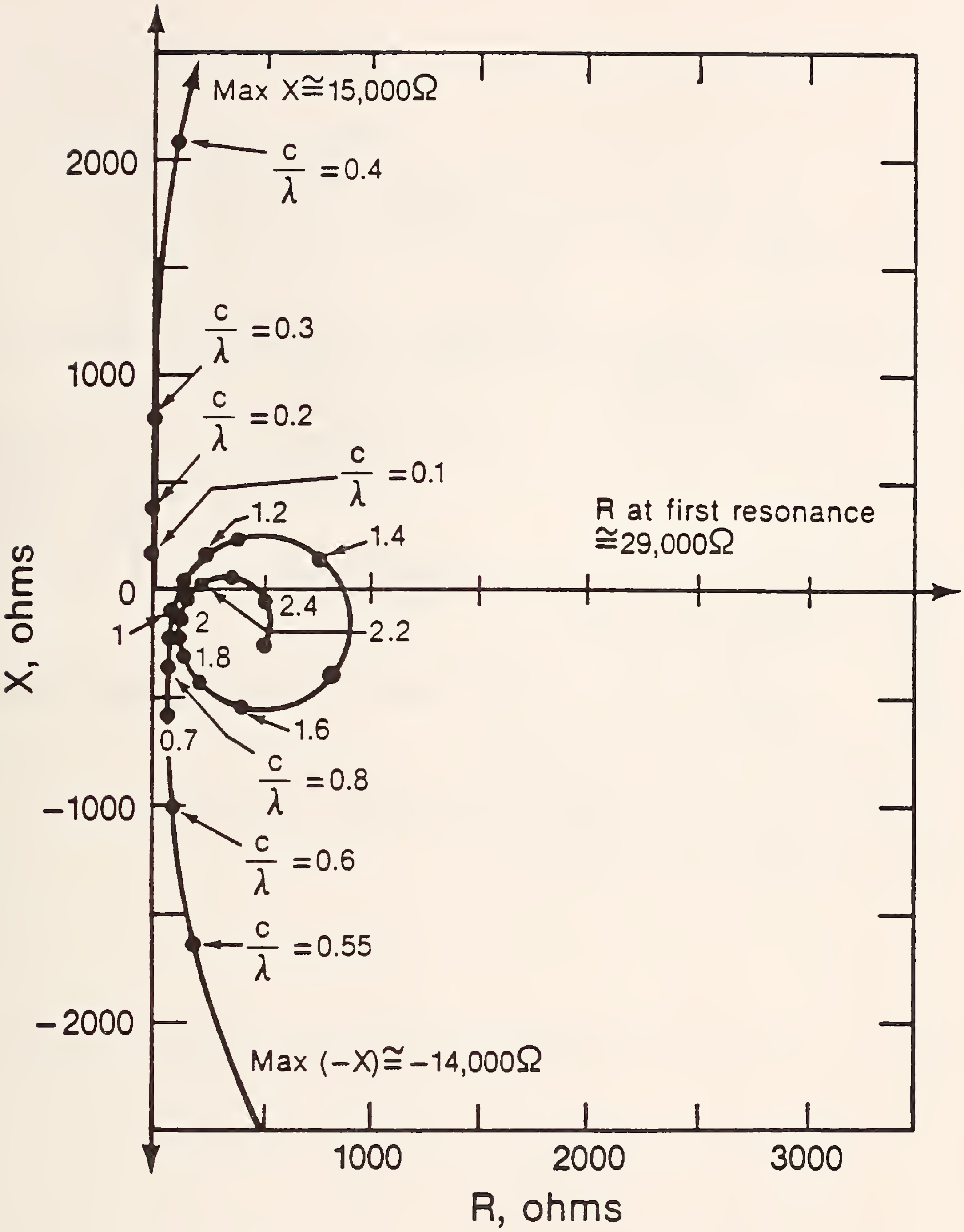

Figure 6.6. Free space impedance of a loop antenna, circumference/wire diameter = 200.

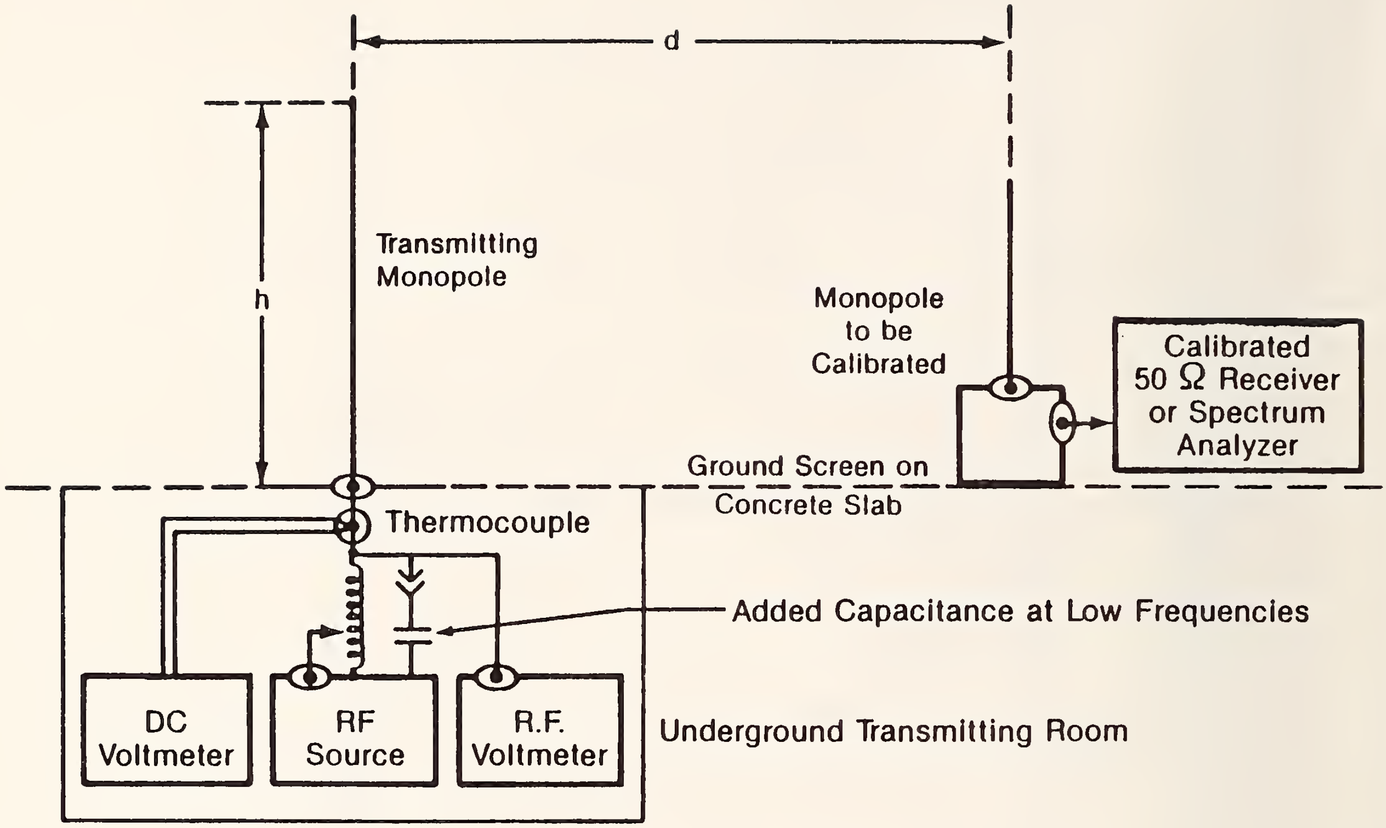

Figure 6.7. Field site instrumentation for calibrating monopole antenna factors.

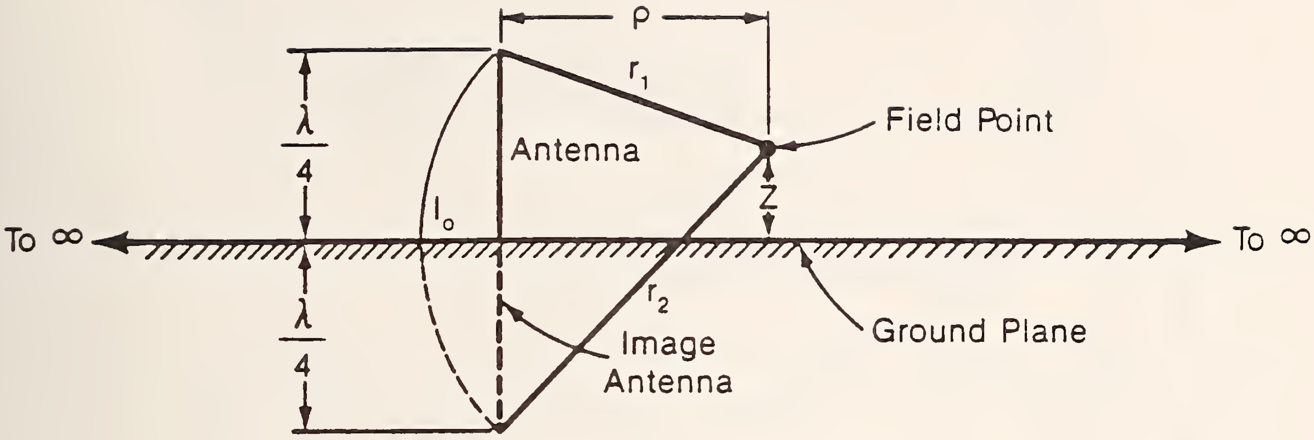

Figure 6.8. Geometry for the EM field of a thin λ/4 transmitting monopole antenna.

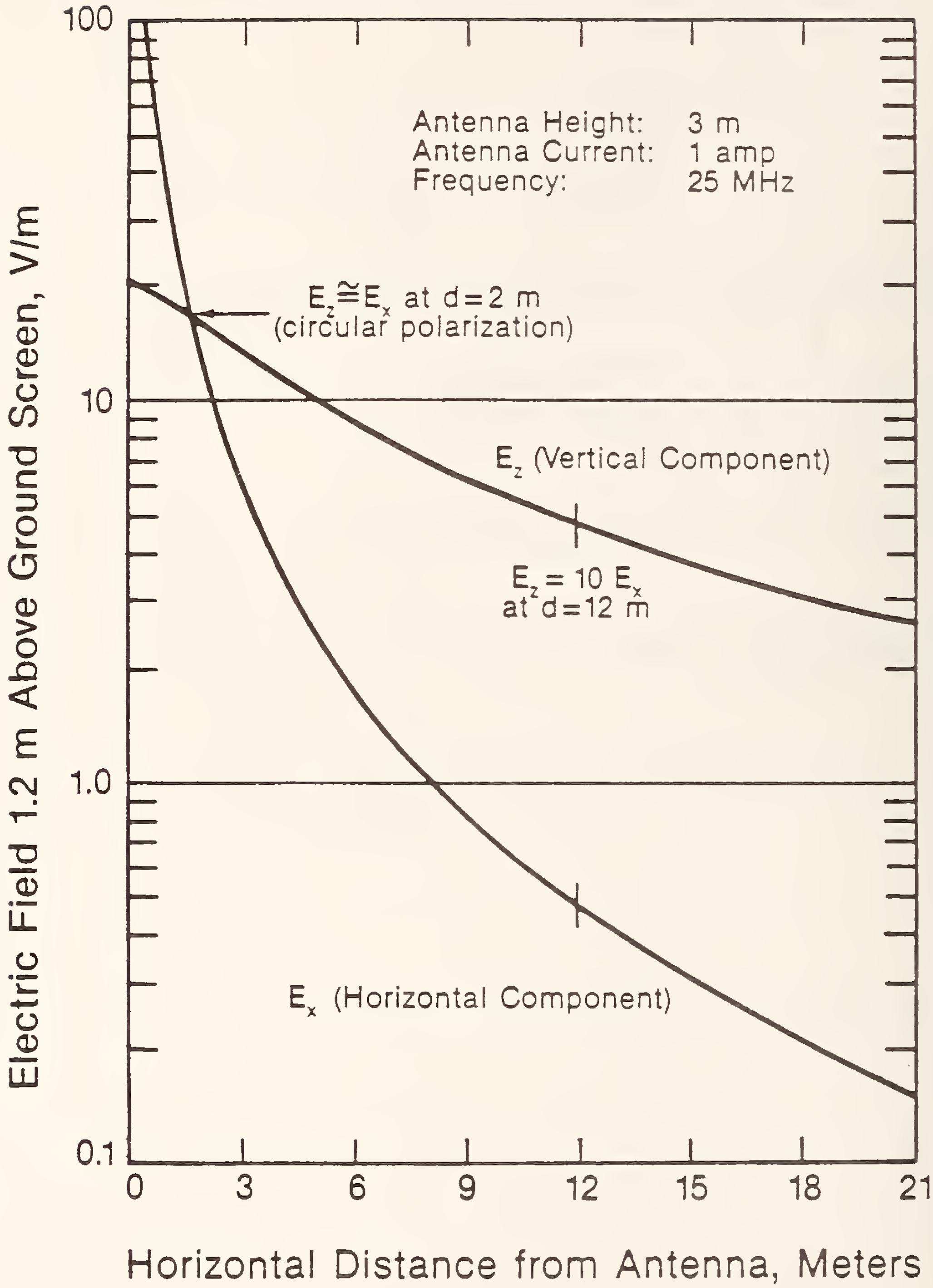

Figure 6.9. Theoretical electric field of a $\lambda/4$ transmitting monopole.

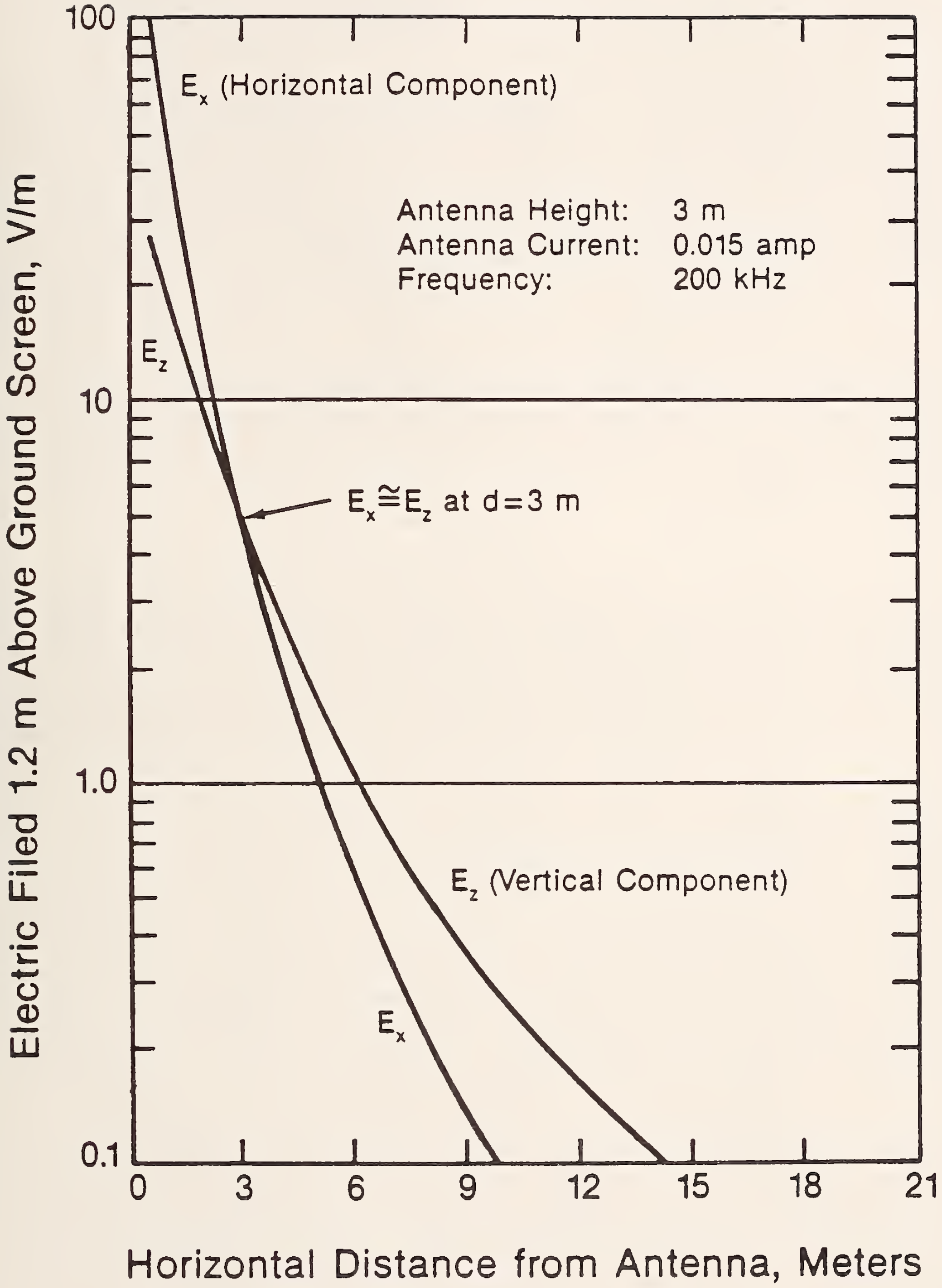

Figure 6.10. Theoretical electric field of a 0.002 λ transmitting monopole.

In order to measure quantitatively the EM environment, a small antenna or probe with an RF detector is often used. After sensing the RF field, the probe produces a dc voltage output which can be processed through the associated instrumentation to indicate the field level. Currently, there are two kinds of probes available, one sensing the electric-field strength and the other the magnetic-field strength.

Two types of instrumentation are normally used in a receiving system: one is the conventional field-strength meter consisting of a tunable meter or spectrum analyzer and a single antenna, which must be oriented for the desired field polarization. This kind of receiver generally offers high sensitivity and selectivity, and is not designed as a portable instrument for making quick surveys of the EM environment. The receiver thus acts as a frequency-selective voltmeter. The required conversion factor between the antenna pickup voltage (volts) and the electric-field strength (volts per meter) is the antenna factor. It must be determined experimentally for each antenna used in the system, at each frequency and orientation by calibrating the antenna in a known standard field. The other type of instrumentation employs a nontunable sensor characterized by lower sensitivity but broad-band response. The antenna involved in this latter type preferably has a flat response over a wide frequency range and a nondirective pattern. It is generally designed for measuring relatively high-level fields exceeding 1 V/m, such as the region close to a transmitting antenna. The frequency of interest is generally above 300 kHz. Thus, it can conveniently be used to assess a microwave hazard environment.

7.1 Earlier Models

The program carried out at NBS in the past was to develop various probes in the frequency range of 100 kHz to 18 GHz for measuring electric-field strengths of at least 0.1 V/m, or measuring magnetic-field strengths of 0.25 mA/m or more. The design principle of early probes was primarily based on temperature rise due to the absorption of RF energy [1]. Field strength was indicated either by the changing color of a liquid-crystal material, the change of resistance in a lossy dielectric, or by a glowing neon gas inside a miniature glass bulb located at the center of the sensor. Other types of probes developed at NBS include center-loading a short dipole with a miniature incandescent bulb about 2-mm long or a thermocouple heater [2]. The current induced in the bulb or heater by the field was then used as a measure of the field strength. All of these early models lacked adequate sensitivity, quick reaction time, good stability for calibration over a long period of time, dependable corrections for variations in ambient temperature, and thus satisfactory measurement repeatability.

Another early probe developed at NBS was an "active" antenna system consisting of three orthogonal dipoles, each sensing one component of the field (x, y, or z) [3]. This arrangement avoids requiring physical rotation of the probe. Because the dipoles are perpendicular to each other, the mutual-coupling effect is relatively insignificant. This system was designed for the frequency range of 15 kHz to 150 MHz. The dipoles, all electrically short over the entire frequency range, are connected to a conventional tunable RF receiver by a fiber-optic link. The antenna pickup is amplified first and then applied as modulation to the infrared (IR) output of a high-speed light-emitting diode (LED). The system is considered active in the sense that the RF signal is amplified before the detection or modulation process. The modulated IR signals are guided through glass fibers to avalanche photodiodes in the metering unit. These glass lines provide essentially perfect electrical isolation between the sensing antennas and metering unit. Photodetectors recover the total RF modulation from the IR carrier for input to the RF receiver. The readout indication at each frequency is proportional to a single component of the probed electric field. A root-sum-square (rss) circuit is also incorporated in the system to give the total magnitude of the three field components.

The most important advantage of this probe is that complete signal information can be recovered, including not only the signal strength but also frequency and phase characteristics. The sensitivity of this system is also adequate. It may be noted that the probe sensitivity decreases rapidly above the designed upper frequency limit of 150 MHz with no unwanted enhancement at the dipole self-resonant frequency. One of the disadvantages is the rather low dynamic range. In fact, both the tangential sensitivity and linear dynamic range depend on the tuned frequency, noise figure, and bandwidth of the auxiliary receiver included in the system. Another disadvantage is the limited upper frequency caused by the limitation of LED speed. [However, heterodyne conversion employing an RF local oscillator inside the active dipole could be used to achieve higher effective signal frequency, but this approach has not been pursued.] In addition, the switching speed between measurements of three field components is relatively slow because only one RF receiver was used for all three dipoles. The level of spurious responses and intermodulation distortion is also rather high.

7.2 Recent Models

One of the recent probes developed at NBS is the broad-band, isotropic, real-time, electric-field sensor (BIRES) [4],[5]. This probe covers a much broader frequency band, typically from 10 MHz to 1 GHz, also using three orthogonal dipoles. Each dipole is fabricated by depositing a thin film of metal alloy with varying resistivity on a glass rod. The alloy, which consists of approximately 70 percent nickel, 15 percent chromium, 10 percent iron, 2 percent titanium, and others, has a high resistivity and low temperature coefficient. The glass rod, 15-cm long and 0.7 cm in diameter, serves as a substrate for the deposited film. The antenna becomes a half-wave dipole at approximately 1 GHz. The required resistive loading is about 5 kΩ/m at the center of each dipole, 10 kΩ/m at midpoint between the center and ends, and infinite at the ends of the dipole. It is possible to calculate the required thin-film thickness. Typically, this is about 240 nm at the center, 100 nm at the midpoint, and zero at the ends.

Because the tapered resistive loading makes the internal impedance per unit length a proper function of position along the dipole, the resulting current distribution on the antenna is a pure outward-traveling wave. Hence the probe has linear amplitude and phase responses over a broad frequency band, and as such may be used to measure fast time-varying signals with minimum pulse-shape distortion. The probe also has a filtering action so that EM signals outside the designed frequency range will be rejected, preventing out-of-band responses. In addition to amplitude, phase, and frequency, the probe also provides polarization information of the EM environment.

The BIRES probe uses metal coax cables to convey RF signals from the antenna to the metering unit. Thus the electrical isolation of the antenna and resulting isotropy is not as good as the other probes discussed previously. Because the RF signal voltage delivered to the conventional 50-Ω receiver from the dipoles is not independent of signal frequency, an RF shaping amplifier is incorporated in the system for frequency compensation. The tangential sensitivity and linear dynamic range also depend on the signal frequency and bandwidth of the auxiliary receiver used.

Quite often, the regions being measured are close to radiating sources. In such cases, the field structure is very complicated, including reactive (stored) and real (propagated) components, standing waves, unknown phases, and unclear field polarization. The most practical manner of surveying this kind of field environment is to use isotropic RF probes, independent of orientation and direction of wave propagation, as hazard meters. It is important that the probe be small in size and thus be able to resolve the spatial variations in field strength. Futhermore, the field being surveyed should not be perturbed substantially by the operator or equipment associated with the measurement. The end result of meeting these requirements is represented by the NBS development of an "isolated" probe system [6]. A typical response at 20 dBV/m (10 V/m) of the NBS isotropic electrical-field monitor (EFM-5) is shown in Fig. 7.1. A family of NBS designed electric-field strength meters using isolated probes has been adopted as commercial meters by private industry.

The probe consists of three short dipoles mounted orthogonally in three notches cut near the end of a plastic tube. The dipoles are then embedded in a form sphere 10 cm in diameter. The difference in transmission line between this probe and the BIRES discussed earlier is that this probe unit employs three high-resistance plastic twinleads inside the dielectric handle to bring the dc voltage to the receiver. These lines also act as RC low-pass filters for the demodulated signal coming from the dipole. Nonlinear circuitry included in the metering unit can be used to give the rss value of the three perpendicular field components at the measuring point, to represent the total effect of all electric field components, all polarizations, all arrival directions, and all frequencies within the passband of the antenna/filter combination. The unit also includes switches to permit measurement of a single field component only, allowing a choice of measuring either the average or peak amplitude of modulated signals. Typical applications for this probe system are 1) measurement of possible RF hazards caused by diathermy equipment, industrial RF heaters, plastic sealers, and near fields of transmitting antennas; 2) survey of ambient fields for low-level RF pollution caused by AM, FM, TV, CB, and other broadcasting services; 3) check of EM fields in sensitive areas containing electro-explosive devices or flammable fluids; and 4) check of field strength in sites having instruments which may be degraded by the presence of RF radiation.

Although the isolated probe has a fairly flat response over the designed frequency range of 0.2 MHz to 1 GHz, it is found that it also responds to higher frequencies. Therefore, RF fields due to harmonics and other frequencies all contribute to the meter indication. Also, the measurement accuracy is normally reduced for pulsed fields that have pulse widths lower than 0.3 ms, because of the limited charging time of the RC filter line included in the system. In addition, a possible erroneous increase in meter indication occurs when measuring multifrequency fields (see chapter 9).

Another isotropic probe (MFM-10) for measuring primarily magnetic-field intensities was developed, based on the same principle, and incorporates much of the instrumentation used for the isolated electric-field probe described above [7]. Three small orthogonal loops were used instead of short dipoles. It provides near-zone measurement of magnetic fields over a dynamic range of 0.1 to 12 A/m with a relatively flat response in the frequency range of 300 kHz to 100 MHz. It also is capable of measuring each of the three orthogonal field components in addition to the total field magnitude.

The mechanical and electrical configuration of an individual loop in this probe are illustrated in Fig. 7.2. The internal portion of each loop is composed of 5 turns of wire with a detector at the loop center and a filter capacitor C_3 connected between the two ends. The diode, D_1, provides rectification of the RF signal induced in the loop. The diode shunting elements, R_1 and C_1, help produce a flat frequency response. The values of R_1, C_1, and C_3 are critical to the proper shaping of this response. A normalized response curve given in Fig. 7.3 shows that the maximum variation with frequency is less than ± 1 dB.

Two subsystems have been developed to be used with any of the broad-band isotropic probes. One of them uses the fast Fourier transfrom (FFT) technique [8]. During each measurement, the total amplitude of antenna pickups over a given frequency band is recorded on a high-speed tape recorder in the time domain. These recordings are later analyzed with a computer by FFT processing to obtain a three-dimensional display of field strength versus frequency, with time as a third parameter. This device, therefore, enables an analysis of changes of the spectrum occupancy with time. Another subsystem provides a microprocessor control for rapid data acquisition of three orthogonal field components and the total field amplitude [9],[10]. Both of these approaches require previous calibration on the antenna factors involved.

7.3 Future Models

A shortcoming of most isotropic broad-band probes is the relatively long response time of the RF sensor. It would be impossible or difficult to measure directly the peak-to-average ratio of a modulated field or the momentary maximum envelope intensity in the beam center of a scanning antenna. It is often advantageous or desirable to have the capability of observing the modulation on a signal being measured. In addition, the biological importance of measuring peak levels of RF pulses has not been established partly because the measuring instrumentation is not yet commercially available. To make up for this shortcoming, a new system employing laser diodes, single-mode fiber-optic guides, and optical modulators to replace the conventional coax cables in any of the isotropic broad-band probes has been developed, fabricated, and tested under laboratory conditions. To date, capability of measuring electric fields of about 0.1 V/m at 1 GHz with 50 kHz bandwidth [11] and about 1 mV/m sensitivity at 10 kHz with 3 kHz bandwidth [12] has been demonstrated. These systems preserve the amplitude and phase information of the electric field, and reduce the measurement errors due to antenna lead pickup and field distortion. Present effort is being directed toward improving system performance by reducing the noise inherent in the probe system in order to expand the measurement bandwidth and by improving the stability against thermal drift. Increased use of optical fiber and integrated optics technologies will improve system performance and lead to lighter weight and more compact transmitter/receiver modules. In view of promising potentials of this system, design considerations of some of the important components included in the system are outlined in Section 7.5.

To date, all the practical field-strength meters measure either the electric field or magnetic field separately. A new probe is being developed at NBS to measure the electric and magnetic fields simultaneously so that an EM environment may be characterized more completely [13]. This type of probe is particularly needed for measuring the near field where the magnitude and phase angle of the wave impedance are unknown, and the electric- and magnetic-field vectors are not necessarily orthogonal to each other nor in the same time phase. Thus the new device is intended to measure not only the polarization ellipse of the field vectors in a near-field environment, but also the time-dependent Poynting vector to indicate the energy flow. The probe consists of three electrically isolated doubly loaded loops with the capability of measuring the sum and difference of the detected voltages at the two opposite ends of each loop. A diagram of a single loop with equal loads of Z_L is shown in Fig. 7.4. Currents developed in the loads correspond to the electric-dipole and magnetic-loop responses. More precisely, across one load, the electric response adds to the magnetic response, while across the other load, the electric response subtracts from the magnetic response. To separate the currents, a 0°/180° hybrid is used to obtain the sum and difference of the currents. Thus, the sum current I_Σ gives a measure of the magnetic field, whereas the difference current I_Δ gives a measure of the electric field.

The calculated sum and difference currents in a loop with a load impedance of 200 Ω are presented in Fig. 7.5. The real part of the currents increases with frequency up to about 200 MHz. The magnetic-loop current is larger than the electric-dipole current up to 100 MHz, while the electric-dipole current becomes more dominant above 100 MHz.

An experimental loop model with a radius of 0.16 m and wire radius of 0.02 m is shown in Fig. 7.6. This loop is doubly loaded with 200 Ω by using 4:1 baluns and 50-Ω resistive loads. Zero-bias Schottky diodes are used as detectors, with high-resistance plastic transmission lines connecting the loop and high-impedance dc voltmeter. Measured values of the real parts of I_Σ and I_Δ for this loop placed in a TEM cell with a known incident electric field of 1 V/m are included in Fig. 7.5. Although there is some discrepancy between the theoretical and experimental results, which may be associated with the balun impedance, the preliminary results indicate the validity of the theory.

Figure 7.7 shows the real parts of the magnetic-loop and electric-dipole currents as a function of load impedance at 10 MHz. It reveals that there is a critical load impedance, for example 260 Ω at 10 MHz, for which the two currents are equal. Below this critical impedance, the magnetic-loop current is greater than the electric-dipole current. Above this impedance, the reverse is true. Critical load impedance has only a slight frequency dependence, ranging from 200 to 260 Ω for the frequency range of 1 to 100 MHz [13].

7.4 Diode Model

Some of the probes described earlier use a diode to convert the electric field being surveyed to a DC voltage. The main advantage of including a diode is to make the frequency response of the probe very flat, so that the system can be used as a portable and compact hazard meter. Otherwise, since the input impedance of a probe (short dipole) without a diode is mostly capacitive, the antenna factor for such a probe is, in accordance with (6.14), frequency sensitive. It would be difficult to determine the unknown field strength without also detecting the frequency by a spectrum analyzer.

A beam-lead Schottky-barrier diode is usually chosen for this purpose. It has a good high-frequency performance due to a small junction capacitance, high sensitivity, and low noise characteristics. When an electrically short dipole is terminated with such a diode, the effect of loading may be analyzed by the simple Thevenin's equivalent circuit shown in Fig. 7.8, where the induced open-circuit voltage $V_i(t)$ at the diode terminal is given by

$$V_i(t) = E_{inc}(t)\, L_{eff} \quad , \tag{7.1}$$

with E_{inc} as the incident electric-field component parallel to the dipole, and L_{eff} the effective length of the dipole. The element C_a in Fig. 7.8 is the equivalent driving-point capacitance of the short dipole, and the parallel combination of capacitance C_d and nonlinear resistance R_d represents a simplified model of the diode.

For an electrically short dipole, the effective length and the driving-point capacitance are given respectively by [14]:

$$L_{eff} = \frac{h(\Omega - 1)}{\Omega - 2 + \ln 4} \quad \text{m} \quad , \tag{7.2}$$

and $$C_a = \frac{2\pi\ \varepsilon_0\ h}{\Omega - 2 + \ell n\ 4} \quad F \quad , \tag{7.3}$$

where h is the half physical length of a dipole in meters, ε_0 is the free-space permittivity in farads per meter, Ω is the antenna thickness factor defined by $\Omega = 2\ \ell n(2h/a)$, and a is the dipole radius in meters. For example, when h = 0.02 m, a = $2.84(10)^{-5}$ m, we have Ω = 14.50, $L_{eff} = 1.94(10)^{-2}$ m, and C_a = 0.10 pF. Note that the symbol Ω should not be confused with the unit for a resistance.

The current flowing through the nonlinear resistance R_d of the diode may be characterized by its v-i relationship

$$i(t) = I_s[\exp(\alpha\ V_o(t) - 1] \tag{7.4}$$

where I_s is the saturation current, which is assumed in this case to be $2(10)^{-9}$ A, $V_o(t)$ is the voltage in volts across the diode junction, $\alpha = q/nKT = 38\ V^{-1}$, q is the electron charge [$1.6(10)^{-19}$ C], n is the diode ideality factor [~ 1.05], K is the Boltzmann's constant [$1.38(10)^{-23}$ J/°K], and T is the absolute room temperature [~ 290°K].

At frequencies approximately higher than 10 MHz, we obtain the detected dc voltage averaged over complete cycle as [15]

$$V_o = -\frac{\alpha}{4}\left[\frac{V_i}{1 + C_d/C_a}\right]^2 = -\frac{\alpha\ L_{eff}^2\ E_{inc}^2}{4(1 + C_d/C_a)^2} \tag{7.5}$$

for a small sinusoidal induced steady-state voltage V_i [≤ 1 V]; and

$$V_o = -\frac{V_i}{1 + C_d/C_a} = -\frac{L_{eff}\ E_{inc}}{1 + C_d/C_a} \tag{7.6}$$

for a relatively strong V_i[> 1 V].

The frequency response of V_o with E_{inc} = 1 V/m for a sample probe and diode system is shown in Fig. 7.9, where the analytical solutions are obtained by solving a first-order nonlinear differential equation in accordance with the equivalent circuit shown in Fig. 7.8, while the numerical solutions are achieved by using an approximate time-stepping difference equation [13]. From Fig. 7.9, we see that the frequency response is indeed very flat. The inverse of these curves represents the antenna factor for the entire system.

7.5 Application of Electro-Optic Techniques for Measuring EM fields

Electro-optic techniques for EM field measurements offer several advantages over conventional measurements. The main advantages are due to the use of non-electrically-conducting fiber-optic links between the field probe and the system readout. The dielectric link produces minimum perturbation of the field being measured and provides immunity from EMI in the data transfer. It also enables field measurements to be made in areas where high voltages or hazardous environments would preclude the use of electrically conducting leads. The large information-carrying capacity of the optical fibers allows the phase and amplitude of the test fields to be recovered and broad bandwidth operation. However, these advantages are not without some drawbacks. The principal one is that the production and detection of the optical carrier signal introduces considerable noise in the system. A less severe restriction is that the optical interaction length necessary to obtain adequate sensitivity in presently available electro-optical materials limits the frequency response to about 10 GHz for low field strengths of interest.

The basic electro-optic field measurement system is shown schematically in Fig. 7.10. Light from a laser source is launched into the uplink optical fiber and propagates to the modulator. Voltage from the antenna is applied to the modulator and changes its transmittance, causing the light intensity in the downlink fiber to vary. At the receiver the light is detected by a photodiode and the intensity fluctuations generate a time-varying electrical signal that is processed by the signal analyzer. The feedback element is often necessary to control the polarization state of the light at the transmitter end of the system in order to compensate for stress or thermally induced birefringence in the fiber or modulator respectively. Such compensation is necessary when the modulator output is sensitive to the input polarization state of the light.

The design and use of an electro-optic probe involves the interaction of all the principal components and must be approached from a systems perspective. Trade-offs between sensitivity, dynamic range and bandwidth must be made. A lower limit on the physically detectable field is set by the antenna factor, voltage sensitivity of the modulator, and system noise. The power levels and wavelength of the optical carrier depend on the susceptibility of the modulator crystal to photon damage, the signal processing requirements (e.g., streak cameras), and available sources.

MODULATORS Probably the most important component of the optically-sensed probe is the modulator. A large effort has gone into developing modulators for fiber-optic communication links. Most of the resulting technology is applicable to the fabrication of field probes. Table 7.1 lists the most promising modulators by type along with some developmental types and their basic characteristics. In all cases, an electric field induced across the material or device causes a change in its optical properties. For the majority, the change is in the relative refractive index along different crystal axes (Pockels effect). This induces birefringence that alters the light propagation characteristics. For best sensitivity and linearity, the modulator should be biased so that approximately 50% of the light is transmitted for zero applied field. Since one objective in using the fiber-optic link is to eliminate the use of conductors to the probe, the appropriate bias point should be maintained passively (inherently built into the device) or by controlling the input polarization state at the optical transmitter. The operation of a modulator is depicted in Fig. 7.11 which shows the change in transmittance, $d(I/I_0)$, for an applied voltage dV. The modulator can be conveniently characterized by its V_π, the voltage required to switch the light from full-off to full-on, and the slope of the curve at the bias point. These values are also included in Table 7.1 for several representative modulators reported in the literature.

One particularly attractive modulator is the Mach-Zehnder interferometer fabricated using optical, integrated-circuit technology on $LiNbO_3$ crystals [12],[20]. It has high sensitivity and can be passively biased by making one interferometer leg one quarter optical wavelength longer than the other. However, in its conventional configuration on z-cut crystals giving the best sensitivity, it has recently been shown that the material large pyroelectric coefficient makes it difficult to maintain the proper bias point with temperature variations [21].

Modulators that provide complementary outputs have some advantages over single output devices. By using separate downlink fibers for the two channels and subtracting the output of one channel from the other after detection, the EM signal of interest is doubled. Furthermore, if the phases in the two downlinks are carefully matched, the noise in the optical source can be subtracted out. Those modulators with the potential for complementary outputs are identified in the table. Unfortunately, they all suffer from having lower sensitivities or, as in the case of the directional coupler, are difficult to fabricate with the appropriate passive bias point.

The sensitivity or V_π voltage of a modulator is, in general, a product of the electric field strength induced in the crystal and its interaction length with the optical carrier. The reason that optical, integrated-circuit devices show very good sensitivity is that because of their small size and electrode spacings of only a few micrometers, high field strengths are obtained. With the high field strengths, short interaction lengths of a few millimeters and high-frequency response are also obtained. It should be noted that although traveling-wave structures have been fabricated which can modulate carriers at frequencies above 10 GHz [22], such devices may not be appropriate for field probes since the traveling-wave electrodes would disturb the dipole characteristics.

RECEIVERS A second important component in the electro-optic probe is the receiver at the downlink end of the system. It consists primarily of a photodiode and amplifier. If complementary outputs are used, it also contains the channel subtraction network. For many applications, the high signal frequencies and the shallow modulation depth of the optical carrier demand the highest performance available for the receiver elements. The primary criterion for adequate performance is that the receiver maintain as high a signal-to-noise ratio as possible.

Several sources of noise in an electro-optic system need to be considered for field probes. These are listed, together with some suggestions for minimizing them, in Table 7.2. The reduction of the noise in the receiver requires that the detector and amplifier be carefully matched, preferably designed to operate together and fabricated into one monolithic structure. Detailed discussions of receiver design and noise characteristics can be found in the literature [23]. For our purposes, a brief comparison of an avalanche photodiode (APD) and a PIN photodiode is instructive. The analysis is outlined in Table 7.3. In both cases, the total gain is 50, which is typical of available APDs. The power in the optical carrier is chosen to be 50 microwatts, which is low enough to limit optical damage in a typical $LiNbO_3$ optical integrated-circuit device. The modulation depth, A, is typical for a field strength of 1 V/m using a dipole antenna with 15-cm-long elements. As indicated, the thermal noise in the 50-Ω input resistance dominates in the PIN receiver, while shot noise dominates in the APD. This is because in the PIN the thermal noise is amplified by the gain, while in the APD the gain occurs prior to the load resistor. The signal-to-noise ratio for the APD is thus superior to that for the PIN receiver.

When shot noise dominates, the signal-to-noise ratio can be approximated by

$$I_s^2 / I_n^2 = \frac{rA^2P_c}{2eB_nF(m)} \quad , \tag{7.7}$$

where the various quantities are defined in Table 7.3. Three parameters can be changed to improve the signal-to-noise ratio. The most desirable is to increase the modulation depth, A, by increasing the modulator sensitivity. However, without materials with considerably larger electro-optic coefficients, improvement in this component may be limited. Increasing the optical carrier power helps, but only with the danger of photon-induced crystal damage. Finally, narrowing the detection bandwidth brings substantial improvement for detecting CW fields. If sufficiently narrow bandwidths to obtain good signal-to-noise ratios are acceptable, low optical power and simple PIN diode receivers can produce excellent results [24].

TRANSMITTERS Desirable characteristics of a transmitter are that it be capable of coupling adequate optical power into the uplink fiber, contribute relatively little noise to the system, and have spectral purity sufficient to meet system bandwidth requirements. Optimizing performance in one of these areas usually means compromising performance in another. Often the input requirements of the modulator considerably restrict the options for the source. In particular, modulators of the integrated-optics type and some of the polarization/analyzer designs require single-mode uplink fibers to match input-mode size and prevent depolarization respectively. Only the output from solid-state or gas lasers can provide the necessary power densities in the few micrometer diameter core of single-mode fibers. Lasers are also necessary to provide the spectral purity required to prevent material dispersion from degrading system bandwidth if high-frequency operation over long fiber links is necessary. If system bandwidth is limited by the modulator characteristics, and multimode fiber can be used on both the uplink and downlink fibers, non-lasing, superluminous diodes may provide a much lower system noise level with adequate optical carrier power.

The choice of the carrier wavelength depends on several system parameters. The most important are the detector spectral response, the desired modulator sensitivity, and its potential for optical damage. The first two requirements call for short wavelengths which, in general, improve modulator sensitivity and for wavelengths between 600 to 900 nm to match the spectral response of silicon photodiodes that are less noisy than the longer-wavelength-responding GaAs-based devices. For $LiNbO_3$-based modulators, photon damage has been seen to occur at wavelengths less than 1.4 μm [25]. Thus, in order to take advantage of shorter-wavelength sensitivity, power levels in these modulators must be kept to a few uW and operation at the HeNe wavelength of 633 nm should be avoided. Narrow spectral line widths are usually desirable to prevent chromatic dispersion in the downlink fiber from degrading system bandwidth if high frequency and long fiber links are required. However, in most applications, the fiber links are short enough that frequency response is limited by the modulator characteristics instead of the fiber downlink. Spectral purity then becomes more of a concern in regards to system noise.

The contribution of the transmitter to the system noise budget is both direct and indirect. Electro-optic light sources are all directly affected with shot or quantum noise in the photon-generation process. However, for a good laser that is operating above threshold, the ratio of the noise power to the output power can be less than -140 dB. In order to reach these low levels of noise, stabilized single-mode operation is a must. This also avoids the problem of mode hopping or mode partition noise that is a problem in multimode lasers. Unfortunately, even single-mode lasers are easily destabilized and exhibit mode hopping if optical feedback occurs due to reflections from fiber ends and other surfaces in the optical system. This problem can be especially severe if modulated light is reflected back to the laser. Every precaution needs to be taken in setting up a probe system to eliminate the possible reflections and to make sure that those which do occur are not propagated back to the laser.

Modal noise in multimode fibers and the less-severe polarization-mode noise in single-mode fibers are due to fluctuations in the energy distributed between the various modes when a very narrow spectral line (single-mode laser) is used. The effect is similar to the dancing speckle pattern seen in laser light reflected from a rough surface. For this reason, a source with a broad spectral line is desirable if multimode fiber is used in a low-bandwidth system.

The characteristics of several candidate transmitter light sources are summarized in Table 7.4. It is clear that the optimum system would use single-mode components throughout the system. This should provide the greatest bandwidth, lowest noise, and highest sensitivity. However, if system bandwidth requirements are low, a system designed to operate with all multimode components and non-lasing superluminous diodes may provide adequate optical carrier power and sufficiently low noise for considerably less expense than a single-mode system.

<u>FIBERS, CONNECTORS, AND COUPLERS</u> As just mentioned, an electro-optic field probe can be designed using either single-mode or multimode optical components. The highest performance is obtained using an all-single-mode system, preferable operating at about 850-nm wavelength. Single-mode fibers and connectors are presently available for such applications. However, the availability of single-mode fiber for 850-nm operation in the future is of concern, since the communication industry is moving to 1.3-μm and 1.55-μm wavelength systems to increase repeater spacing. Fibers designed for single-mode operation at these longer wavelengths will, in general, be multimode at the shorter wavelength due to their larger core diameters and resulting higher cutoff wavelengths [26]. Multimode fibers for 850-nm operation are readily available because of their common use in local area networks. Both single-mode and multimode fibers are available in multifiber cables, often in short sections left over from large manufacturing runs. When using fibers in sensor applications, some care needs to be taken to avoid sharp bends or stress which will induce severe birefringence.

Connectors are commercially available for both single-mode and multimode systems. Multimode systems require less precision in aligning fiber ends and are therefore easier to use. Connectors to the probe which are in the measurement field and near the antenna should be nonmetallic in order to avoid field distortions. Plastic and ceramic units are available to meet this need. Metallic connectors may be used at the transmitter/receiver unit.

Coupling light into fibers, especially single-mode fibers, is fairly difficult and is sensitive to the system mechanical stability. Therefore, it is highly desirable to have lasers with fiber pigtails and use all-fiber components to divide, switch and control the light propagation. Fortunately, many of the components necessary for these operations are now available due to their development for the telecommunications industry. Their use also increases the optical stability and considerably reduces the size and weight over that of a system using discrete open-beam-path components, such as beam splitter prisms, microscope objectives, etc., and their usual mounting hardware. The continued rapid development of this technology should make still better components available in the near future.

REFERENCES

[1] Bowman, R. R. Some recent developments in the characterization and measurement of hazardous electromagnetic fields. Proc. Int. Symp. on Biolog. Effects and Health Hazards of Microwave Rad; 1973 October; Warsaw, Poland. 217-227.

[2] Aslan, E. Electromagnetic radiation survey meter. IEEE Trans. Instrum. Meas. IM-19: 368-372; 1970 November.

[3] Larsen, E. B.; Andrews, J. R.; Baldwin, E. E. Sensitive isotropic antenna with fiber-optic link to conventional receiver. Nat. Bur. Stand. (U.S.) Int. Rept. 75-819; 1976 September.

[4] Kanda, M. A relatively short cylindrical broadband antenna with tapered resistive loading for picosecond pulse measurements. IEEE Trans. Antennas Propag. AP-26(3): 439-447; 1978 May.

[5] Kanda, M.; Ries, F. X. A broadband isotropic real-time electric-field sensor (BIRES) using resistively loaded dipoles. IEEE Trans. Electromag. Compat. EMC-23(3): 122-132; 1981 August.

[6] Larsen, E. B.; Ries, F. X. Design and calibration of the NBS isotropic electric-field monitor (EFM-5), 0.2 to 1,000 MHz. Nat. Bur. Stand. (U.S.) Tech. Note 1033; 1981 March.

[7] Driver, L. D.; Cruz, J. E. Development of the NBS isotropic magnetic-field meter (MFM-10), 300 kHz to 100 MHz. IEEE Int. Symp. on EMC; 1982 September; Santa Clara, CA. 460-467.

[8] Bensema, W. D. A noise spectrum measurement system using the fast Fourier transform. IEEE Trans. Electromag. Compat. EMC-19(2): 37-43; 1977 May.

[9] Reeve, G. R.; Synthesized isotropic pattern antennas for EM field measurements. IEEE Int. symp. on EMC; August 1981; Boulder, CO. 36-42.

[10] Bensema, W. D. Broadband orthogonal array system microprocessor control and computation. IEEE Int. Symp. on EMC; 1981 August; Boulder, CO. 43-46.

[11] Wyss, J. C.; Sheeran, S. A practical optical modulator and link for antennas. J. Lightwave Technology, LT-3(2): 316-320; April 1985.

[12] Bulmer, C. H.; Hiser, S. C. Linear Ti: $LiNbO_3$ modulators at 1.3 μm for electromagnetic field sensing. Integrated Optical Circuit Engineering, SPIE, vol. 517; 1984.

[13] Kanda, M. An electromagnetic near-field sensor for simultaneous electric- and magnetic-field measurements." IEEE Trans. Electromag. Compat. EMC-26(3): 102-110; 1984 August.

[14] King, R. W. P. The Theory of Linear Antennas. Cambridge, MA: Harvard University Press; 1956. 184 and 487.

[15] Kanda, M. Analytical and numerical techniques for analyzing an electrically short dipole with a nonlinear load. IEEE Trans. Antennas Propag. AP-28(1): 71-78; 1980 January.

[16] Yoshino, T.; Ose, T. New approach to fiber-optic sensors using fiber Fabry-Perot interferometers. paper WL6, CLEO Digest of Technical Papers, Optical Society of America; 1982 April.

[17] Yao, S. K.; Findakly, T.; Cordero-Iannarella, R.; Thaniyavarn, S.; Hayward, G.; Chen, B. Electromagnetic sensor using integrated optic channel waveguide modulator and polarization preserving fiber. SPIE Proc., 412: 154-159; 1983.

[18] Yen, H. W. private communication, Hughes Research Laboratories, Malibu, CA.

[19] Wood, T. H.; Burrus, C. A.; Miller, D. A. B.; Chemia, D. S.; Damen, C.; Gossand, A. C.; Wiegmann, W. High-speed optical modulation with GaAs/GaAlAs quantum wells in a P-i-n diode structure. Applied Physics Letter, 44: 16; 1984.

[20] Alferness, R. C. Waveguide electrooptic modulators. IEEE Trans. Microwave Theory and Techniques, MTT-30(8): 1121-1137; 1982 August.

[21] Bulmer, C. H.; Burns, W. K. Integrated-optic modulator for electromagnetic field sensing. Paper THAA1, OSA/IEEE 3rd Int. Conf. on Optical Fiber Sensors; 1985 February; San Diego, CA.

[22] Becker, R. A. Traveling-wave electro-optic modulator with maximum bandwidth-length product. Applied Physics Letter, 45(11): 1168; 1984 1 December.

[23] Muoi, T. V. Receiver design for high-speed optical-fiber systems. J. Lightwave Technology, LT-2(3): 243-267; 1984 June.

[24] Bulmer, C. H.; Burns, W. K. Linear interferometric modulation in Ti: $LiNbO_3$. J. Lightwave Technology, LT-2(4): 512-521; 1984 August.

[25] Halman, R. L.; Busch, J. R.; Verber, C. M.; Wood, V. E.; Hartman, N. F.; Cressman, P. J. Z-axis propagation and the avoidance of optical damage in Lithium Niobate waveguides. IEEE/OSA Seventh Topical Meeting on Integrated and Guided-Wave Optics; 1984 April; Kissimmee, FL.

[26] Jeunhomme, L. B. Single-Mode Fiber Optics, Principles and Applications. New York, NY: Marcel Dekker, Inc.; 1983.

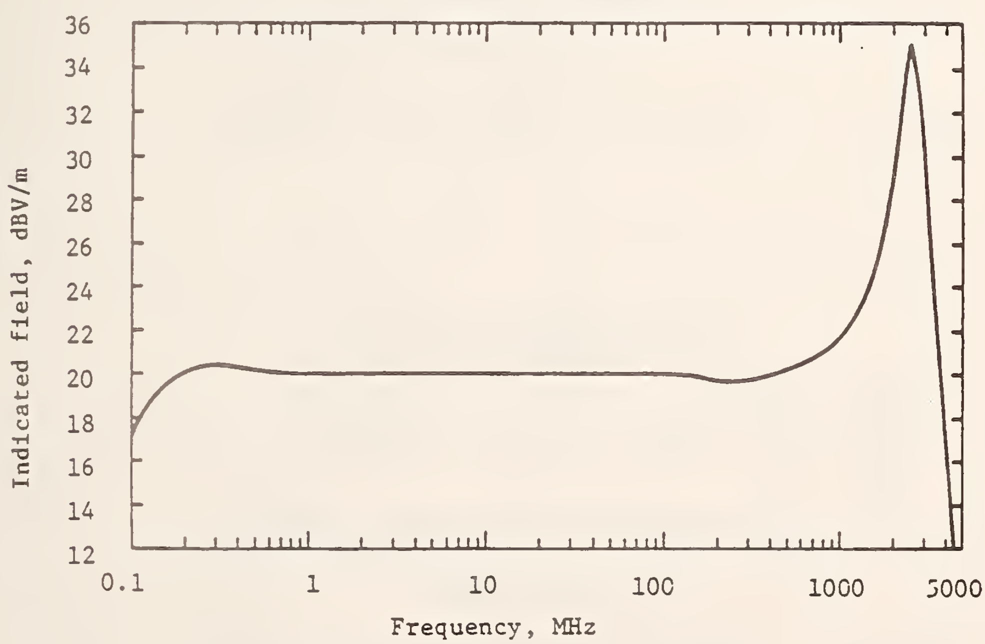

Figure 7.1 Typical response of the NBS isotropic electric-field monitor (EFM-5).

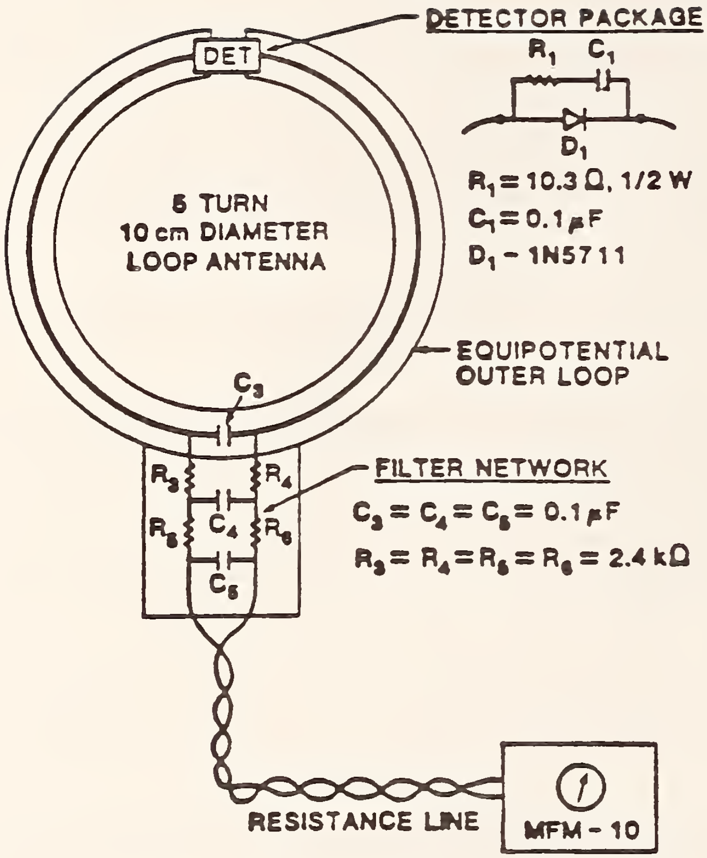

Figure 7.2 NBS magnetic-field meter (MFM-10).

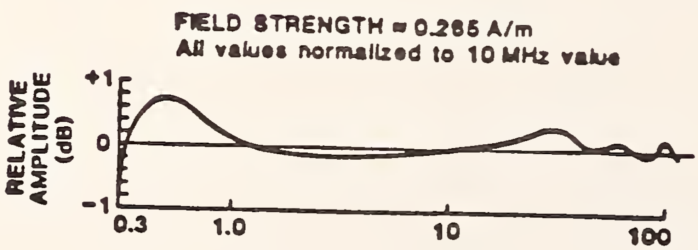

Figure 7.3 Normalized response curve of MFM-10.

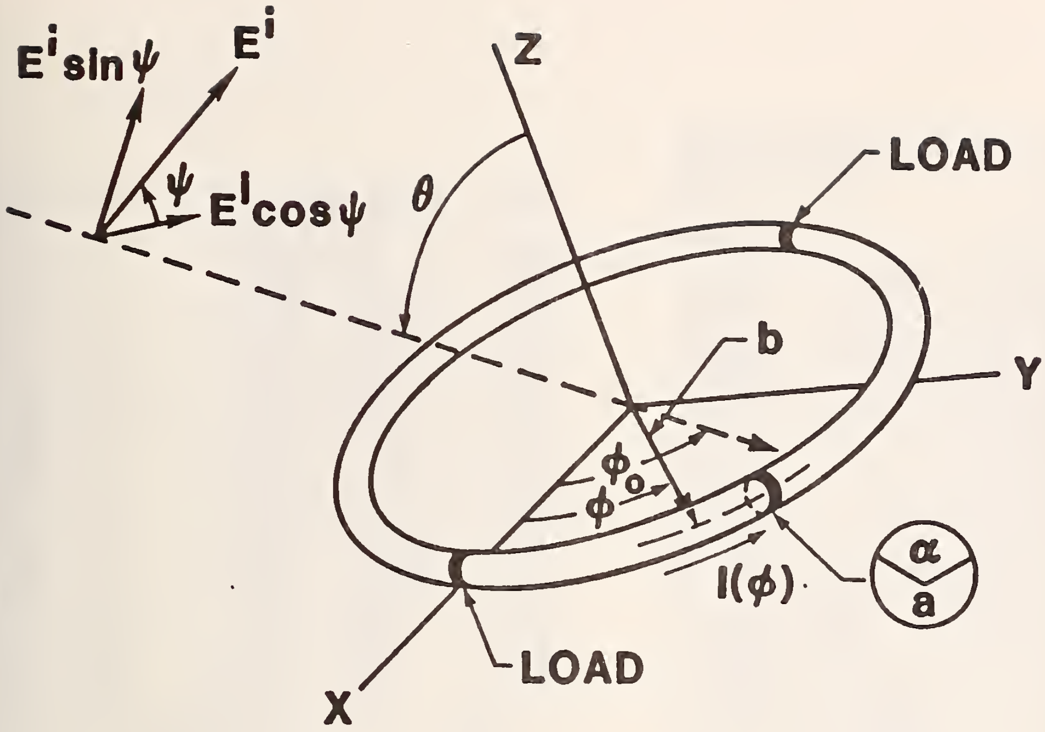

Figure 7.4 A single loop with equal loads in a new probe for measuring simultaneously the electric and magnetic fields.

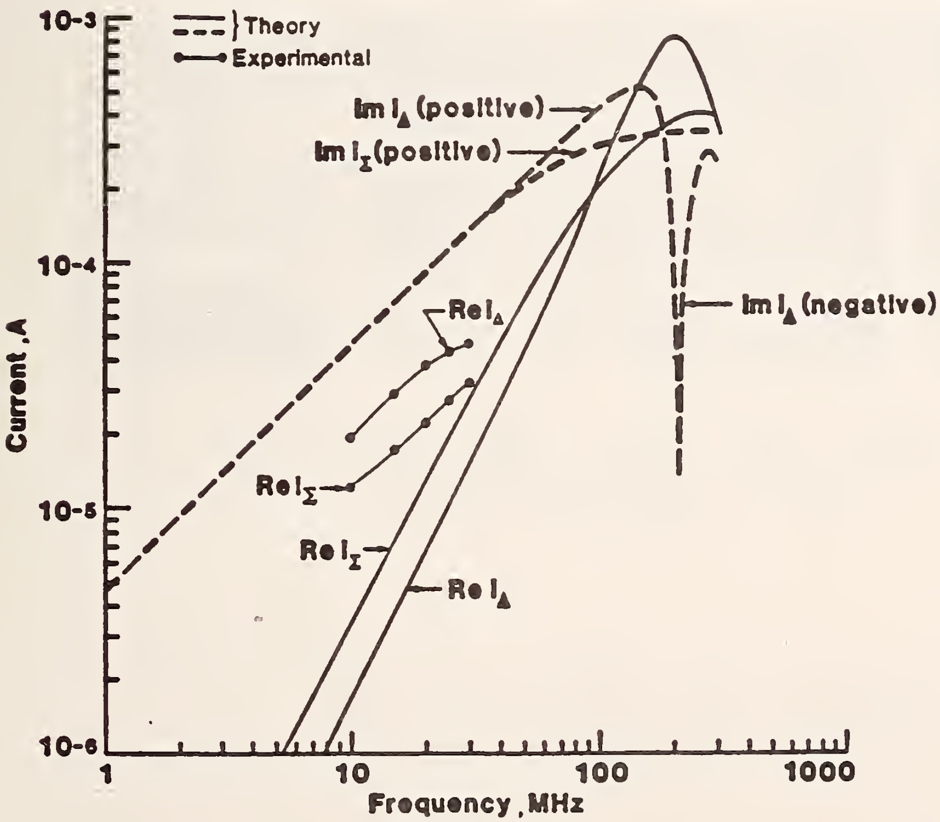

Figure 7.5 Magnetic-loop (I_Σ) and electric-dipole (I_Δ) currents of a loop antenna with Z_L = 200 Ω.

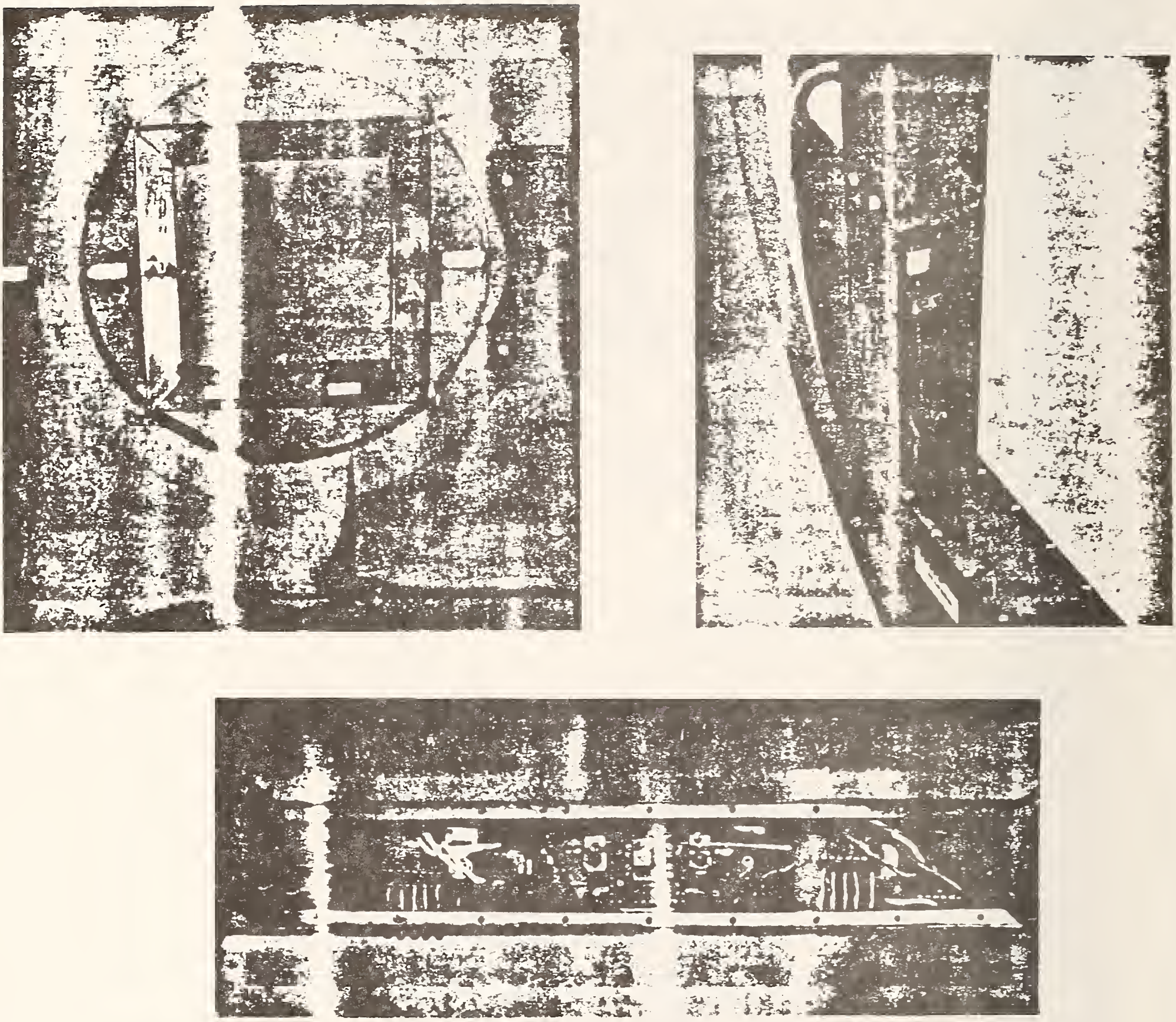

Figure 7.6 An experimental loop model for measuring simultaneously the electric and magnetic fields.

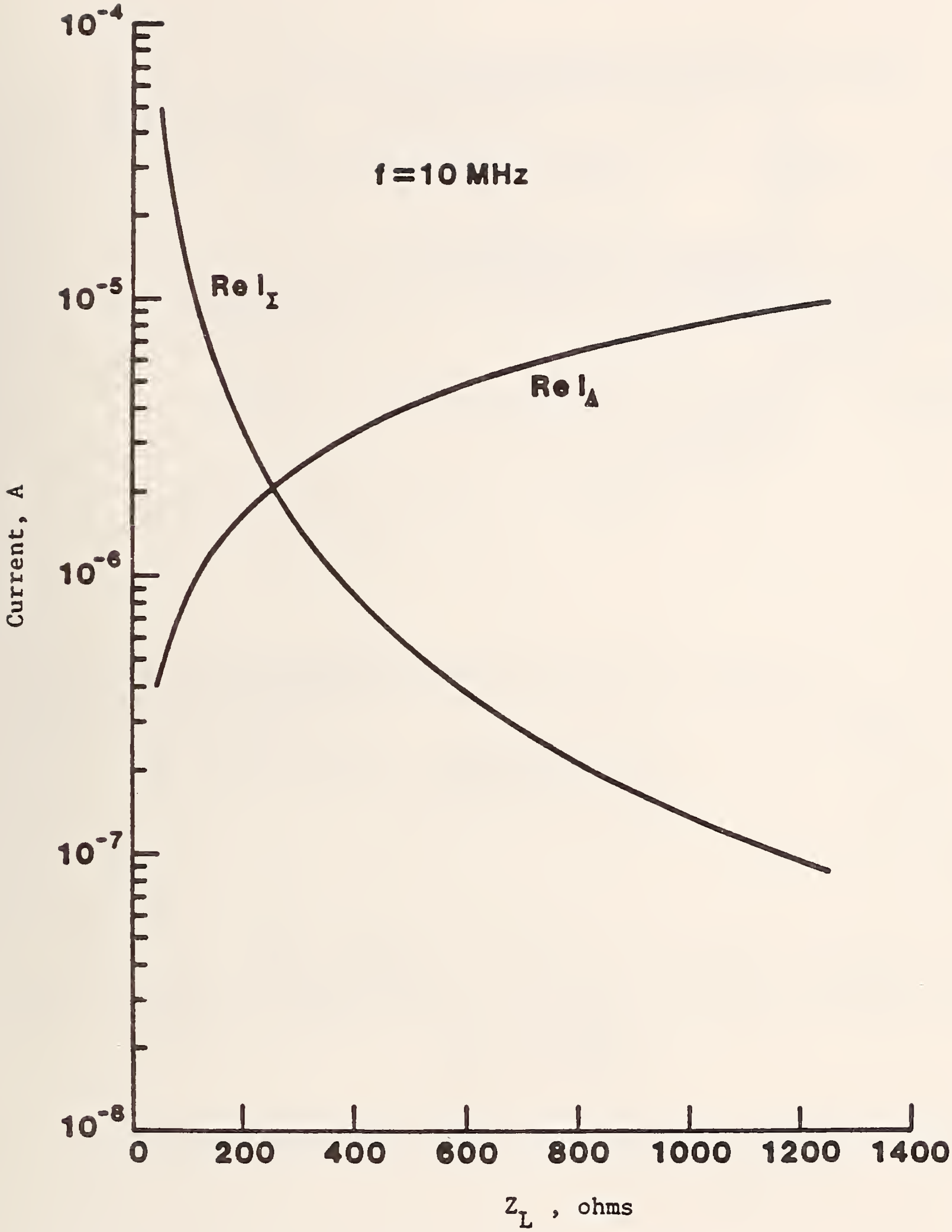

Figure 7.7 Real parts of magnetic-loop and electric-dipole currents of a loop antenna as a function of load impedance at 10 MHz.

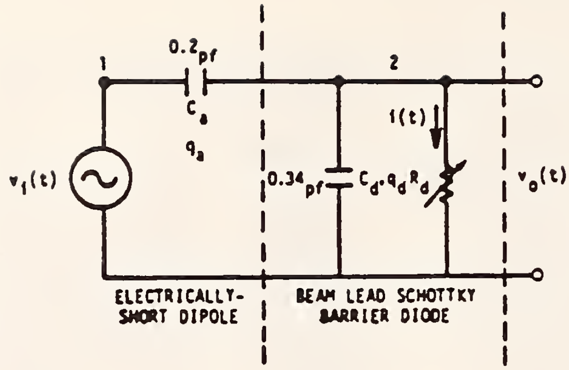

Figure 7.8 Thévinin's equivalent circuit of a probe-diode system.

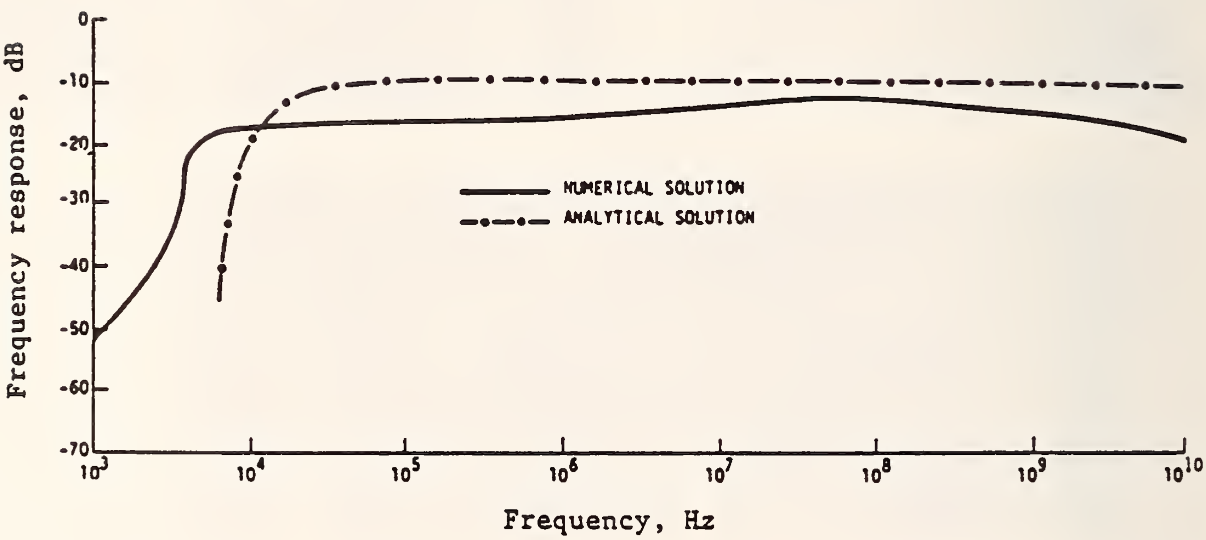

Figure 7.9 Frequency response of a typical probe-diode system with E_{inc} = 1 V/m.

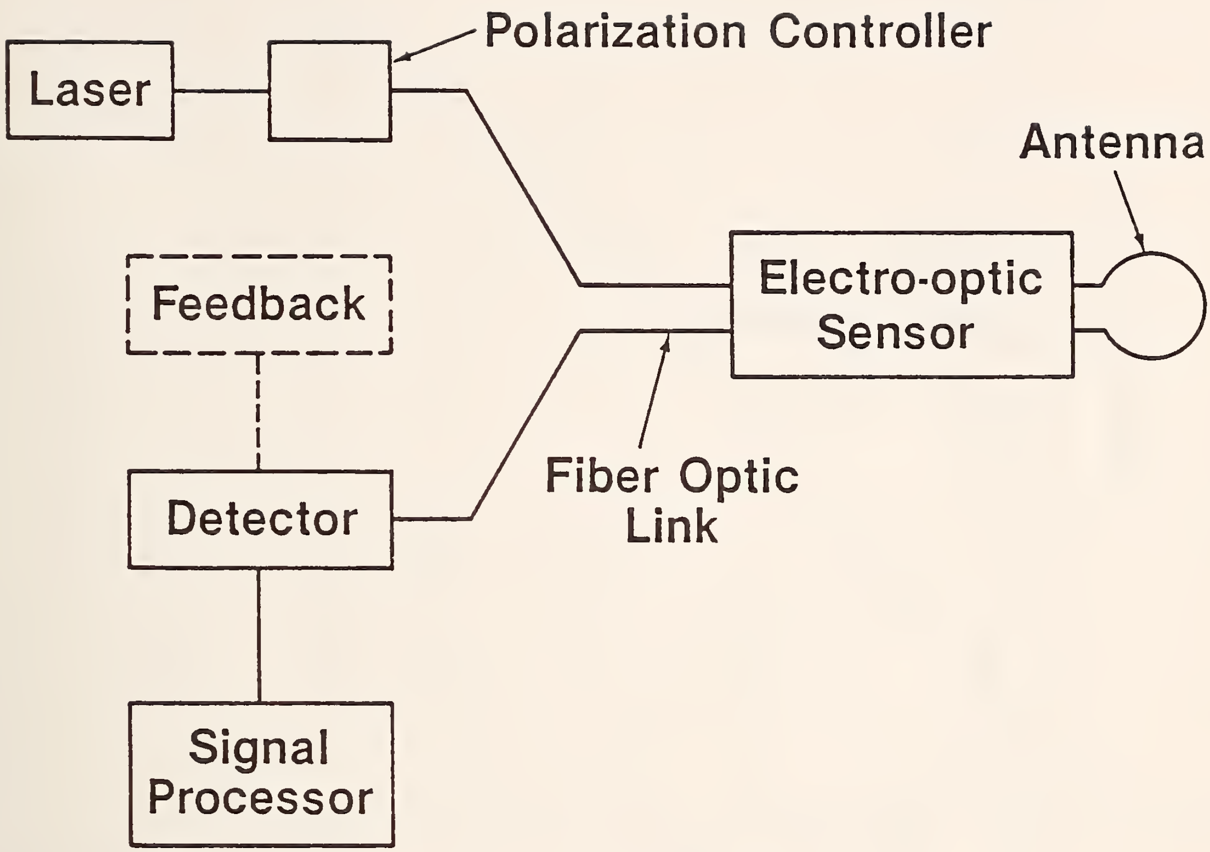

Figure 7.10 Block diagram showing basic concept of electro-optic field probe.

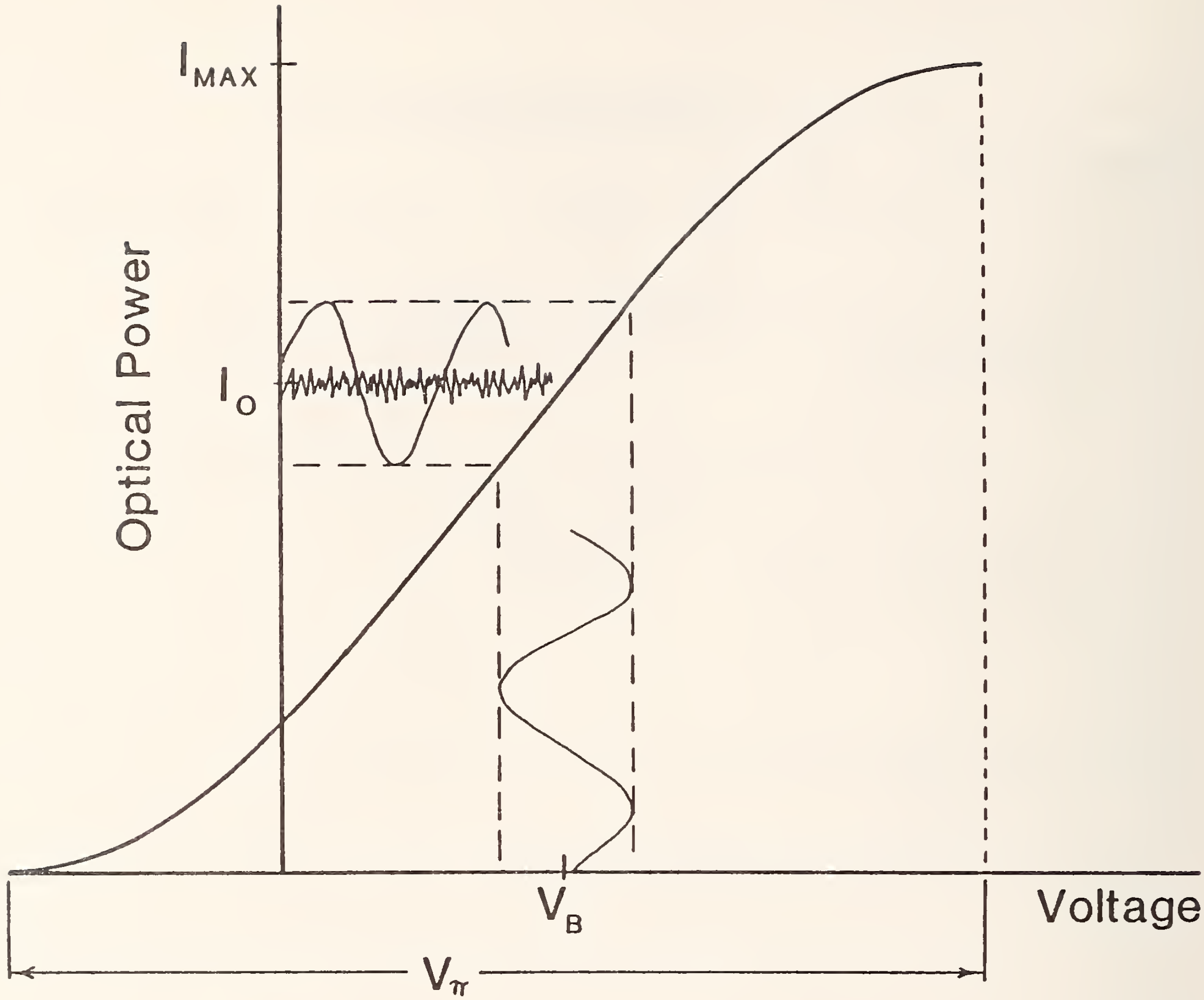

Figure 7.11 Characteristic operating mode for electro-optic modulator.

Table 7.1. Modulator Characteristics

Type	Transmittance τ	Bias* θ_o [method obtained]	Sensitivity $S = d\tau/dV$	Sensitivity typical value	Parameters*
Bulk Crystal Birefringence [11]	$\sin^2(\theta/2)$	$\pi/2$ [Input polarization]	$\frac{\pi}{2V_\pi}\sin(\pi V/V_\pi)$	0.006	$V_\pi = 248V$ [11]
Mach-Zehnder Integrated Optic Interferometer [12]	$\cos^2(\theta/2)$	$\pi/2$ [Asymmetry in legs]	$\frac{\pi}{2V_\pi}\sin(\pi V/V_\pi)$	0.5	$V_\pi = 3V$ [12]
Fabry-Perot etalon Interferometer [16]	$\frac{\tau_{max}}{1 + F\sin^2(\theta/2)}$	For $F = 400$, $\tau = 0.5\,\tau_{max}$, $\theta_o = 5.7°$ [wavelength]	$\frac{\pi}{2V_\pi}\frac{\tau^2 F\sin\theta}{2\tau_{max}}$	0.6	$V_\pi = 13V$
Integrated Optics directional Coupler [12],[17]	$\frac{\kappa^2 L^2\sin^2(\theta/2)}{(\theta/2)^2}$ where $\theta^2 = 4\kappa^2 L^2 + (\Delta\beta L)^2$	$\kappa L = \pi/2$, $\Delta\beta L = 4\pi/5$ [Length L and propagation constant β]	$f(\kappa,L,\Delta\beta)\frac{d}{dV}(\Delta\beta)$	0.25	$V_\pi = 6V$ [17]
Band edge absorption [18]	----	[carrier wavelength]	20 dB/3 volts	0.3	
Quantum well absorption [19]	----	[carrier wavelength]	0.5/4 volts	0.1	

*The argument θ of the transmittance can be written as $\theta = \theta_o + \frac{\pi V(t)}{2V_\pi}$, where θ_o is the desired bias point for maximum sensitivity and linear dynamic range, $V(t)$ is the applied signal voltage, and V_π is the voltage to switch the modulator from maximum to minimum transmittance. V_π is determined by the geometry of the device, electrooptical coefficients of material, and wavelength of the carrier.

Table 7.2 Principal Noise Sources for Optically Sensed Probes

Noise Sources	Mitigation
1. Laser	use common mode rejection detection scheme
Quantum noise	operate above threshold
Mode partition noise	stabilized, single mode laser
Optically feedback noise	a. use coupling optics to reduce feed back b. use Faraday isolator
2. Fiber	
Modal noise	a. carefully align and match fibers and couplers b. use source with broad spectral width c. use single mode fiber
Modal polarization noise	a. use low birefringent fiber b. use polarization maintaining fiber
3. Receiver	use low-noise amplifiers carefully matched to detector
Shot noise	limit carrier power
Thermal noise in load	a. use avalanche photodiode b. cool electronics
Dark current noise	insignificant for this type system

Table 7.3 Signal and Noise Calculations for Typical PIN and Avalanche (APD) Photodiodes

Signal current $I_s = MgrP_oA$

Mean-square noise current $\overline{I_n^2}$

$$= 2g^2B_n[M^2\,F(M)\,erP_o \quad + \quad M^2\,F(M)\,eI_d \quad + \quad \frac{2kT}{R_L}\,]$$

(shot noise) (dark noise) (thermal noise)

where

M = avalanche gain: 1 for PIN; 50 for APD
g = amplifier gain: 50 for PIN; 1 for APD
r = primary responsivity: ≈ 0.4 A/W for silicon photodiode at λ = 850 nm
P_o = intensity of optical carrier: 50 μW
A = modulation depth of carrier by signal voltage: 0.01
B_n = bandwidth of detection system: 10 MHz
$F(M)$ = excess carrier noise factor: 1 for PIN; 4 for APD with M = 50
e = charge of electron: $1.6(10)^{-19}$ C
I_d = detector dark current before gain : 200 pA
k = Boltzmann constant: $1.38(10)^{-23}$ J/°K
T = temperature: 300°K
R_L = load resistance: 50 Ω

	PIN	APD
$\overline{I_n^2}$	$= 1.6(10)^{-11}$ (shot)	$= 6.4(10)^{-11}$ (shot)
	$+ 1.6(10)^{-15}$ (dark)	$+ 6.4(10)^{-15}$ (dark)
	$+ 8.25(10)^{-9}$ (thermal)	$+ 3.3(10)^{-12}$ (thermal)
	$= 8.3(10)^{-9}\ A^2$	$= 6.7(10)^{-11}\ A^2$
I_s^2	$= (10)^{-10}\ A^2$	$= (10)^{-10}\ A^2$
S/N	$= 1.2(10)^{-2}$	1.5 (just detectable)

Table 7.4 Typical Characteristics of Several Light Sources for Electro-Optic Sensors

Source	Wavelength (nm)	Spectral line width (nm)	Single Mode (SM)/ Multi Mode (MM)	Output Power (mW)
Light emitting diodes				
Ga Al As	780-850	≈ 40	NA	2 - 10
Ga As	940	≈ 40	NA	2 - 6
In Ga As	1060	50	NA	0.2
Laser diodes				
Ga Al As	780-850	2 - 3	MM	2 - 10
Ga Al As	780-850	0.005 - 2	SM	2 - 10
In Ga As P	1300	3 - 4	MM/SM	1 - 10
Gas lasers				
He Ne	632.8	5 MHz*	SM	0.5 - 10
He Ne	1152	5 MHz*	SM	0.05 - 1

*5 MHz corresponds to $6.5(10)^{-15}$ m = $6.5(10)^{-6}$ nm.

The limitation on operating frequency for TEM cells as described in Chapter 3 could be a drawback for certain applications. Furthermore, since the polarization of the field generated inside a TEM cell is fixed, the radiated emission and susceptibility tests for an EUT using TEM cells require physical rotations (or different orientations) as discussed. This requirement of EUT rotation could be another inconvenient aspect.

A relatively new EMC/EMI measurement technique, which does not require EUT rotations, is to utilize reverberating chambers to generate an average uniformly homogeneous and isotropic field within a local region inside a metal enclosure [1]-[9]. A reverberating chamber is a shielded room with a rotating stirrer to mix the field generated by a transmitting antenna. The polarization of this homogeneous and isotropic field is randomly varying. It is precisely because of this special property that the physical rotation of test objects can be avoided. The homogeneous and isotropic field is achieved by rotating an irregularly shaped mode stirrer or tuner, either continuously or in steps [7]. Naturally, the associated boundary conditions are changing with respect to time so that the possible modes existing simultaneously inside a given shielded metal chamber (cavity) are perturbed accordingly.

Two analytical approaches for treating this type of EM field problem and for providing basic knowledge for design purposes are possible. One involves the direct solution of Maxwell's equations with time-varying boundary conditions. A formal solution using this direct approach is rather difficult to obtain. In the other approach, suitable linear combinations of basic eigenmodes of the unperturbed cavity (without mode stirrer or tuner) with time-dependent expansion coefficients are taken to represent the field and to satisfy approximately the boundary condition on the surface of the rotating mode stirrer or tuner [7]. The main advantage of this latter approach is that the unperturbed eigenfrequencies and eigenmodes are much easier to calculate, and the problem can be reduced to a more familiar one under special conditions. A necessary condition for the validity of this method is, however, that the total number of eigenmodes which can exist inside a chamber be large for a specified frequency and chamber size. Thus, the measurement technique using reverberating chambers is good for very high frequency application, and may serve as a powerful supplementary tool to TEM cells. Typical frequencies of operation are from a few hundred megahertz to 20 GHz or above.

The reverberating chamber is also capable of providing a very efficient conversion of source power to high-strength fields inside a shielded enclosure for performing EMC/EMI tests of large equipment and whole systems. The limiting factors are that users may have difficulties interpreting the measurement results taken inside the chamber and relating them to actual operating conditions, and that polarization properties are not preserved for characterizing an EUT.

8.1 Some Design Considerations

As expected, the total possible number of modes, N(f), inside an unperturbed, lossless, rectangular chamber of dimensions (a x b x d) increases in steps with frequency. A smooth approximation to N(f) may be given by [7],[8]:

$$N_s(f) = \frac{8\pi}{3}\, abd\, \frac{f^3}{c^3} - (a + b + d)\,\frac{f}{c} + \frac{1}{2} \quad , \tag{8.1}$$

where abd in cubic meters represents the chamber volume, f the operating frequency in hertz, and c the speed of wave propagation in the chamber (usually air) in meters per second.

Note that the first term in (8.1) is identical to Weyl's formula [7] derived originally for the same problem by a different approach, and is proportional to the chamber volume and the third power of frequency. The second term may be recognized as the edge term, which is proportional to the sum of the linear dimensions of the chamber and modifies Weyl's result; this term is especially significant in the lower frequency range. The inner surface area of the chamber, S = 2(ab + bd + da), is not involved in (8.1). An example is given in Fig. 8.1 showing N(f) as Curve 1, $N_s(f)$ as Curve 2, and Weyl's formula as Curve 3 for the NBS chamber. Note that the dimensions of the NBS chamber, 2.74m x 3.05m x 4.57m, are all unequal. Designs of chambers having two or three sides equal but with the same volume will increase mode degeneracy, thus decreasing the total number of distinct modes with respect to a given operating frequency. Under this condition, wider steps in Curve 1 than those shown in Fig.

8.1 will be observed, even though the smooth approximation (Curve 2) remains almost unchanged. To demonstrate this point, specific examples are shown in Fig. 8.2 for a square-based chamber (2.17m x 4.19m x 4.19m) and in Fig. 8.3 for a cubic chamber (3.37m x 3.37m x3.37m).

While the total number of eigenmodes inside an unperturbed chamber is an important design criterion, another equally important factor to consider is the mode density function, dN/df, which represents the change in the number of modes in a given frequency interval. Of course, the exact shape of dN/df involves impulse functions as it is the derivative of step functions. An alternative quantity for exhibiting this property is to examine

$$\Delta N = \int_{\Delta f} \frac{dN}{df}\, df \quad , \tag{8.2}$$

which represents the increase or decrease in mode number within a frequency interval of Δf.

Results of ΔN when Δf = 1 MHz are presented in Fig. 8.4 for the NBS chamber, in Fig. 8.5 for the square-based chamber, and in Fig. 8.6 for the cubic chamber, all with the same volume. Clearly, the uniformity of mode distribution in the frequency interval of 1 MHz is good for the NBS chamber, fair for the square-based chamber, and poor for the cubic chamber, where no change in mode number is possible in a relatively larger portion of frequency sub-bands. The general design criteria for a reverberating chamber are then to make the volume as large as possible and the ratio of squares of linear dimensions as nonrational as possible.

A third design criterion, namely, the quality factor (Q), should also be considered to characterize a chamber when it is made of lossy material. Since there are so many modes existing in an unperturbed chamber with each mode carrying its own Q value [7],[8],[10], it is not trivial to define a quality factor for the chamber as a whole. One method of defining a composite quality factor for an unloaded chamber (without an EUT in it) within a specified frequency range gives the following simple, approximate result [7]:

$$\tilde{Q} = \frac{3}{2}\left(V/S\delta_s\right) \frac{1}{1 + \frac{3\pi}{8k}\left(\frac{1}{a} + \frac{1}{b} + \frac{1}{d}\right)} \tag{8.3}$$

where V denotes the chamber volume (abd) in cubic meters, and δ_s the skin depth in meters of the material of which the chamber is made.

The physical meaning of (8.3) may be interpreted by comparing it with the individual Q-values of all the modes in the form of a cumulative distribution. Since $V/(S\delta_s)$ is a common factor whether the composite quality factor defined above or the quality factor for individual modes is considered, it is more convenient to present the results in terms of 1/Q values normalized with respect to $S\delta_s/V$. Thus, the variable used herein is

$$\alpha = \frac{1}{Q}\left(V/S\delta_s\right) \quad . \tag{8.4}$$

Examples of the cumulative distribution of α for the NBS chamber are given, respectively, in Figs. 8.7-8.9 for three different frequency bands. For the frequency band of 180 to 200 MHz in Fig. 8.7, the total number of modes existing in this band of 20 MHz is 69, with each mode having its own Q-value. The probability of having a high upper-bound value of $\alpha \leqq 0.80$ (or a lower bound for Q) is almost 100 percent, and that for a low bound of $\alpha \leqq 0.48$ (or a high value for Q) is only about 10 percent. This implies that almost all of the 69 modes in this particular frequency band have $\alpha \leqq 0.80$. The arithmetic mean of 0.623 and the standard deviation of 0.090 are also indicated in the figure. The probability of having $\alpha \leqq 0.623$ (arithmetic mean) is, of course, 50 percent, meaning that at least one half of the 69 modes have $\alpha \leqq 0.623$.

For the case presented in Fig. 8.8, where the frequency band is from 330 to 350 MHz, also of a bandwidth of 20 MHz, there are 261 modes, an increase in number of modes relative to that in Fig. 8.7. This is because of higher frequency. A similar interpretation of the α-values (or Q-values) carried by these modes in terms of probability applies. Note that there are now a small number of modes (low probability) carrying a value of α as low as 0.43 (high Q). The arithmetic mean and standard deviation are, respectively, 0.630 (higher than the corresponding value in Fig. 8.7) and 0.085 (lower than the corresponding value in Fig. 8.7). A higher value of arithmetic mean implies that one half or more of the 261 modes carry a higher value of α

(lower Q) compared to the frequency band considered in Fig. 8.7. A decrease in standard deviation reveals that a greater number of modes have an α value closer to the arithmetic mean.

If we consider a still higher frequency range 480 to 500 MHz, such as that illustrated in Fig. 8.9, 534 possible modes will exist in the same bandwidth of 20 MHz. The arithmetic mean increases further to 0.646 while the standard deviation decreases further to 0.074, indicating that a greater number of modes will have still higher α values near the arithmetic mean. This general tendency, increasing in arithmetic mean and decreasing in standard deviation with increased frequency, yields a limiting mean of $\alpha \leqq 0.667$ with a 50-percent probability, which also agrees precisely with the limiting value for the composite $\tilde{\alpha}$ derived from (8.3) and (8.4).

Thus, even though there are a large number of possible modes existing in a specified operating frequency band for a reverberating chamber, with each mode carrying its own value of α or Q, the probability that $\alpha \leqq 2/3$ (or $Q \geqq 1.5V/S\delta_S$) is 50 percent. This fact implies that one half of the modes have α values less than 2/3. Preliminary estimation of a quality factor to characterize the reverberating chamber as a whole, based on the simple expression $\tilde{Q}$ in (8.3), for the purpose of predicting the field-strength level to be generated in the test zone, is indeed very useful. The composite quality factor so estimated is considered as the upper-bound value because it does not take into account losses other than that due to wall conductivity.

Since compromises between low conductor losses (high Q) and broad model coverage (low Q) are almost always necessary in the practical design of reverberating chamber, the results for ΔN in (8.2) and $\tilde{Q}$ in (8.3) will be found convenient and helpful.

8.2 Recent Measurement Results

The basic measurement system used at NBS is shown in Fig. 8.10. The test field is established by means of one or more RF sources feeding one or more transmitting antennas placed inside the chamber. We use the log-periodic antenna (0.2 to 1.0 GHz), corrugated horn (1.0 to 4.0 GHz), or double-ridged circular horn (4.0 to 18 GHz) as the transmitting antenna. Modes excited inside the chamber by the transmitting antenna are then tuned or stirred by rotating one or more field-perturbing devices referred to as "Paddlewheel tuners". The tuners are typically electrically large metal blades or irregularly shaped structures that are mounted on the enclosure walls or ceiling driven by electrical motors. The reason for using the irregular shape is to help scatter the field more evenly in all directions. Figure 8.11 shows the NBS tuner. The field generated at the test zone is then measured by a calibrated probe as a function of frequency and tuner position. Note that there is another receiving antenna placed inside the chamber to measure the maximum and minimum received powers (see Fig. 8.10). The long-wire antenna (0.2 to 1.0 GHz), corrugated horn (1.0 to 4.0 GHz), or double ridged circular horn (4.0 to 18 GHz) is employed as this receiving antenna. The measured data of these received powers are useful for assessing the effectiveness of the tuner, the relative uniformity of the field, and the quality factor of the chamber.

In the mode-stirred case [1],[6], the tuner rotates continuously, thus changing the chamber boundary conditions, the voltage standing-wave ratio (VSWR) of the transmitting antenna, the net input power to the chamber, and the field polarization and strength. The resultant field is then recorded by detectors with sampling rates much faster than the tuner's rotating speed, and statistically processed. In the mode-tuned case [9],[11], the tuner position is stepped at discrete intervals. Measurements of the net power delivered to the transmitting antenna, power received by the reference antenna, and perhaps also the monitor response of the EUT being tested are taken for each tuner position and frequency. This mode of operation makes possible corrections for the variations in field strength due to changes in the VSWR. An example of the transmitting antenna VSWR variation in the NBS chamber is presented in Fig. 8.12, giving the maximum, average, and minimum VSWRs as a function of frequency, obtained by rotating the tuner through a complete revolution with 200 steps (1.8° increments). Note the large variation at the lower-frequency end. Failure to correct for this change could result in errors in determining the test field level [12]. At higher frequencies above approximately 2 GHz, variations in VSWR become much more reasonable.

To evaluate the tuner effectiveness, the ratio of maximum-to-minimum received powers for a complete revolution at 200 steps is shown in Fig. 8.13 as a function of frequency, showing an average of 30 dB. The net input power to the transmitting antenna has been maintained constant for this measurement. If the tuner were not as effective, the maximum-to-minimum received power ratio would be very low. This fact can be verified by using a much smaller size of tuner with a rather regular shape.

Another important feature characterizing the chamber is the measured difference between the net input power to the transmitting antenna and the power available at the reference antenna terminals. This difference represents the chamber loss, which may be used to estimate the actual mean quality factor of the chamber. This information, of course, is important for considering the power requirement and broad modal coverage. The loss characteristics for the NBS chamber, both the average and minimum losses obtained by rotating the tuner by one complete revolution in 200 steps, are shown in Fig. 8.14. The smooth solid curves represent estimated fits from the measured data. Based on the measured minimum loss data, the actual mean chamber quality factor (Q') may be estimated by [2]:

$$Q' = 16\pi^2 \frac{V}{\lambda^3} (P_r/P_t) \quad , \tag{8.5}$$

where P_r is the minimum power available at the reference antenna terminals, P_t is the net power delivered to the transmitting antenna in the same unit as that of P_r, V is the chamber volume in cubic meters, and λ is the operating wavelength in meters.

The result of (8.5) is plotted in Fig. 8.15 as Curve (a). For comparison purposes, the composite quality factor ($\tilde{Q}$) as computed by (8.3) is also shown in the same figure as Curve (b). The ratio of $\tilde{Q}/Q'$ is presented in Fig. 8.16, showing that Q' approaches closer to $\tilde{Q}$ for higher frequencies where more modes are available and the field strength inside the chamber is relatively more uniform.

The maximum and average electric-field strengths generated inside the chamber, as adjusted to 1-W net input power, are presented in Fig. 8.17 as a function of frequency. The field strengths were measured using an electric-field probe (1-cm dipole) placed at the center of the test zone, with 200 tuner positions. The probe was rotated through three orthogonal orientations aligned with the chamber axes. The magnitude of the total electric field was taken as the square root of the sum of the squared values of the three components. The probe response was calibrated in a planar field environment at frequencies up to 2.4 GHz. The field strengths at frequencies above 2.4 GHz were also determined by using the same probe response.

An increase in field strength at approximately 15 GHz as shown in Fig. 8.17 is believed due to the probe resonant characteristic rather than due to the chamber. It can be corrected, if necessary, by recalibrating the probe at 15 GHz. Also included in Fig. 8.17 are the field strengths calculated from the power P_r received by the reference antenna in accordance with the following:

$$E_c = \frac{4\pi}{\lambda} (30P_r)^{1/2} \qquad \text{V/m} \qquad . \tag{8.6}$$

The above expression was derived based on the assumption of far-field environment. Obviously, such condition does not exist inside a multimode chamber. The expression has been used frequently within the EMC community even though it has received only marginal justification [1]. The results presented in Fig. 8.17, however, demonstrate good agreement between the direct measurements and that derived from (8.6). To increase further our own confidence, we also independently measure the maximum, average, and minimum magnetic-field strengths with a magnetic-field probe (a loop antenna of 1-cm diameter) in a similar manner. The corresponding ratios of the electric field to the magnetic field may be loosely referred to as wave impedances. Results for the wave impedance are given in Fig. 8.18, showing wide variations, as expected, with frequency. However, the average wave impedance at frequencies above 200 MHz (the lower frequency limit recommended for the NBS chamber) is approximately 120π. This serves as an additional check to the validity of (8.6). Thus, it appears that (8.6) can be used as a preliminary means to determine the level of the test field.

It is important to note that the reference antenna type is not significant, except that it is desirable to have its impedance reasonably matched to the power detector, especially for high frequencies when more modes are available in the chamber, so that its average VSWR behaves well. Hence, antennas within their designed frequency bands may be used as a reference. Their gain characteristics are rather unimportant.

After a reverberating chamber is designed and its basic characteristics determined as outlined above, the radiated susceptibility measurements can be performed by placing the EUT at the test zone, routing its control cables to monitors outside the chamber, and preventing leakage to the exterior environment by using proper filtering processes, if needed. A test field has, of course, to be generated first by supplying power to the transmitting antenna. The desired field level may be established, as required, by gradually increasing the input power. The EUT operation is monitored for malfunction while the tuner/stirrer is rotated through a complete revolution. The rotating rate should be slow enough to allow sufficient time for the EUT to respond to the change in test-field level. If a malfunction of EUT is observed for a particular tuner/stirrer position, the tuner/stirrer should be stopped and the net power to the transmitting antenna should be reduced until the malfunction ceases. The test results are then recorded and the test proceeds to the next frequency, etc., until the test is completed.

Radiated emission measurements are performed in a fashion reciprocal to susceptibility measurement or by using a substitution technique. In this case, the transmitting antenna is removed from the chamber because the EUT itself is the radiator. The power received by the reference antenna may be measured and used to determine the total power radiated by the EUT with the aid of the chamber quality factor (8.5), or the equivalent radiated far field by (8.6). Alternatively, the power radiated by the EUT may also be determined by measuring the equivalent power applied to a transmitting antenna substituting for the EUT, provided, of course, the same power is received by the reference antenna.

REFERENCES

[1] Bean, J. L.; Hall, R. A. Electromagnetic susceptibility measurements using a mode-stirred chamber. IEEE Int. Symp. on EMC; June 1978; Atlanta, GA.

[2] Corona, P. Electromagnetic reverberating enclosures: behavior and applications. Alta Frequ., 49, 54-158; 1980.

[3] Corona, P.; Latmiral, G.; Paolini, E.; Piccioli, L. Performance of a reverberating enclosure for power measurements in the microwave range. Proc. second Symp. Tech. Exhibition on EMC; 1977; Montreux, Switzerland. 419-423.

[4] Corona, P.; DeBonitatibus, A.; Ferrara, G.; Paolini, E. Electromagnetic enclosures behavior -- comparison data analysis. Proc. third Symp. Tech. Exhibition on EMC; 1979; Zurich, Switzerland. 231-236.

[5] Corona, P.; Latmiral, G.; Paolini, E. Performance and analysis of a reverberating enclosure with variable geometry. IEEE Trans. Electromag. Compat. EMC-22(1): 2-5; 1980 February.

[6] Corona, P.; Latmiral, G.; Paolini, E.; Piccioli, L. Use of a reverberating enclosure for measurements of radiated power in the microwave range. IEEE Trans. Electromag. Compat. EMC-18(2): 54-59; 1976 May.

[7] Liu, B. H.; Chang, D. C.; Ma, M. T. Eigenmodes and the composite quality factor of a reverberating chamber. Nat. Bur. Stand. (U.S.) Tech. Note 1066; 1983 August.

[8] Liu, B. H.; Chang, D. C.; Ma, M. T. Design consideration of reverberating chambers for electromagnetic interference measurements. IEEE Int. Symp. on EMC; 1983 August. Arlington, VA.

[9] Mendez, H. A. A new approach to electromagnetic field-strength measurements in shielded enclosures. Wescon Record; Los Angeles, CA; 1968 August.

[10] Harrington, R. F. Time-Harmonic Electromagnetic Fields, New York, NY: McGraw-Hill; 1961.

[11] Roe, J. M. An improved technological basis for radiated susceptibility and emission specifications. IEEE Int. Symp. on EMC; 1978 June; Atlanta, GA.

[12] Crawford, M. L. Evaluation of a reverberating chamber facility for performing EM radiated field susceptibility measurements. Nat. Bur. Stand. (U.S.) Int. Rept. 81-1638; 1981 February.

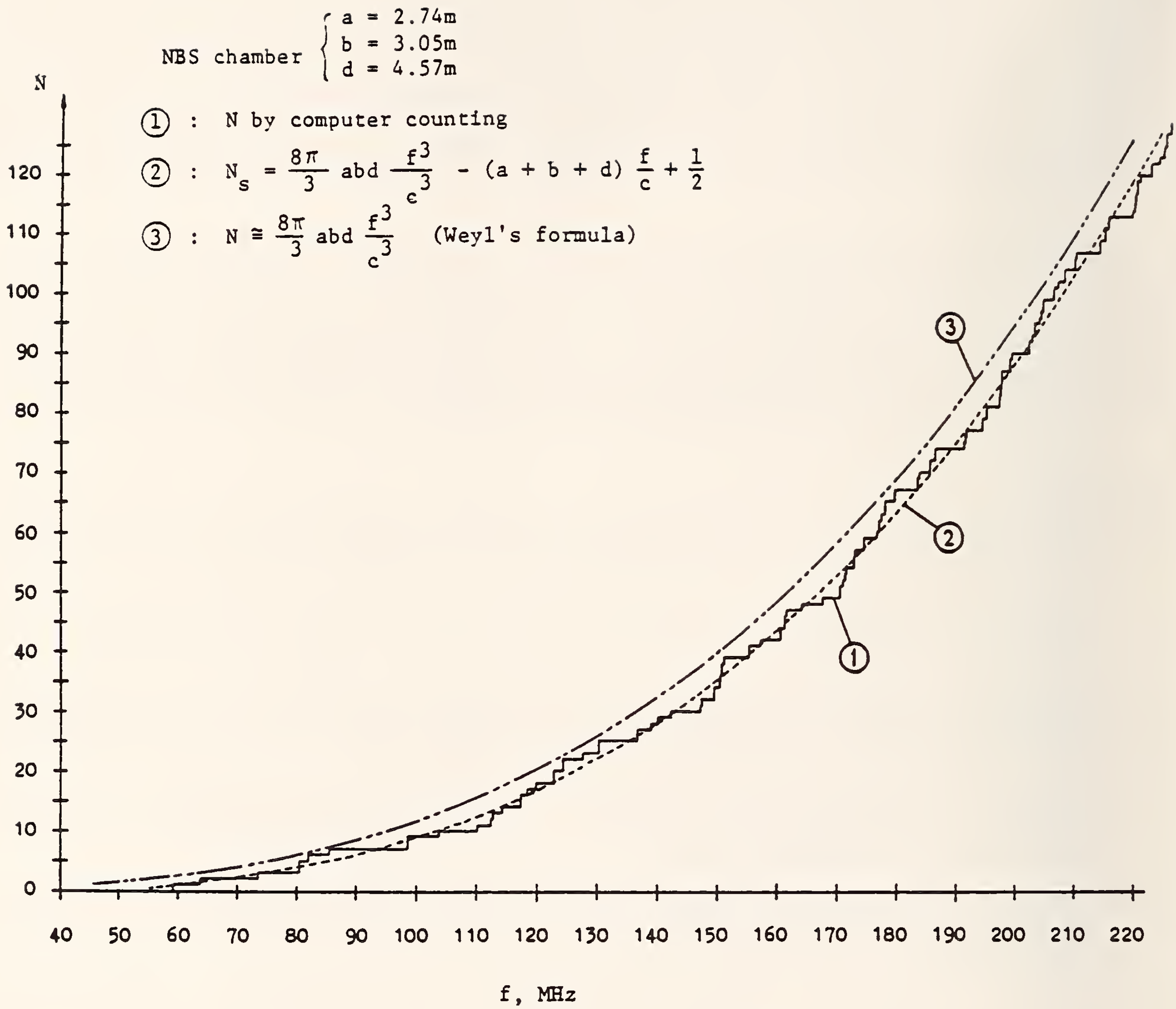

Figure 8.1 Total number of modes as a function of operating frequency for the NBS chamber.

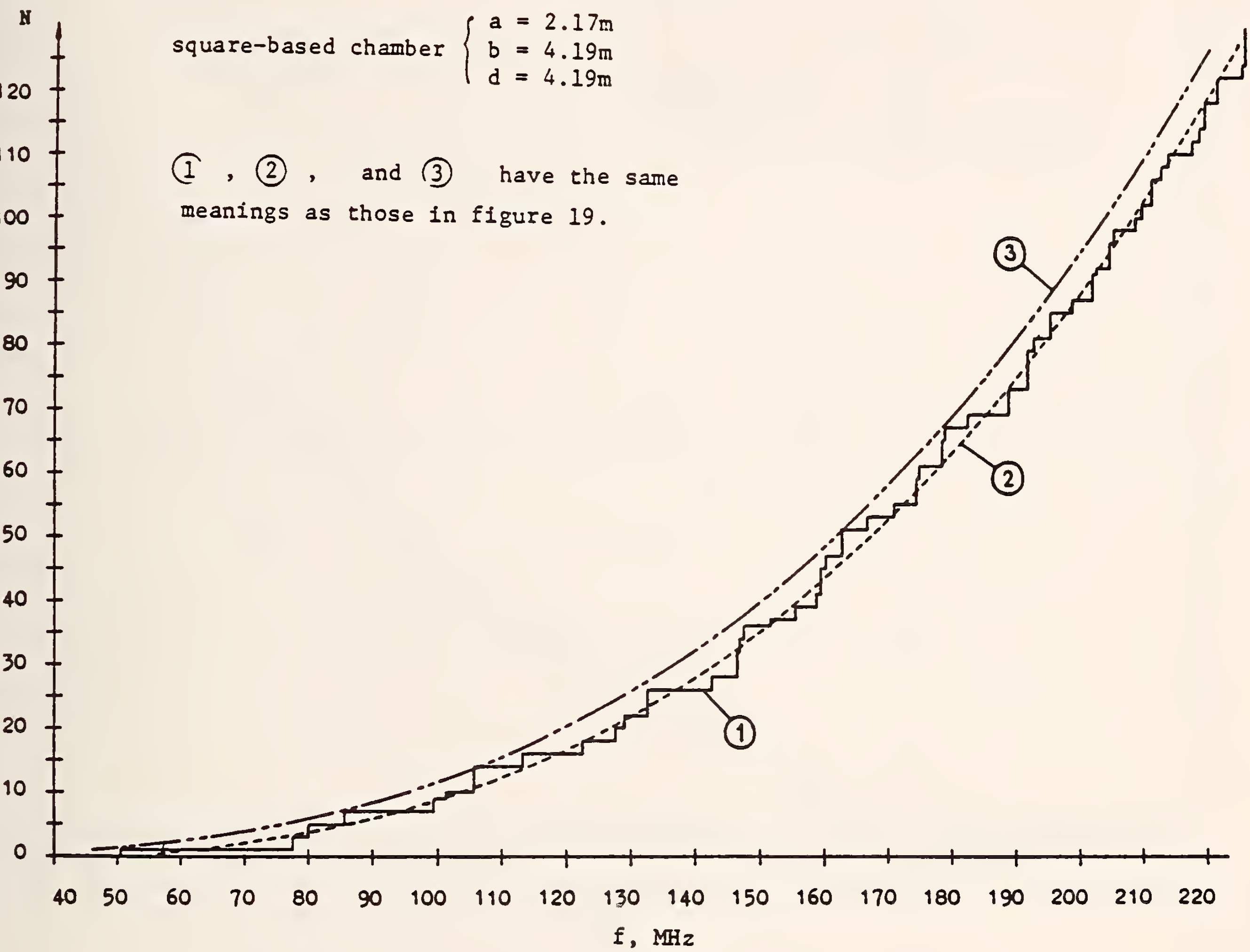

Figure 8.2 Total number of modes as a function of operating frequency for a square-based chamber whose volume is the same as that of NBS chamber.

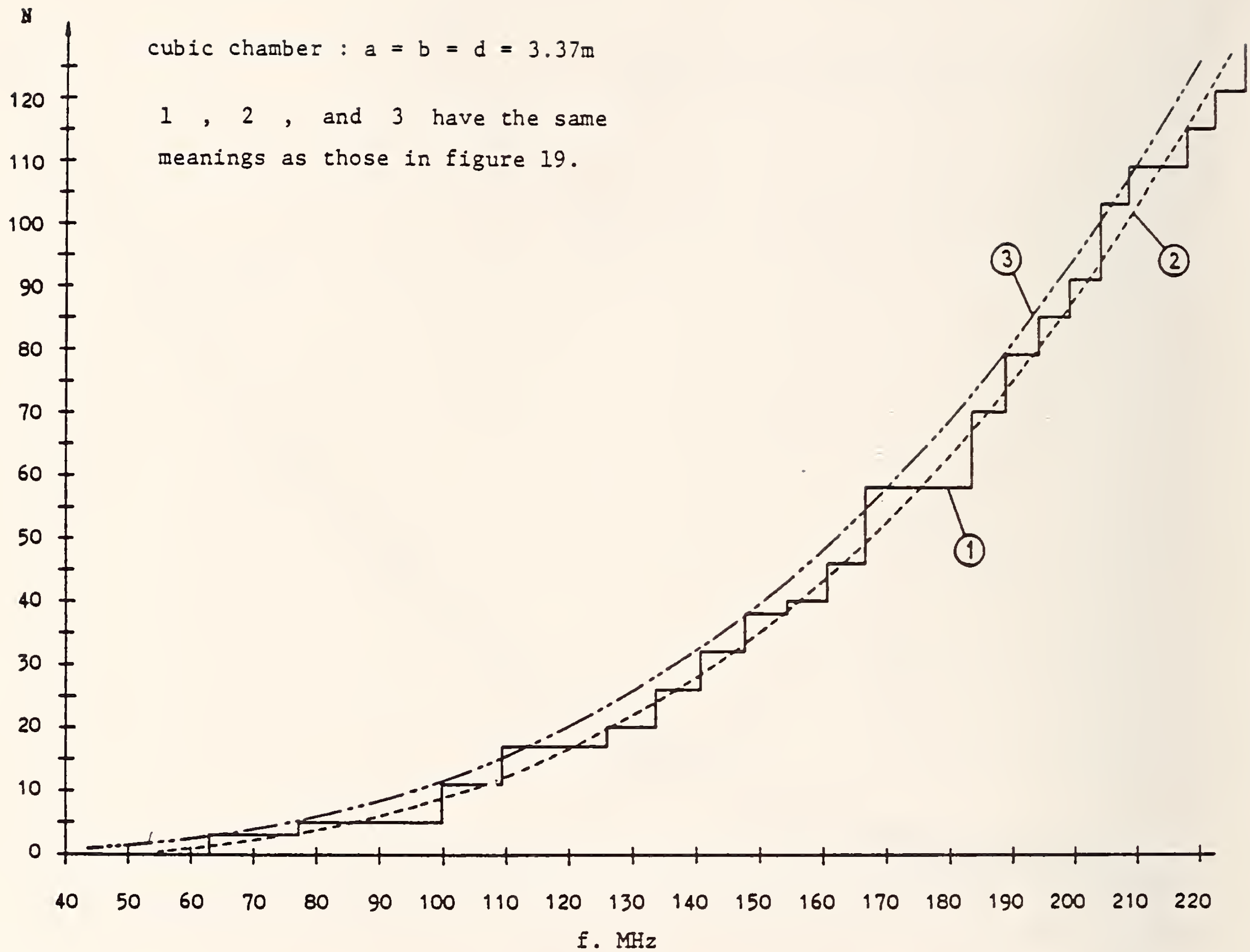

Figure 8.3 Total number of modes as a function of operating frequency for a cubic chamber whose volume is the same as that of NBS chamber.

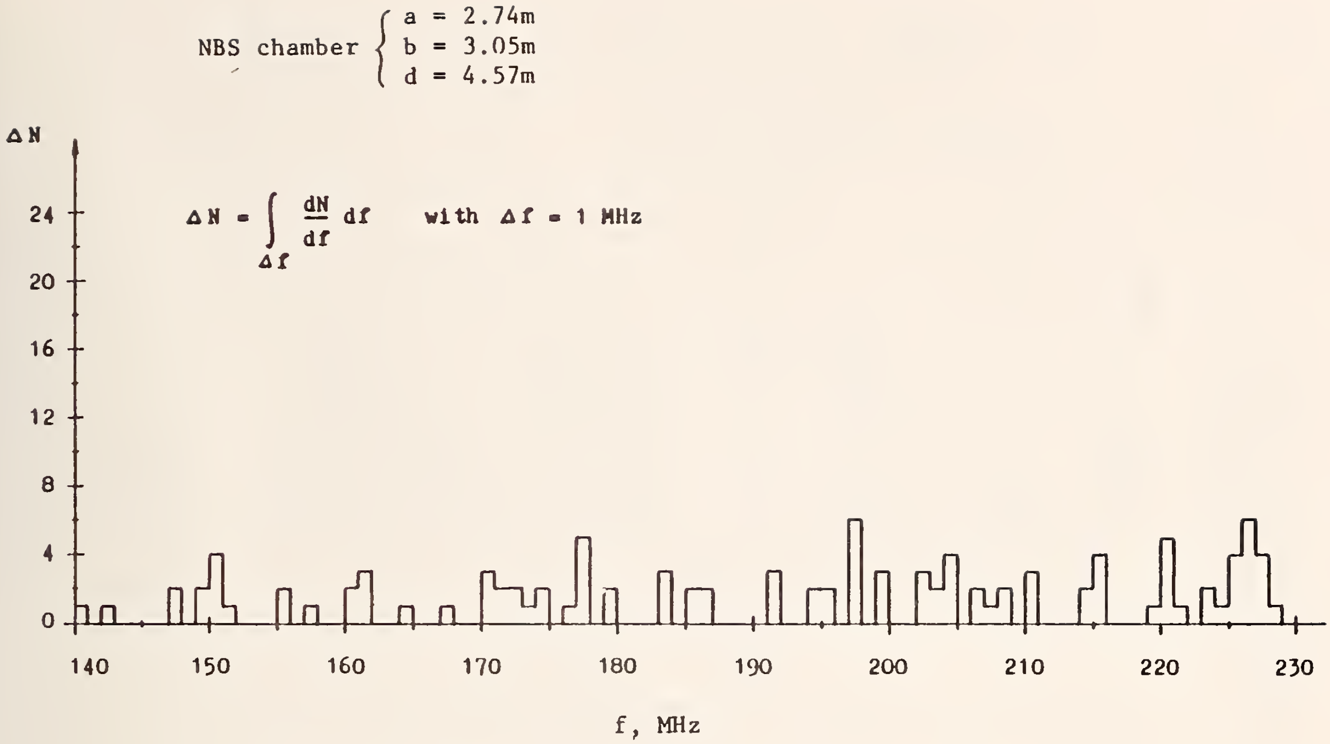

Figure 8.4 An illustration of mode degeneracy (NBS chamber).

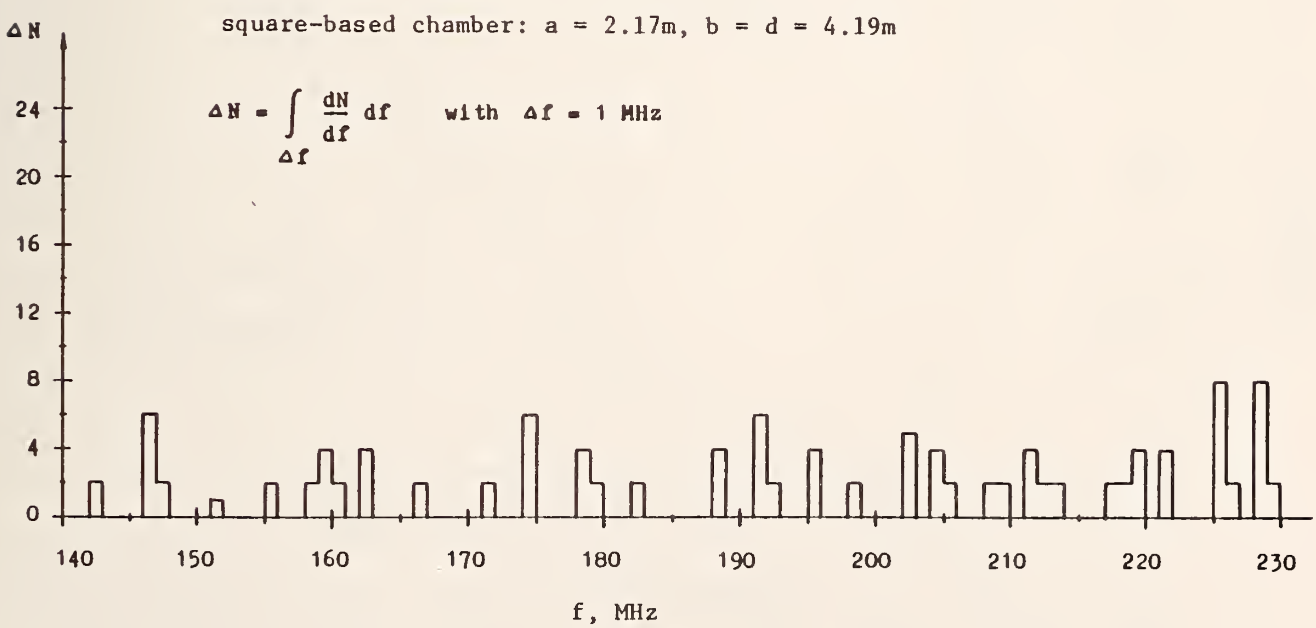

Figure 8.5 An illustration of mode degeneracy (square-based chamber).

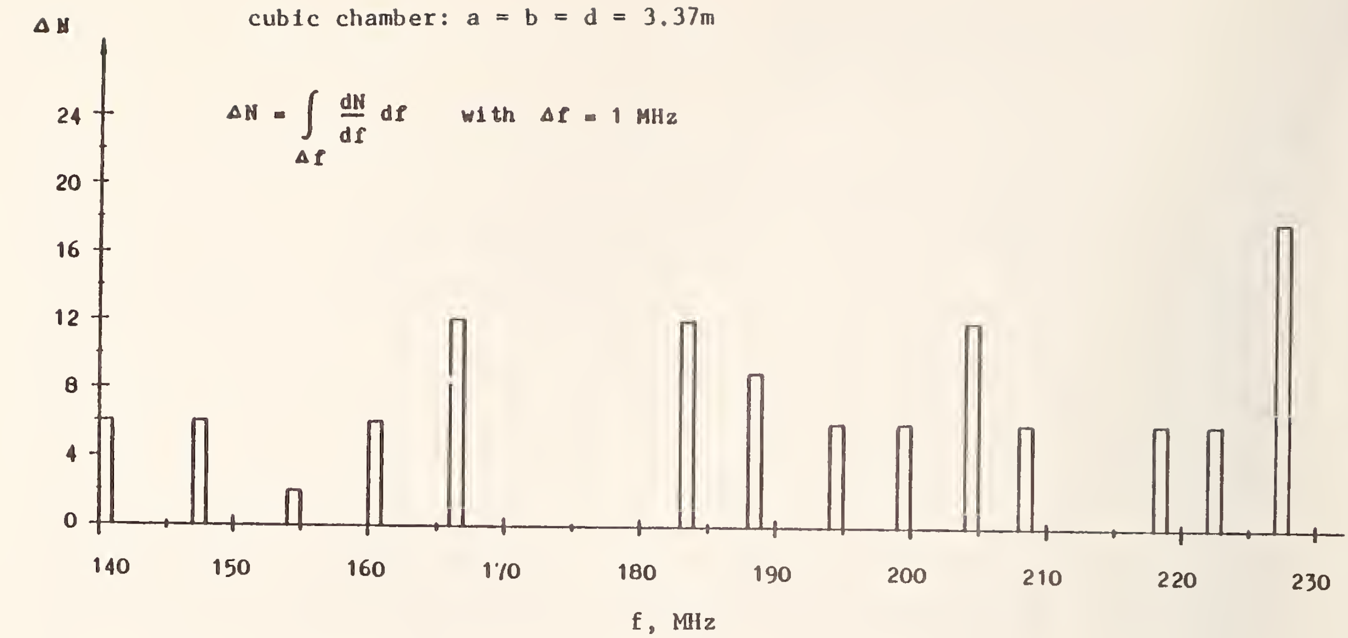

Figure 8.6 An illustration of mode degeneracy (cubic chamber).

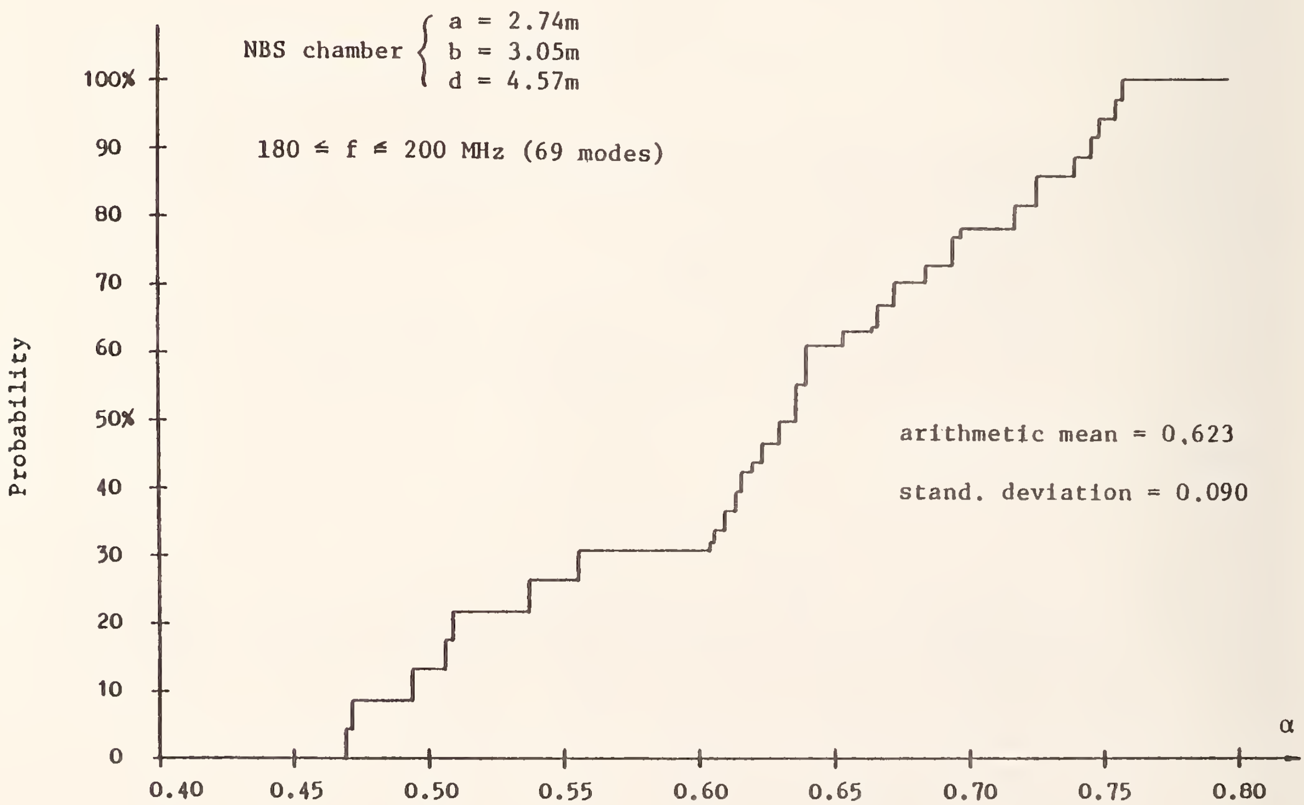

Figure 8.7 Cumulative distribution curve of the normalized 1/Q values in the 180-MHz to 200-MHz frequency band for the NBS chamber.

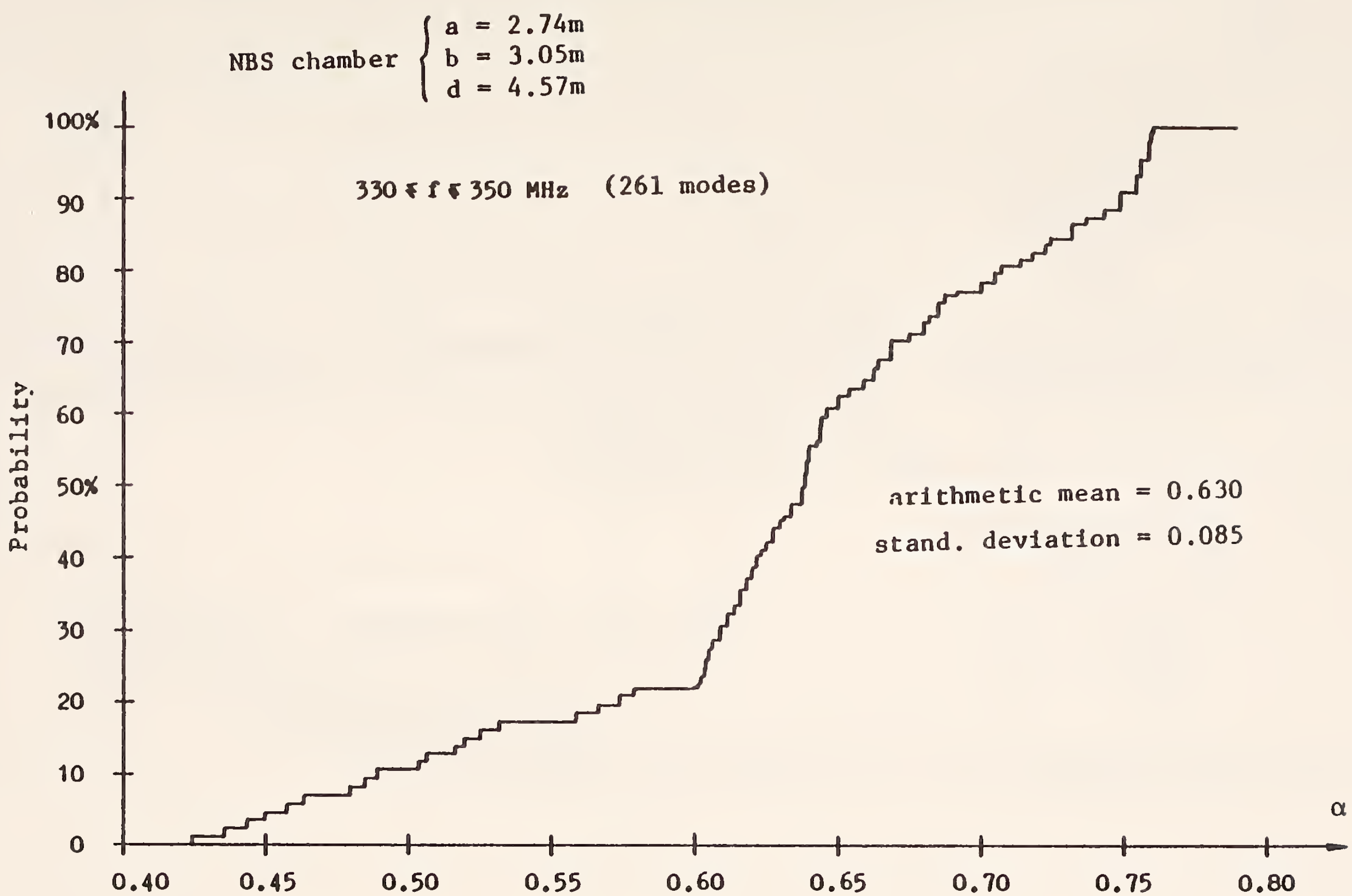

Figure 8.8 Cumulative distribution curve of the normalized 1/Q values in the 330-MHz to 350-MHz frequency band for the NBS chamber.

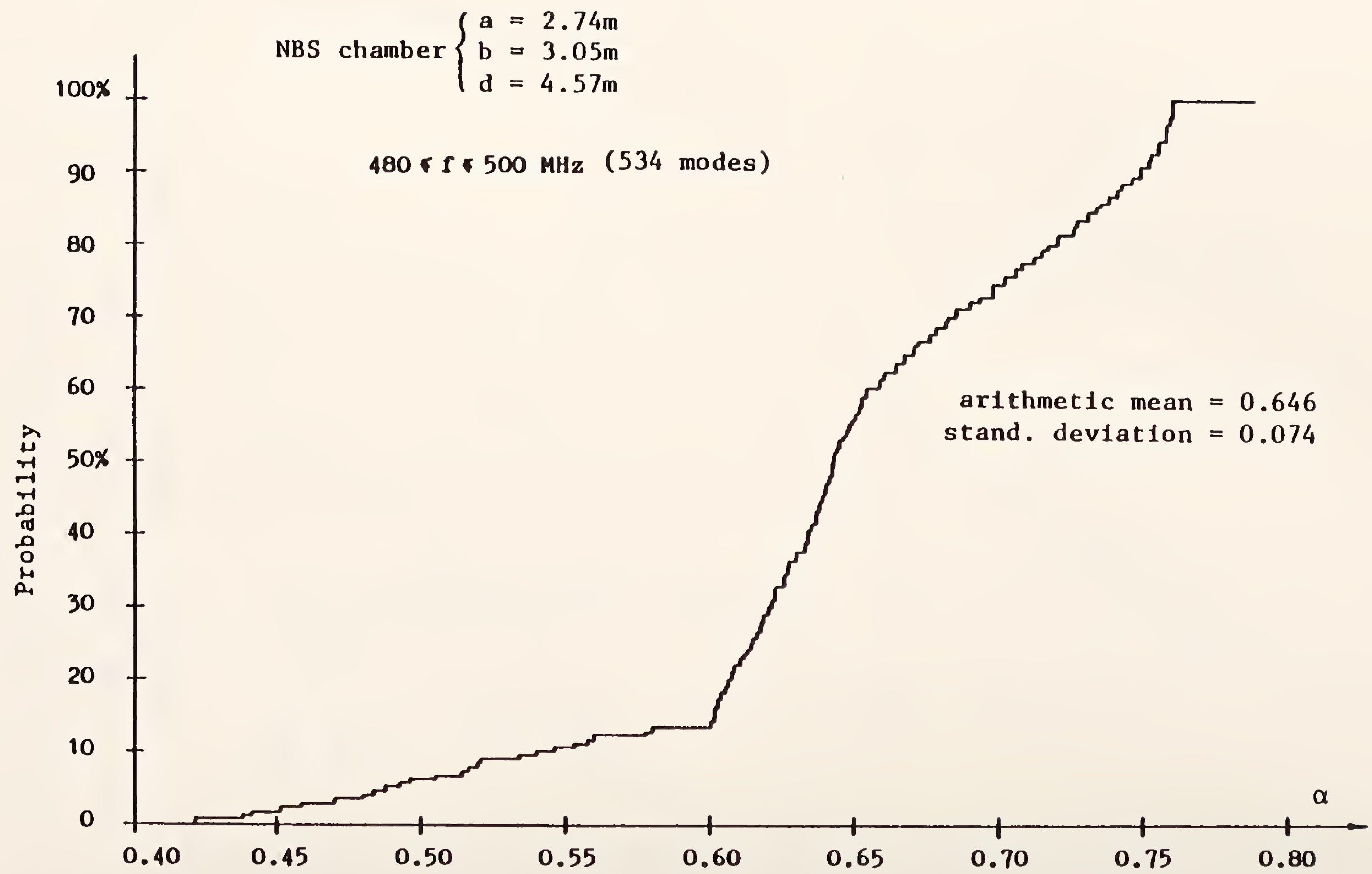

Figure 8.9 Cumulative distribution curve of the normalized 1/Q values in the 480-MHz to 500-MHz frequency band for the NBS chamber.

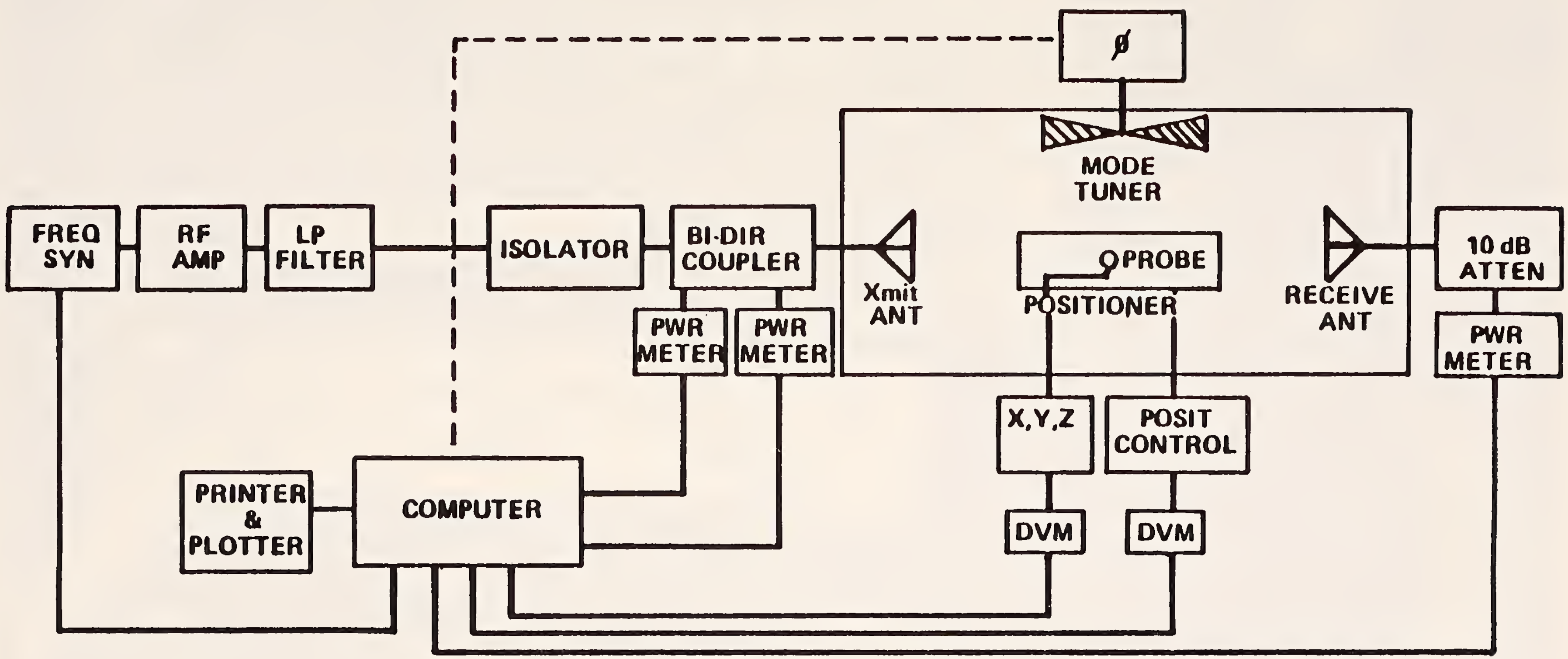

Figure 8.10 Block diagram of NBS modified mode-tuned enclosure system for EMC measurements.

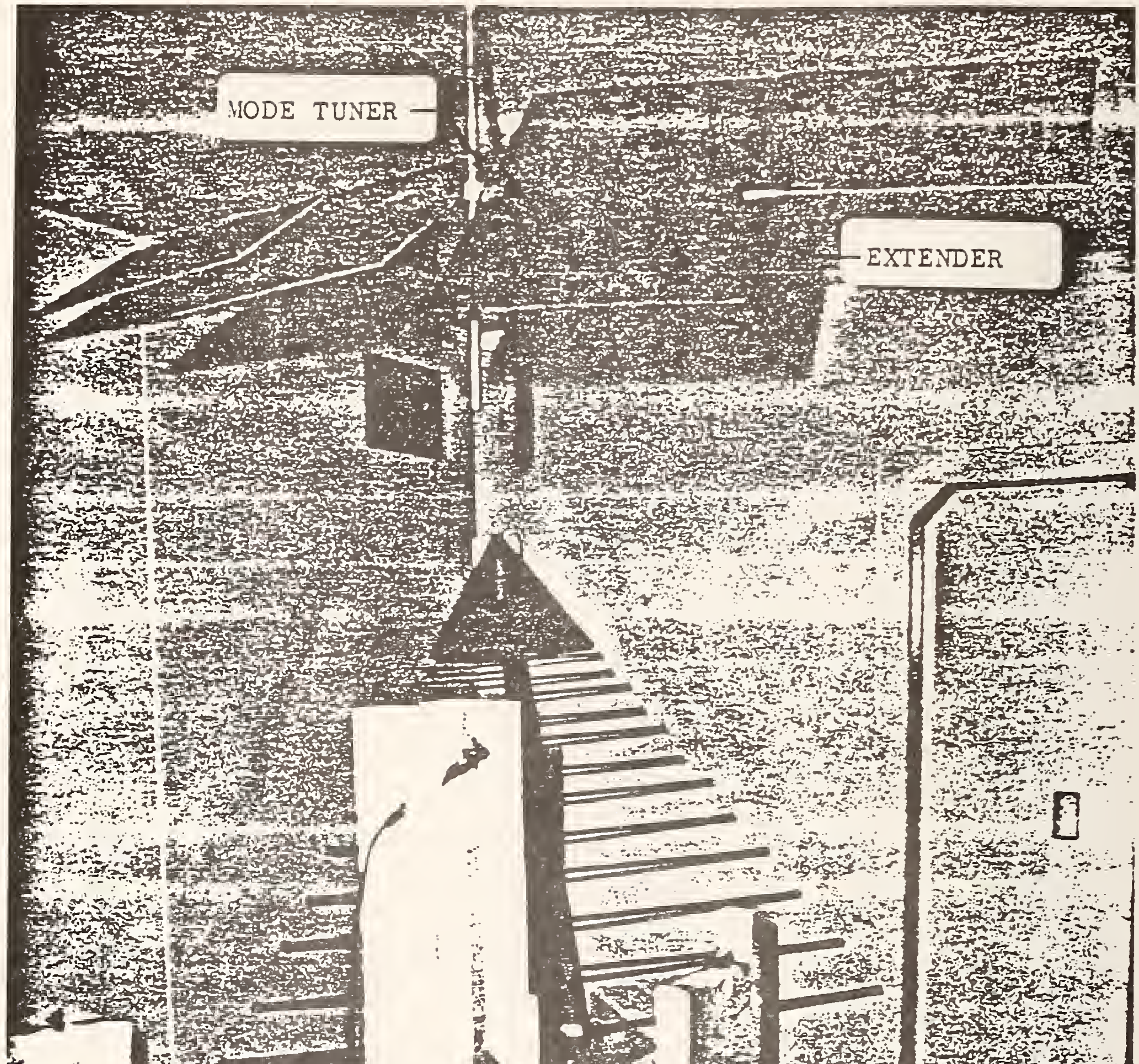

Figure 8.11 Photograph of tuner inside NBS reverberating chamber.

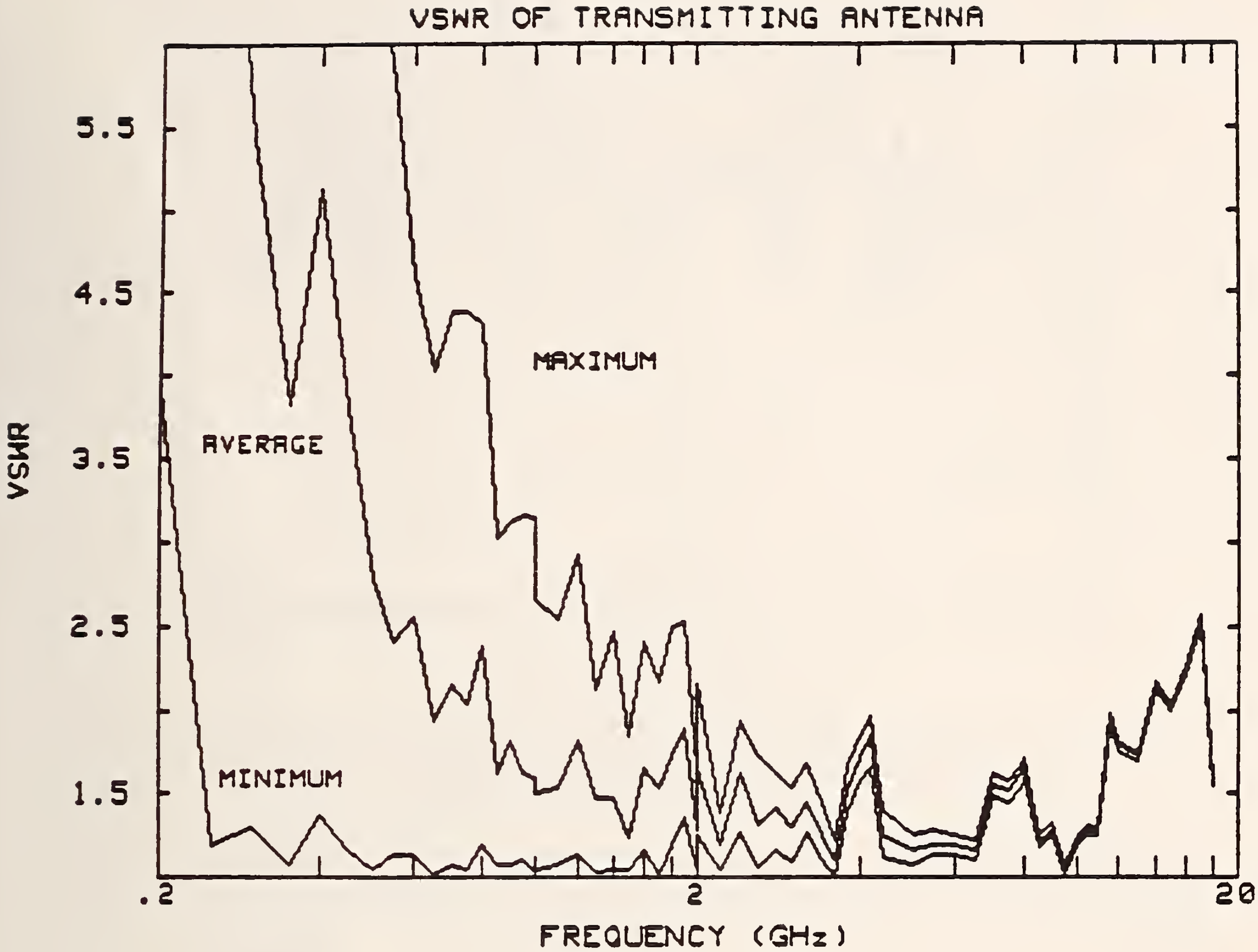

Figure 8.12 Variations in VSWR of transmitting antennas placed inside the NBS reverberating chamber.

Log-periodic: 0.2 - 1.0 GHz,

Corrugated horn: 1.0 - 4.0 GHz,

Double-ridged circular horn: 4.0 - 18.0 GHz.

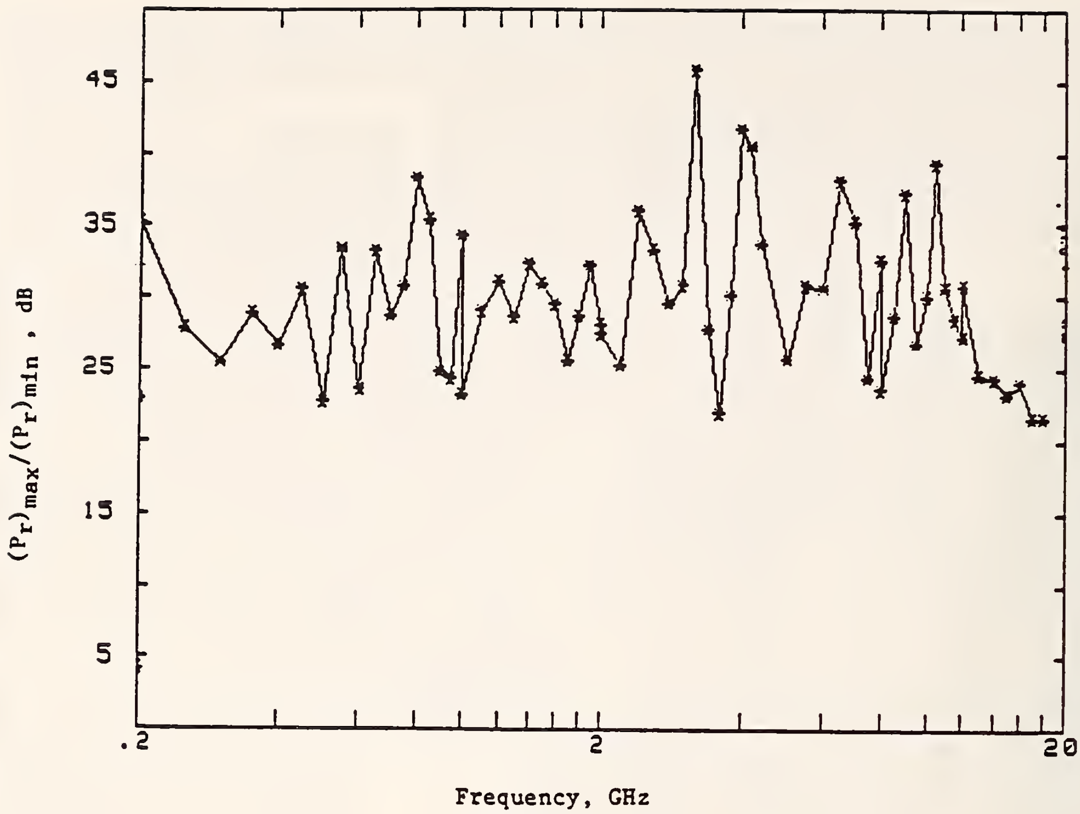

Figure 8.13 Maximum to minimum received power ratio as a function of frequency for the NBS chamber and tuner.

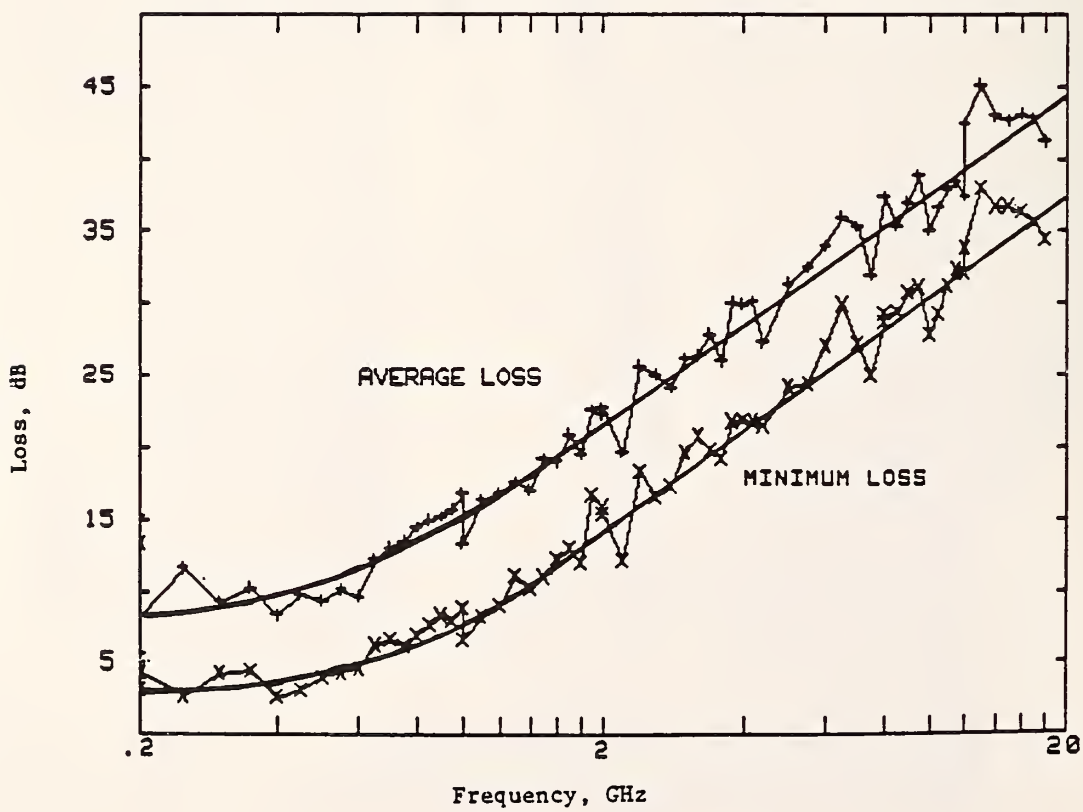

Figure 8.14 Loss characteristics for the NBS chamber (empty) with the smooth solid curves representing estimated fits from the measured data.

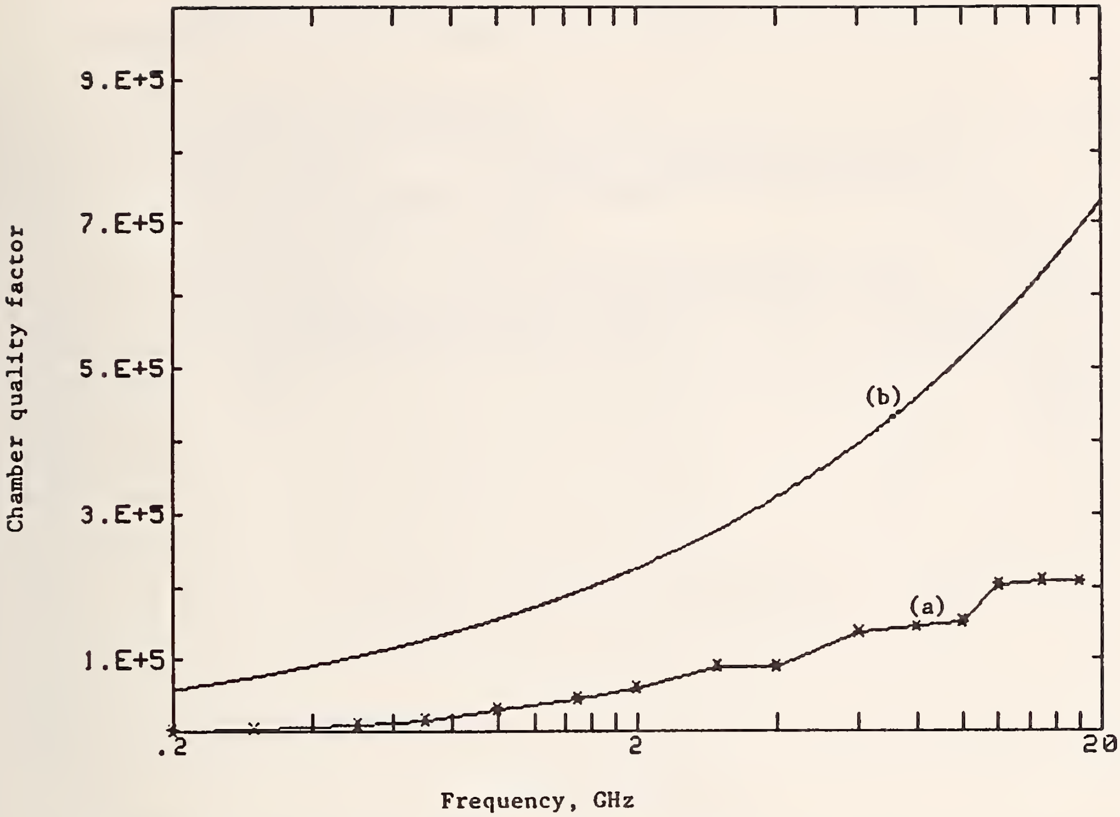

Figure 8.15 Quality factor of the NBS chamber: (a) experimental mean Q' obtained from (8.5) based on measured received power, and (b) theoretical composite $\tilde{Q}$ as compared from (8.3).

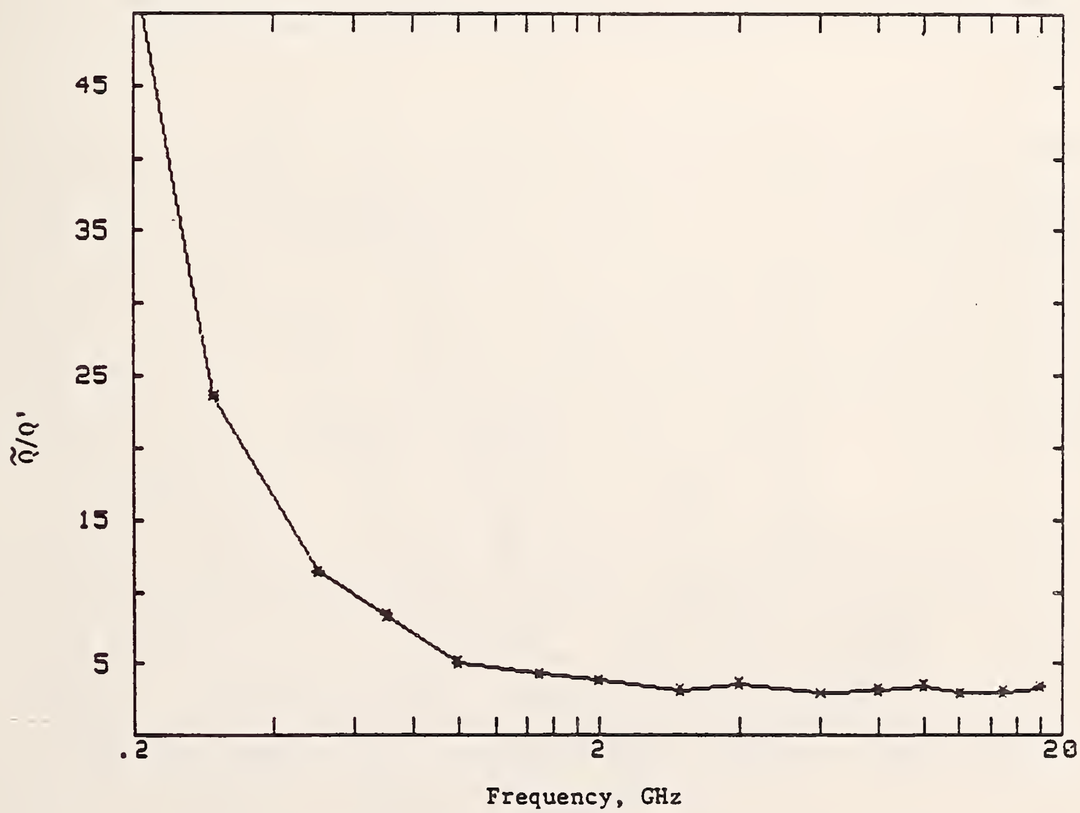

Figure 8.16 Ratio of theoretical composite $\tilde{Q}$ to experimental mean Q'.

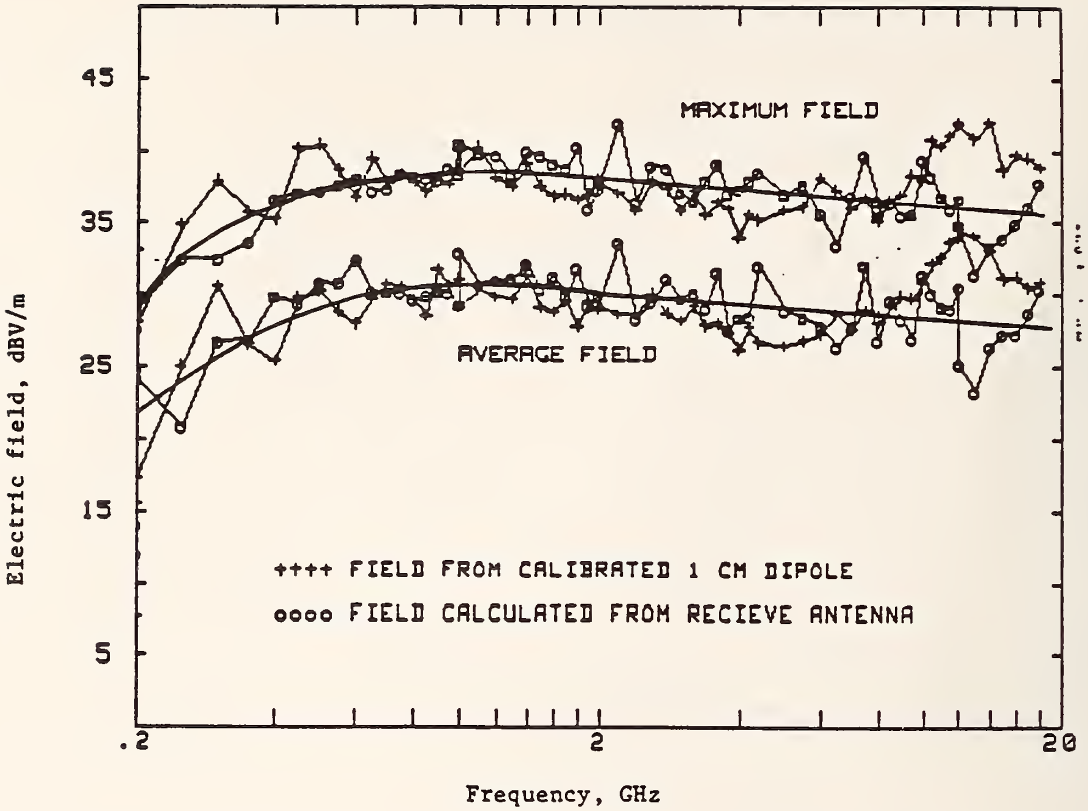

Figure 8.17 Maximum and average electric-field strengths generated inside the NBS chamber (empty, mode-tuned).

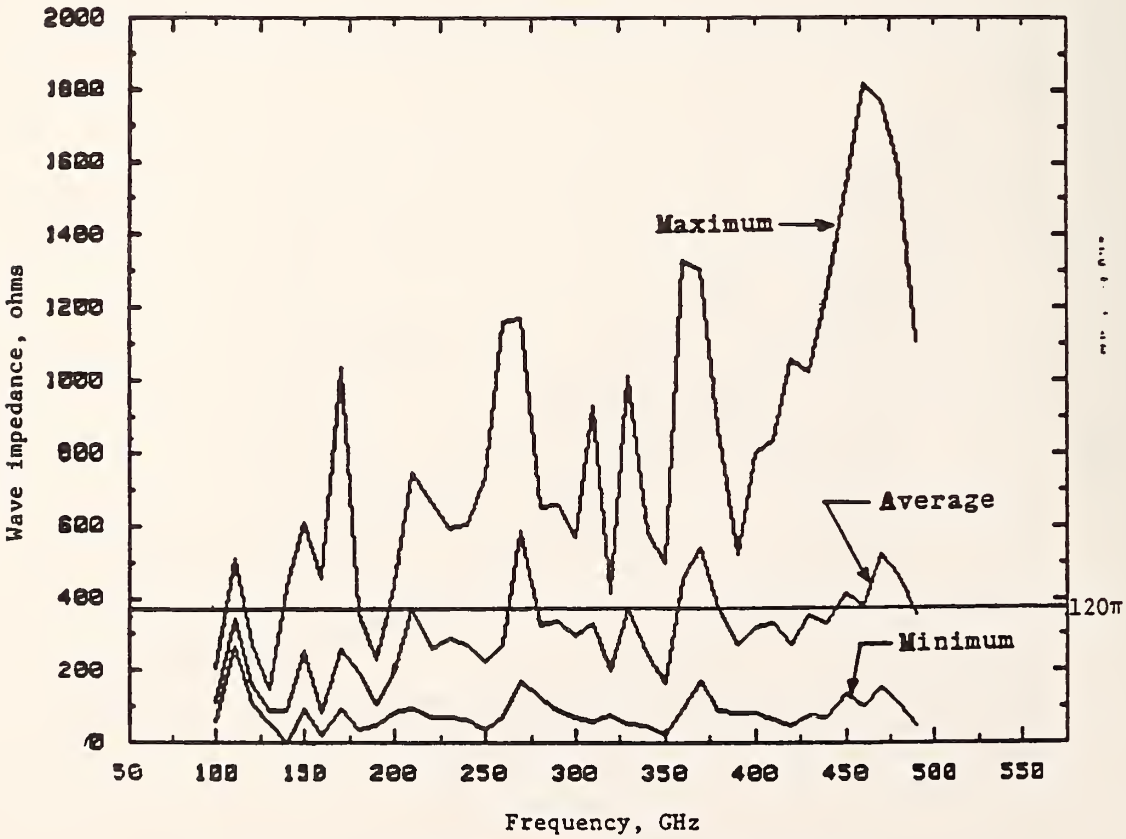

Figure 8.18 Wave impedance of the NBS chamber.

9.a MEASUREMENTS IN, AND OF, COMPLICATED ELECTROMAGNETIC ENVIRONMENTS

It is quite appropriate that the subject of complex EM environments occurs in the Contemporary EMC Topics chapter of this short course, for it will present more problems than solutions. The field is still in its infancy, and many of the problems are not yet even well-defined, much less solved. Nevertheless, it is a very important area in EMI/EMC, and one that cannot be ignored.

The standard methods of electromagnetics tend to assume and exploit various simplifying features such as single frequency, single source, plane-wave fields, simple geometry, etc. There are a number of good, valid reasons for making such assumptions: a) it may be pedagogically desirable to keep examples free of non-essential complications; b) simplifying assumptions may be necessary in order to solve a problem at all (Some problems are just intractably complex.); c) for linear problems, the multiple-frequency solution can be constructed by the superposition of single-frequency solutions; d) in design problems, for example, one is free to choose simple geometries if they permit the design of the device or system desired. However, complicated problems do still exist. The real world is full of EM environments with multiple (often unknown) sources, both primary sources and scatterers, with multiple frequencies and nonsinusoidal waveforms, complicated asymmetric geometries, near fields, and nonlinear devices or materials. These complex environments may involve sensitive electronics, ordnance, communication systems, and people. The problem is to develop methods of measuring and characterizing an EM environment so that one knows whether it will affect whatever goes into it. The question of just what EM characteristic is important (maximum electric field, average total power density, fraction of the time the field exceeds some threshold value, etc.) depends on the device or system, and is an interesting problem in itself. We will concentrate on how and what does one measure in a complex EM environment.

Two separate questions will be addressed: how do probes react in a complex environment, and how can one obtain useful information from relatively few measurements. In treating probe response, we first consider actual errors in a meter for measuring the electric field and then the errors inherent in trying to measure total power density using a probe which is sensitive only to either the electric or the magnetic field, but not both. This problem will be discussed in Section 9.a.1. Section 9.a.2 is devoted to measuring characteristics of complex environments. The primary emphasis is on a statistical approach, but we also briefly mention other approaches currently under development.

9.a.1 An Electric-Field Meter (EFM) in a Complex Environment

A. Meter Errors This section will follow closely the treatment of [1], to which the reader is referred for details and derivations. We consider first the errors in the electric field actually measured. EFM's are typically calibrated using single-frequency, single-source standard fields, and their response to more complex fields can be different than for the calibrating fields. The type of EFM we have analyzed is a common (see e.g., [2]) configuration exemplified by, but not restricted to, the NBS EFM-5 [3]. (When specific values of meter parameters were needed, those of the EFM-5 were used. The qualitative results, however, apply to any meter sharing the same design.) The meter consists of a short dipole antenna with a diode detector as a probe, with a transmission line connecting it to the box containing the metering electronics. For an isotropic probe, three orthogonal dipole antennas are used, each with its own independent transmission line within the cable joining probe and box. Details are described in Chapter 7.

Because the dipole antenna is short compared to the wavelengths of the radiation being measured, the electric field does not vary significantly over the volume of the probe, so that it effectively is sensitive to the electric field at a single point as a function of time, $\bar{E}(\bar{x} = 0, t)$. An important consequence follows immediately: for meter errors the number of sources is immaterial, and all that matters is the temporal waveform of the electric field at the probe position. Only if the field's time dependence is a single sinusoid is the probe operating under the calibrating conditions. A corollary result is that the presence of reflections does not introduce new multiple-source and frequency errors since they have the same frequency as the field from the primary source and combine with it to yield a net $\bar{E}(\bar{x} = 0, t)$ which is still a single sinusoid in time.

When the incident field at the probe position does not have a single sinusoid for its temporal waveform, errors arise from a collusion of the nonlinear response of the diode detector and the filtering effect of the transmission line. The antenna plus diode plus transmission line can be represented by the equivalent circuit of Fig. 9.a.1. The filter line is represented only by a black box which is assumed to transmit dc, filter RF, and have little effect on the effective load of the antenna. The input voltage $v_i(t)$ is proportional to the electric field at the probe position; and an expression for the output voltage $v_o(t)$ can be obtained in terms of the input voltage and three parameters of the antenna-diode combination. The three parameters are an effective time constant (a^{-1}) and two voltage scales (b^{-1}, α^{-1}), which for the EFM-5 have the values

$$a = 33.8 \text{ kHz}, \quad b = 4.22 \text{ V}^{-1}, \quad \alpha = 38 \text{ V}^{-1}. \tag{9.a.1}$$

Provided the input signal is periodic, with period (p) short compared to a^{-1} ($ap << 1$), the voltage across the diode can be written

$$v_d(t) \approx b\,\alpha^{-1}\,\tilde{v}_i(t) - \alpha^{-1}\,\ell n\left\{p^{-1}\int_0^p e^{b\,\tilde{v}_i(t')}dt'\right\}$$

$$\tilde{v}_i(t) = v_i(t) - \langle v_i\rangle \qquad . \tag{9.a.2}$$

Note that the argument of the logarithm is time-independent, which is not true at lower frequencies. The effect of the filter line then is to remove the RF component of $v_d(t)$, resulting in an output signal of

$$v_o(t) \approx -\,\alpha^{-1}\,\ell n\left\{\int_0^1 e^{b\,\tilde{v}_i(t' = xp)}dx\right\} \qquad . \tag{9.a.3}$$

In the limiting cases of small or large incident fields ($b|\tilde{v}_i|_{max} << 1$ and $b(\tilde{v}_i)_{max} >> 1$ respectively), the output voltage assumes the simple forms

$$v_o \approx -\,b^2(2\alpha)^{-1}\,\langle\tilde{v}_i^{\,2}\rangle \qquad \text{for small } |E_i|,$$

$$\approx -\,b\,\alpha^{-1}\,\tilde{V}_i \qquad \text{for large } |E_i|, \tag{9.a.4}$$

where $\tilde{V}_i$ is the peak value of $\tilde{v}_i(t)$. These are the usual square-law and linear regimes; the crucial point is that the square-law and linear dependences are on different variables. For small incident fields, the signal reaching the meter is directly proportional to the average of $(E_i - \langle E_i\rangle)^2$, and completely insensitive to the peak value, whereas for large incident fields the opposite is true. Therefore, only the average reading need be correct for small fields and only the peak reading for large fields (both assuming $\tilde{v}_i = v_i$). For intermediate-magnitude incident fields, neither peak nor average reading need be correct. The magnitude of the meter error depends on the actual waveform, the field intensity, and whether peak or average is measured.

In order to compute the error for a given $E_i(t)$ [and hence $v_i(t)$], we first use (9.a.3) to calculate the resulting output voltage v_o. We then find the value of V such that an input voltage of V cosωt would produce the same v_o. Since the meter was calibrated with a single sinusoid, it associates V cos ωt with v_o, and it will read V_{pk}(meter) = V and V_{avg}(meter) = $(V^2/2)^{1/2}$. The errors in peak and average readings for E^2 are therefore given by

$$\Delta_{pk} = 10 \log\,(v_{i\,max}^2/V^2) \qquad ,$$

$$\Delta_{avg} = 10 \log\,(\langle v_i^2\rangle/0.5V^2) \qquad . \tag{9.a.5}$$

The errors calculated in this manner for a few representative waveforms are shown in Figs.9.a.2 -9.a.4. In each case, Δ_{avg}, the dB error in the average E^2, is plotted as a function of incident field strength. The Δ_{pk} value is related to Δ_{avg}, as given in the figure captions. For a waveform like a narrow pulse, the error in the measured peak or average strength can be as large as 10 dB, but more typical values are on the order of 2 dB. These results are frequency-independent, provided $a\rho \ll 1$ ($f > 1$ MHz for the EFM-5).

We also investigated the case of various numbers of randomly distributed sources with different strengths and frequencies, finding that the average meter error was around 2 to 4 dB, but that the maximum possible errors were much larger.

A few qualifications and clarifications of these results should be noted. The first point is that our analysis is only valid for incident fields with periods which are short relative to a certain characteristic time scale of the antenna plus diode. For longer-period signals including those with only high-frequency Fourier components such as AM radio, our analysis does not apply. In addition, even for short periods, it is quite possible with the EFM configuration considered here to choose the meter parameters such that one is always effectively in the large-field domain or always in the small-field region; and therefore it is possible for the meter to measure accurately <u>either</u> the peak field <u>or</u> the average field squared, even for complex, multifrequency fields. It is <u>not</u>, however, possible to measure both peak and average with a single probe of this configuration, and meters which try to do so will err on one or the other (or both) at any given field strength.

B. <u>Energy-Density Inference Errors</u> Meters which only measure either the electric or the magnetic field cannot measure the true total EM energy density. That requires simultaneous measurement of both electric and magnetic fields. In order to infer a total energy density from a measurement of either the electric- or magnetic-field strength, some relationship between electric and magnetic energy densities must be assumed. The assumption usually made is that the two are equal, as is true for a single plane wave. This section considers the errors involved in that assumption.

We define

$$\Delta(E/H) = 10 \log (2u_E/u_{tot}) = 10 \log \frac{2|\bar{E}|^2}{|\bar{E}|^2 + (\mu/\varepsilon)|\bar{H}|^2} , \qquad (9.a.6)$$

where u_E and u_{tot} are the electric-field and total energy densities respectively. It is clear that this "error" is a property of the environment and not of the meter used; in fact we shall assume that the electric field is known exactly. Thus, $\Delta(E/H)$ represents the deviation between $(u_E + u_H)$ and $2u_E$, expressed in dB. In the near field of an antenna (or reflecting surface), it is well known that this error can be large, e.g., in the near field of an antenna one can find $|\bar{H}|^2/|\bar{E}|^2 \to \infty$. Such near-field problems are well known, and we shall not belabor them. The question we address is the size of $\Delta(E/H)$ when there are a number of plane waves present, i.e., multiple sources and/or reflections. The results for these situations are less obvious and less well known.

The energy-density errors have been studied for both peak and average energy-density measurements, for numbers of plane-wave sources ranging from two to twenty. For more than two sources, it is impractical to use anything other than a statistical approach, since the error depends on so many variables such as the relative strengths, phases, polarizations, directions of arrival, and frequencies. Accordingly, for each number of sources we have generated 100 or 1000 random configurations (directions, magnitudes, etc.) and computed the mean, standard deviation, and the extreme values of $\Delta_{pk}(E/H)$ and $\Delta_{avg}(E/H)$.

For the average energy density, there is <u>no</u> error if no two sources have the same frequency. The errors are largest when all sources have the same frequency, as with multiple reflections for example. Results for all sources having equal frequency are shown in Fig. 9.a.5. For each number of sources, 1000 random configurations were generated, and the mean and standard deviation of $\Delta_{avg}(E/H)$ were computed for that ensemble. The typical errors were from -2 to +2 dB, but the extremes were -10 to -12 dB and +3 dB. This was true whether the sources were distributed in two or three dimensions.

For the error in the peak energy density, we used ensembles of 100 random configurations. (The computation requires considerably more time than that for Δ_{avg}.) Unlike Δ_{avg}, $\Delta_{pk}(E/H)$ is not zero when all the frequencies are different. Figure 9.a.6 contains results for $\Delta_{pk}(E/H)$. The mean of $\Delta_{pk}(E/H)$ tends to be around -0.3 dB with a standard deviation of 0.7 dB or less. If all frequencies are constrained to be equal, the standard deviation increases to around 2 dB.

9.a.2 Characterization of Complex Environments

A. <u>Generalities</u> We now turn to the problem of how to characterize an EM environment. In truth we are a long way from being able to do so comprehensively. The questions of what are the quantities or characteristics of interest will depend on what must function in the given environment. The important quantity could be the average total power density, the maximum electric or magnetic field, the fraction of the time the field level exceeds certain threshold value, etc. For some very important cases such as the human body, the quantity to which it is most sensitive is not even known yet. A complete characterization of the EM environment would amount to knowledge of the field at every point in space, which would require measurements throughout the volume at a spacing of no more than one half wavelength (for the maximum frequency present). That is usually impractical and almost never convenient. A direct solution of Maxwell's equations is not feasible either, particularly since one typically does not know the source.

Given this situation, most current work on the problem attempts to determine some potentially useful characteristics of the environment from a manageable number of measurements [4]. There is as yet no really "good" (systematic, efficient) method which is fully developed; but the field is still quite new, and progress is being made. We will discuss in a little detail a statistical approach to complex environments, and will briefly mention two other lines of attack.

B. <u>Statistical Approach</u> Statistical methods (see for example [5]-[7]) are the only methodical approach to be used in evaluating complex environments. In the absence of information about radiating sources or propagation paths, one treats the sources or paths as random variables of position or time. (A good pedagogical treatment is contained in [5].) If a large number of random sources contributes to the field at a given point and if the standard deviation of any one source is not too large, then one can apply the central limit theorem. It basically states that the sum of an infinite number of random variables has a gaussian probability distribution. Thus, if one component of the electric field is given by

$$E_x = X + jY = \sum_i A_i\, e^{j\phi_i} \quad , \tag{9.a.7}$$

where A_i and ϕ_i are random variables, then the probability distribution functions for the real and imaginary parts of E_x take the form

$$\begin{aligned} p(X) &= \frac{1}{(2\pi)^{1/2}\,\sigma_X} \exp[-(X - \bar{X})^2/2\,\sigma_X^2] \quad , \\ p(Y) &= \frac{1}{(2\pi)^{1/2}\,\sigma_Y} \exp[-(Y - \bar{Y})^2/2\,\sigma_Y^2] \quad , \end{aligned} \tag{9.a.8}$$

where $\bar{X}$, $\bar{Y}$, σ_X, σ_Y are determined by the distributions of the A_i and ϕ_i. In practice, these distributions are unknown. Provided the phases ϕ_i are uniformly distributed, (9.a.8) leads to a Rayleigh distribution for the magnitude of E_x,

$$\begin{aligned} p(|E_x|) &= \frac{2|E_x|}{\alpha} \exp[-|E_x|^2/\alpha] \quad , \\ p(|E_x| > E_o) &= \exp(-E_o^2/\alpha) \quad , \\ E_x^{rms} &= \sqrt{\alpha} \quad . \end{aligned} \tag{9.a.9}$$

This is a remarkably simple result; it says that we need measure only one parameter ($\alpha = \langle E_x^2 \rangle$) in order to determine the complete probability distribution function. Such a result is obviously too simplistic. Nevertheless, it does serve as a very useful first approximation, and in some cases is even a good representation of the full answer.

There are numerous relevant examples in the literature, and two will be presented here. Figure 9.a.7 shows the results of measurements made at a large number of positions within a metal building which is irradiated from outside [8]. As is customary for such measurements, the data are plotted on "Rayleigh paper" { $-0.5 \log[-\ln p(E > E_o)]$ vs. $|E_o|$ in dB }. The straight line representing the cumulative amplitude distribution obtained from a Rayleigh distribution, (9.a.9), clearly fits the data very well over the full range of measurements. A second example is shown in Fig. 9.a.8, which is the result of measurements of the magnetic field at one position (in a mine) at many different times [9]. (Note that the axes are interchanged relative to Fig.9.a.7.) Again, most of the data are represented very well by a Rayleigh distribution, although this time there is a clear departure at the low-probability end (< 1%). Numerous other studies have been made of urban and suburban radio noise, atmospheric noise, noise from automobiles, high-speed trains, power lines, etc. [5]-[7], [10]-[16], all of which confirm the validity of the Rayleigh distribution for the bulk of the data.

This suggests that, in order to characterize a complex EM environment, one needs to measure E_{rms} and the rest follows from (9.a.9). As we indicated above, however, life is not so simple. One problem is that, in all applications referenced, one determines E_{rms} from the full distribution -- no work is saved. This problem is probably surmountable. More serious is the low-probability, high-amplitude portion of the curve, where the distribution deviates from Rayleigh behavior. It is precisely this high-amplitude region in which our interest is most likely to lie. Unfortunately, the characteristics of this troublesome region vary from case to case, as can be seen from Figs. 9.a.7 and 9.a.8, for example. In fact this "low-probability" region can extend up to 30% to 50%; and its shape and maximum height vary as well. If the statistical approach is to be useful in EM environment characterization, the deviations from Rayleigh behavior must be understood.

The origin of the unwelcome bump in Fig. 9.a.8 is easy to understand qualitatively. If one had only the Gaussian background (9.a.9), one would just get the Rayleigh amplitude probability distribution represented by the solid line in Fig. 9.a.9. If instead there were just one strong source which happened to radiate 2% of the time always at a level 30 dB above some reference amplitude, it would appear as the dashed line in the figure. If the strong source, instead of always having an amplitude of 30 dB when it was on, had a random amplitude with the distribution peaked around 30 dB, then the corner indicated in the dashed line in Fig. 9.a.9 would be rounded, and the vertical and horizontal lines would be less steep and less flat respectively. It is then easy to see how the combined effect of strong source plus Gaussian noise could produce a distribution like that of Fig. 9.a.8. The fact that the low-probability bump is due to one or more strong sources which radiate some fraction of the time (or influence some fraction of the positions) has led to its being called the impulsive component of the noise.

A more quantitative presentation can be made by writing the field at some point as the sum of a dominant contribution, E_d, from the strong source plus contributions from all other random sources, E_Σ, [5]. The probability density function for the dominant term, $p_d(E_d)$, is not known -- it could be a constant, normal, log-normal, whatever. From the central limit theorem, the sum of the other contributions will have a Gaussian distribution for real and imaginary parts, or a Rayleigh distribution for the amplitude,

$$p_\Sigma(E_\Sigma) = \frac{2E_\Sigma}{\alpha} \exp(-E_\Sigma^2/\alpha) \quad .$$

The probability density function for the net component of the field is then

$$E_x = E_{x\,d} + E_{x\,\Sigma} \quad ,$$

$$p(E_x) = \frac{2E_x}{\alpha} \int \exp[-(E_x^2 + z^2)/\alpha]\, I_o(2E_x z/\alpha)\, p_d(z)\, dz \ , \qquad (9.a.10)$$

where I_o is the modified Bessel function. The limiting behavior for large or small E is then

$$p(E) \approx (2E/\alpha) \exp(-E^2/\alpha) \quad , \quad E^2 \ll \alpha,$$
$$\approx p_d(E) \quad , \quad E^2 \gg \alpha, \tag{9.a.11}$$

where by E we mean $|E_x|$. Thus, the small-E (high probability) behavior is given by the Rayleigh distribution, but the large-E impulsive component is controlled by the probability distribution function of the dominant source(s). Since this impulsive component varies from case to case, hope for a simple, universal statistical description fades.

More-complicated treatments have been developed, most notably by Middleton [17]-[19]. His interest is primarily in communications systems and in the effect of noise on the receiver. He therefore distinguishes between noise which has a bandwidth smaller than that of the receiver (Class A) and noise whose bandwidth is greater than that of the receiver (Class B). For the case of multiple sources of impulsive noise (assumed to have a Poisson distribution) plus a gaussian background noise, general forms for the resulting probability distribution functions have been obtained in terms of a few parameters -- three for Class A and seven for Class B [17]. These general forms reproduced various measured probability distributions very well, as can be seen in Fig. 9.a.10. Unfortunately, there are rather severe restrictions on the general applicability of the formulae. The paper by Berry [18] gives a clear account of both the derivation and the limitations of Middleton's "canonical" forms. The major unforeseen limitation is that the distance from observation point to the first impulsive-noise source must be much greater than the path difference between the observation point and any two sources --essentially, they must all be at about the same distance. In addition, there is the requirement of Poisson statistics for the sources of impulsive noise.

By including correction terms (and therefore more parameters) these restrictions can be eased [19], but this approach is still not the general EMC tool we are seeking. The problem is that there is virtually no predictive power. In all applications to date, the distribution has been measured and the parameters determined from it rather than the reverse. What one has then is a convenient representation of the noise-measurement results. This is very useful in the design of communications systems (which was its purpose, after all), but it does not enable one to characterize an EM environment by making just a few measurements. The same comment applies to other statistical quantities which have been employed, such as pulse-width distributions, average crossing rates, Allan variance analyses, etc.: it is true that they characterize the environment, but they require nearly complete measurement of the environment to be determined.

C. Other Possible Approaches Although they are not yet at the production stage, other approaches to complex environments are being investigated and developed. The goal of these approaches is to extract some useful information about the environment from a relatively small number of measurements.

An approach which holds some promise for large, open environments is directional scanning [22]. The idea is to use a directional probe to measure the field in a number of directions, distributed over the full 4π solid angle. These measurements can be used to determine the coefficients in a (discretized) plane-wave expansion. In principle, once the coefficients have been determined, the plane-wave expansion determines the field throughout the volume scanned. In practice, the accuracy is limited by the fact that each measurement averages over some finite solid angle. Simulations indicate that the field reconstruction is rather poor, but that useful upper bounds on the field can be obtained, and the rms field (where the average is over the volume) can be determined quite well. Work still to be done includes scanning in the presence of the earth or above a ground plane rather than in free space, inclusion and assessment of measurement errors, various technical refinements, and eventually practical tests.

Another method is based on a finite-element form of the EM action functional [4],[23]. The action is just an integral over position and time of some function which involves the scaler and vector potentials. It has the property that, if the potentials at each point are allowed to vary, then a stationary point of the action with respect to this variation yields potentials which lead to EM fields satisfying Maxwell's equations. In the approach being developed, one first discretizes the volume of interest (for the sake of the computer) and enforces boundary conditions and measurement results by fixing the potentials to be equal to the appropriate values at those points. The potentials are then varied at all other points until a stationary point of action is found. The values of the fields which yield the stationary point are solutions of Maxwell's equations which are consistent with the boundary conditions and which have their measured values at measurement points. In practice, all this is more easily said than done. Numerous technical difficulties arise; but none seems insurmountable, and the work is progressing. This technique would complement the directional scanning technique since the finite-element method is best suited to relatively small (dimensions of order a few wavelengths or less), closed environments.

There are also other possible approaches which warrant some attention. It may be possible to measure directly the parameters in Middleton's formula without measuring the full distribution. In some situations, if the sources are local and identifiable, it may be practical to characterize the radiating sources using just a few measurements, much as can be done in EMC emissions testing [24].

When it comes to characterizing a complex EM environment, there is no technique which is systematic and efficient. Some environments have been characterized quite well statistically, and these characterizations are useful for communications systems in particular. These statistical characterizations, however, require extensive measurement effort and have virtually no predictive power. The work being developed here will benefit significantly from a better understanding of what are the EM characteristics of interest.

REFERENCES

[1] Randa, J; Kanda, M. Multiple-source, multiple-frequency error of an electric-field meter. IEEE Trans. Antennas and Propag. AP-33(1): 2-9; 1985 January.

[2] Bassen, H. I.; Smith, G. S. Electric field probes - a review. IEEE Trans. Antennas and Propag. AP-31(5): 710-718; 1983 September.

[3] Larsen, E. B; Ries, F. X. Design and calibration of the NBS isotropic electric-field monitor (EFM-5), 0.2 to 1000 MHz. Nat. Bur Stand. (U.S.) Tech. Note 1033; 1981 March.

[4] Kanda, M; Randa, J.; Nahman, N. S. Possible estimation methodologies for electromagnetic field distributions in complex environments. Nat. Bur. Stand. (U.S.) Tech. Note 1081; March 1985.

[5] Beckman, P. Probability in Communication Engineering. New York, NY: Harcourt, Brace, and World; 1967.

[6] Skomal, E. Man-Made Radio Noise. New York, NY: Van Nostrand Reinhold; 1978.

[7] Lee, W. C. Y. Mobile Communications Engineering. New York, NY: McGraw-Hill; 1982.

[8] Hoffman, H. H.; Cox, D. C. Attenuation of 900 MHz radio waves propagating into a metal building. IEEE Trans. Antennas and Propag. AP-30(4): 808-811; 1982 July.

[9] Kanda, M. Time and amplitude statistics for electromagnetic noise in mines. IEEE Trans. Electromag. Compat. EMC-17(3): 122-129; 1975 August.

[10] Haskard, M; Miller, M.; Johnson, A.; Marconi, P. Radio noise measurements in an urban environment. J. Elec. Electron. Eng., Australia, 2, no. 2: 94-102; 1982 June.

[11] Struzak, R.; Rymarowicz, Z; Moron, W. Urban MF radio noise survey in Poland. Proc. 5th Symp. and Tech. Exhibition on EMC; 1984 March; Zurich, Switzerland. 1-6.

[12] Parsons, J.; Sheikh, A. Statistical characterization of VHF man-made radio noise. Radio Elec. Eng., 53(3): 99-106; 1983 March.

[13] Nakai, T.; Kawasaki, Z. I. Automotive noise from a motorway: I, measurements. IEEE Trans. Electromag. Compat. EMC-26(4): 169-174; 1984 November.

[14] Shepherd, R. Measurements of amplitude probability distributions and power of automobile ignition noise at high frequency. IEEE Trans. Vehicular Tech. VT-23(3): 72-83; 1974 August.

[15] Nakai, T.; Kawasaki, Z. I. APD's and CRD's for noise from bullet trains in Japan. IEEE Int. Symp. on EMC; 1984 October; Tokyo, Japan. 250-255.

[16] Sheikh, A.; Parsons, J. Statistics of electromagnetic noise due to high-voltage power lines. IEEE Trans. Electromag. Compat. EMC-23(4): 412-419; 1981 November.

[17] Middleton, D. Statistical-physical models of electromagnetic interference. IEEE Trans. Electromag. Compat. EMC-19(3): 106-127; 1977 August.

[18] Berry, L. Understanding Middleton's canonical formula for Class-A noise. IEEE Trans. Electromag. EMC-23(4): 337-344; 1981 November.

[19] Middleton, D. Canonical and quasi-canonical probability models of Class-A interference. IEEE Trans. Electromag. Compat. EMC-25(2): 76-106; 1983 May.

[20] Adams, J. W.; Bensema, W. D.; Kanda, M. Electromagnetic noise: Grace Mine. Nat. Bur. Stand. (U.S.) Int. Rept. 74-388; 1974.

[21] Bolton, E. C. Simulating LF atmospheric radio noise at 60, 76, 200 kHz. Office of Telecommunications, OT-TM-97; Boulder, CO. 1972.

[22] Randa, J.; Kanda, M. Directional scanning of complex electromagnetic environments. IEEE Trans. Antennas and Propag. AP-33, no. 12: 1413-1416; December 1985; Also, A directional scanning technique for characterization of complex electromagnetic environments. Proc. IEEE Int. Symp. Antennas and Propag.; 1985 June; Vancouver, Canada.

[23] Randa, J.; Kanda, M. A finite-element action approach to the characterization of complex electromagnetic environments. Proc. Int. Symp. Antennas and EM Theory; 1985 August; Beijing, China.

[24] Ma, M. T.; Koepke, G. H. A method to quantify the radiation characteristics of an unknown interference source. Nat. Bur. Stand. (U.S.) Tech. Note 1059; October 1982; Also A new method for determining the emission characteristics of an unknown interference source. Proc. IEEE Int. Symp. EMC; 1982 September; Santa Clara, CA. 151-156.

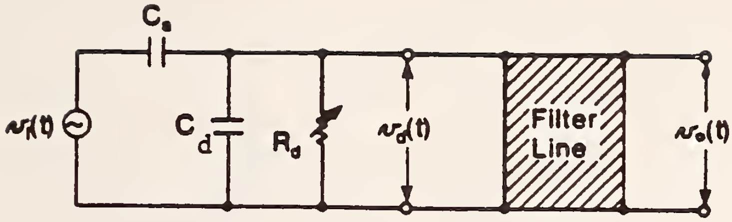

Figure 9.a.1 Equivalent circuit for a single antenna plus diode, with filter line also indicated.

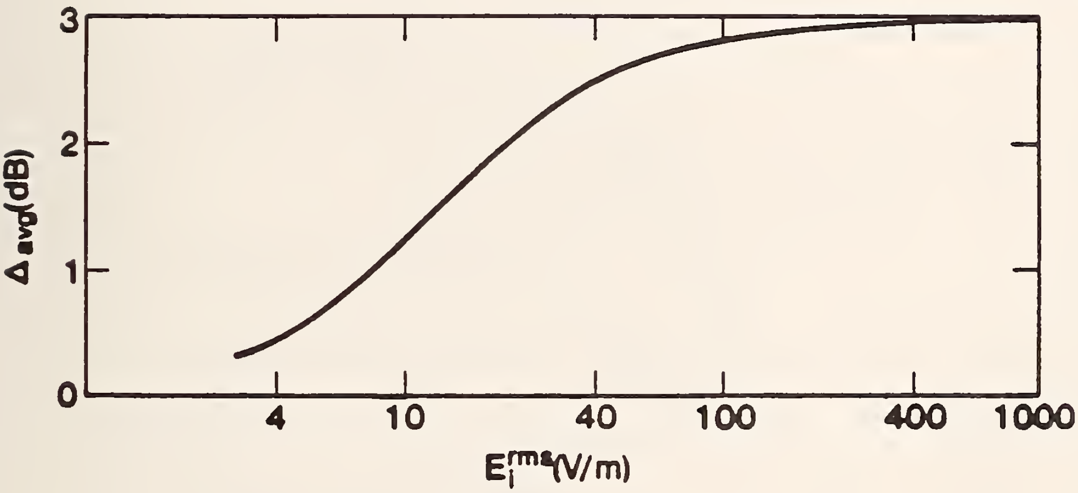

Figure 9.a.2 Error in average electric field strength for $E_i(t) = E_i^{rms}$ (cos ωt + cos 2ωt). Error in peak strength is given by $\Delta_{pk} = \Delta_{avg} - 3$ dB.

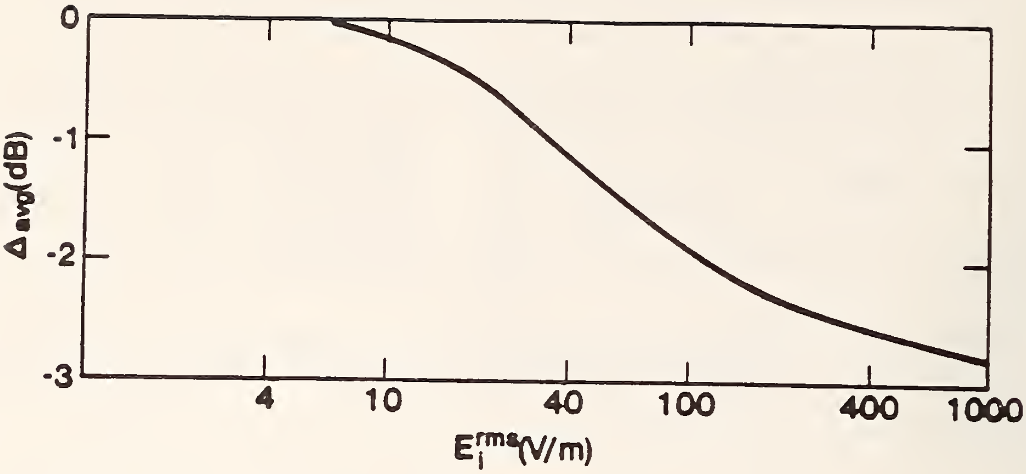

Figure 9.a.3 Error in average electric field strength for a periodic square wave, $\pm E_i^{rms}$. In this case, $\Delta_{pk} = \Delta_{avg} + 3$ dB.

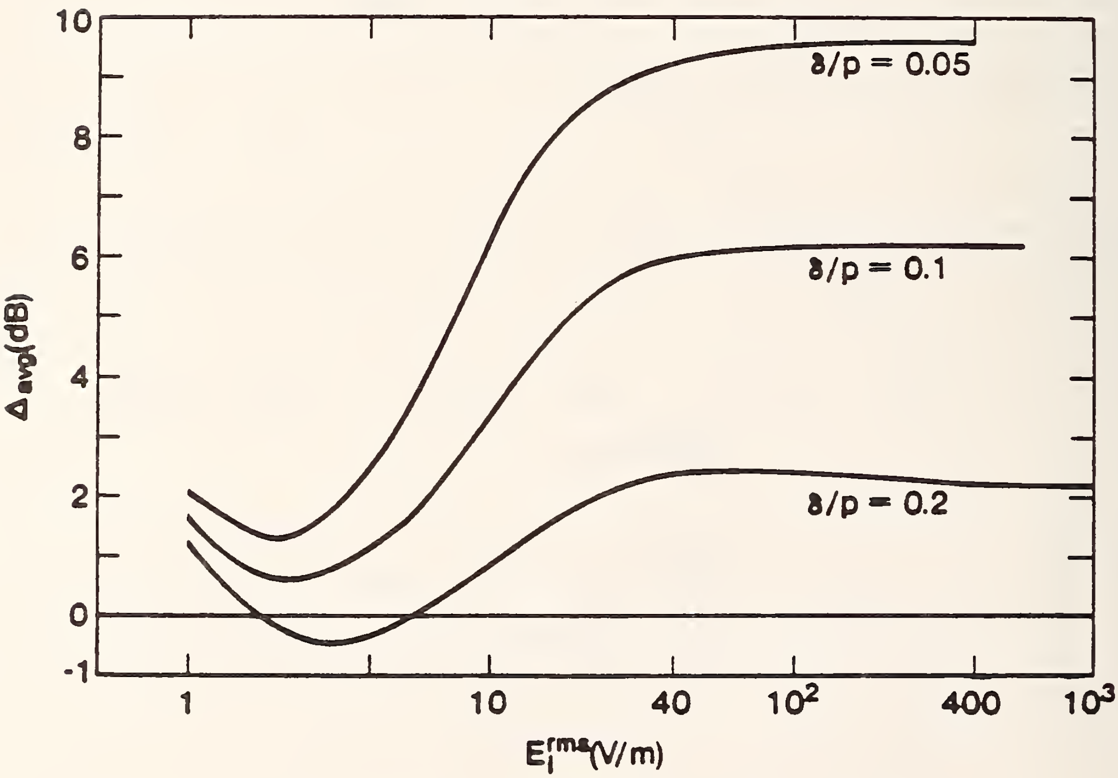

Figure 9.a.4 Error in average electric field strength for a periodic square pulse with various ratios of width (δ) to period (p). Peak value is $E_i^{pk} = E_i^{rms}\sqrt{p/\delta}$. The error in the peak strength is given by $\Delta_{pk} - \Delta_{avg} = -10$ dB, -7 dB, -4 dB for $\delta/p = 0.05$, 0.1, and 0.2 respectively.

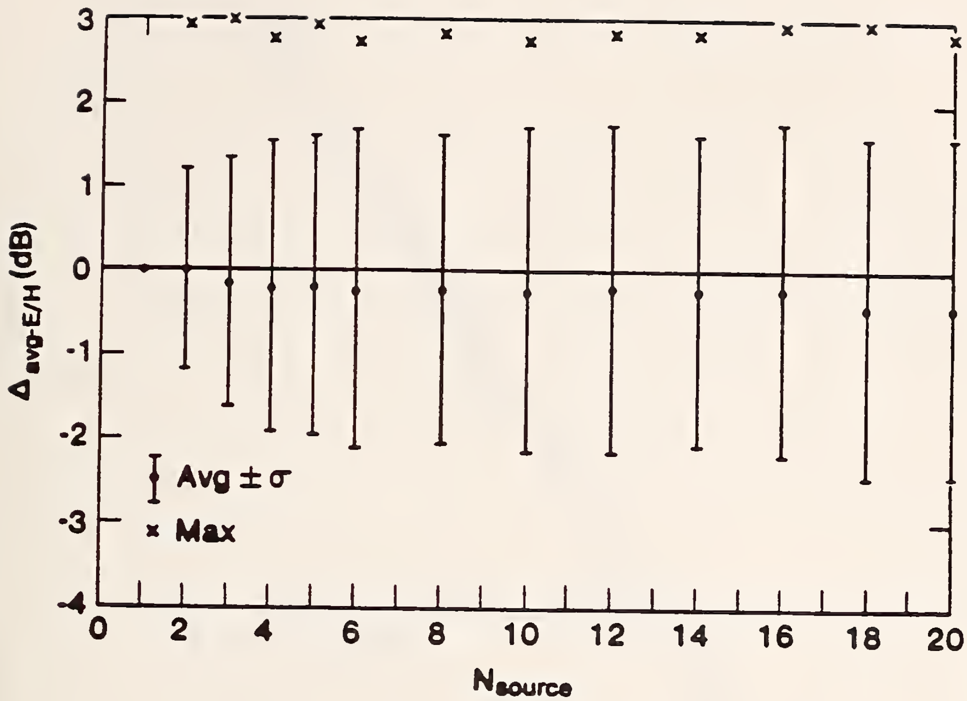

Figure 9.a.5 Mean, standard deviation, and maximum values of the error $\Delta_{avg}(E/H)$, as functions of the number of sources. For each N_{source}, 1000 random configurations were used.

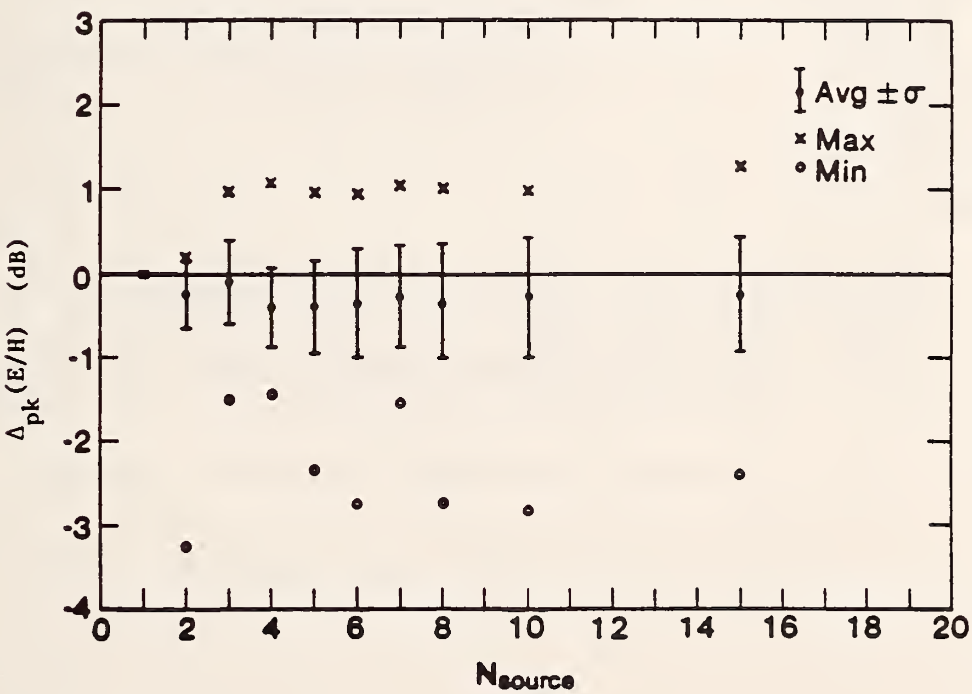

Figure 9.a.6 Mean, standard deviation, and maximum and minimum values of $\Delta_{pk}(E/H)$, using 100 random configurations for each N_{source}.

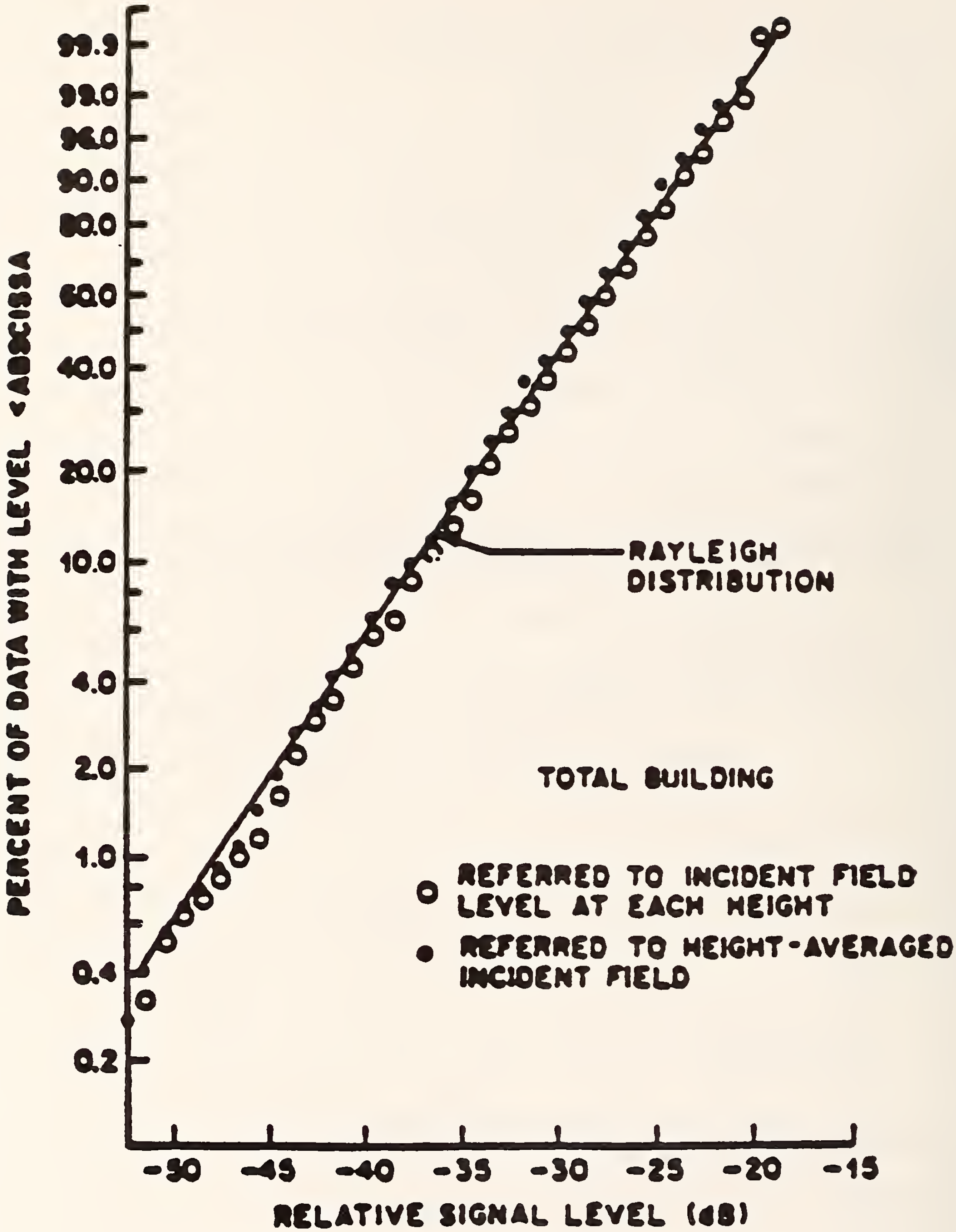

Figure 9.a.7 Overall signal-level distribution, from [8].

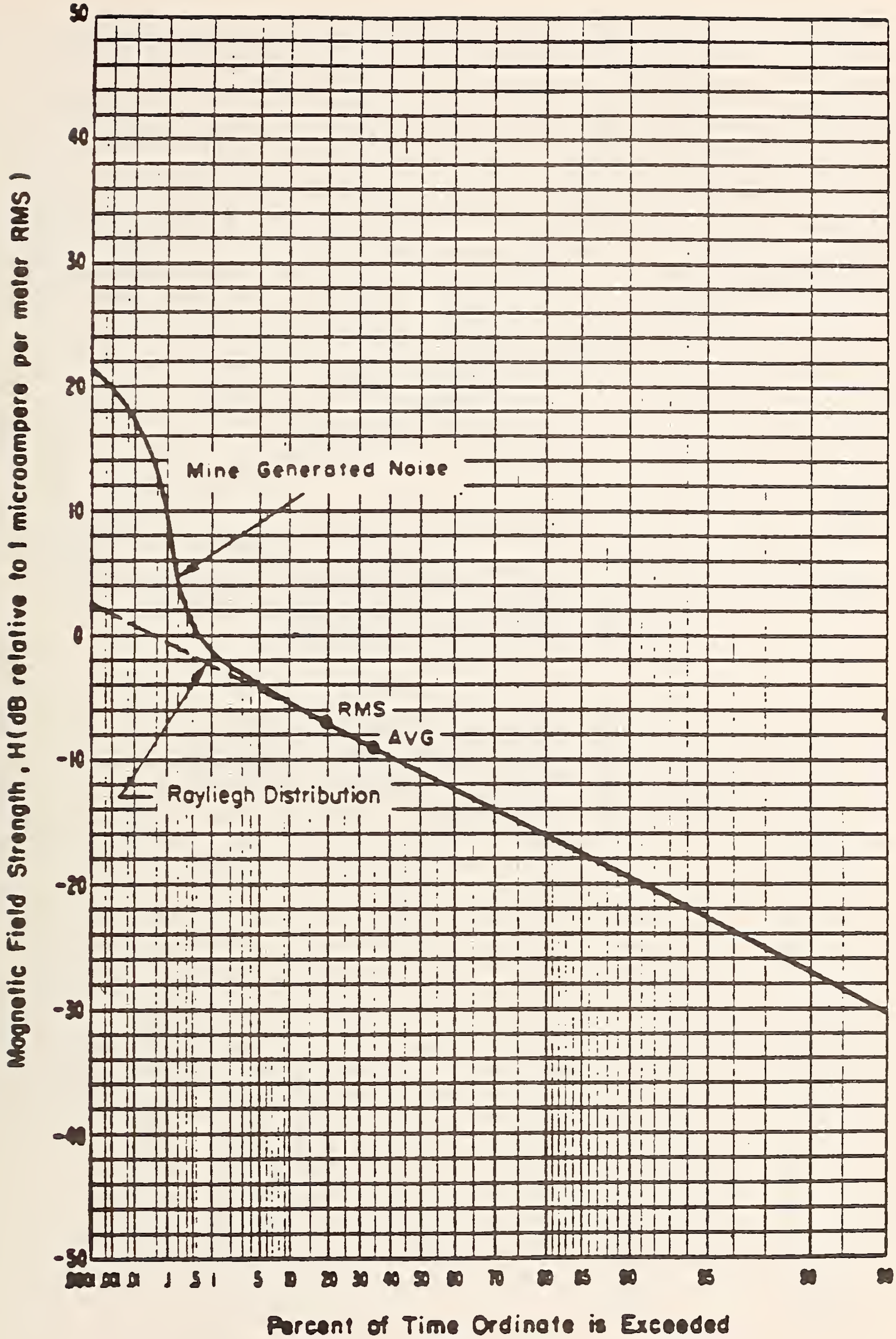

Figure 9.a.8 Cumulative amplitude probability distribution of EM noise in a mine [9].

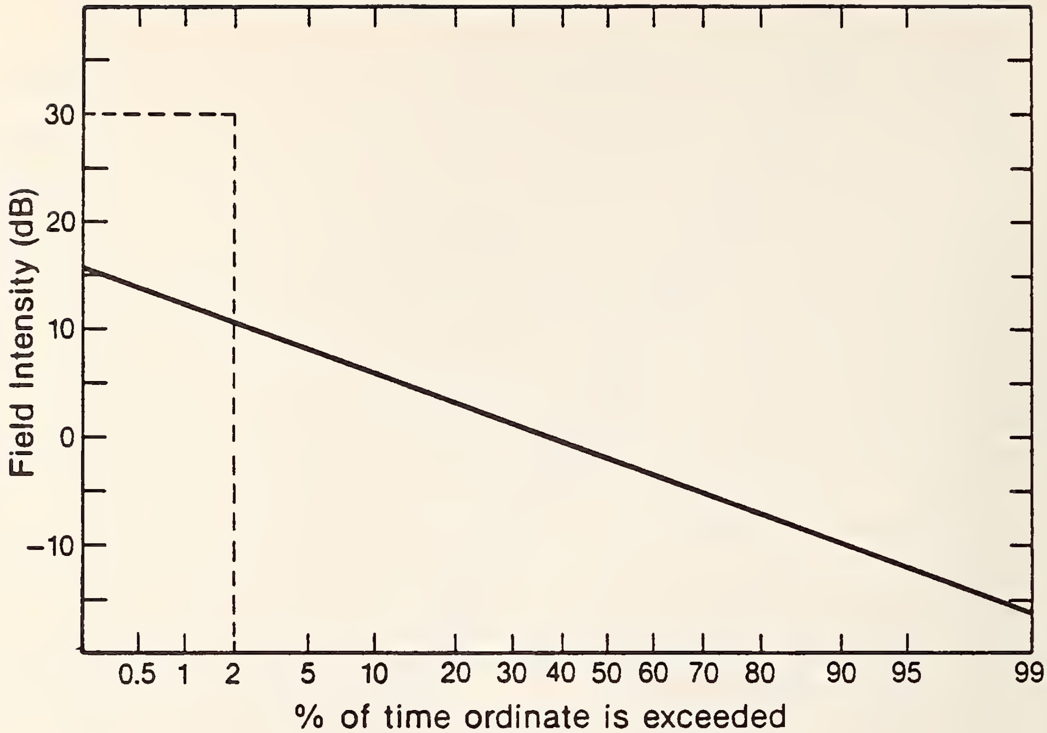

Figure 9.a.9 Solid line represents a Rayleigh amplitude probability distribution, and the dashed line is the idealized impulsive component discussed in the text.

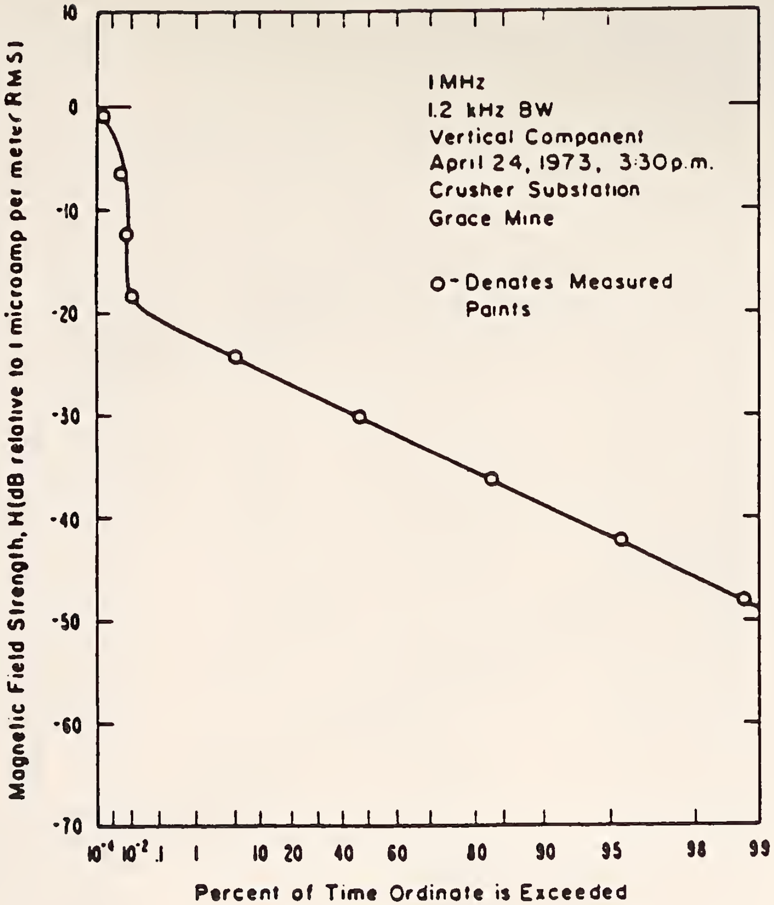

(a)

Figure 9.a.10 Comparison of measured envelope distribution, $p(E > E_o)$, with Middleton's Class A or B models. Figures are taken from [17].

(a): Class A, interference from ore-crushing machinery, data from [20];

(b): Class A, interference from power line, data from [21];

(c): Class B, interference from flourescent lights, data from [20];

(d): Class B, interference from automobile ignition, data from [14].

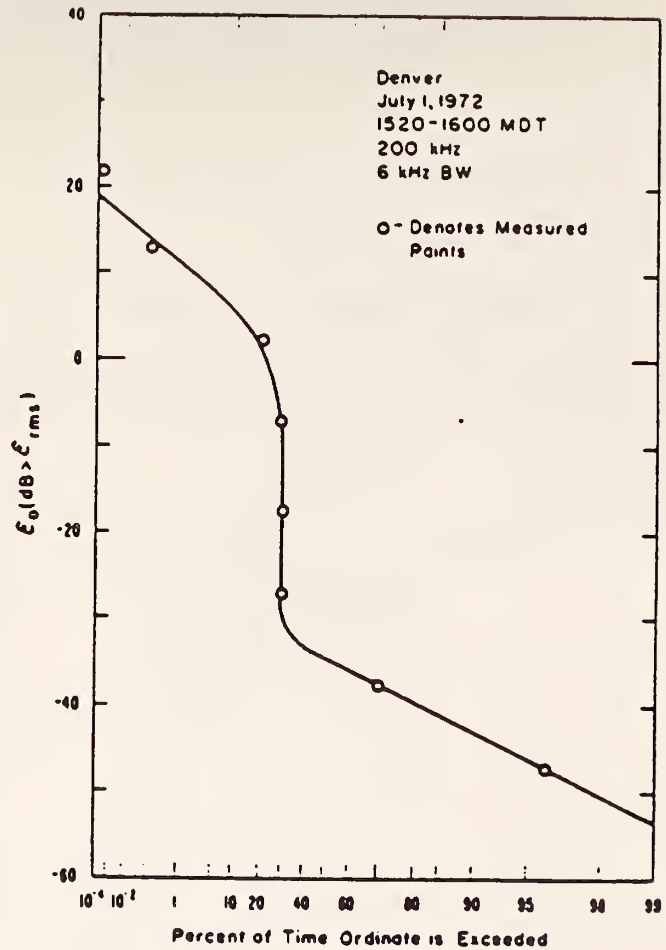

(b)

Figure 9.a.10 Continued

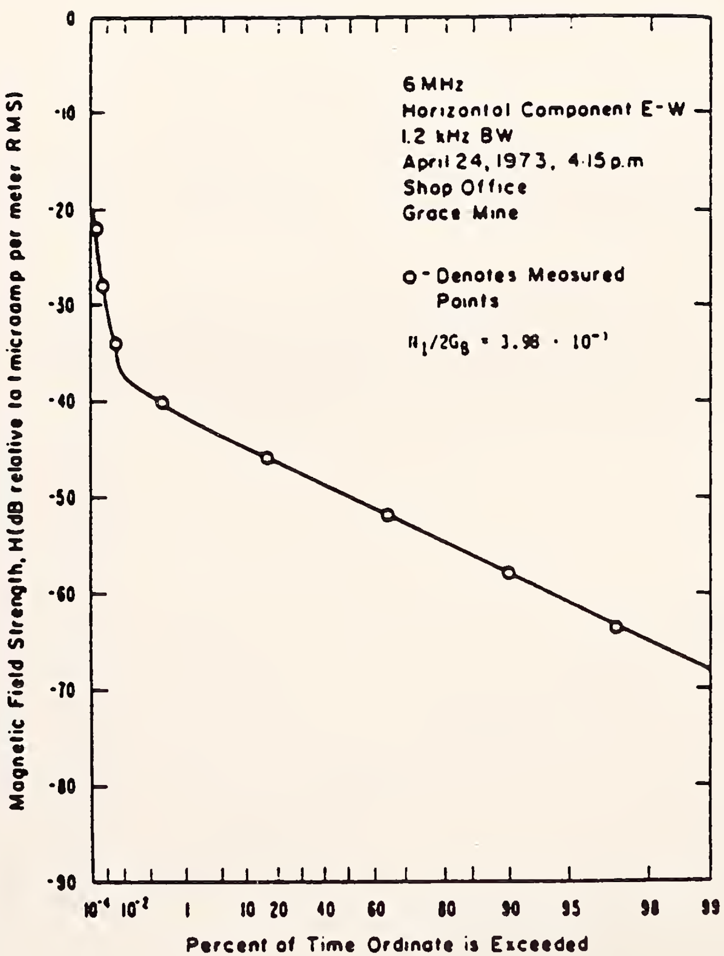

(c)

Figure 9.a.10 Continued

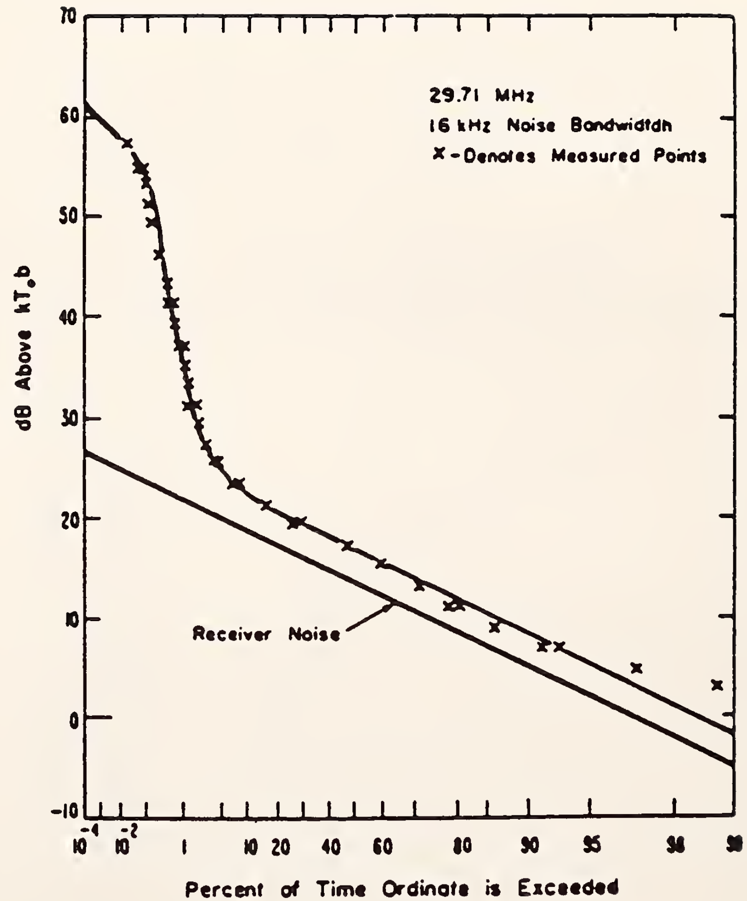

(d)

Figure 9.a.10 Continued

9.b OUT-OF-BAND EMC PROBLEMS

Interfering signals at out-of-band frequencies can be either intentional, as in jamming with high-power microwave beams, or unintentional, as in typical EMC problems. In either case, it is important that the EMC analyst be able to understand and to predict out-of-band coupling phenomena. The importance of the out-of-band response of antennas [1],[2] and antenna feed systems [3] in EMC problems has been recognized for some time.

Our initial research at NBS in this area has concentrated on the out-of-band response of reflector antennas [4]. Reflector antennas are of particular interest because they are used so frequently at microwave frequencies and because they have a strong response to above-band frequencies. The characterization of the above-band response of reflector antennas is complicated because of the presence of higher-order propagating modes in typical waveguide feeds. This problem is avoided in the receiving-mode analysis presented in Section 9.b.1, where the total received power carried by all the propagating modes is computed. The power coupled from the waveguide to the detector depends on the specific feed system, and, in Section 9.b.2, we analyze the out-of-band response of a typical coax-to-waveguide adapter. We also combine the theoretical results for reflector antennas and coax-to-waveguide adapters for comparison with measured data at out-of-band frequencies [2]. Section 9.b.3 contains conclusions regarding reflector antennas and a brief description of our present work on phased-array antennas.

9.b.1 Reflector Antennas

Reflector antennas typically use waveguide feeds, and frequencies well below the in-band frequency are not important because they are cut off by typical waveguide feeds. Consequently, "out-of-band" will refer only to above-band frequencies. We choose to analyze reflector antennas in the receiving mode using a two-step method. In the first step, we use the physical optics approximation to compute the fields in the focal region of a parabolic reflector. In the second step, we integrate the Poynting vector over the aperture of the feed horn to determine the total received power. The mathematical details are given in [4], and here we will just describe the general procedure.

A perfectly conducting, paraboloidal reflector of diameter D and focal length f is shown in Fig. 9.b.1. The origin of a rectangular coordinate system (x, y, z) is located at the focus of the paraboloid. A plane wave is incident at an angle θ_s to the z-axis in the xz plane. The physical optics surface current $\underline{J}$ on the reflector is given by

$$\underline{J} = 2\,\hat{n} \times \underline{H}_i \quad , \tag{9.b.1}$$

where $\hat{n}$ is the unit normal to the reflector and $\underline{H}_i$ is the incident magnetic field. An infinitesimal surface current patch of area dS at a point P_1 on the reflector produces electric and magnetic fields [5],[6] at the point P_2:

$$d\underline{E} = \frac{-jk\eta_0}{4\pi}\left[\underline{J} - \underline{u}_R(\underline{J}\cdot\underline{u}_R)\right]\frac{e^{-jkR}}{R}\,dS$$

$$d\underline{H} = \frac{jk}{4\pi}(\underline{J} \times \underline{u}_R)\frac{e^{-jkR}}{R}\,dS \quad , \tag{9.b.2}$$

where η_0 is the intrinsic impedance of free space. As indicated in Fig. 9.b.1, R is the distance between P_1 and P_2, and $\underline{u}_R$ is the unit vector directed from P_1 to P_2. To compute the fields in the vicinity of the focal region, it is necessary to integrate (9.b.2) over the surface of the reflector. In general, numerical integration is required; but simple, approximate expressions for the electric and magnetic fields, $\underline{E}$ and $\underline{H}$, and the Poynting vector, $\underline{S} = \mathrm{Re}(\underline{E} \times \underline{H}^*)/2$, have been obtained [4],[6]. Here Re indicates real part, and * indicates complex conjugate.

A waveguide feed and a feed horn whose aperture is centered at the focal point of the paraboloid are shown in Fig. 9.b.2. Normally, the feed-horn aperture dimensions are on the order of a wavelength at the in-band frequency. Consequently, the aperture dimensions can be assumed to be electrically large at above-band frequencies, and we can make the Kirchhoff approximation for the aperture field [4]. The received power is then given by the integral of the Poynting vector over the aperture, A,

$$P_r = -\int_A S_z \, dA \quad , \tag{9.b.3}$$

where S_z is the z-component of the Poynting vector, and the geometry is shown in Fig. 9.b.2. Since we assume that no power is dissipated in the walls of the horn and waveguide, the power propagating down the waveguide is also given by P_r in (9.b.3). Because the waveguide will normally be multimoded at above-band frequencies, P_r is the total received power in all the propagating waveguide modes. For general feed-horn apertures, the integration in (9.b.3) must be done numerically; but for circular apertures, a simple approximation has been obtained for P_r [4].

We can define a generalized effective aperture A_e as the total received power divided by the incident power density,

$$A_e = P_r / \left(\frac{1}{2} \eta_0 \, |H_i|^2 \right) \quad . \tag{9.b.4}$$

It is often convenient to normalize A_e to the physical area of the reflector antenna, $A_p = \pi D^2/4$. For the case of on-axis incidence ($\theta_s = 0$) where A_e is maximum, A_e/A_p can be approximated by [4],[5]

$$A_e/A_p = 1 - J_0^2(k\theta_m\rho_m) - J_1^2(k\theta_m\rho_m) \quad , \tag{9.b.5}$$

where k is the free-space wavenumber $(2\pi/\lambda)$, θ_m is the angle defined in Fig. 9.b.1, ρ_m is the radius of the feed horn, and J_0 and J_1 are zero-order and frist-order Bessel functions. The ratio A_e/A_p is sometimes called aperture efficiency and is less than unity. For sufficiently high frequencies ($k\theta_m\rho_m >> 1$), A_e/A_p approaches unity.

For the off-axis case ($\theta_s \neq 0$), an approximation similar to (9.b.5) has been obtained [4]:

$$A_e/A_p = \begin{cases} 1/2\,[2 - J_0^2(k\theta_m\rho_+) - J_1^2(k\theta_m\rho_+) - J_0^2(k\theta_m\rho_-) - J_1^2(k\theta_m\rho_-)] \, , \\ \qquad\qquad f \sin\theta_s < \rho_m \\ \phi_c/\pi\,[J_0^2(k\theta_m\rho_-) + J_1^2(k\theta_m\rho_-) - J_0^2(k\theta_m\rho_+) - J_1^2(k\theta_m)] \quad , \\ \qquad\qquad f \sin\theta_s > \rho_m \end{cases} \tag{9.b.6}$$

where

$$\rho_\pm = |f \sin\theta_s \pm \rho_m| \quad , \qquad \text{and} \qquad \phi_c = \sin^{-1}(\rho_m / f \sin\theta_s) \; .$$

This approximation yields the receiving pattern and the beamwidth. Measured receiving patterns have been published for a 3 GHz reflector antenna at frequencies up to 10 GHz [2]. A comparison of theory [4] and experiment [2] is shown in Fig. 9.b.3 for a frequency of 6 GHz. The agreement in Fig. 9.b.3 is typical of that obtained at other frequencies. The theory which represents total received power in all the modes tends to provide an upper-bound envelope for the measured power.

A number of extensions to the basic reflector-antenna analysis have been made [4]. The transient response has been studied by inversely transforming the frequency-domain expressions to the time domain. The effect of reflector roughness has been examined using the classical result from Ruze [7]. Offset parabolas and dual reflectors have also been treated by using the equivalent diameter and equivalent focal length concept of Hannan [8].

9.b.2 Coax-to Waveguide Adapter

In many out-of-band EMC problems, the response of the feed system is at least as important as the antenna response. In attempting to interpret the out-of-band measurements of Cown et al. [2] on a 3-GHz reflector antenna, we found that we needed to know the out-of-band response of the coax-to-waveguide adapter which was used in that feed system. Such adapters are also used with many other antennas which employ waveguide feeds, and its frequency response illustrates the complexity of the out-of-band problem [4].

The probe-type adapter which we consider is shown in Fig. 9.b.4. Collin [9] has analyzed this structure using a variational technique, but his computational technique is valid only for in-band frequencies where the waveguide supports only a single propagating mode. We have extended his analysis to allow for higher-order propagating modes which occur at above-band frequencies [4]. Here we will show some typical results, but will skip the mathematical details given in [4].

If the coaxial cable is sufficiently small, then it will support only the dominant TEM mode even though the waveguide supports higher-order propagating modes. The main task is to compute the input impedance Z_{in} of the probe as seen from the junction with the coaxial cable ($y = 0$). Z_{in} can be written as a mode sum,

$$Z_{in} = R_{in} + j\,X_{in} = \sum_{n=1,3,5}^{\infty} \sum_{m=0}^{\infty} Z_{nm} \tag{9.b.7}$$

where $$Z_{nm} = R_{nm} + j\,X_{nm} \quad ,$$

R_{nm} is the resistance associated with the nm waveguide mode, and X_{nm} is the reactance associated with the nm waveguide mode. The probe excites only TM^y_{nm} modes that are transverse magnetic to y. The fields of the TM^y_{nm} mode have n half cycles in the x direction and m half cycles in the y direction. The terms for n even do not contribute to Z_{in} because the probe is located at the center of the waveguide ($x = a/2$). Only the propagating modes contribute to the real part of Z_{in}, and Collin [9] treated the case where only the TM^y_{10} mode was propagating. The double sum in (9.b.7) can be transformed to improve the numerical convergence [4].

In considering the power transmission from the coaxial cable to the waveguide, we assume that the coaxial cable has a real characteristic impedance R_c. Then the voltage reflection coefficient, Γ_v, is given by

$$\Gamma_v = (Z_{in} - R_c)/(Z_{in} + R_c) \tag{9.b.8}$$

The power reflection coefficient is then given by $|\Gamma_v|^2$, and the transmission coefficient T_t for the total power supplied to the waveguide is

$$T_t = 1 - |\Gamma_v|^2 = \frac{4R_{in}R_c}{(R_{in} + R_c)^2 + X_{in}^2} \tag{9.b.9}$$

We can also define the transmission coefficient for the nm mode T_{nm} as the ratio of the power transmitted to the nm mode to the incident power in the coaxial cable, and T_{nm} is given by [4]

$$T_{nm} = \frac{4R_{nm} R_c}{(R_{in} + R_c)^2 + X_{in}^2} \quad . \tag{9.b.10}$$

The total transmission coefficient T_t can also be written as the sum of the modal transmission coefficients

$$T_t = \sum_n \sum_m T_{nm} \quad . \tag{9.b.11}$$

The sum in (9.b.11) is always finite because only a finite number of waveguide modes propagate and carry power.

In the receiving antenna problem, we are interested in the reciprocal problem where a propagating waveguide mode transmits power to the coaxial cable. By reciprocity, we can show that the power transmission coefficient T_{nm} as given by (9.b.10) also applies to this case. In Fig. 9.b.5, we show the transmission coefficients for the dominant mode (TM_{10}^y) and the first higher-order propagating mode (TM_{11}^y). The adapter parameters were chosen to match those used in the reflector antenna that was studied experimentally by Cown et al. [2],[10]: a = 7.112 cm, b = 3.302 cm, d = 1.9 cm, ℓ = 2.4 cm, t = 7.0 mm, and R_c = 50 Ω. The in-band frequency is 3 GHz, and T_{10} is nearly unity from about 2.5 to 5.0 GHz. At 5.0 GHz, the first higher-order mode appears, and other higher-order modes appear above 6 GHz.

In an earlier comparison between theory and experiment for the on-axis gain of the antenna, the experimental values were well below the theoretical results. The main problem with the comparison was that the theory included only the antenna response, while the experimental included the antenna plus the adapter response. If we take the total transmission coefficient T_t as given by (9.b.9) or (9.b.11) and multiply it by the effective aperture of the antenna, then a corrected frequency response is obtained as shown in Fig. 9.b.6. To convert from effective aperture to gain, we divide A_e by the effective aperture for an isotropic antenna ($\lambda^2/4\pi$). No precise correction can be made because we do not know the modal content incident on the adapter from the waveguide, but the adapter correction does improve the agreement significantly, particularly below 7.5 GHz. Above 7.5 GHz, the adapter theory is probably not valid because the adapter probe no longer behaves like a thin, linear antenna.

Other adapters, such as those with loops rather stubs, could be studied theoretically or experimentally at out-of-band frequencies. Many other antenna types and feed systems are also worthy of out-of-band analysis or measurement. Recent unpublished experimental results with a variety of antenna types show fairly large mismatch losses at out-of-band frequencies [11].

Our present out-of-band work at NBS involves the analysis and measurement of large phased-array antennas. These antennas have rather complicated patterns [12] because of the presence of grating lobes at above-band frequencies.

REFERENCES

[1] Lind, W. R. Out of band performance of antennas. Moore School of Electrical Engineering Report No. 65-18; 1965.

[2] Cown, B. J.; Ryan, C. E.; Weaver, E. E. Antenna pattern measurements to characterize the out-of-band behavior of reflector antennas. Georgia Institute of Technology, Engineering Experiment Station, Report ECAC-TR-83-003; 1983.

[3] Levinson, D. S. Transmission-line measurement technique. Rome Air Development Center Technical Report No. RADC-TR-65-187; 1965.

[4] Hill, D. A. Out-of-band response of reflector antennas. Nat. Bur. Stand. (U.S.) Int. Rept. 85-3021; 1985.

[5] Minnett, H. C.; Thomas, B. M. Fields in the image space of symmetrical focusing reflectors. Proc. IEE, vol. 115: 1419-1430; 1968.

[6] Valentino, A. R.; Toulios, P. P. Fields in the focal region of offset parabolic antennas. IEEE Trans. Antenna Propag. AP-24(6): 859-865; 1976 November.

[7] Ruze, J. Antenna tolerance theory - a review, Proc. IEEE, vol. 54(4): 633-640; 1966 April.

[8] Hannan, P. W. Microwave antennas derived from the Cassegrain telescope. IEEE Trans. Antennas and Propag. AP-9(2): 140-153; 1961 March.

[9] Collin, R. E. Field Theory of Guided Waves. New York, NY: McGraw-Hill, 1960; sec. 7.1.

[10] Cown, B. J.; Ryan, C. E. Near-field theory and techniques for wideband radiating systems at in-band and out-of-band frequencies. Georgia Institute of Technology, Engineering Experiment Station, Contract No. DAAG29-78-C-0029; 1982.

[11] Hill, D. A.; Francis, M. H. Out-of-band response of antenna arrays. Nat. Bur. Stand. (U.S.) Int. Rept. 86-3047; 1986 June.

[12] Cown, B. J; Cain, F. L.; Duffy, E. G. Statistical prediction model for EMC analysis of out-of-band phased array antennas. IEEE Trans. Electromag. Compat. EMC-18(4): 163-170; 1976 November.

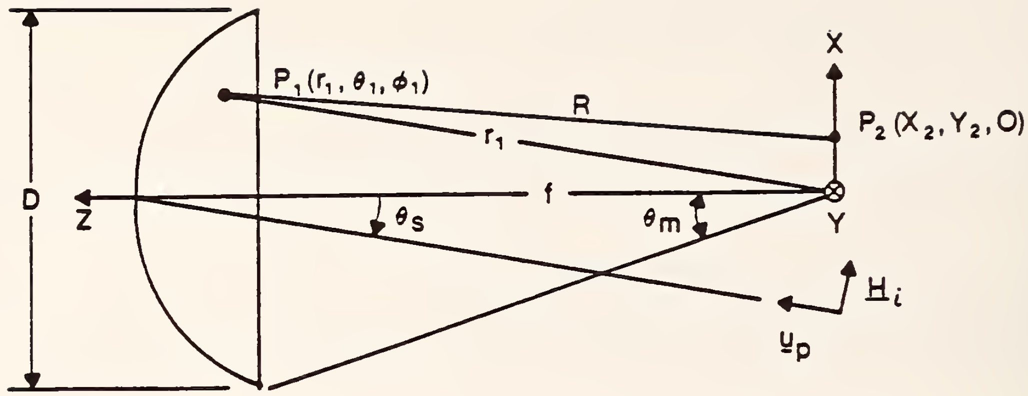

Figure 9.b.1 Geometry for a plane wave incident on a symmetrical paraboloidal reflector.

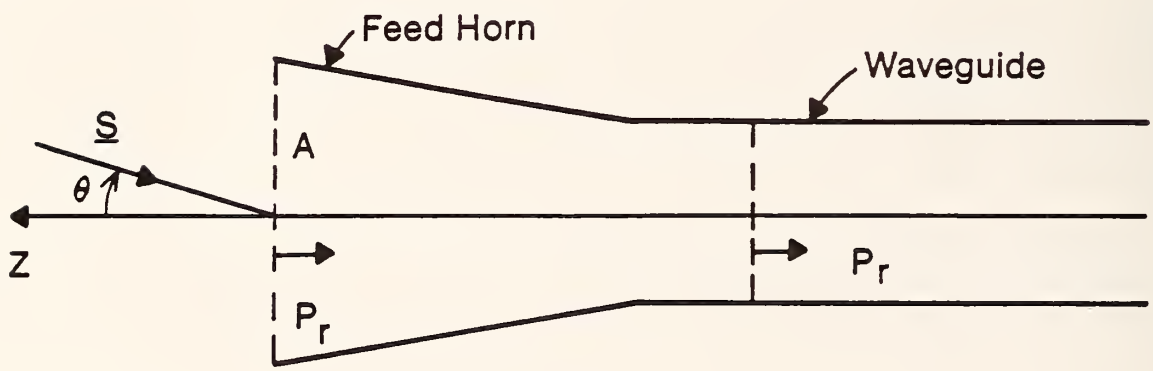

Figure 9.b.2 Geometry for the feed horn and waveguide.

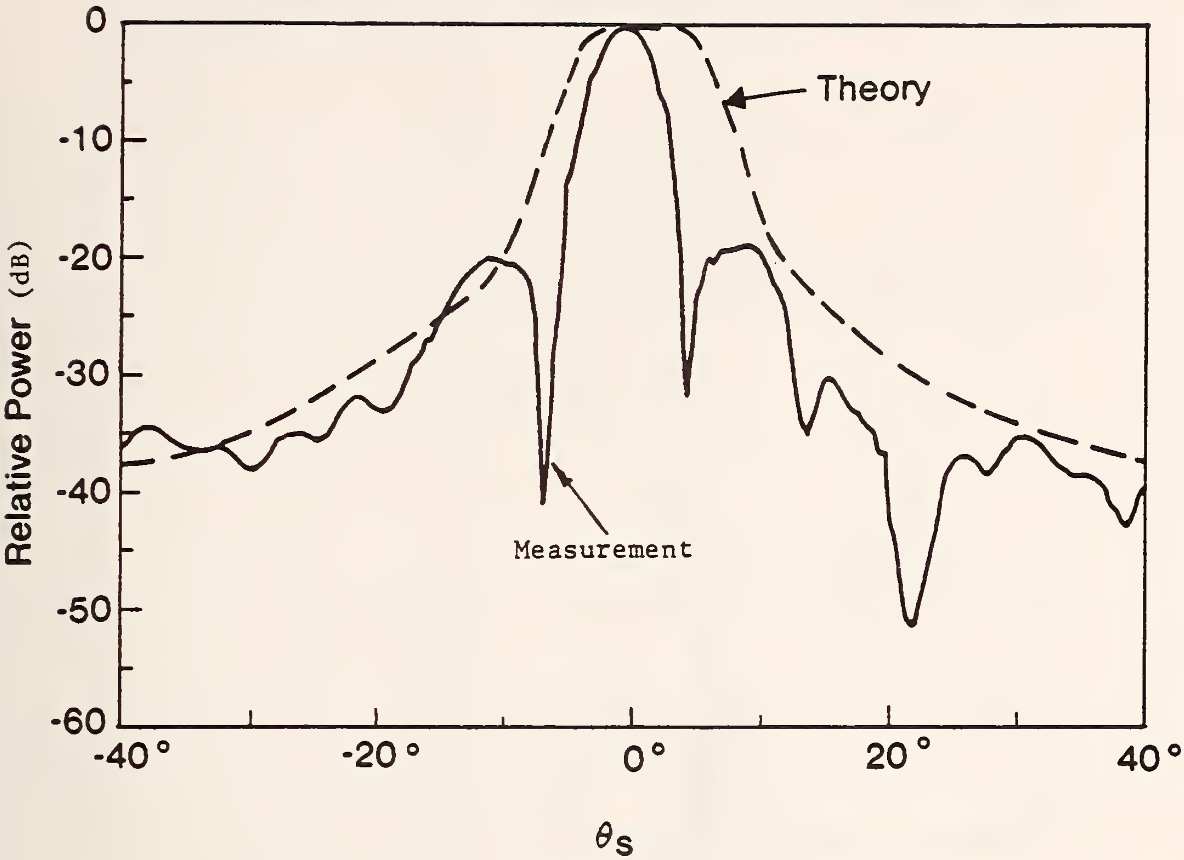

Figure 9.b.3 Comparison of theory [4] and experiment [2] for the above-band frequency of 6 GHz. Antenna parameters are: D = 1.22 m, f/D = 0.32, and ρ_m = 3.39 cm.

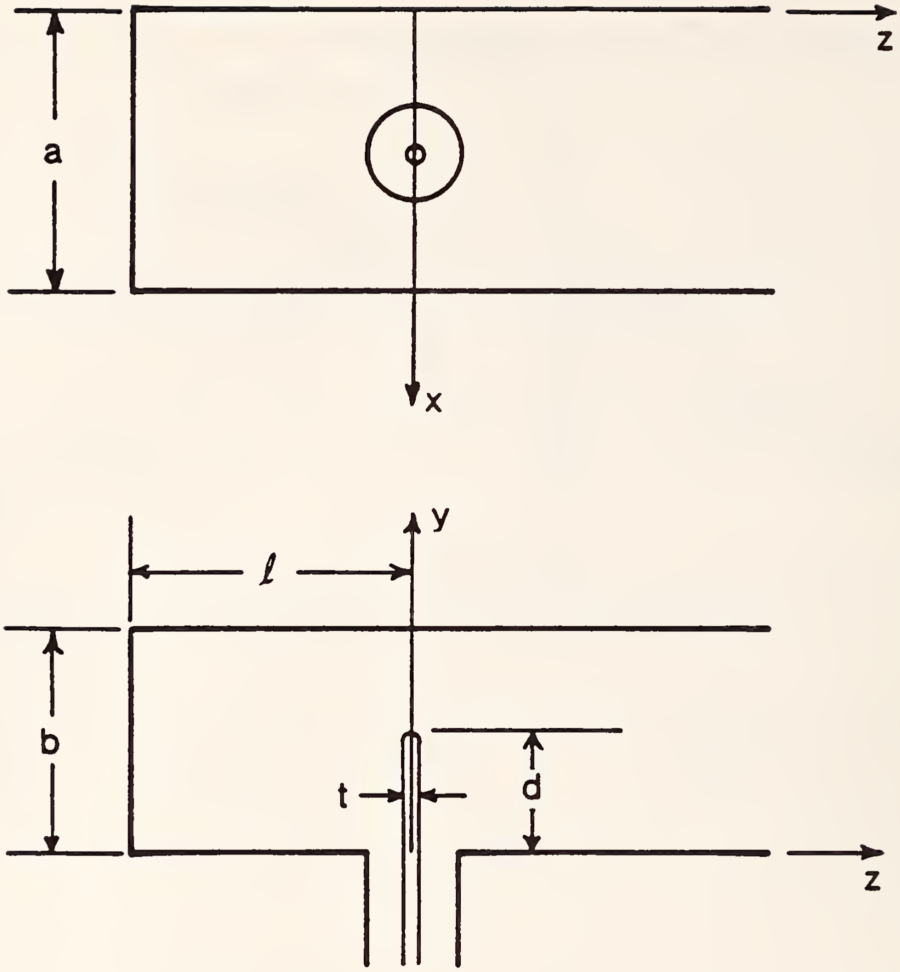

Figure 9.b.4   Probe type of coax-to-waveguide adapter.

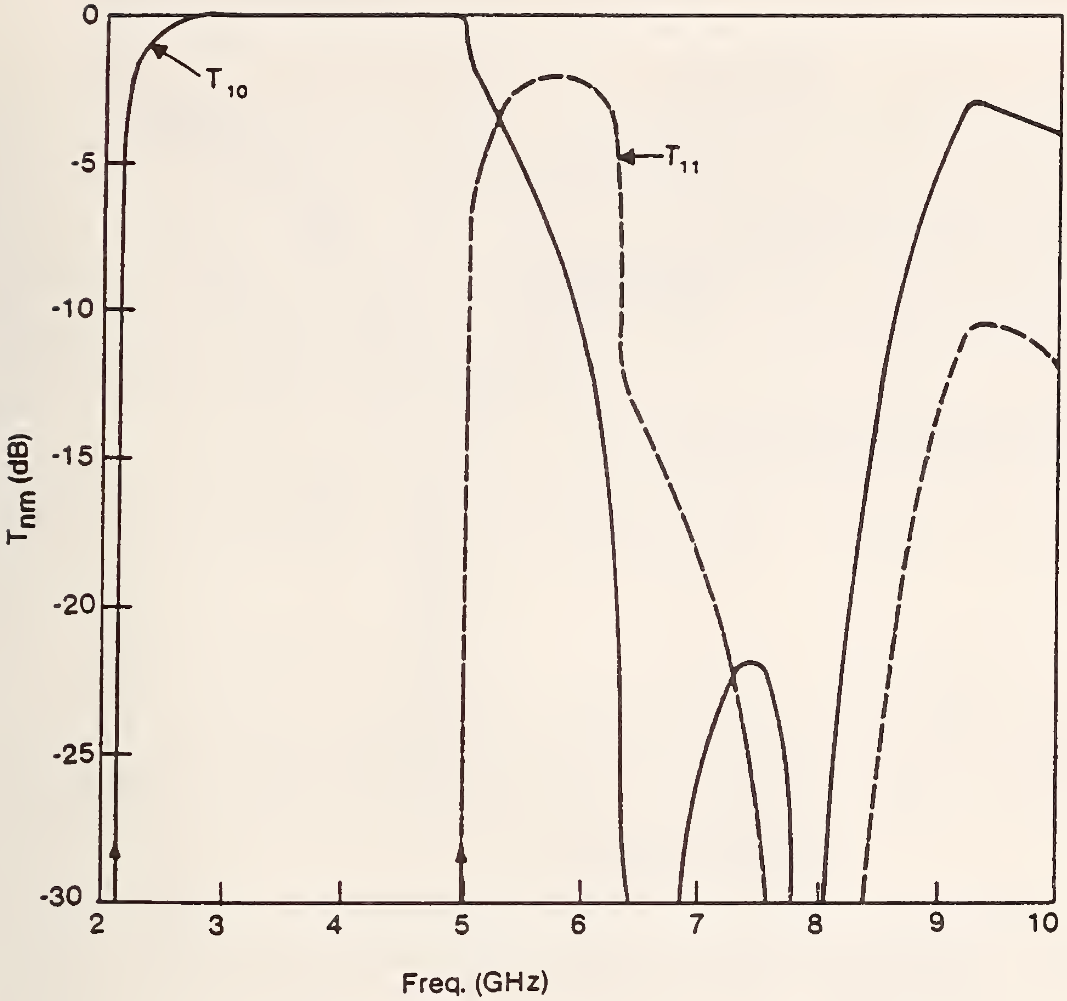

Figure 9.b.5 Transmission coefficients for an S-band coax-to-waveguide adapter. The cutoff frequencies for the dominant (TM^y_{10}) and first higher order (TM^y_{11}) modes are indicated by arrows.

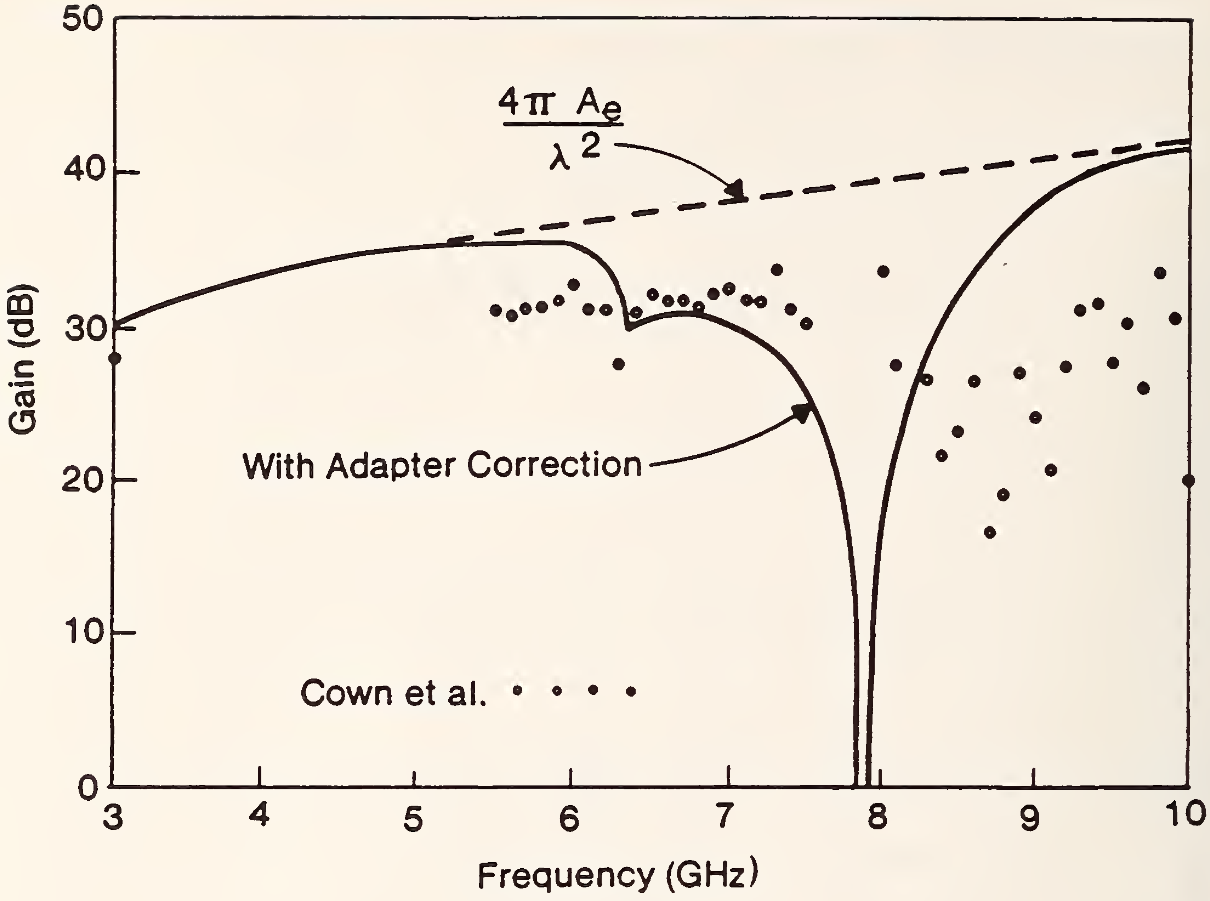

Figure 9.b.6 Comparison of theory (with adapter correction) and experiment [2] for antenna gains as a function of frequency.

9.c CONDUCTED EMC PROBLEMS

As part of the overall EMC goal in an undesired-source environment, one often encounters what are mainly conducted EMI (CEMI) problems. Figure 9.c.1 depicts the basic interference mechanisms between an emitter and a susceptor [1]. The undesired coupling due to radiation is indicated by Paths 1, 2, 3, and 4. Perhaps the most common case of CEMI is the direct conduction of interference via the power line shown as Path 5. However, as indicated in Fig. 9.c.2, other less obvious forms of CEMI occur due to conductive coupling via common ground lines and capacitive and inductive transfers. These paths generally provide well-defined transfer functions, such that the coupled interference can be determined in terms of stray capacitance (C), mutual and self inductances (M and L), and coupling resistance (R). However, leakage paths, pick-up, and reradiation affect the total amount of interference that would otherwise be transmitted along a conducted path. The distinguishing feature of conducted interference is that a conducted path is the primary means by which the source is connected to the susceptor [2].

Thus, the CEMI problems can be approached by examining the three basic areas of emitters, susceptors, and the coupling or transmission paths which inadvertently combine to cause interference. The following discussion provides a brief description of some CEMI problems that are representative of the present attempts to achieve compatibility in the EM environment.

9.c.1 Characterizing CEMI Sources

Unwanted conductive emissions originate in ac power systems due primarily to the direct transients caused by switching reactive loads, relay or breaker contact bounce and restrikes, thyristor (solid-state) phase control, etc., and to induced transients caused by lightning discharges, the coupling from cordless phones, computers, RF-energized lightbulbs, and motorized equipment. One of the fundamental CEMI problems, therefore, is to characterize and model (if possible) the nature of these transients on ac power systems.

An appreciable body of data exists which provides a basis for characterizing the transient disturbances likely to be encountered on land-based ac power systems intended for industrial and residential use [3]-[5]. Although the exact amplitude, waveshape, and duration of these disturbances depend on the cause (lightning, switching transient, induced RF, etc.) and location in the power system (generator, main transmission line, substation, local distribution line, etc.), Fig. 9.c.3 shows a compilation of the frequency of occurence vs. peak amplitude of voltage transients that occur in 220-V and 120-V systems [1]. Obviously, transients often can occur which are 10 times the nominal peak voltage and sometimes can be nearly 100 times larger.

Of primary interest, of course, is the kind of overvoltage transients that can occur at the local distribution transformer, service entrance, and branch circuits of buildings and homes. A considerable amount of study has gone into this problem in order to protect transformers, switchgear, and consumer appliances from damage due to transient "surges" [4]-[9]. From these studies has come a set of test waveforms whose amplitudes, shapes, and durations represent (by consensus) the actual multitude of random, arbitrarily-shaped (conductive) interference waveforms that can appear on an ac power line (see Fig. 9.c.4). Figure 9.c.5 shows the IEEE Std. 587 (now designated ANSI/IEEE C62.41-1980) consensus waveforms and where they are applicable for testing purposes relative to the ac power feeder line [10]. Similarly, Subcommittee 28A of the International Electrotechnical Commission (IEC) has prepared a report in which "Installation Categories" are defined [8].

Nevertheless, problems do remain in that there is still a lack of enough definitive data on the duration, waveform, and source impedance of transient disturbances in land-based ac power circuits. Consequently, attempts to accurately model ac power systems for CEMI analyses, or for component design purposes, are difficult and cumbersome. Bull [11] reports that the impedance of an ac power system seen from the outlets exhibits the characteristics of a 50-Ω resistor with 50 μH in parallel. However, attempts to combine the IEEE Std. 587 6-kV open-circuit voltage with the assumption of a 50-Ω/50-μH impedance resulted in low energy deposition capability in a transient voltage suppression device, contrary to the field experience of these devices [7]. Also, there are some significant differences between the concepts of the IEEE Std. 587 and the IEC 664 report. At present, source impedances (and, thus, current levels) have not been defined in the 664 document.

The problem of characterizing transient disturbances of shipboard power systems has become critical as electronic systems more susceptible to transient interference are placed on the ship powerline buses. The following quote is taken from a recent paper on this subject [12]:

> "Digital systems are particularly susceptible to this wideband interference. It is suspected that many computer programs are reloaded too often because their electronics and/or their signal cables have been exposed to transients, which are either conducted on, or radiated from, powerline buses. Presently, a meager data base exists to describe the magnitude and other characteristics of these powerline transients."

In contrast to land-based ac power systems, there has not been very much information gathered concerning the characteristics of shipboard ac power systems, probably because of the varying configurations and performance requirements for different classes of ships. With the advent of transistors and solid-state electronics appearing in shipboard equipment during the 1960s, staff at the David Taylor Naval Ship Research and Development Center (DTNSRDC) in Annapolis, MD began to concern themselves with transients on shipboard power systems. Some definitive work in establishing a baseline of statistical data was carried out in the late 1960s to gather information on the magnitude of transient disturbances and their frequency of occurrence [13]. Figure 9.c.6 shows a seven-day histogram of the number of transients vs. peak amplitude taken on ships having both 120- and 440-V systems. Note the similarity with land-based frequency of occurrence transients given in Fig. 9.c.3. It appears that the magnitude of shipboard ac power line disturbances and their occurrences correspond approximately to what is considered a low exposure level for land-based systems [7]. This seven-day histogram subsequently became incorporated as part of DoD-Std-1399 [14]. It is interesting to note, however, that the frequency of occurrence histograms given in [12] (taken in 1983) show peak amplitudes considerably lower than the data taken in 1960s (see Fig. 9.c.7).

The lack of a statistically significant data base to characterize the transients on shipboard power systems became problematic when in August, 1982 a program to develop recommendations for voltage "spike" suppressor specifications for Navy ships was undertaken by NBS [15]. The objective of the program was to provide a sound technical basis for shipboard application of transient suppressors, based on analysis of existing field data gathered from shipboard testing. Subsequent investigation of available reports and other data gathered as part of the overall Navy Electric Power Interface Compatibility (EPIC) program revealed that the existing data were far from adequate to develop a meaningful specification.

The EPIC program was established to identify, if possible, the sources of incompatibility between shipboard power systems and user equipment. Some of the main areas of study were voltage interruptions, voltage drops, harmonic distortion, and voltage spikes. For the voltage-spike area, the EPIC test procedures called for specific measurements of spike amplitude, waveshape, frequency of occurrence, and broadband impedance. These quantities are needed in order to determine the peak current and total energy dissipated in a clamping type of suppressor. Figure 9.c.8 shows two examples of the effect of clamping-type suppressors on transients superimposed on a steady-state-power voltage wave. The top example (a) has the clamping level set correctly, whereas the bottom example (b) has the level set too low. Selecting the steady-state voltage rating is obviously important so that the suppressor does not have to absorb excessive amounts of energy in the absence of spikes 1,3, and 5. Figure 9.c.9 shows a circuit for calculating both the peak current and the energy dissipated in a clamping suppressor due to voltage spike, V_s, superimposed on a steady-state voltage, V_{ss}. A total voltage, $V_s + V_{ss}$, is thus imposed upon a circuit which is protected by a clamping suppressor having a clamping voltage V_c, through a source impedance Z_s. Current i_s then exists when $V_s + V_{ss} > V_c$. During this time, the suppressor must absorb energy, E_s:

$$E_s = V_c \int_{t_1}^{t_2} i_s \, dt \, , \tag{9.c.1}$$

where t_1 to t_2 is the time interval during which $V_s + V_{ss} > V_c$, and V_c is assumed to be constant (ideal suppressor). Since it is difficult to measure i_s in practice, an alternate method of determining E_s is to use a recording of the voltage spike together with the measured source impedance as a function of frequency. Then, since $i_s = (V_s + V_{ss} - V_c)/Z_s$, (9.c.1) becomes

$$E_s = \int_{t_1}^{t_2} \frac{V_c(V_s + V_{ss} - V_c)}{Z_s}\, dt, \tag{9.c.2}$$

where $V_c > V_{ss}$, and Z_s is assumed to be constant between times t_1 and t_2.

From the above discussion, it is apparent that data on spike voltage waveshape and duration are important, as are source impedance data, in determining realistic suppressor specifications for energy absorption and peak current ratings. Although a few records were obtained from several ships showing spike voltage waveforms, and a very limited amount of impedance data was taken on two ships, the information available from EPIC program at that time contributed minimally to the development of a possible voltage-spike-suppressor specification. A broadband impedance measuring system (BIMS) was developed for the Navy by a private contractor which can measure the complex impedance at multiple points in a shipboard power system without de-energizing the line or interfering with it. Some of the initial results obtained with this device were reported by NBS [15].

9.c.2 Reducing CEMI Coupling by Grounding Computer Facilities

The principles of good grounding practice are generally well known and described in the literature [2],[5]. However, for the installation and operation of many automatic data processing (ADP) facilities, the problems of CEMI coupling have become significant towards achieving adequate system performance. A special conference on the subject of "Power and Grounding for a Computer Facility" was held at NBS, Gaithersburg, MD in May, 1984. The Institute for Computer Science and Technology at NBS has recently issued a federal information processing standard (FIPS) publication describing techniques of electrical power for ADP installations which deals, among other topics, with problems of grounding [16].

Three fundamental grounding concepts are shown in Fig. 9.c.10. The floating or isolated ground technique is, of course, the most effective means for preventing current in one circuit from coupling into another circuit. Transformer and optical isolation methods are often used for this purpose where the effects of stray winding and case capacitances are minimized by means of electrostatic shields. Single-point grounding is the method by which all ground-return currents are routed to a single reference potential (typically, earth ground), thus preventing any unwanted voltage drops between separate circuit grounds. Where large amounts of line power are supplied to equipment, such as in an ADP facility, maintaining a good single-point ground at the entry for utility, telecommunications, and ADP power is essential. Multipoint grounding is possible where (ideally) a zero-potential, zero-impedance ground plane is available. At frequencies where ground leads and cable lengths become comparable to signal wavelengths, single-point grounding becomes impractical, and multipoint grounding is used to minimize ground lead lengths. If possible, a large conductive body is used for the ground plane to minimize ground loops and equalize "ground potential".

Because of the trend toward increased speed (higher signal bandwidths) and lower signal levels in ADP equipment, computer facilities face stringent grounding requirements. For avoiding CEMI problems, most ADP centers use the approach shown in Fig. 9.c.11 which illustrates several concepts. First, as mentioned above, all electrical services required are located together where interconnecting conducting straps between service-entrance panels can equalize ground voltage differences (for frequencies up to 1-10 MHz). Second, to keep power, neutral, and ground leads short (10 meters or less), a power center (typically, isolation transformer) is used to service each cluster of ADP equipment. This unit provides another degree of single-point and isolated grounding, minimizing any noise-voltage differences that may exist between the service-entrance earth ground and the local room structure grounds. Third, a raised floor support structure is often employed which is intended mainly as a multipoint ground (or signal reference grid) for equalizing potentials between ADP units from either radiated or conducted emissions having frequencies above 1-10 MHz.

Quantifying the effectiveness of these grounding measures remains a problem. Differential and common-mode currents generated by nonlinear loads in ADP equipment can propagate back through isolation transformers and into other victim equipment. These currents collect in ground-plane structures and must be measured with special current probes. The design of such probes and their placement for obtaining a profile of CEMI coupling effects is the subject of present research and development efforts [1]. Noise transients couple into computer systems via rectification processes in dc power supplies, by discharge from statically charged human bodies, via interconnecting data cables, and through small potential differences induced in multipoint grounds. Test-equipment noise simulators are now available which claim to be capable of determining noise voltage and current threshold levels in ADP facilities and other field environments [17].

9.c.3 Measuring CEMI Emission and Susceptibility Levels

A. Emission Testing Because of FCC EMI regulations which must be complied with as of October, 1983, conducted emission limits and the means for testing to meet these limits have become the subjects of many trade-journal articles [18]-[20]. Figure 9.c.12 illustrates the basic conducted emission conditions (noise feedback into the ac power line) that the FCC regulations are aimed at controlling. With the equipment under test powered on, together with associated connecting cables, any conducted coupling (via stray reactances, etc.) can cause common- and differential-mode CEMI currents, I_C and I_D, to be generated on the power line cord. Since the magnitude of these currents depends on the varying ac power line source impedance, the FCC Part 15 Rules establish test procedures that make use of a line-impedance stabilization network (LISN) which has an impedance characteristic as shown in Fig.9.c.13. Various designs for LISN circuits can be used to achieve the desired characteristics. The conventional 50-Ω, 50-μH LISN characteristic is also shown in Fig. 9.c.13. However, a two-section LISN recommended by the VDE also prescribes an impedance characteristic down to 6 Ω at 10 kHz [19] (see Fig. 9.c.14). As indicated in Fig. 9.c.14, conducted emission testing is accomplished by observing the common- and differential-mode peak voltages measured with a spectrum analyzer having a controllable bandwidth [19]. Alternatively, ANSI/IEEE C62.2 calls for a radio-noise-meter measurement in place of spectrum analyzer. Evaluating the conducted emissions from a piece of equipment would ideally require a virtually noise-free environment. A shielded room is recommended (although the FCC does not use one [20]), together with heavy filtering of the ac power lines, and test equipment with noise levels below the specification limits. Because of pickup on the power-line cord (acting as an antenna) by emissions (generally above 10 MHz) from the I/O cables, cable placement should be varied, keeping the line cord rigid, to obtain the highest reading conditions.

Probably the biggest problem in conducted emission testing is keeping tabs on the various FCC (USA), VDE (West Germany/European Common Market), CSA (Canada), SEV (Switzerland), and IEC specifications. Also, in selecting the line filter and/or line capacitors for attenuating noise currents (I_C and I_D in Fig. 9.c.12), the allowable safety limits shown in the following table require tradeoffs to be made [19].

Table 1: Capacitive Current Limits for Grounded Equipment

	Regulation	Limits
United States	UL 478	5 mA, 120 V, 60 Hz.
	UL 1283	0.5 to 3.5 mA, 120 V, 60 Hz.
Canada	CSA 22.2 No. 1	5 mA, 120 V, 60 Hz.
Switzerland	SEV 1054-1 IEC 335-1	0.75 mA, 250 V, 50 Hz.
West Germany	VDE 0804	3.5 mA, 250 V, 50 Hz.

For example, a capacitor that draws a 3.5 mA ground current from the line also provides 15 dB more attenuation to noise emissions above 1 MHz than a capacitor drawing only 0.5 mA of the ground current. Thus, meeting both safety restrictions and passing acceptable conducted emission testing levels (which are subject to change) presents serious considerations. For military applications, there are also a number of EMC standards dealing with component and system performance. MIL-STD-461B, "Electromagnetic Emissions and Susceptibility Requirements for Control of EMI", defines emission and susceptibility limits applicable under various test conditions. Figure 9.c.15 shows the present and proposed conducted emission levels set by the FCC and VDE for both consumer (Class B) and industrial (Class A) "digital" equipment. [FCC Docket 20780 defines equipment in this category as "a device or system that generates timing pulses at rates in excess of 10,000 pulses (cycles) per second and uses digital techniques."] Class B devices comprise computing equipment -- personal computers and peripherals, electronic (TV) games, calculators, watches, etc. -- marketed for home usage. Class A devices include computing products intended for use in commercial, industrial, and business environments. Presently exempt from FCC Part 15 Rules are automotive electronics, industrial control systems, test equipment, medical equipment, and home appliances. FCC conducted emission limits start at 0.45 MHz and extend to 30 MHz, while the VDE regulates down to 0.15 MHz and is proposing limits down to 10 kHz. The upper VDE 0871A specifications (for industrial devices) do not allow the additional 9.5-dB limit above 1.6 MHz permitted by present FCC levels.

One more hitch to the conducted emission testing problem is the question of peak versus "quasi-peak" (QP) measurements. Whereas the peak detector is ideal for observing low-repetition-rate impulses which might cause military systems to malfunction (hence, peak detection is called for in MIL-STD-461B), a QP detector's response is proportional to the subjective annoyance effect experienced by radio broadcast listeners. The Special International Committee for Radio Interference (CISPR) of the IEC also recommends limits that have been adopted by many national regulations throughout the world, based on QP measurements. Figure 9.c.16 shows the relative response of various detectors to an impulse passed through a filter with a -6 dB bandwidth of 9 kHz (as used for conducted emission testing from 150 kHz to 30 MHz) [2]. The CISPR and ANSI detectors are of the QP type (ANSI meter has 600-ms discharge-time-constant). Recently, NBS has been asked to provide traceability for QP-reading meters by calibrating the spectral flatness of impulse generators used to align and calibrate QP meters, particularly those used for emission testing in the military's TEMPEST program [21].

B. Susceptibility Testing The CEMI problems associated with susceptibility testing are mainly (a) characterizing surge protection devices, and (b) determining the conducted impulse susceptibility of line operated devices. In both of these kinds of tests, a reliable source of impulsive waveforms is needed having peak amplitudes in the 1- to 10-kV range with fast front-edge slopes on the order of 1000 V/μs or faster. Such impulse generators are then used to simulate the kind of lightning impulse and other waveshapes discussed in section 9.c.1 specified by IEEE Std 587 [7]. Some initial work in characterizing the breakdown voltage of gas-tube lightning arresters was performed at NBS which relied on the development of a basic circuit for such testing purposes. Errors in the voltage divider (due to time-constant differences between the high- and low-side resistors) were determined for the circuit since these errors are what limit the measurement accuracy in most surge testing applications [22].

Characterizing the properties of surge protection devices has been of major interest, of course, to the manufacturers of these devices. Numerous application guides, handbooks, technical tips, etc. are available for describing these products [23]-[25]. These devices generally fall into two types: crowbar and clamping. Crowbar devices consist mostly of gas breakdown tubes (or "spark gaps"), carbon-block protectors, and solid-state thyristors. Crowbar devices provide a blocking voltage which when exceeded (or when the device is triggered) causes a high-conduction "short" which will continue until the current through the device is brought back to some low level. Clamping devices, on the other hand, perform a voltage-limiting function and depend on their nonlinear impedance, acting in conjunction with the transient source impedance, to limit the surge current. Typical clamping devices consist of reverse selenium rectifiers, avalanche (zener) diodes, and varistors made of materials such as silicon carbide, zinc oxide, etc. The difficulty with all of these devices is that they exhibit properties such as maximum dv/dt or di/dt limits, nonlinear energy absorption ratings, etc., which make their performance in a given application somewhat unpredictable, unless there is a significant data base on which to select a design [4],[6],[7],[15],[23].

Conducted impulse susceptibility testing can be carried out in the inverse fashion used for emission testing. Rather than measuring the emission levels out of the power line cord from equipment under test (see Figs. 9.c.12 and 9.c.14), an impulsive transient or source of noise is injected into the equipment (either in the common or differential mode) by a generator via a suitable LISN circuit. Commercial surge generators are now available on the market which provide plug-in modules that permit surge tests to be made conforming to most of the IEEE, ANSI, IEC, and other telecommunications and automotive engineering surge testing standards [26]. Nevertheless, there are practical difficulties encountered when trying to propagate these standard waveforms through various isolating transformers, filters, lines, and cables [27].

REFERENCES

[1] Showers, R.; et al. Electromagnetic compatibility in power systems. Tutorial Session, Power Electronics Specialists Conference; NBS, Gaithersburg, MD; 1984 June 18-24.

[2] Keiser, B. E. Principles of Electromagnetic Compatibility. Artech House Inc., Revised Edition, 1983; 57-64.

[3] Golde, R. H. The frequency of occurrence and the distribution of lightning flashes to transmission lines. AIEE Trans. 64; 1945.

[4] Martzloff, F. D.; Hahn, G. J. Surge voltage in residential and industrial power circuits. IEEE Trans. Power Apparatus and Systems; PAS-89(6): 1049-1056; 1970 July-August.

[5] Greenwood, A. Electrical Transients in Power Systems. New York, NY: Wiley Interscience; 1971.

[6] IEEE Surge Protective Devices Committee, Bibliography on surge voltages in AC power circuits rated 600 V or less. IEEE Trans. Power Apparatus and Systems, PAS-89(6): 1056-1061; 1970 July-August.

[7] Martzloff, F. D. The development of a guide on surge voltages in low voltage AC power circuits. Report 81CRD047, General Electric, Schenectady, NY; 1981 (Basis for IEEE Standard 587-1980).

[8] IEC Working Group 28A, Insulation coordination within low-voltage systems, including clearances and creepage distances for equipment. IEC Report 664; 1980.

[9] Fisher, F. A.; Martzloff, F. D. Transient control levels. IEEE Trans. Power Apparatus and Systems, PAS-95(1); 1976 January-February.

[10] Fisher, F. A.; Martzloff, F. D. Surge Protection Test Handbook, Burlington, MA: KeyTek Instrument Corp.; 1982.

[11] Bull, J. H. Impedance on the supply mains at radio frequencies. Proc. 1st Symp. Tech. Exhibition on EMC; 1975 May; Montreux, Switzerland. .

[12] Dixon, D. S.; et al. Measurement of voltage transients on the 60 Hz powerline of an operational Naval platform. IEEE Symp. on EMC; 1984 April; San Antonio, TX.

[13] Cannova, S. F. Investigation of short-time voltage transients in shipboard electric power systems. Lab Project 940-55, Progress Report 1, U. S. Naval Applied Science Laboratory; 1968 September 12.

[14] Cannova, S. F. Interface standard for shipboard systems. DoD-STD-1399 (Navy), Section 300; 1978 August 1.

[15] Laug, O. B.; Hillhouse, D. L. Analysis of requirements for shipboard voltage spike suppressors. Nat. Bur. Stand. (U.S.) Int. Rept. 84-2855 (For official distribution only); Gaithersburg, MD; 1984 March.

[16] Laug, O. B.; Hillhouse, D. L. Guideline on electrical power for ADP installations. FIPS PUB 94, 29-51; 1983 September 21.

[17] Vogul, W. The susceptibility of computer systems to noise transients; countermeasures and test equipment. CIGRE paper published by Study Committee 36 (Interference), ELECTRA, no. 83.

[18] Head, M. Know RF-emission regulations pertaining to your designs. 149-154, EDN; 1981 August 19.

[19] Mitchell, W. T. FCC and VDE impose tight conducted RFI/EMI specs. 141-147, Electronic Design; 1982 December 23.

[20] Dash, G. Understanding EMI test methods eases product acceptance. 183-191, EDN; 1983 May 26.

[21] Private communication from J. Durant, Eaton Instruments Division of AILTECH Corp. to B. A. Bell, Electrosystems Division, NBS.

[22] Hillhouse, D. L. Circuit for impulse testing of gas tube lightning arrestors. IEEE Trans. Communications, COM-20(5): 936-941; 1972 October.

[23] Hillhouse, D. L. Transient Voltage Suppression Manual, Auburn, NY: 4th edition, Semiconductor Products Dept., General Electric, 1983.

[24] Gloer, H. N. Voltage transients and the semiconductor. The Electronic Field Engineer, 2, no. 2; 1979 March/April.

[25] Clark, O. M. EMP Transient suppression Using the Transzorb. Tempe, Arizona: General Semiconductor Industries, Inc., 1979.

[26] Clark, O. M. Transient testing is spreading to systems designers. Electronic Design; 1976 May 10.

[27] Martzloff, F. D. The propagation and attenuation of surge voltages and surge currents in low voltage AC circuits. IEEE Trans. Power Apparatus and Systems, PAS-102, no. 5; 1983 May.

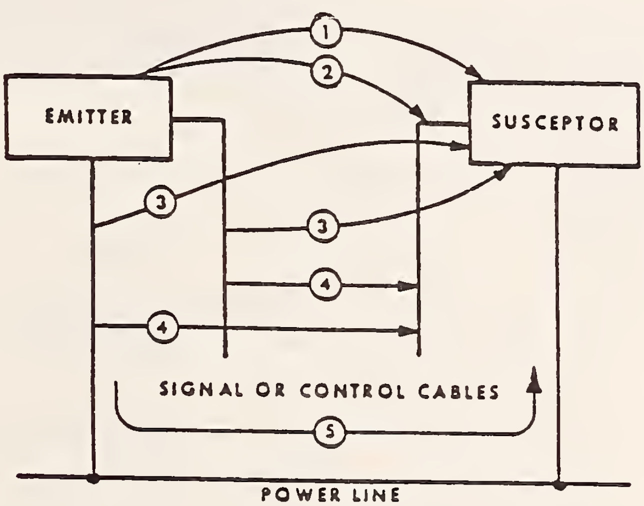

A. RADIATION FROM SOURCE CASE TO SUSCEPTOR CASE AND CABLES (1 and 2).

B. RADIATION FROM SOURCE CABLES (ESPECIALLY THE POWER CABLE) TO SUSCEPTOR CASE AND CABLES (3 and 4).

C. DIRECT CONDUCTION FROM SOURCE TO SUSCEPTOR VIA A COMMON CONDUCTOR, FOR EXAMPLE, THE POWER LINE (5).

Figure 9.c.1 Basic interference coupling mechanisms (from [1]).

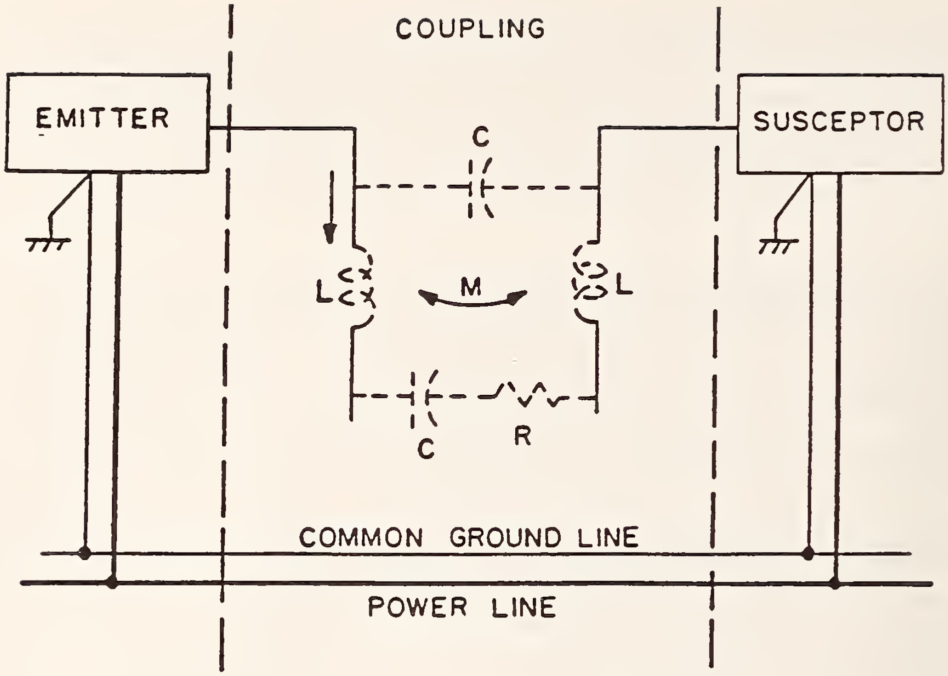

Figure 9.c.2 Ground line and reactance-coupled CEMI.

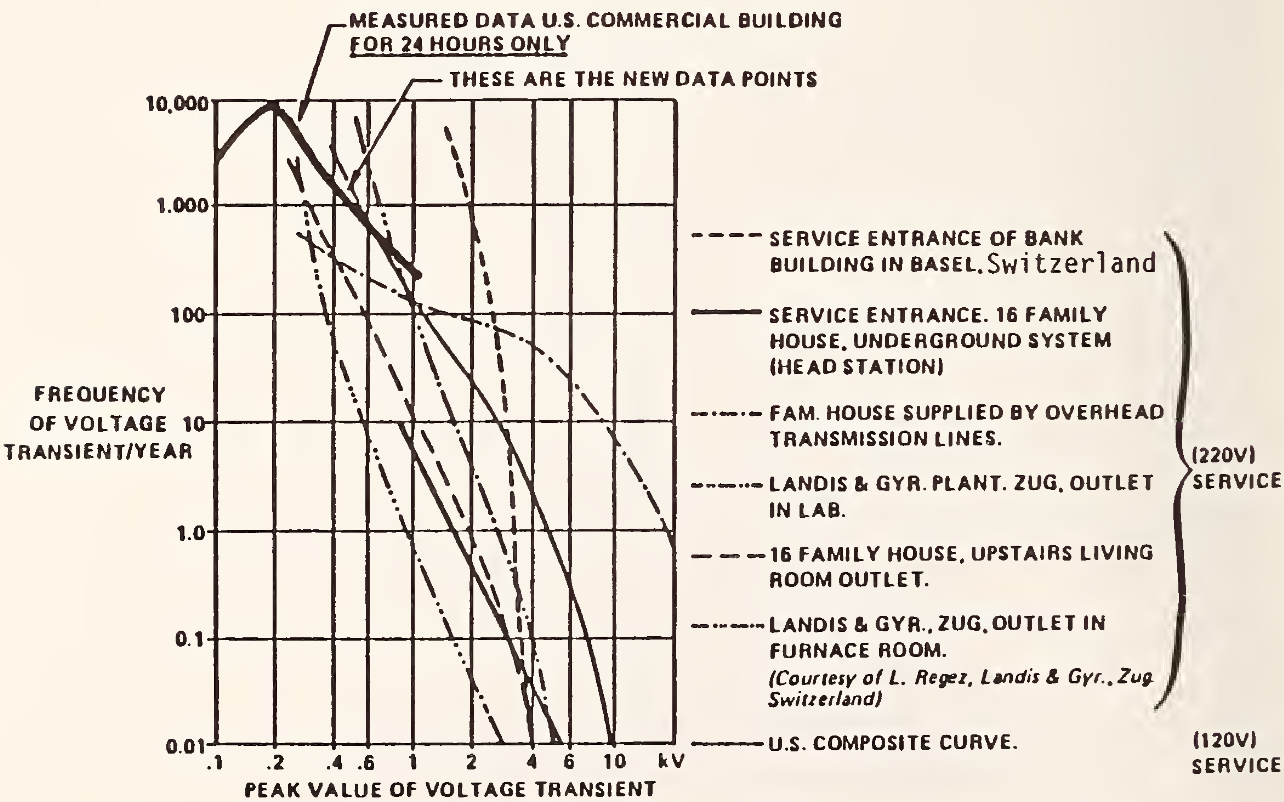

Figure 9.c.3 Frequency of occurrence of transient overvoltages in 220-V and 120-V systems (from [1]).

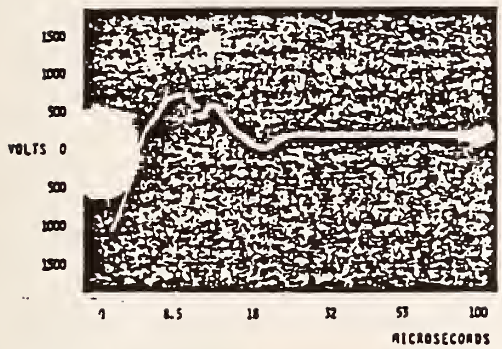

Figure A1. Transient recorded during starting of a furnace blower at service box

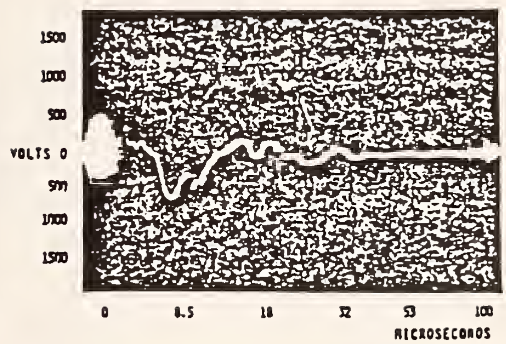

Figure A3. Transient recorded during unidentified disturbance at service box

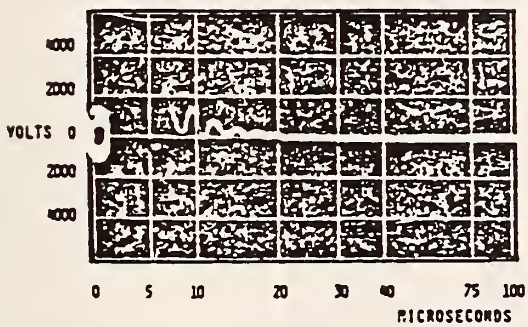

Figure A2. Transient recorded during lightning storm on street pole

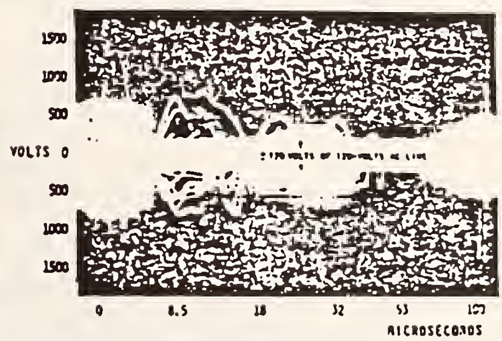

Figure A4. Composite recording of furnace ignition transformer transients over 24 hours at service box

Figure 9.c.4 Typical waveshapes of ac power line transients (from [9]).

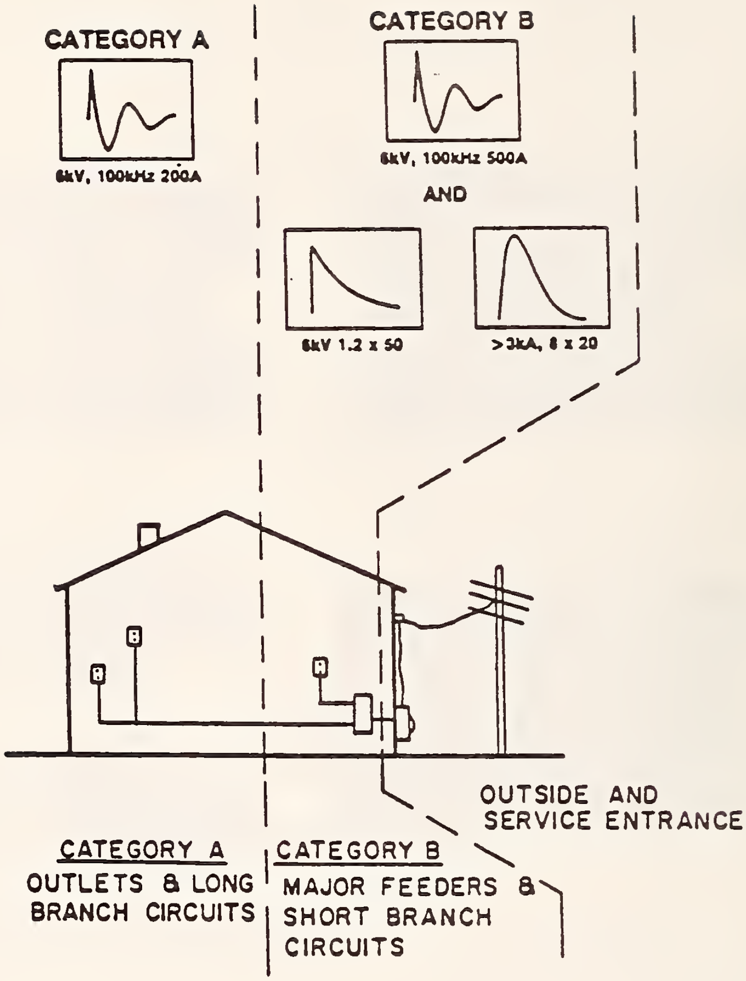

Figure 9.c.5 IEEE Std. 587 test waveforms relative to the ac power feeder line (from [7] and [10]).

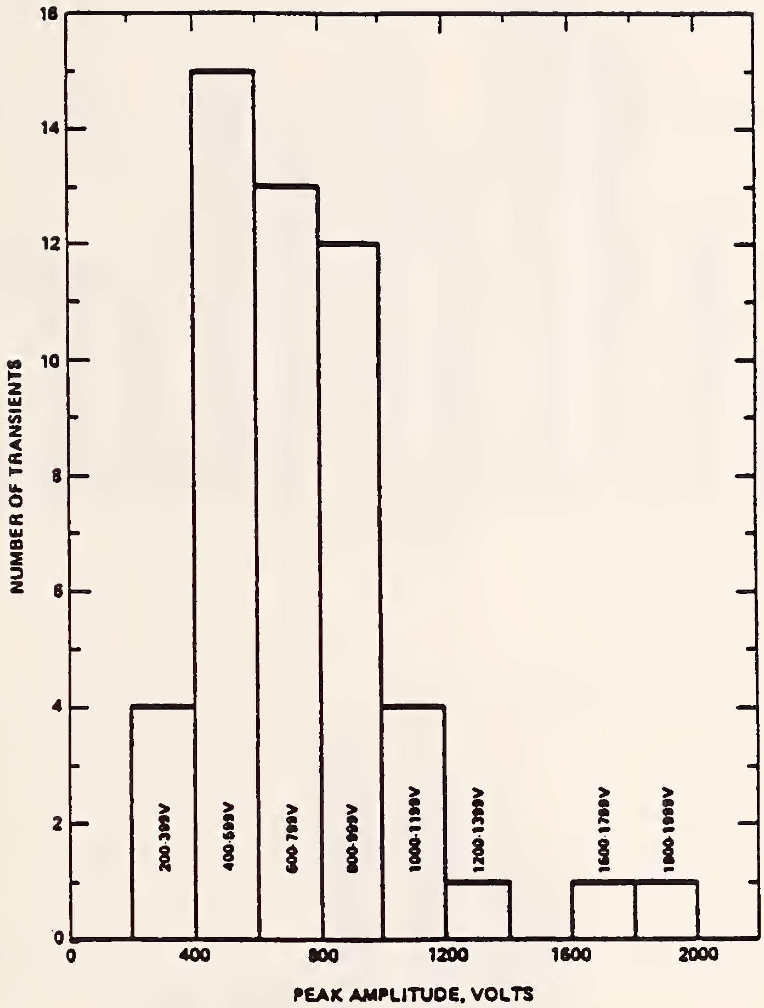

Figure 9.c.6 Seven-day histogram of shipboard transient voltages in 120- and 440-V systems (from [13] and [14]).

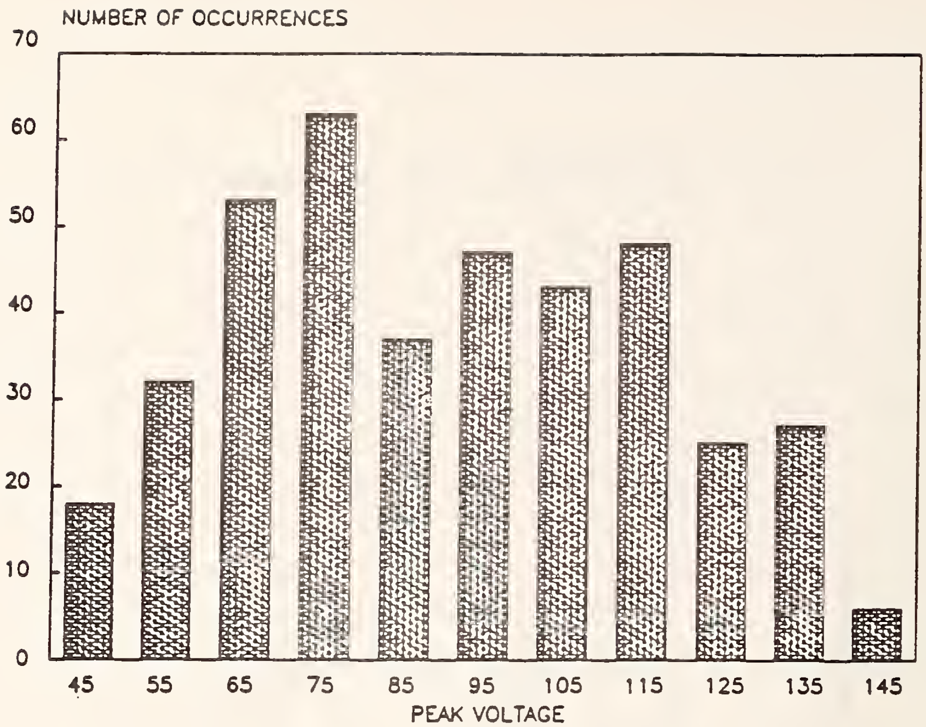

(a)

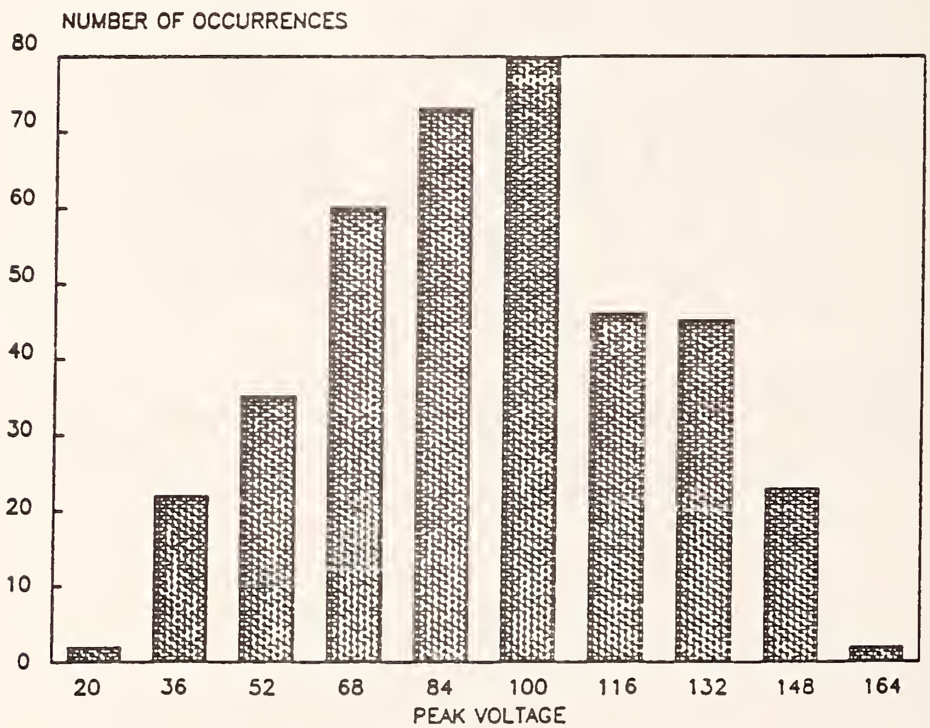

(b)

Figure 9.c.7 75-hour histograms of voltage transients recorded on the 450-V, 60-Hz power panel of an operational Naval platform, (a) measurement system #1, (b) measurement system #2 (from [12]).

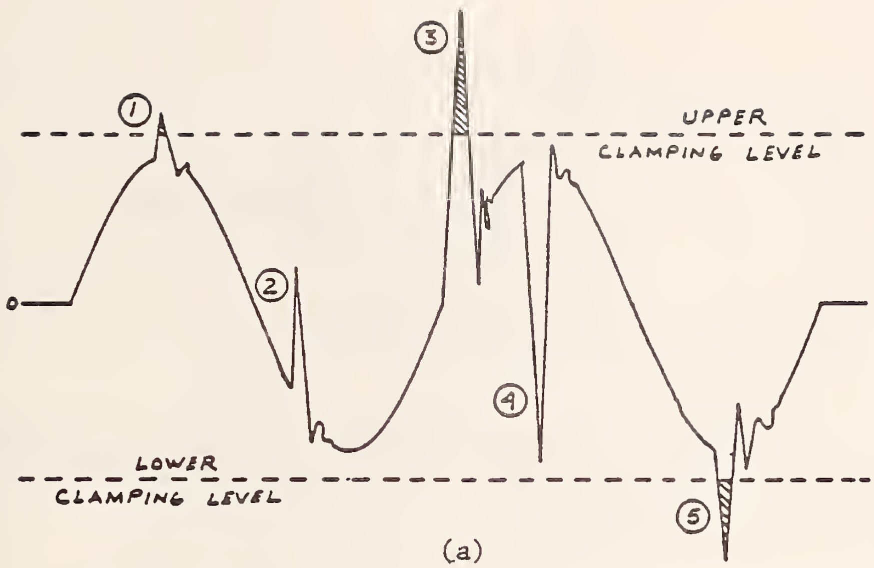

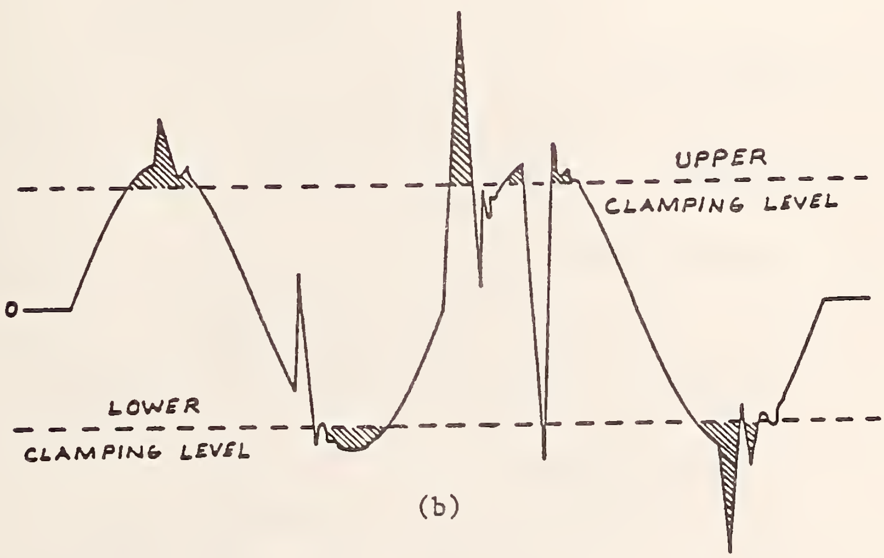

Figure 9.c.8 Steady-state power voltage wave (60 or 400 Hz) with superimposed transients, showing the effect of clamping-type suppressors on such transients (a) when the clamping level is set correctly; and (b) when the clamping level is set too low.([15]).

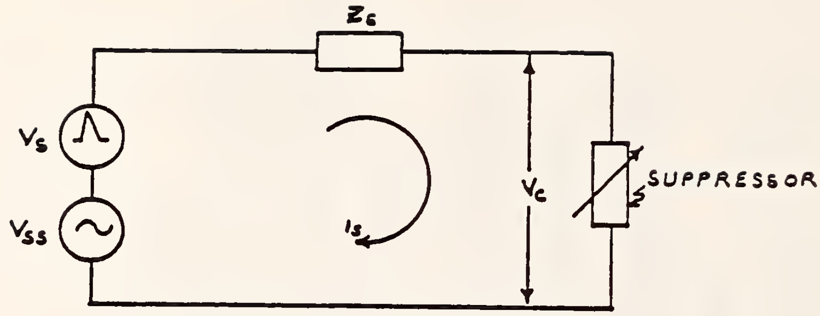

Figure 9.c.9. Circuit for calculating the current and energy dissipated in a clamping suppressor (from [15]).

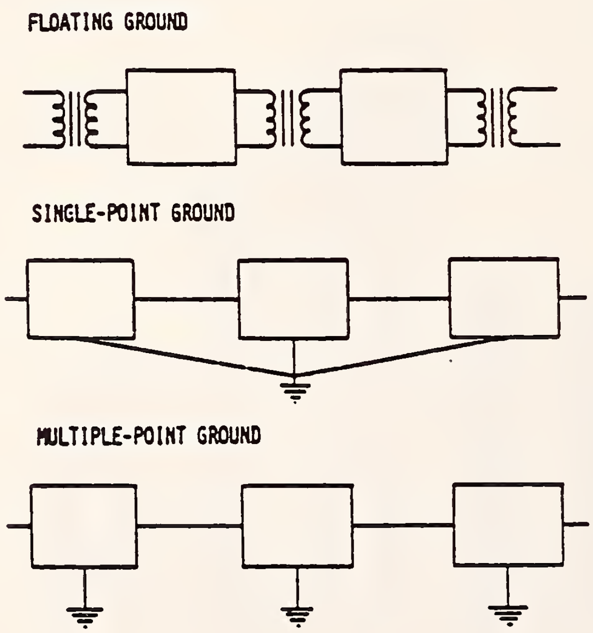

Figure 9.c.10 Fundamental grounding concepts (from [2]).

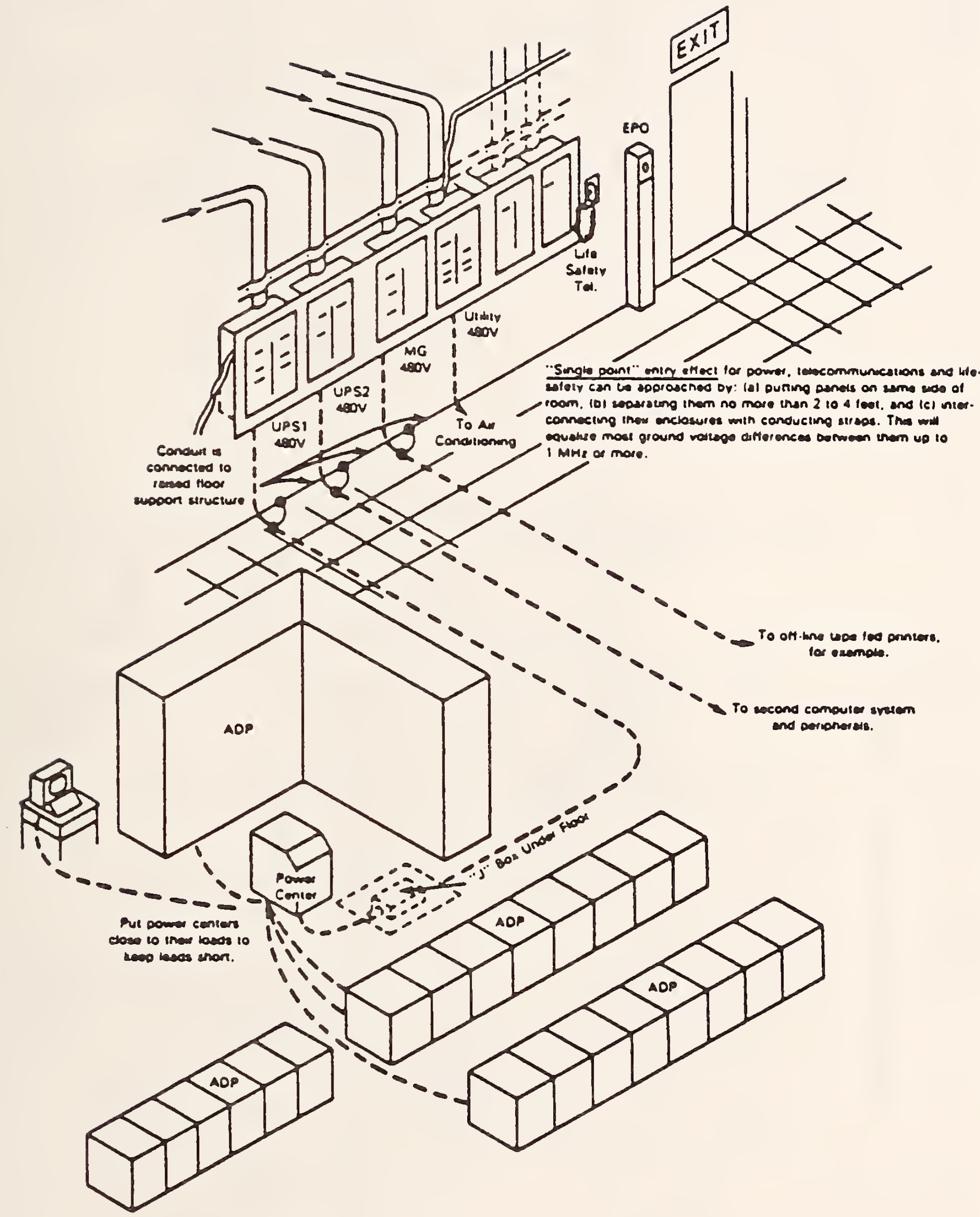

Figure 9.c.11 Electrical interface location for an ADP facility (from [16]).

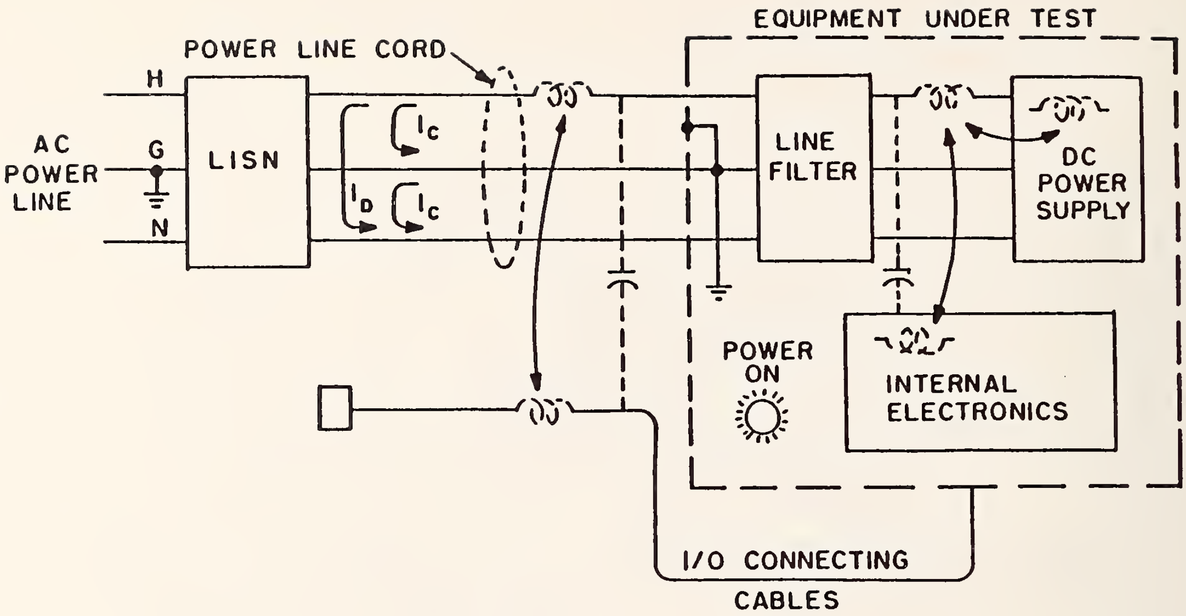

Figure 9.c.12. Basic conducted emission test conditions controlled by FCC (parts 15 and 18) Rules.

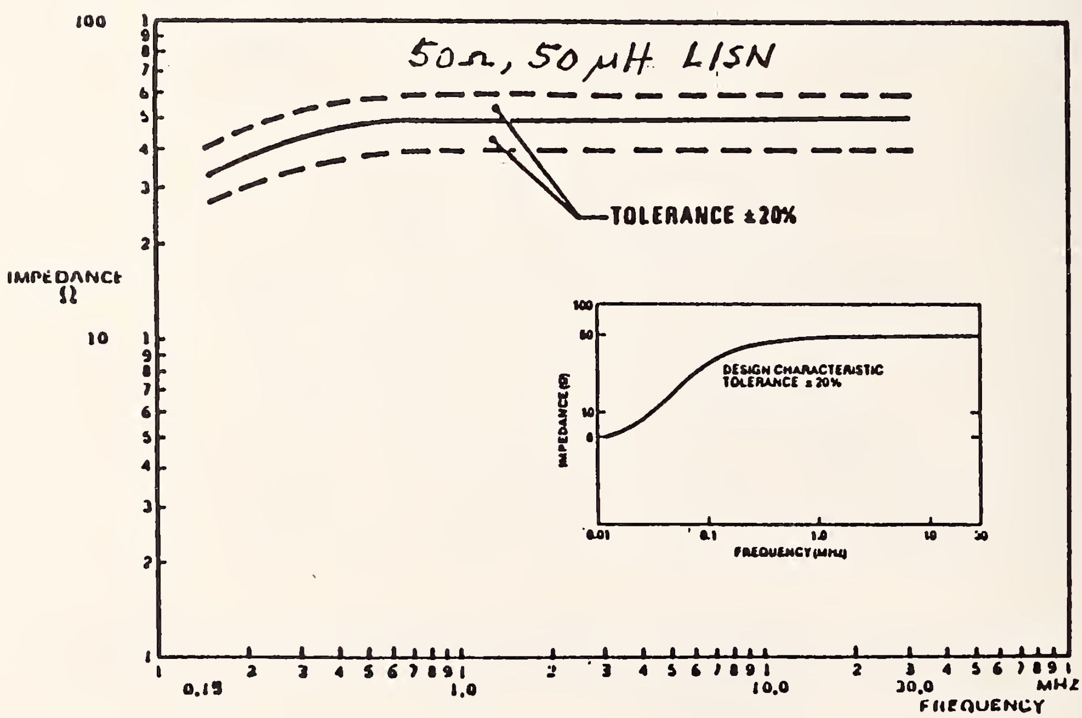

Figure 9.c.13 Line-impedance characteristic (inset) for making conducted emission measurements, as mandated by FCC Docket 20780, (from [1] and [18]).

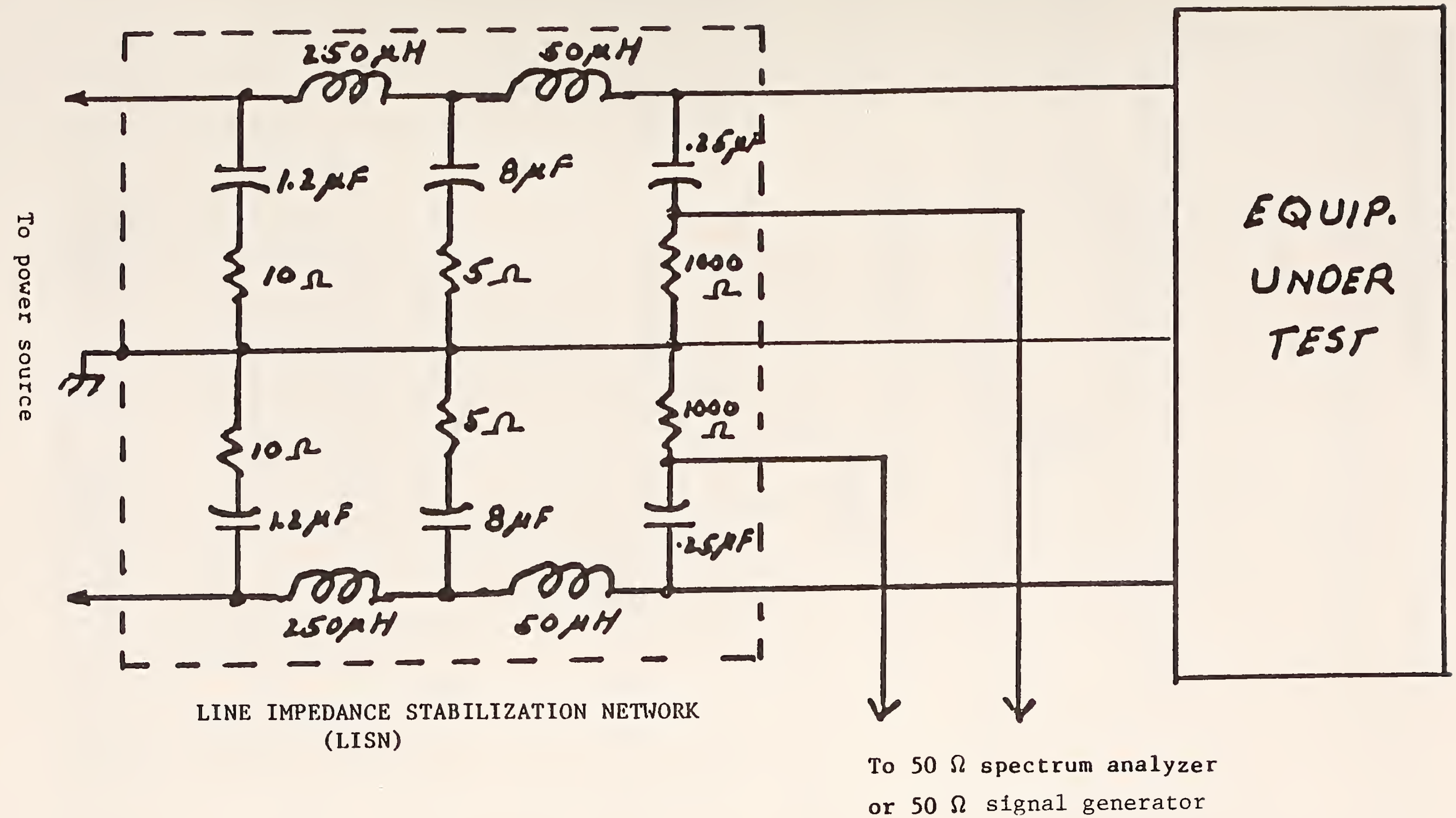

Figure 9.c.14 Circuit details of 50-Ω-level LISN for monitoring conducted noise emissions of equipment (from [19]).

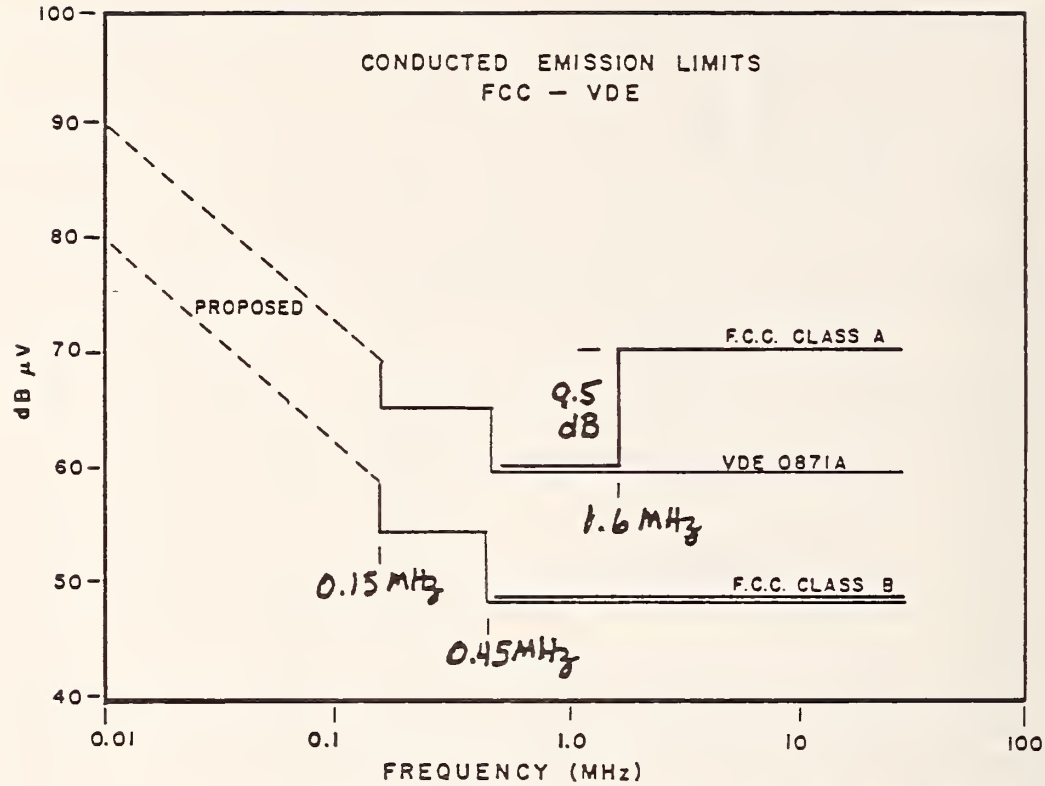

Figure 9.c.15 Conducted emission limits set by the FCC and VDE (from [19]).

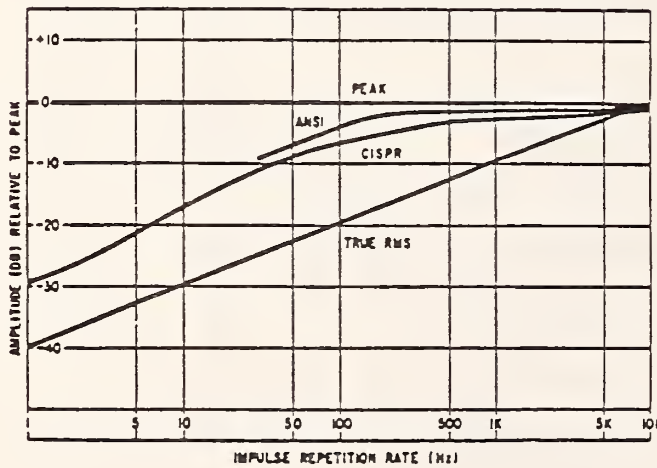

Figure 9.c.16 Relative response of various detectors to an impulse passed through a filter with a -6 dB bandwidth of 9 kHz (from [2]).

☆U.S. GOVERNMENT PRINTING OFFICE: 1986 672-641/45286

NBS-114A (REV. 2-80)

U.S. DEPT. OF COMM. BIBLIOGRAPHIC DATA SHEET (See instructions)	1. PUBLICATION OR REPORT NO. NBS/TN-1099	2. Performing Organ. Report No.	3. Publication Date July 1986

4. TITLE AND SUBTITLE

Electromagnetic Compatibility and Interference Metrology

5. AUTHOR(S)

M. T. Ma and M. Kanda

6. PERFORMING ORGANIZATION (If joint or other than NBS, see instructions)

NATIONAL BUREAU OF STANDARDS
DEPARTMENT OF COMMERCE
WASHINGTON, D.C. 20234

7. Contract/Grant No.

8. Type of Report & Period Covered

9. SPONSORING ORGANIZATION NAME AND COMPLETE ADDRESS (Street, City, State, ZIP)

10. SUPPLEMENTARY NOTES

☐ Document describes a computer program; SF-185, FIPS Software Summary, is attached.

11. ABSTRACT (A 200-word or less factual summary of most significant information. If document includes a significant bibliography or literature survey, mention it here)

The material included in this report is intended for a short course on electromagnetic compatibility/interference (EMC/EMI) metrology to be offered jointly by the staff of the Fields Characterization Group (723.03) and the Interference Characterization Group (723.04) of the Electromagnetic Fields Division (723). The purpose of this short course is to present a review of some of the radiated EMC/EMI measurement methods, to which the National Bureau of Standards (NBS) at Boulder, Colorado, has made significant contributions during the past two decades. The technical foundation for these methods, and interpretations of the measured results are emphasized, as well as strengths and limitations. The entire course is presented in nine chapters with the introductory part given as Chapter 1. The particular measurement topics to be covered are: i) open sites (Chapters 2 and 6), ii) transverse electromagnetic cells (Chapter 3), iii) techniques for measuring the electromagnetic shielding of materials (Chapter 4), iv) anechoic chambers (Chapter 5), and v) reverberating chambers (Chapter 8). In addition, since small probe antennas play an important role in some of the EMC/EMI measurements covered herein, a separate chapter on various probe systems developed at NBS is given in Chapter 7. Selected contemporary EMI topics such as the characterization and measurement of a complex EM environment, interferences in the form of out-of-band receptions to an antenna, and some conducted EMI problems are also briefly discussed (Chapter 9).

12. KEY WORDS (Six to twelve entries; alphabetical order; capitalize only proper names; and separate key words by semicolons)

anechoic chamber; complex electromagnetic environment; conducted electromagnetic interference (CEMI); electromagnetic compatibility (EMC); measurement methodology; open sites; out-of-band responses; probes; radiated electromagnetic interference (EMI); reverberating chamber; shielding of materials; transverse electromagnetic (TEM) cell.

13. AVAILABILITY

☒ Unlimited
☐ For Official Distribution. Do Not Release to NTIS
☒ Order From Superintendent of Documents, U.S. Government Printing Office, Washington, D.C. 20402.
☐ Order From National Technical Information Service (NTIS), Springfield, VA. 22161

14. NO. OF PRINTED PAGES

178

15. Price

USCOMM-DC 6043-P80

NBS Technical Publications

Periodical

Journal of Research—The Journal of Research of the National Bureau of Standards reports NBS research and development in those disciplines of the physical and engineering sciences in which the Bureau is active. These include physics, chemistry, engineering, mathematics, and computer sciences. Papers cover a broad range of subjects, with major emphasis on measurement methodology and the basic technology underlying standardization. Also included from time to time are survey articles on topics closely related to the Bureau's technical and scientific programs. Issued six times a year.

Nonperiodicals

Monographs—Major contributions to the technical literature on various subjects related to the Bureau's scientific and technical activities.

Handbooks—Recommended codes of engineering and industrial practice (including safety codes) developed in cooperation with interested industries, professional organizations, and regulatory bodies.

Special Publications—Include proceedings of conferences sponsored by NBS, NBS annual reports, and other special publications appropriate to this grouping such as wall charts, pocket cards, and bibliographies.

Applied Mathematics Series—Mathematical tables, manuals, and studies of special interest to physicists, engineers, chemists, biologists, mathematicians, computer programmers, and others engaged in scientific and technical work.

National Standard Reference Data Series—Provides quantitative data on the physical and chemical properties of materials, compiled from the world's literature and critically evaluated. Developed under a worldwide program coordinated by NBS under the authority of the National Standard Data Act (Public Law 90-396).
NOTE: The Journal of Physical and Chemical Reference Data (JPCRD) is published quarterly for NBS by the American Chemical Society (ACS) and the American Institute of Physics (AIP). Subscriptions, reprints, and supplements are available from ACS, 1155 Sixteenth St., NW, Washington, DC 20056.

Building Science Series—Disseminates technical information developed at the Bureau on building materials, components, systems, and whole structures. The series presents research results, test methods, and performance criteria related to the structural and environmental functions and the durability and safety characteristics of building elements and systems.

Technical Notes—Studies or reports which are complete in themselves but restrictive in their treatment of a subject. Analogous to monographs but not so comprehensive in scope or definitive in treatment of the subject area. Often serve as a vehicle for final reports of work performed at NBS under the sponsorship of other government agencies.

Voluntary Product Standards—Developed under procedures published by the Department of Commerce in Part 10, Title 15, of the Code of Federal Regulations. The standards establish nationally recognized requirements for products, and provide all concerned interests with a basis for common understanding of the characteristics of the products. NBS administers this program as a supplement to the activities of the private sector standardizing organizations.

Consumer Information Series—Practical information, based on NBS research and experience, covering areas of interest to the consumer. Easily understandable language and illustrations provide useful background knowledge for shopping in today's technological marketplace.

Order the **above** *NBS publications from: Superintendent of Documents, Government Printing Office, Washington, DC 20402.*

Order the **following** *NBS publications—FIPS and NBSIR's—from the National Technical Information Service, Springfield, VA 22161.*

Federal Information Processing Standards Publications (FIPS PUB)—Publications in this series collectively constitute the Federal Information Processing Standards Register. The Register serves as the official source of information in the Federal Government regarding standards issued by NBS pursuant to the Federal Property and Administrative Services Act of 1949 as amended, Public Law 89-306 (79 Stat. 1127), and as implemented by Executive Order 11717 (38 FR 12315, dated May 11, 1973) and Part 6 of Title 15 CFR (Code of Federal Regulations).

NBS Interagency Reports (NBSIR)—A special series of interim or final reports on work performed by NBS for outside sponsors (both government and non-government). In general, initial distribution is handled by the sponsor; public distribution is by the National Technical Information Service, Springfield, VA 22161, in paper copy or microfiche form.

U.S. Department of Commerce
National Bureau of Standards
Gaithersburg, MD 20899

Official Business
Penalty for Private Use $300